SYNTHESIS OF HIGHLY ACTIVE UNSUPPORTED MOLYBDENUM SULFIDE CATALYSTS FOR HYDRODESULFURIZATION AND HYDRODEOXYGENATION

by

Haiping Zhang

M.Sc.E., Tianjin University, P. R. China

A Dissertation Submitted in Partial Fulfillment
of the Requirements for the Degree of

Doctor of Philosophy (Ph.D)

in the Graduate Academic Unit of **Chemical Engineering**

Supervisor:	Ying Zheng, Ph.D, Chemical Engineering
Examining Board:	Sara Eisler, Ph.D, Chemistry
	Yonghao Ni, Ph.D, Chemical Engineering
	Laura Romero-Zerón, Ph.D, Chemical Engineering
External Examiner:	Ajay K. Dalai, Ph.D, Department of Chemical & Biological Engineering, University of Saskatchewan

This dissertation is accepted by the

Dean of Graduate Studies

THE UNIVERSITY OF NEW BRUNSWICK

October 2014

ABSTRACT

The rigorous regulation on sulfur emission calls for newly designed catalysts with deep hydrodesulfurization capability. This has triggered a significant increase in research activities to seek suitable materials and synthesis techniques. Unsupported MoS_2 becomes a good candidate as it possesses high catalytic activity and thermo stability. However, so far it is still a challenge to synthesize a dispersed MoS_2 catalyst with low-cost precursors and simple methods. In this thesis, a novel hydrothermal method was developed using MoO_3, Na_2S, and HCl as precursors for the synthesis of unsupported MoS_2. Several key factors that influence the catalyst synthesis and performance were carefully investigated, including the ratio of precursors, synthesis temperature, initial temperature, solvents, and promoters. Various characterization techniques, including XRD, TEM, SEM, XANES, EXAFS, Auto-sorb, TPR, microprobe analyzer, XPS, EDX, etc., were used to identify the crystalline structures of synthesized catalysts and to establish the relationship between their structures and hydrotreating activities.

The hydrothermal synthesis method was successfully established. Results show that the weakly acidic medium is beneficial to the formation of MoS_2. Proper MoO_3/Na_2S ratios lead to characteristics, such as nanocrystalline structure and large surface areas and pore volumes. Both the synthesis temperature and the initial temperature are key factors for the nucleation and growth of MoS_2. A minimum synthesis temperature exists for the formation of crystalline structure, and high synthesis temperatures results in curved and shortened slabs. A high initial temperature benefits fast nucleation, thus leading to shorter slabs. Organic solvent (decalin) and supercritical heptane can dramatically change the

aqueous environment. MoS_2 slabs could be bent with the addition of decalin, and the curvature degree increases with the increase of decalin amounts. Supercritical heptane aids the creation of highly curved catalysts with better HDS performance (92.95% S conversion).

The synthesized MoS_2 catalysts were applied for the HDS of light cycle oil and for deoxygenation of waste cooking oil and canola oil to investigate the catalysis mechanisms. A new insight is proposed to distinguish the roles of promoters on deoxygenation pathways. NiMoS creates abundant sulfur vacancies that improve the hydrodeoxygenation, while CoMoS shows saturated edge sites in hydrogen atmosphere and facilitates the hydrodecarbon(x)ylation. From a kinetic model of deoxygenation process over CoMoS, it is found that direct hydrodecarbonylation of fatty acids dominates the hydrodecarbon(x)ylation routes; in the hydrodeoxygenation route, the reduction of fatty acids to alcohols is the rate limiting step in the production of C_{18} hydrocarbons from fatty acids.

ACKNOWLEDGEMENT

Foremost, I would like to express my deepest gratitude to my supervisor Prof. Ying Zheng for her persistent guidance and continuous encouragement throughout my Ph. D study. This thesis would not have been done without her help and support. I was impressed by her enthusiasm with research and I benefited from every insightful discussion and constructive suggestions she gave me.

I would also like to show my sincere appreciation to Dr. Hongfei Lin, who warmly and generously provided help and valuable advice during my research from the very beginning to the end of my thesis.

My special thanks goes to Dr. Qikai Zhang for his warm encouragement on my research and great help in experimental design.

I also want to thank all my good friends and colleagues, Hui Wang, Xue Han, Peng Feng, Majid sharif Vaghefi, Jillian Blanchard and Kyle Rogers. Thanks for the companions, support and friendship. It was such a pleasure working with all of them.

Last but not the least, I want to show my deepest thankfulness to my husband, Weizhi Wang, who has always been there for me. I also want to thank my parents and parents in law for their patience and support.

TABLE OF CONTENT

LIST OF TABLES

LIST OF FIGURES

LIST OF ABBREVATIONS

1, 2 or 3MBT: Benzothiophene with one, two or three methyl substitutes

1, 2, or 3 MDBT: Dibenzothiophene with one, two or three methyl substitutes

4, 6-DMDBT: 4, 6-dimethyldibenzothiophene

ABT: Alkyl benzothiophene

ADBT: Alkyl dibenzothiophene

API: American Petroleum Institute

BT: Benzothiophene

CN: Coordination number

COR: Catalyst to oil ratio

DBT: Dibenzothiophene

DDO: Direct deoxygenation

DDS: Direct desulfurization

DFT: Density functional theory

DMDS: Dimethyl disulfide

EDX: Energy-dispersive X-ray spectroscopy

EMP: Electron microprobe

EXAFS: Extended X-ray absorption fine structure

FAME: Fatty acid methyl ester

FCC: Fluid catalytic cracking

FID: Flame Ionization Detector

FTIR: Fourier transform infrared spectroscopy

GC: Gas chromatography

GC-MS: Gas chromatography and mass spectrometry

GHG: Green-house gas

HDN: Hydrodenitrogenation

HDO: Hydrodeoxygenation

HDS: Hydrodesulfurization

HPLC: High performance liquid chromatography

HYD: Hydrogenation

LCO: Light cycle oil

MDBT: Methyl substituted dibenzothiophene

NMR: Nuclear magnetic resonance

PFPD: Pulsed flame photometric detector

SAD: Selected area electron diffraction

SEM: Scanning electron microscopy

STM: Scanning tunneling microscope

TAN: Total acidity number

TCD: Thermal conductivity detector

TEM: Transmission electron microscopy

TPR: Temperature-programmed reduction

ULSD: Ultra-low sulfur diesel

WCO: Waste cooking oil

XAFS: X-ray absorption fine structure

XANES: X-ray absorption near edge structure

XPS: X-ray photo electron spectroscopy

Chapter 1 Introduction

1.1 Unsupported sulfide catalysts as model system in hydrodeoxygenation

With the growing awareness of the global energy crisis and concern of green-house gas (GHG) and other toxic gas emissions, people have been driven to seek alternative resources for the replacement of the existing petroleum-derived fuels. Biomass-derived diesel that has near zero net life-cycle GHG and reduced or no toxic gas emissions (e.g. NO_x, SO_x) is one of the good candidates [1, 2]. The first generation of biodiesel was fatty acid methyl ester (FAME) produced from agricultural crops through transesterification [3-5]. However, the high oxygen content in FAME leads to poor storage stability and cold flow properties, which lower its compatibility with petroleum diesel and existing auto engines [6, 7].

To overcome these drawbacks, second generation biodiesel goals are to produce oxygen-free hydrocarbons through a hydrotreating process. The corresponding upgrading process is called hydrodeoxygenation (HDO), which requires an appropriate catalyst. Among all the possible candidates, researchers are committing to use sulfided molybdenum based catalysts (i.e. traditional HDS catalysts) in order to utilize the current infrastructure [8, 9]. However, due to the distinct differences in the sulfur and oxygen compounds, the role of catalysts in HDO reactions could be altered significantly. Without clear knowledge of the mechanisms, the development of suitable catalysts will be difficult to achieve. Therefore, theoretical study on the catalytic mechanism of HDO becomes significantly important.

Currently, sulfided molybdenum catalysts are commonly used with porous support, such as Al_2O_3 and zeolites [10, 11]. However, these support materials usually have acidity and interact with active metals, which may cover the intrinsic characteristics of the metals. It is reported that the catalyst support alumina has catalytic activity in hydrotreating reactions due to the presence of Lewis acid sites [12]. Thus, the use of unsupported catalysts, without the interference of support, is a good alternative to investigate the role of the active phase as a model system [13]. Additionally, the system can also be simplified by minimizing the secondary effects, e.g. adsorption, re-adsorption, and mass transfer resistance that may affect the reaction kinetics.

1.2 Synthesis of nanosized unsupported MoS_2

Unsupported MoS_2 can be synthesized in many ways, including solid-gas sulfidation, thermal decomposition, solution reactions, hydrothermal and solventothermal preparations, etc. [14-18]. Within these methods, the hydrothermal preparation is a promising technique, and is rapidly being developing [19-21]. The catalysts synthesized by the hydrothermal method usually exhibit high purity and high dispersion properties. Besides, the easy control of various operating conditions allows researchers to try more combinations for the improvement of catalysts. It has been reported that a number of factors in a sythesis reaction can influence the quality of the catalysts, including precusor ratios, solvent, pH value, gaseous enviroment, temperature, etc. [20-22]. Each factor may have a unique effect on the catalytic performance or may interact with other factors. Since the performance of a MoS_2 is associated with its crystalline structures, such effects must take place via the alternation of the crystalline structure of MoS_2.

The basic crystalline structure of MoS_2 has been well documented [14, 23, 24]. It has a stacked layered structure where layers are bonded by weak Van der Waals forces. Within a layer, each Mo (IV) center is bounded to six sulfurs to form a trigonal prismatic coordination, while every sulfur atom is connected with three Mo centers, forming pyramidal interstices. It is generally accepted that the catalytic activity is attributed to the defects (imperfections in the MoS_2 matrix) on the edge plane, while the basal plane is catalytically inert [25-27]. However, recent studies discovered that active sites can also be generated on curved basal planes, which provides a new insight on the synthesis of MoS_2 [19, 28, 29]. According to these findings, this thesis focuses on increasing the edge area, decreasing crystalline sizes, and enlarging curvatures on basal planes of MoS_2.

1.3 Introduction of new challenges in fuel industry

In recent years, the environmental legislation of transportation fuel is becoming increasingly rigorous than ever [30]. The first revision was made in 1993 to reduce the emission allowance from 0.20-0.50 wt% to 500 ppm in the US [31, 32]. Another two amendments have been made by the Environmental Protection Agency (EPA) since then. The current specification of sulfur emission of on-road diesel is 15 ppm since 2006 [33, 34]. The specification was extended to non-road engine diesel fuels in 2010, and the acceptable diesel is called ultra-low sulfur diesel (ULSD) [35]. In some specific applications, sulfur-free diesel has also been proposed as a future specification [36].

In the meantime, the market demand for transportation diesel fuels is increasing dramatically in most countries, e.g. in the US market, it increased from 3.16 Mb/d (million barrels per day) in 2005 to 3.31 Mb/d in 2010 [37]. As a supplement, light cycle

oil (LCO) from the fluid catalytic cracking (FCC) unit is increasingly added to the diesel pool [38]. This action significantly raises the difficulty in producing clean diesel, since LCO contains more refractory sulfur compounds, such as dibenzothiophene (DBT) and alkyl substituted dibenzothiophene (alkyl DBT). Additionally, the contents of nitrogen, aromatics, and large molecular components in LCO are also higher, which may deteriorate the efficiency of sulfur removal [39, 40].

Currently, conventional hydrodesulfurization processes cannot produce ULSD required by the latest regulations [41, 42]. For the sake of deep hydrodesulfurization, refineries call for newly designed catalysts with enhanced desulfurization activity for refractory sulfur compounds. Unsupported catalysts with high loading of active phase are excellent candidates [13]. Their performance benefits in HDS have been demonstrated by a large number of laboratory research and industrial applications [13, 18]. The *NEBULA* catalysts have been successfully applied in refineries. Their activity was reported to be three to four times higher than the activity of conventional HDS catalysts [43, 44].

1.4 Scopes, objectives and outlines

The scope of the present thesis focuses on the synthesis of unsupported MoS_2 with high catalytic activity using the hydrothermal method, as a response to the current stringent regulation on sulfur emissions. The effect of the promoters and operating conditions were carefully investigated. The performance of the synthesized catalysts was associated with their characterizations to illustrate the role of crystalline properties in altering the catalytic activity. The deactivation behaviour was also studied after a long-term HDS reaction. Additionally, the synthesized cobalt and nickel promoted MoS_2 were applied in

the hydrogenation processes of waste cooking oil and canola oil. The catalytic activity and selectivity were studied and the reaction mechanisms were illustrated by step-by-step reaction routes.

The objectives of this thesis are given as follows:

1. To synthesize high-performance MoS_2 using the hydrothermal method.
2. To reveal the effect of different operating conditions, reaction environments, and promoters on catalytic activity and selectivity.
3. To associate activity/selectivity with the crystalline structures, and the chemical and physical properties.
4. To clarify the hydrodesulfurization kinetics on unsupported MoS_2.
5. To illustrate the mechanism of catalyst deactivation in the hydrodesulfurization process.
6. To reveal the role of nickel and cobalt in deoxygenation and to demonstrate deoxygenation kinetics.

In Chapter 2, an extensive literature review is provided on the synthesis, properties, and activities of unsupported Mo-based catalysts. The hydrothermal technique for the preparation of unsupported MoS_2 and the effect of the process parameters are described. An introduction of the catalysis mechanism of unpromoted and promoted MoS_2 is also provided, as well as their application in hydrodesulfurization and hydrodeoxygenation.

In Chapter 3, the characterization techniques for unsupported MoS_2 catalysts are provided. The hydrotreatment experimental setup and product analysis are described.

In Chapter 4, unsupported nanosized MoS_2 was synthesized by a novel hydrothermal method. The synthesis mechanism was carefully investigated in different conditions of medium acidity, precursor ratio, and gas environments. The performances of the catalysts were evaluated in terms of the hydrodesulfurization, hydrodenitrogenation, and hydrocracking of LCO. Efforts were made to illustrate the relationship between the synthesis conditions, catalyst properties, and catalytic activities.

In Chapter 5, the catalysts were synthesized using the same method introduced in Chapter 4 with different operating conditions. The effect of the synthesis temperature (sTemp) and the initial temperature (iTemp) were evaluated. Efforts were made to illustrate the roles of sTemp and iTemp in the catalytic activity when dealing with LCO.

In Chapter 6, an attempt to increase the curvature on the basal plane of crystalline was made by introducing an organic solvent (decalin) during the hydrothermal synthesis. Decalin to water ratios and agitation energy were investigated to illustrate their roles in creating an isolated water environment. In order to break up the solution into droplets, the study was extended to supercritical fluid with a fixed heptane to water ratio and agitation speed.

In Chapter 7, cobalt was introduced to increase the activities of MoS_2. Several key factors were carefully investigated, including the Co to Mo ratios and medium acidity. The performance of cobalt was evaluated by the HDS process of LCO and the results were compared with unpromoted MoS_2.

In Chapter 8, a kinetics study on the hydrotreatment of light cycle oil was performed over an unsupported MoS_2. A detailed analysis on sulfur and nitrogen compounds was conducted to illustrate the hydrodesulfurization and the hydrodenitrogenation kinetics. Hydrocracking and hydrogenation ability was also investigated.

In Chapter 9, the deactivation of unsupported MoS_2 was investigated under long-term HDS reactions. The experiment was carried out on a fixed bed microreactor for 160 hours, using LCO as tested oil. The research focuses on the investigation of the catalyst activity variation and the catalyst deactivation behaviour as a function of reaction time.

In Chapter 10, synthesized cobalt and nickel promoted MoS_2 were applied in the hydrodeoxygenation of canola oil. The chapter focuses on distinguishing the differences of the promoting effect in terms of hydrodeoxygenation activity and selectivity. Hydrodeoxygenation reaction schemes for both catalysts are also proposed.

In Chapter 11, the synthesized CoMoS catalyst was applied in the hydrodeoxygenation of waste cooking oil (WCO). A comprehensive kinetics analysis was carried out to

understand the deoxygenation process. Reaction mechanisms and catalyst deactivation were investigated using kinetic modeling based on proposed reaction networks.

In Chapter 12, a summary of the conclusions and recommendations for future work are presented.

Chapter 2 Literature review

2.1 Importance of unsupported catalysts

2.1.1 Application in upgrading of petroleum oil

Diesel is a regular engine fuel that is widely used on on-road and off-road motor transportations. It is generally produced from a blend of straight-run gas oil (SRGO) and other low-quality oils, e.g. light cycle oil [45, 46]. In recent decades, due to the decrease of light crudes and the increase in diesel demand, the low-quality oils with high sulfur content are increasingly added to the diesel pool [38]. In the meantime, the regulation on sulfur emissions has become more stringent. The current S allowance for on-road diesel is as low as 15 ppm (ultra-low sulfur diesel, ULSD), effective since 2006 and the specification was extended to non-road engine diesel fuels in 2010 [33, 34]. Moreover, a motion to further limit sulfur content in transportation fuels is currently under consideration [36]. The strict regulation demands a deep hydrodesulfurization of refractory sulfur e.g. alkyl dibenzothiophene, which has triggered a great interest within the research community [47, 48]. Since hydrodesulfurization is a catalytic process, developing new catalysts with deep-desulfurization activity, i.e. the elimination of the refractory sulfur compounds, becomes of great importance [49, 50]. Among all the possible candidates, the bulk sulfide-based Mo catalysts show good performance in terms of activity and thermo stability, compared to the traditional supported sulfide catalysts [14, 18, 51-53]. One of such catalysts, *NEBULA* (brand name), has been successfully applied in refineries, exhibiting 3 to 4 times higher activity than conventional supported catalysts [13].

Another drive for the study of unsupported catalysts is their potential application in the upgrading of heavy oils [39, 40]. For hydrotreating heavy oils with residual matters, supported catalysts in conventional fixed-bed processes are easily deactivated due to the formation of coke deposits on the surface [40, 54]. Unsupported catalysts, on the other hand, show no deactivation issues since they can be used as once-through catalysts. Besides, unsupported catalysts possess higher catalytic activity due to the high loading and large exposed surface area [55-57]. These advantages make unsupported catalyst a promising candidate in the slurry process in heavy oil refinery [55, 58].

2.1.2 Application in production of bio-diesel

The increasing awareness of energy crisis and environmental concerns about exhaust gas emissions trigger the scientific world to seek alternative fuel resources. Biodiesel as a clean and renewable fuel is an excellent candidate [1, 2]. Traditional biodiesel is the fatty acid methyl ester (FAME) that is produced from plant and/or animal oil through the transesterification approach [3-5, 59-61]. FAME has many desirable qualities; however, it still has several disadvantages, e.g. poor storage stability, marginal cold flow properties, low blending degree with petroleum diesel, engine compatibility issues, etc. [4, 5]. To overcome these drawbacks, hydrotreatment has become a prevalent means. As seen from Table 2.1, the oxygen-free biodiesel from the hydrotreating process has a high cetane value, a low gravity, good cold flow properties, excellent storage stability, and good compatibility with petro-diesel and the current transportation infrastructure [6, 62, 63].

Table 2.1 Comparison of properties of green diesel to FAME and petroleum fuel [6]

	Fatty acid methyl ester (FAME)	Oxygen-free biodiesel (C_xH_y)	Ultra-low sulfur diesel (ULSD)
Oxygen (%)	11	0	0
Specific gravity	0.88	0.78	0.84
Sulfur, ppm	<1	<1	<15
Heating Value (MJ/kg)	38	44	43
Cetane number	50-65	70-90	40
Stability	Marginal	Good	Good
Compatible with petro-diesel	Not good	Good	---

Different kinds of catalysts were studied in hydrodeoxygenation process, e.g. noble metal palladium (Pd) and platinum (Pt) [64-66], traditional sulphided Co/Ni Mo-based catalysts [9, 67-70], and phosphide[71, 72], nitride[73, 74], carbide[75, 76], and oxide catalysts [64], etc. Among all the available catalysts, CoMo and NiMo are the most frequently used catalysts [8].

The commercial Mo-based sulfide catalysts (CoMo or NiMo) are generally loaded on support materials, e.g. alumina. The hydrodeoxygenation performance may involve the contribution of support material. For instance, catalyst support alumina alone has catalytic activity in hydrotreating reactions due to the Lewis acid sites [12]. This fact has also been supported by Centeno et al. when investigating the effects of different support materials on the reaction pathways and product distribution. Their results showed that the acidity of the support materials can influence the formation of catalyst active sites for hydrogenation and decarboxylation of diethylsebacate [77]. Therefore, in order to investigate the intrinsic activity of the active phase, elimination of the effect of the

support is necessary. In this aspect, the use of unsupported catalysts is a good alternative. In addition, mass transfer resistance can also be minimized.

2.2 Structure-activity relationship

2.2.1 Active site types

MoS_2 is the most commonly used catalyst in the industry, which makes it a good start point for research activities. It has a crystalline structure with stacked multiple layers which are bonded by weak Van der Waals forces. Within a layer, each Mo (IV) center is bound to six sulfurs to form a trigonal prismatic coordination, while every sulfur atom is connected with three Mo centers, forming pyramidal interstices, as seen in Figure 2.1. It is worth noting that the sites on the edge planes are not identical. On Mo edge, each Mo atom connects with 2 exposed S atoms, while on S edge, each Mo atom is bonded by 4 exposed S atoms [78].

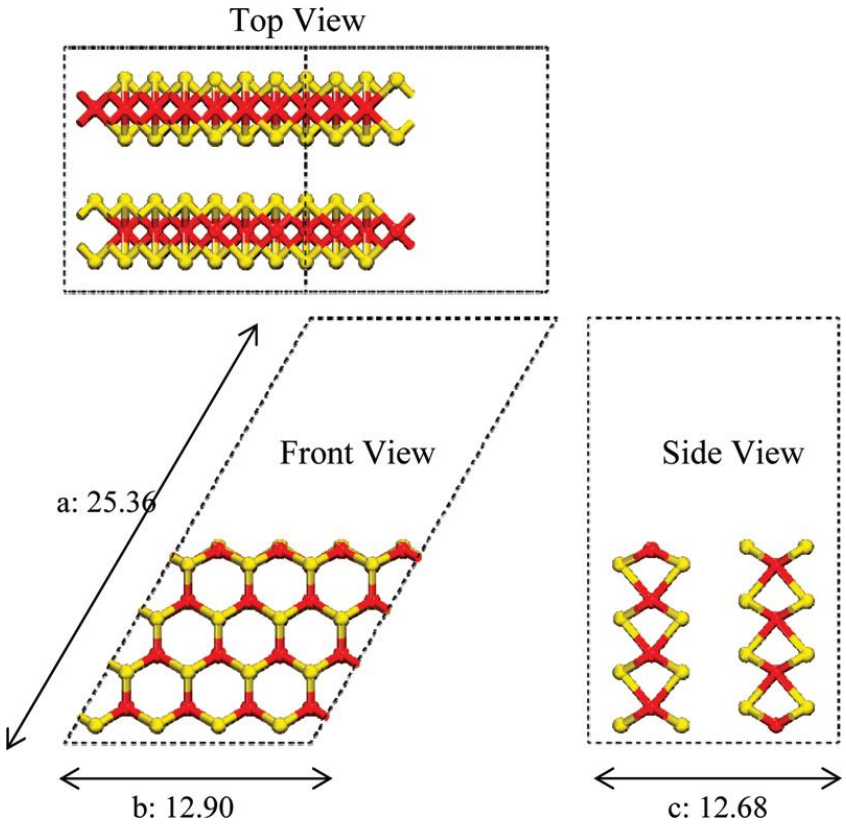

Figure 2.1 MoS_2 crystallite structures [79]
Red: molybdenum; yellow: sulfur

The catalytic activity of MoS_2 is originated from its crystalline structure. It is generally accepted that catalytic reaction occurs on the sites of exterior surface of a crystal where the Mo atom is coordinatively unsaturated. Such sites can be created from the intrinsic defects of a crystal or a reaction in which one or more S atoms are stripped off from the MoS_2 surface. Research shows that the formed S vacancy is necessary for HDS reactions and highly associated with the catalytic activity, so it is called "active sites" [80-82]. Figure 2.2 presents the adsorption and desorption processes of a thiophene compound based on the S vacancy theory. It is seen that the vacant site is exposed directly to adsorbates, which significantly decreases the reaction barrier. The reactant adsorbed will

follow a series intermediate reaction on the active site and finally be desorbed as product [83].

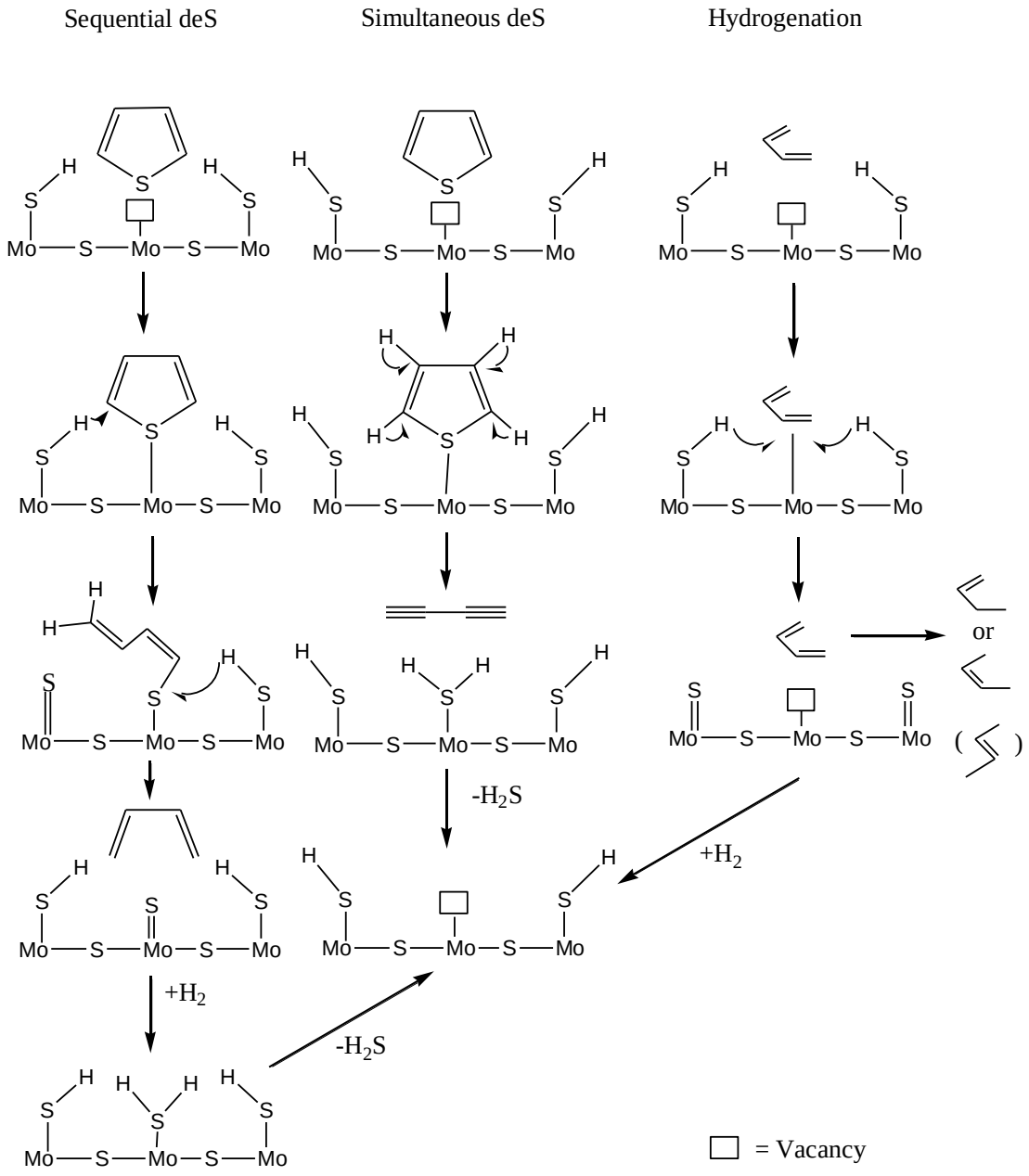

Figure 2.2 Sulfur vacancy model of the HDS mechanism
(Figure 2.2 is redrawn faithfully to the original work) [83]

Molecular modeling calculations have revealed that S vacancies may not be the only active sites [84]. Substances, such as thiophene can also adsorb on a fully saturated sulfur

site through S-S bond [85, 86]. More recent studies based on STM measurements and DFT calculations also suggested that fully sulfided Mo-edges might contribute to hydrogenation reaction [87, 88]. S-H group with the ability to provide proton might be responsible for the activity. Other indirect evidence was provided through deactivation studies in which the loss of sulfur from the active phase led to a decrease in the thiophene conversion, while the activity was partially recovered by re-sulfidation [89].

2.2.2 Local structure of actives sites

The activity of MoS_2 is highly associated with the crystalline structure of the catalyst, especially the structure of the active sites. Although a number of theories are proposed to describe the mechanism, the local structure of the active sites and their functions are still in debate [90].

The most popular theory is the active sites on the edge plane, which separates the catalytic function of the edge plane from the basal plane [91-93]. According to the theory, the basal plane is catalytically inert because of the full saturation of S atoms on each Mo atom. Catalytic activity is mainly attributed to the unsaturated Mo atoms on edge site, due to the partial loss and depletion of S [94]. The theory demonstrates that the catalytic performance only associates with the amount of active sites on the rim, thus, only a small number of Mo sites are involved during the reactions [28].

Daage and Chianelli further developed the edge sites theory and proposed a rim-edge model [26]. According to the model (Figure 2.3), the border was divided into two kinds of sites, sites on the exposed basal planes (rim sites) and sites on the interior layers (edge

sites). This model is intended to correlate the morphology of MoS_2 crystalline structure with the catalytic selectivity in HDS reactions. The two exterior layers are responsible for both direct desulfurization (DDS) and hydrogenation reactions (HYD) and the layers in between only contribute to DDS.

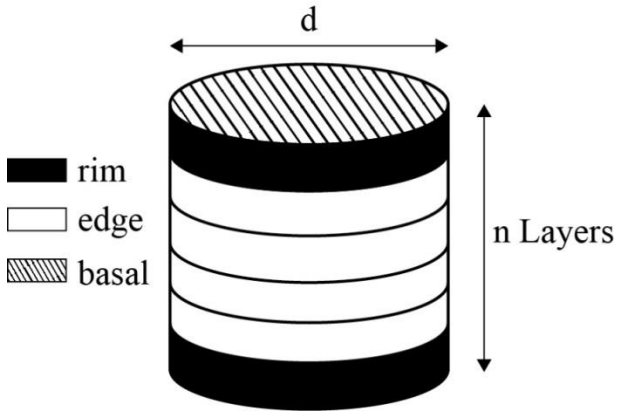

Figure 2.3 The rim-edge model
(Figure 2.3 is redrawn faithfully to the original work) [26]

Recently, Lauritsen et al. proposed a new interpretation called "brim sites" [88]. The proposition is based on the observation of MoS_2 nano-clusters using scanning tunneling microscopy (STM). The "brim sites" are a region adjacent to the edges of MoS_2 nano-clusters, which shows a distinct metallic character. The "brim sites" are believed to have the ability to donate and accept electrons similar to other ordinary catalytically active metals. For HDS reactions, the author stated that the brim sites might contribute to the first step of hydrodesulfurization. Considering the structure and activity relationship, the specific position of brim sites on the two exterior layers (top and bottom) is similar to the rim sites in the rim-edge model [28].

Although the rim-edge model predicts that the basal plane is catalytically inert, recent studies discover that curved points on the basal plane can also generate active sites and this is considered responsible for catalysts' high activity [19, 28, 29]. Chianelli et al. measured the bond length and found elongated Mo-S bond at the inflection point, which suggested Mo-S bond was weakened and defects were possibly created in the basal sheet [95]. Datye et al. prepared MoS_2 with highly curved slabs on the surface of titania-silica and suggested that the stained MoS_2 might generate active sites by losing sulfur atoms on the basal planes [96]. Similar conclusion was also drawn by Iwata et al. A relationship was established between the number of hydrogenation active sites and the inflection on the curved basal plane of unsupported MoS_2 [56]. From these studies, it can be seen that the curvature can greatly contribute to the number of active sites on catalysts, which provides a new insight on the synthesis of crystalline MoS_2 with higher activity. Moreover, it is worth mentioning that the latest model calculation of density functional theory (DFT) suggested that row-vacancy structure could be formed on the basal plane of single layer MoS_2 and may enhance the catalytic activity of the basal planes [97].

2.2.3 Promotion effect

Molybdenum based catalysts have been used extensively in petroleum refining industry [98]. It is widely accepted that the activity of catalysts based on molybdenum could be dramatically promoted by the coating of cobalt or nickel [99, 100]. There are several mechanisms of the promotion effect. The most accepted theory is that cobalt and nickel atoms are decorated on the edge of MoS_2 sheets in the form of Co(Ni)-Mo-S (decoration model) [101]. In such structure, they contribute to the activity by transferring electrons to

Mo atoms to weaken the metal-sulfur bond [102-105]. Figure 2.4 shows the examples of cobalt located on the different edges of MoS_2.

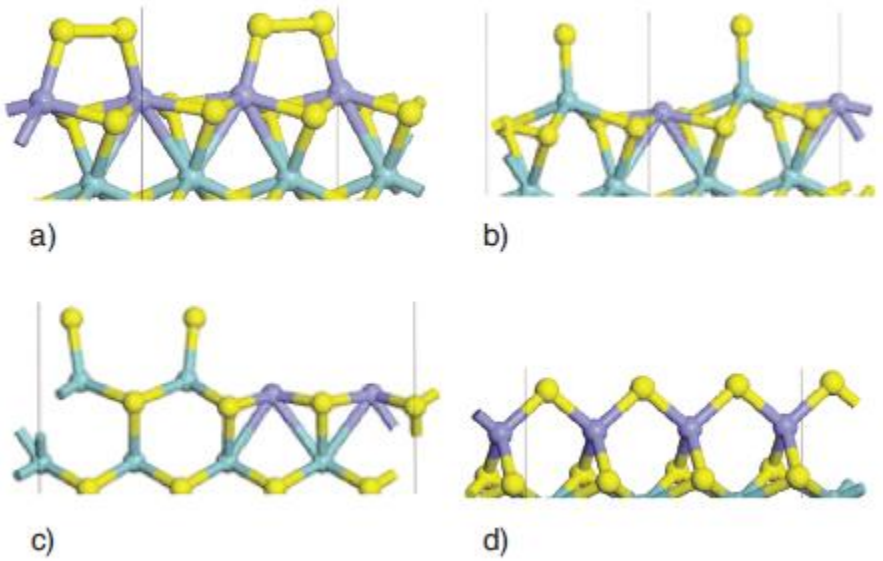

Figure 2.4 Examples of Co on edge of MoS_2
a) M-edge with 100% Co and 50% S, b) M-edge with 50% Co and 25% S, c) M-edge with 50% Co and 25% S, d) S-edge with 100% Co and 50% S. Yellow balls: Sulfur, green balls: molybdenum, blue balls: cobalt [106].

An alternative theory considers that the introduction of Co or Ni increases the structural disorders of MoS_2 crystalline [107-109]. In the growth of a MoS_2 crystal, Co or Ni works are impurities that increase the defects in the MoS_2 structure and decrease the crystal size. As mentioned in Section 1.2.2, the active sites are located on the edge of MoS_2 sheets. Thus the decrease in crystal size will enhance the activity by increasing the number of active sites.

Other opinions involve the formation of Co_9S_8 or Ni_3S_2 (NiS). One explanation for the enhanced activity is that cobalt or nickel sulfides are real active sites. There is evidence

for their high activity without the involvement of molybdenum [110, 111]. Another theory called “remote control” or “synergy model” considers that the promotion effect is from a close contact between two phases without the generation of binary sulfides Co(Ni)-Mo-S. Hydrogen first dissociates on cobalt or nickel sulfide and then spills over to the surface of MoS_2, which will facilitate the formation of unsaturated active sites [112-115]. For unsupported catalysts, the cobalt/nickel sulfide can also act as a support for highly dispersed MoS_2 crystallites, which provides more accessible active sites to increase the activity [116].

For a Co or Ni promoted MoS_2 catalyst, more than one promotion effect may be involved depending on the promoter loading. Generally, when promoter/(promoter+Mo) ratio is low (<0.2, changing with the crystalline length), Co or Ni ions are preferentially situated at the edges of MoS_2 crystallite in the form of Co/Ni-Mo-S. On the other hand, when Co/(Co+Mo) ratio is greater than 0.2, the edge sites are saturated and the excess of cobalt or nickel would exist in the form of cobalt or nickel sulfide. Effect involving separated promoter phase would occur [116]. The optimal promoter/(promoter+Mo) ratios are in the range of 0.3-0.54 and 0.55-0.7 for unsupported CoMoS and NiMoS catalysts, respectively [117-120].

2.3 Unsupported MoS_2 synthesis

Currently, there are many techniques to synthesize dispersed MoS_2, including solid-gas sulfidation, thermal decomposition solution reactions, hydrothermal and solventothermal preparations, etc. The detailed description of synthesis methods was listed in Section 2.3.1 and the introduction of hydrothermal method was provided in Section 2.3.2.

2.3.1 Introduction of synthesis techniques

Solid-gas sulfidation

Solid gas sulfidation of the corresponding oxides is the most common technique in the preparation of supported MoS_2. This method is also applied to synthesize unsupported catalysts. Hydrogen sulfide and hydrogen are routinely used to vulcanize oxides and reduce Mo(VI) species to the Mo(IV) at elevated temperature (Reaction 2.1) [14].

$$MoO_3 + 2H_2S + H_2 \rightarrow MoS_2 + 3H_2O \qquad \text{Reaction 2.1}$$

Sulfidation of oxide-state precursors is a promising technique for the preparation of supported heterogeneous catalysts. However, it is less desirable for the synthesis of unsupported materials. The finely dispersed MoS_2 can be hardly generated in this preparation, due to the poor dispersion of solid MoO_3. Besides, the sulfidation is a topotactic process. Complete sulfidation is hard to achieve, as seen from Figure 2.5a. The solid-gas method is a convenient technique, but not a good method for the preparation of well dispersed hydrotreating catalysts.

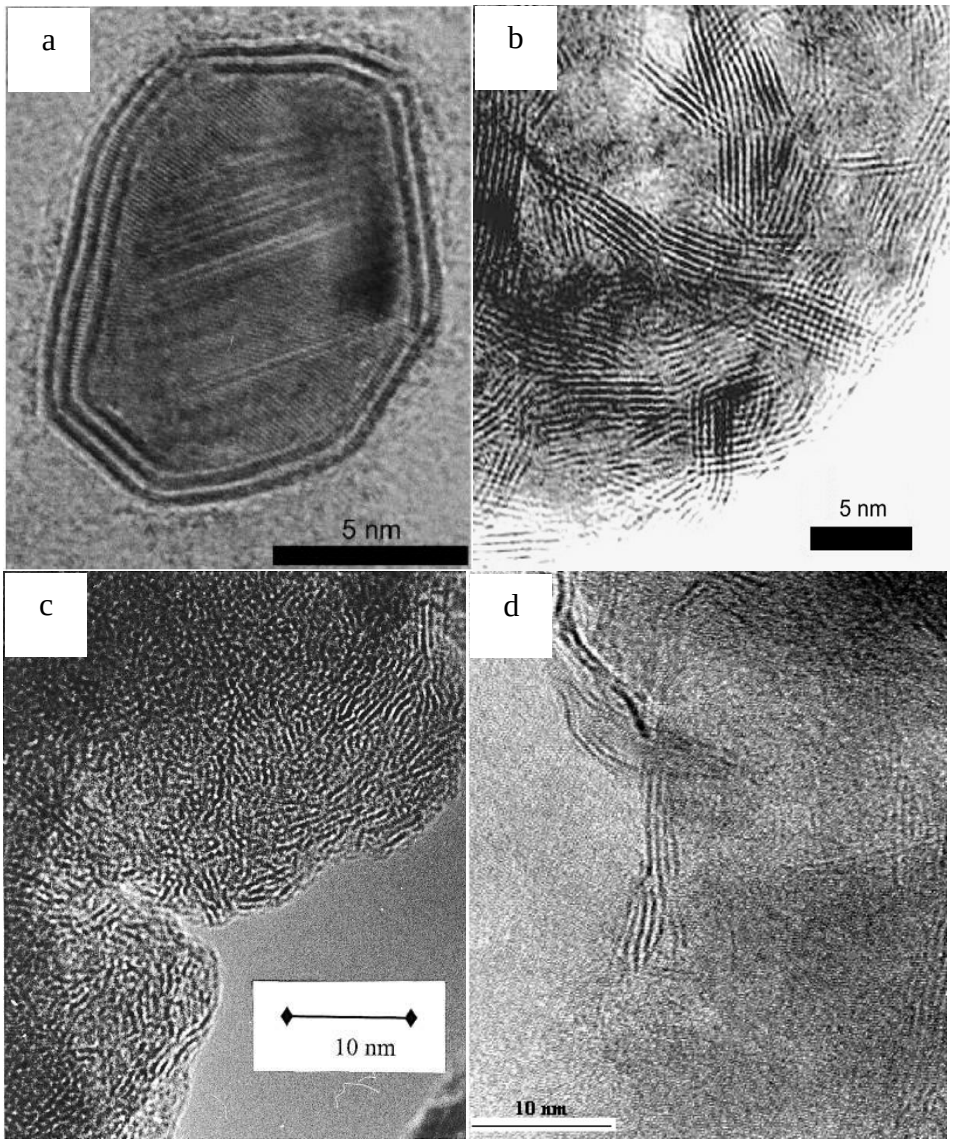

Figure 2.5 TEM images for MoS_2 synthesized by different techniques
a: MoS_2 slabs on the particle of MoO_2 from the sulfidation of dispersed MoO_3 at 400 ℃ [14]; b: MoS_2 from decomposition of ammonium thiomolybdate at 400 ℃ [14]; c: MoS_2 through solution synthesis at 90 ℃ using ATM-N_2H_4 [17]; d: MoS_2 from hydrothermal method at 350 ℃ using ammonium tetrathiomolybdate ($(NH_4)_2MoS_4$) [18].

Thermal decomposition of precursors

Some precursors contain both sulfur and coordinated molybdenum. MoS_2 can be obtained via direct thermal decomposition of this kind of precursor without introduction of exterior sulfiding agent. Ammonium tetrathiomolybdate is the most commonly used precursor [15,

16, 121]. When heated over 120 ℃, it first decomposes to amorphous molybdenum trisulfide (Reaction 2.2), which will gradually lose sulfur to generate ultimately MoS_2 at higher temperature over 400 ℃ (Reaction 2.3). H_2S will be produced instead if in the presence of hydrogen (Reaction 2.4) [122, 123].

$$(NH_4)_2MoS_4 \rightarrow MoS_3 + 2NH_3 + H_2S \qquad \text{Reaction 2.2}$$

$$MoS_3 \rightarrow MoS_2 + 1/8S_8 \qquad \text{Reaction 2.3}$$

$$MoS_3 + H_2 \rightarrow MoS_2 + H_2S \qquad \text{Reaction 2.4}$$

Catalysts synthesized from thermal decomposition are typically 4-7 layers and 5-8 nm in length, as seen from Figure 2.5b [14]. They are always substantially better in dispersion and catalytic properties than those formed from gas-solid sulfidation. Furthermore, the properties can be further improved by using organic thiosalts precursors [98, 124, 125]. It is reported that decomposition of tetraalkylammonium thiomolybdate $(NR_4)_2MoS_4$ in H_2S/H_2 yielded highly dispersed and activated catalysts [58]. Carbonaceous matter plays an important role in stabilization of catalyst structure [103].

There are still drawbacks of the current technique. From the applied point of view, the toxicity and costly synthesis procedure of making thiomolybdates is the main problem, which limits the application and scale-up of the technique [14]. The attempt to decrease the cost and simplify the procedure may be a feasible solution for future applications of thermal decomposition.

Solution synthesis (thermal decomposition)

To clarify from hydrothermal synthesis, solution synthesis is described as a reaction conducted in a homogeneous solution without elevated pressure. MoS_2 can be generated directly in some circumstances. However, in most cases, amorphous molybdenum sulfide MoS_x (x>2) is produced instead. Therefore, a follow-up thermal decomposition is generally needed for the production of crystal MoS_2.

Ammonium thiometallates are commonly used precursors in aqueous synthesis with HCl or NH_3 as pH adjustor. Figure 2.5c shows the morphology of MoS_2 directly synthesized from solution reaction without further treatment. Short slabs are observed, which provide abundant edge sites and thus a high catalytic activity.

Slow reaction at low temperature of the initial amorphous precipitate offers great potential for controlling morphology. Compared to solid-gas reaction, aqueous solution provides more operation parameters for process control. Surfactant assistance is also available for the aqueous system, which could facilitate a better dispersion of catalysts [101, 126].

2.3.2 Hydrothermal synthesis

Introduction of hydrothermal synthesis

Hydrothermal synthesis techniques are becoming the most efficient routes for the preparation of advanced nano-materials. The term “hydrothermal” is originally from geology. It was first used by a British geologist Sir Roderick Murchison in the mid-19th century for the description of the action of water at elevated temperature and pressure in changing the earth crust leading to the formation of rocks and minerals [127]. In

"Handbook of hydrothermal technique", hydrothermal was first defined by Byrappa and Yoshimura as homogeneous or heterogeneous chemical reaction in the presence of a solvent above room temperature and at pressures greater than atmospheric pressures in a closed system [128]. Novel hydrothermal processing is a recent concept, which can be described in a broader sense covering conventional hydrothermal (with aqueous solvent in the system), solvothermal (with non-aqueous solvent in the system), and supercritical hydrothermal (either aqueous or non-aqueous under supercritical conditions) processes [129].

Hydrothermal synthesis of MoS_2

As mentioned earlier, hydrothermal method is a widely used synthesis approach. It is a promising technique for unsupported MoS_2 synthesis and it is developing rapidly [19-21]. Several important features, e.g. high purity and high dispersion properties, can be achieved by hydrothermal syntheses.

Both thiomolybdate and oxides can be used as precursors. For the first one, hydrothermal decomposition is sufficient since it contains sulfur and molybdenum already; adscititious sulfiding agent is essential for the latter type. MoS_2 synthesized by hydrothermal method has a needle-like morphology. The length of slabs is generally larger than that from other techniques (generally over 10 nm), while the layer number is not very high (Figure 2.5d).

Synthesis parameters

A number of operation parameters can influence the production of MoS_2, including media acidity/basicity, synthesis temperature, precursor concentration, synthesis time, agitation, heating protocol, etc. Among these factors, temperature and media properties are of most significance. The former one directly influences the chemical reaction, while the latter one determines the crystal growth.

Media acidity/basicity

The production of MoS_2 in aqueous phase is a chemical reaction process involving redox and precipitation, which are subjected to the acid-basic properties of media. When synthesizing MoS_2 with ammonium tetrathiomolybdate $(NH_4)_2MoS_4$ (ATM), Devers et al. found out that in a basic environment at pH between 9 and 10, trimolybdate or dimolybdate was produced instead of MoS_2. On the other hand, in the weakly acidic media (pH 3), MoS_2 and MoS_x were formed. It was concluded that softly acidic medium is more favorable for the generation of molybdenum sulfide [20]. Similar phenomenon was also observed by Li, et al. that a low concentration of HCl (<0.2 mol/L), corresponding to a high pH, failed to produce MoS_2 [21]. In addition, they also discovered that the excess of HCl (strong acidity) led to the production of MoO_2. Pure MoS_2 can only be obtained in an appropriate pH range with HCl addition of 0.4-0.6 mol/L. It can be seen that acidity/basicity can significantly affect product distribution, which needs to be carefully adjusted for the desired product.

Synthesis temperature

In hydrothermal synthesis, temperature is a key factor in controlling material properties [130, 131]. The effect of temperature on material properties enters through the impact on the crystalline nucleation and growth kinetically and thermodynamically [132, 133]. External energy (heating) is needed to overcome the activation energy barriers for the nucleation. Meanwhile, activation energy of different crystal facets is also affected by temperature through the effect on interfacial energy [134]. In addition, variation of crystallization temperature changes equilibrium solubility of the subjected material, i.e. the supersaturation state. An elevated supersaturation will significantly enhance the growth on preferred surface [135]. In dynamics, the growth is influenced by temperature through the diffusion and growth rate coefficients. Generally, at higher temperature, diffusion is a rate-limiting process, while at low temperature, interface reaction is the main force in the crystallization [135]. Different morphologies can be created in different rate-limiting situations.

In the synthesis of crystal MoS_2 catalyst, temperature also plays an important role in influencing crystalline size, morphology, and crystallinity. It has been reported that MoS_2 crystals fail to be generated at too low or high temperatures [20, 21]. When MoS_2 was successfully produced, the morphology and crystalline size could also be strongly affected by temperature. At low temperatures ranging from 120 to 150 ℃, Tian et al. observed that increasing temperature led to larger particle sizes [136]. Similar trend was also found between 230-260 ℃ by Li et al. with different morphologies observed [21]. At high temperature range 300-375 ℃, on the other hand, the sizes of promoted MoS_2

crystalline decrease with increasing temperature. The morphology also changed with temperature evidenced by the increased curvature of MoS_2 slabs [22].

2.3.3 Application of co-solvent

Organic solvent

The application of a second solvent immiscible with water has been reported in the synthesis of nanoparticles [137]. The presence of organic solvent could isolate the continuous aqueous phase into separated water droplets. This would decrease the mass transfer and thus reduce the crystal growth rate [22]. Additionally, the introduction of second phase may also orient growth along the curved interface and more defects are therefore expected to be created. The positive effect on MoS_2 property and activity has been documented with an enhanced HDS conversion after addition of organic solvent in the synthesis [22, 138]. To improve catalyst quality, the organic solvent needs to be carefully selected. Immiscibility is essential for providing the second phase, as well as the stability at the hydrothermal conditions (elevated temperature) and inertness with precursor and water media. Furthermore, vigorous agitation is required in the synthesis process for the efficient dispersion of water and solvent phases.

Supercritical fluid

Supercritical fluid is another alternative solvent, which exhibits unique effects for the nucleation and growth of crystals [139]. When a solvent reaches the supercritical conditions, the chem-physical properties like viscosity, density, and surface tension could be dramatically decreased [140-142]. This results in a good dispersion of solvent in the aqueous solution, which consequently increases the contacting area with precursors. By

adjusting the temperature and pressure, one can easily control supercritical properties to obtain the desired environment, in which the nucleation and growth of crystals can be significantly altered [137, 143].

2.4 Reaction mechanism of hydrodesulfurization and hydrodeoxygenation

2.4.1 Hydrodesulfurization of light cycle oil

Light cycle oil from fluid catalytic cracking unit is a blend to straight run gas oil for the diesel production (Figure 2.6) [45, 46]. It has a low cetane number, a high density and a high content of sulfur, nitrogen and aromatic components, etc. [144]. A variety of sulfur compounds can be found in LCO. Typical sulfur compounds are listed in Figure 2.7 [145]. These sulfur compounds are generally catalogued into “easy” sulfurs and “hard” sulfurs based on their reactivity. Easy sulfurs include thiophenes, benzothiophenes (BT), and their alkyl substitutes, which are more reactive. Hard sulfurs are sulfur species with much lower HDS activity, such as dibenzothiophenes (DBT), naphthothiophenes, and alkyl-substituted dibenzothiophenes [146]. In hard-sulfur category, alkyl DBTs with substitutes on the adjacent carbon to the sulfur atom (β-DBTs) are the most refractory components, e.g. 4-MDBT, 4,6-DMDBT [147, 148]. It is reported that the reactivity of 4,6-DMDBT over CoMo and NiMo catalysts is 4 to 10 times less than DBT due to the tremendous steric hindrance [149, 150].

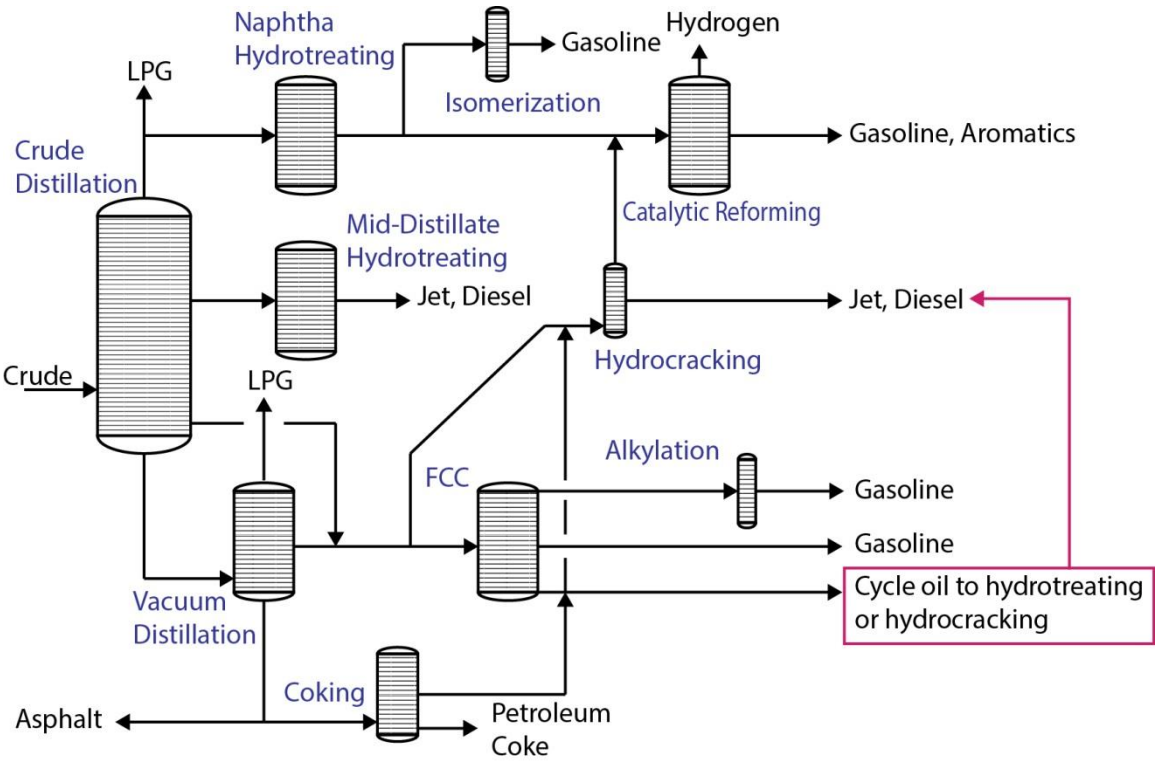

Figure 2.6 Petroleum process schematic
(Figure 2.6 is redrawn faithfully to the original work, pick lines are added by the author of this thesis) [151]

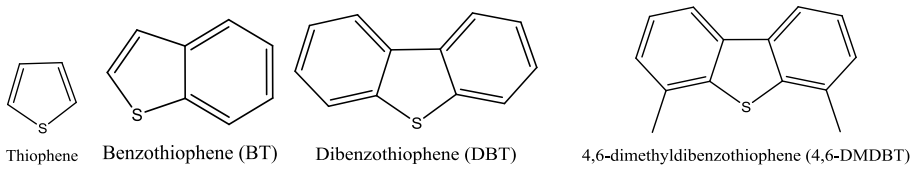

Figure 2.7 Common types of sulfur containing compounds [145]

The difficulty in upgrading of LCO is the deep HDS of hard sulfur. In research community, DBT and 4,6-DMDBT are two representative compounds for the refractory sulfurs. The main products of DBT are biphenyl (BP), cyclohexylbenzene (CHB), tetrahydro-dibenzothiophene (THDBT), and bicyclohexyl (BCH). BP is produced through the direct desulfurization while THDBT is via hydrogenation. CHB and BCH are the hydrogenolysis product of THDBT or hydrogenation production of BP (Figure 2.8)

[152, 153]. The HDS of 4,6-DiMeDBT (same as 4,6-DMDBT) has identical reaction routes (DDS and HYD) to DBT, with the production of 3,3-DiMe-BPH, 3-MeCHT, respectively (Figure 2.9) [154]. However, due to the steric hindrance effect, HYD route is more dominant after the introductions of alkyl substituents in the 4 and/or, 6-positions of the DBT molecules [42, 155]. Isomerization was also observed in the HDS of 4,6-DMDBT in some studies using acidic zeolite as support. The transfer of methyl groups of 4, 6 positions to other positions, e.g. 3, 6 (Figure 2.10), would reduce the steric hindrance and thus enhance the HDS activity [156, 157].

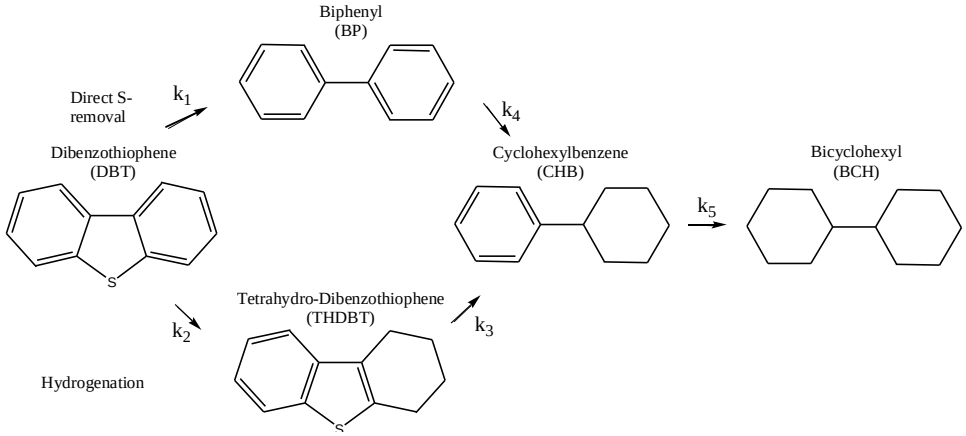

Figure 2.8 Reaction network of dibenzothiophene
(Figure 2.8 is redrawn faithfully to the original work) [152]

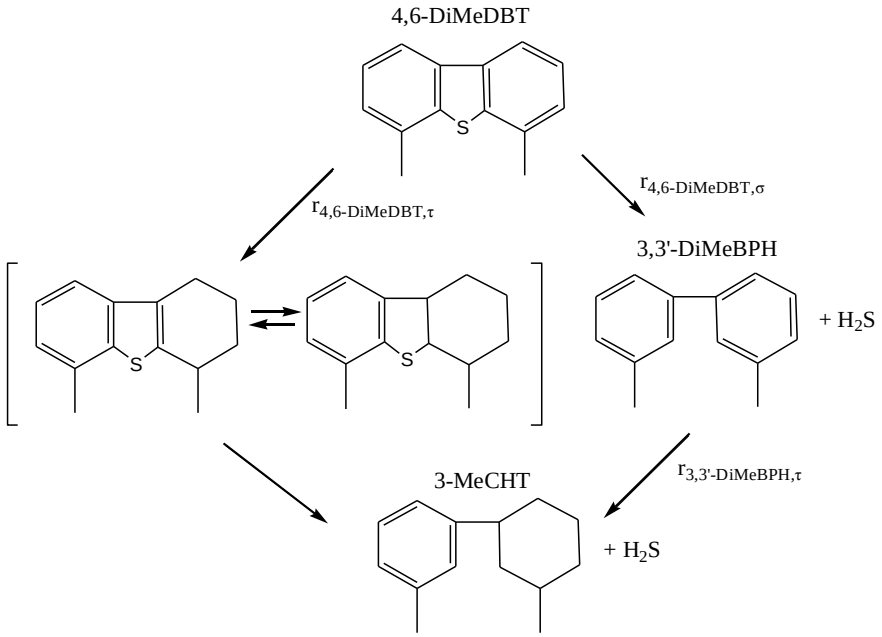

Figure 2.9 Reaction network for the HDS of 4,6-DMDBT
(Figure 2.9 is redrawn faithfully to the original work) [154]

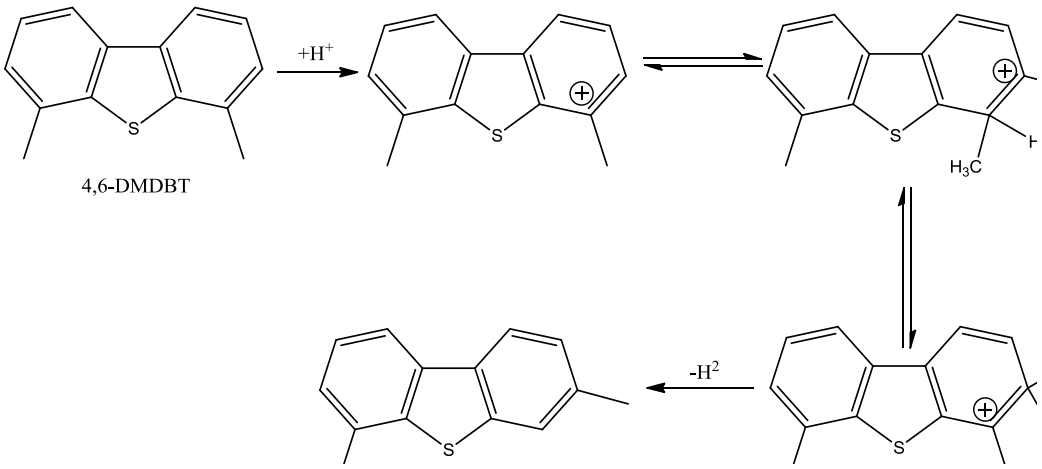

Figure 2.10 Isomerization reaction of 4,6-DMDBT
(Figure 2.10 is redrawn faithfully to the original work) [156]

2.4.2 Hydrodeoxygenation of vegetable oil

There are two common bio-oil resources, vegetable oils and oils derived via pyrolysis or liquefaction of ligno-cellulosic biomass. The former is composed of triglycerides and the latter contains mainly oxygenous aromatics, e.g. phenols. Reaction pathways on phenol-type oils are similar to HDS of thiophene due to the similar aromatic structure of the substrates, including hydrogenation (HYD) and direct deoxygenation (DDO) [158, 159].

Different reaction pathways were proposed for triglycerides other than the routine routes of HYD and DDS (DDO) for aromatic heteroatoms. As shown in Figure 2.11, triglycerides are first decomposed to aliphatic acids and other intermediates, which will go through two parallel paths: hydrodeoxygenation (HDO) route (Reaction 2.5) and hydrodecarbonylation/ decarboxylation (HDC) routes (Reaction 2.6 and Reaction 2.7). A main difference between the two pathways is the carbon yield in the final products: hydrodecarbonylation/decarboxylation route leads to hydrocarbons with one carbon number lower than the feed oxygenates due to formation of CO or CO_2, while hydrodeoxygenation product maintains the same carbon number [7, 10, 160, 161].

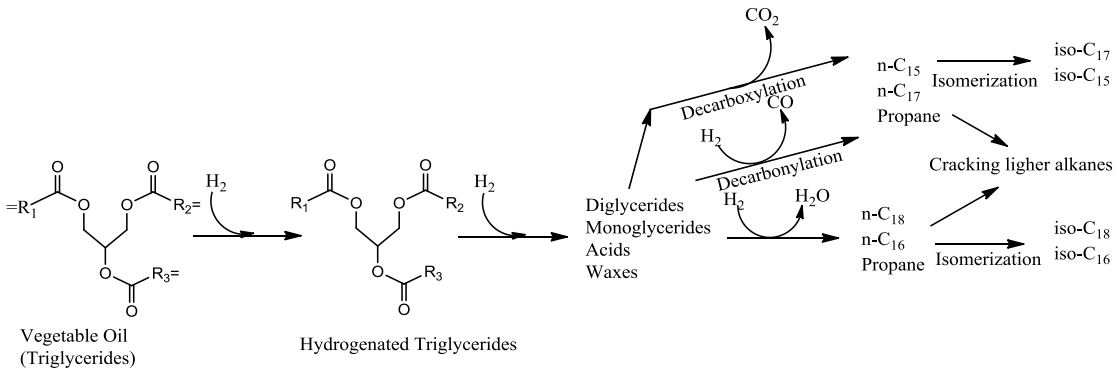

Figure 2.11 Reaction pathway for conversion of triglycerides to alkanes
R=: alkyl chain with double bond; R: saturated alkyl chain
(Figure 2.11 is redrawn faithfully to the original work) [9]

Studies on the sulfided catalysts show that the main product from hydrodeoxygenation of vegetable oils falls into the bio diesel range. Since most bio-derived triglycerides contain 18 carbons in branched chains, C_{18}/C_{17} hydrocarbon ratio is always used as an important criterion to distinguish the primary deoxygenation reaction route [9, 10, 68, 160, 162]. When C_{18}/C_{17} over 1 indicates HDO dominates the reaction pathways. For instance, Toba et al. demonstrated the C_{18}/C_{17} ratios for Co or Ni-promoted supported MoS_2 is in the range of 1.5-4 when hydrotreating of waste cooking oil, indicating HDO is 1.5-4 times of HDC route. Similarly, Bezergianni et al. proposed that the HDC is more dominant way when the C_{18}/C_{17} ratio is less than 1 [163].

$$Hydrodeoxygenation\ C_{n-1}H_{2n-1}-COOH+H_2 \rightarrow C_nH_{2n+2}+H_2O \qquad \text{Reaction 2.5}$$

$$Hydrodecarbonylation\ C_{n-1}H_{2n-1}-COOH \rightarrow C_{n-1}H_{2n-2}+CO+H_2O \qquad \text{Reaction 2.6}$$

$$Hydrodecarboxylation\ C_{n-1}H_{2n-1}-COOH \rightarrow C_{n-1}H_{2n}+CO_2 \qquad \text{Reaction 2.7}$$

Detailed kinetics studies were generally conducted with synthesized model oil due to its simplicity in composition [7, 74, 164]. Aliphatic esters and acids are frequently employed to represent the typical components (or intermediate) in vegetable oils. Aldehydes and alcohols are reported as two major oxygenate intermediates from fatty esters or acids [7, 165]. A detailed hydrodeoxygenation mechanism over sulfided catalysts NiMo/γ-Al_2O_3 and CoMo/ γ-Al_2O_3 is shown in Figure 2.12 using methyl heptanoate and methyl hexanoate as model compounds [165, 166]. Three reaction pathways were identified for the aliphatic esters. The first reaction path was the conversion of esters to two alcohols followed by dehydration. The second reaction path is the de-esterification of esters to an alcohol and a carboxylic acid that was further converted to hydrocarbons. Direct decarboxylation of esters was proposed to be a third reaction route.

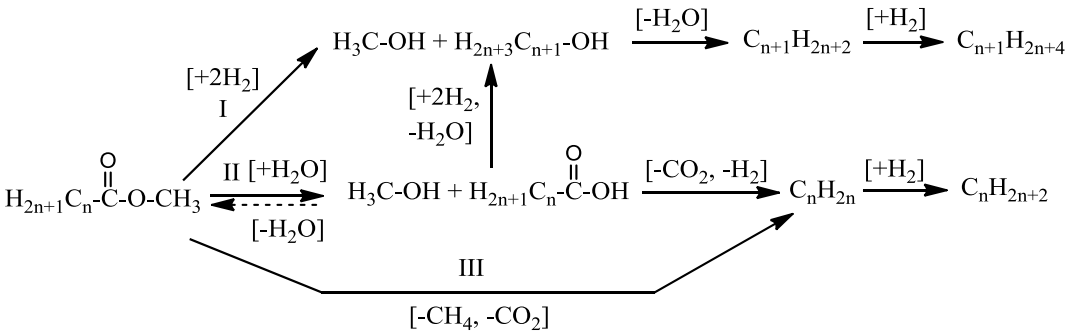

Figure 2.12 Hydrodeoxygenation reaction scheme of aliphatic methyl esters
(Figure 2.12 is redrawn faithfully to the original work) [165]

Chapter 3 Analytical procedures for catalyst characterization and evaluation

3.1 Characterization techniques for catalysts

The characterization methods that were used in the thesis include:

(1) Transmission electron microscopy (TEM), equipped with selected area electron diffraction (SAD) and energy-dispersive X-ray spectroscopy (EDX). The analysis was performed at the microscopy facility at University of New Brunswick.

(2) Scanning electron microscopy (SEM). The analysis was performed at the microscopy facility at University of New Brunswick.

(3) Nitrogen adsorption-desorption. The analysis was performed in the Catalytic Process Lab at University of New Brunswick.

(4) Electron microprobe (EMP). The analysis was performed at the microscopy facility at University of New Brunswick.

(5) X-ray diffraction (XRD). The analysis and data processing were performed at chemistry and geology department at University of New Brunswick.

(6) Temperature programmed reduction (TPR). The analysis and data processing were performed in the Catalytic Process Lab at University of New Brunswick.

(7) X-ray absorption near edge structure (XANES). The analysis was conducted at the Canadian Light Source (CLS; Saskatoon, SK, Canada).

(8) Extended X-ray absorption fine structure (EXAFS). The analysis was conducted at the Canadian Light Source (CLS; Saskatoon, SK, Canada). Mo K-edge data were recorded at a beamline at APS.

(9) X-ray photoelectron spectroscopy (XPS). Analysis was performed at the Alberta Centre for Surface Engineering and Science (ACSES) at University of Alberta.

(10) Temperature programmed oxidation (TPO). The analysis was performed in the Catalytic Process Lab at University of New Brunswick.

3.1.1 Transmission electron microscopy (TEM)

Transmission electron microscopy (TEM) was performed on an electron microscope (JEOL 2011 STEM, JEOL Ltd., Tokyo, Japan) operating at 200 keV. The catalyst powder was ultrasonically dispersed in ethanol and deposited on a carbon-coated copper grid, then vacuum-dried for 12 hours before analysis. The layer numbers, thickness and length of catalyst crystalline structure were determined using image analysis software and their average were calculated according to Equation 3.1-Equation 3.3 based on at least 100 measures from various particles. The standard deviation of the crystalline size parameters are calculated based on different particles. The fraction of edge sites was calculated using Equation 3.4-Equation 3.7 [167]. Selected area electron diffraction (SAD) pattern was used for the determination of catalyst crystal structure. The atomic ratio of the catalyst was estimated by energy dispersive X-ray emission (EDX) coupled with TEM.

$$Average\,layer\,number\ \bar{N} = \frac{\sum_{i=1,2\ldots n}^{n} N_i}{n} \qquad \text{Equation 3.1}$$

$$Average\,slab\,thickness\ \bar{T} = \frac{\sum_{i=1,2\ldots n}^{n} T_i}{n} \qquad \text{Equation 3.2}$$

$$Average\ slab\ length\ \bar{L} = \frac{\sum_{i=1,2\ldots n}^{n} L_i N_i}{\sum_{i=1,2\ldots n}^{n} N_i}$$ Equation 3.3

where L, T, N and n stand for slab length, slab thickness, number of layers in each crystal, and the total number of crystalline measured, respectively.

$$Mo_t = 3n^2 + 3n + 1$$ Equation 3.4

$$Mo_e = 6n$$ Equation 3.5

$$\bar{L} = 2n \times 0.316\ (d_{Mo-Mo} = 0.316nm)$$ Equation 3.6

$$a = {Mo_e}/{Mo_t}$$ Equation 3.7

where Mo_t is the total number of Mo atoms in the slab; Mo_e is the number of Mo edge atoms, presumed to be catalytically active; n equals to one for the smallest entity; a is the faction of edge sites; $\bar{L}$ is the average length determined from TEM measurements, which is the longest dimension of the hexagonal crystallites.

3.1.2 Scanning electron microscopy (SEM)

The morphologies of catalysts were observed by scanning electron microscopy (SEM, JEOL JSM6400) operating at 25 kV. Before imaging, samples were mounted on carbon planchettes with carbon paste, and sputtered with gold to ensure sufficient conductivity.

3.1.3 Nitrogen adsorption-desorption

Nitrogen adsorption-desorption isotherm was measured at 77 K using Autosorb-1 (Quantachrome Instruments, Florida, US). Approximate 100 mg of powder samples were degassed in a sample preparation station at 200 ℃ for 3 hours prior to measurement, then switched to the analysis station for adsorption and desorption under liquid nitrogen at 77

K with an equilibrium time of 3 minutes. The specific surface area of the catalyst powder was calculated using the Brunauer-Emmett-Teller (BET) method with linear region in the P/Po range of 0.10 to 0.30. The total pore volume was calculated from the volume of nitrogen adsorbed at the relative pressure p/p_0 0.995. Pore size distribution was analyzed from the adsorption branch of isotherms by the Barrett-Joyner-Halenda (BJH) method.

3.1.4 Electron microprobe (EMP)

The elemental analyses for molybdenum and sulfur of the catalyst were conducted on electron microprobe (JEOL-733 Superprobe). The test was operating at 15 keV and 100 nA using element molybdenum and sulfur as reference.

3.1.5 X-ray diffraction (XRD)

The crystallinity of catalyst was characterized by powder X-ray diffraction (XRD), which was recorded on a diffractometer (Bruker AXS D8 XRD) using Cu Kα radiation with the 2θ range of 5-85 ° and the scan speed of 1°/min. The sizes of the crystalline domains for all the catalysts are calculated by Scherrer Equation from 002 and 110 planes (Equation 3.8) [24].

$$\tau_{hkl} = \frac{K_{hkl}\lambda}{\beta_{hkl}\cos\theta} \qquad \text{Equation 3.8}$$

Where τ, K, λ, β, and θ denote the average size of crystalline domains, dimensionless shape factor (0.76 for 002 and 110 planes [24, 168]), wavelength of the X-ray (1.5406 Å [152]), the line broadening at half the maximum intensity, and the Bragg angle, respectively.

3.1.6 Temperature programmed reduction (TPR)

The temperature programmed reduction was conducted on Autosorb-1 (Quantachrome Instruments). The wet catalyst, which was previously stored in toluene, was loaded in a quartz tube and then purged for 0.5 hour at room temperature. Then the catalyst was dried at 150 ℃ for 2 hours under 50 ml/min argon. After in-situ drying, catalyst was cooled down below 100 ℃ and then heated to 700 ℃ at a rate of 10 ℃/min under a 50 ml/min flow of 2% H_2 in Ar. The consumption of H_2 and production of H_2S was monitored by a mass spectrometer (Residual gas analyzer, RGA200, Stanford Research Systems, Inc.). The peak area was integrated using Origin and calibration curves for both gases were made to establish the relationship between the peak area and the concentrations.

3.1.7 X-ray absorption near edge structure (XANES)

The X-ray absorption near edge structure (XANES) of S K-edge and Mo L3-edge were measured at the Soft X-ray Microanalysis Beamline (SXRMB) of the Canadian Light Source (CLS; Saskatoon, SK, Canada). The sample was dispersed on double-sided conducting carbon tapes under a dry nitrogen atmosphere, and the spectra were recorded in a total electron yield mode at room temperature using a Si (111) double crystal monochromator. Data analysis of the XANES spectra was performed using Athena software.

3.1.8 Extended X-ray absorption fine structure (EXAFS)

The extended X-ray absorption fine structure (EXAFS) spectra of Mo K-edge were recorded in the transmission mode at room temperature. The beam intensity was measured before and after the sample (I_0 and I, respectively) using ionization chambers filled with mixtures of 15% Ar and 85% N_2 for I_0 and 50 % Ar and 50% N_2 for I. The

structure parameters around Mo were obtained by Fourier transformation using FEFF 6 software.

3.1.9 X-ray photoelectron spectroscopy (XPS)

The catalyst samples were stored in Ampule bottle under the protection of argon before XPS analysis. The measurements were performed on AXIS 165 spectrometer (Kratos Analytical) at the Alberta Centre for Surface Engineering and Science (ACSES). The base pressure in the analytical chamber was lower than 3×10^{-8} Pa. Monochromatic Al Kα source (hν = 1486.6 eV) was used at a power of 210 W. The analysis spot was 400 x 700 μm. The resolution of the instrument is 0.55 eV for Ag 3d and 0.70 eV for Au 4f peaks. The survey scans were collected for binding energy extending from 1100 eV to 0 with analyzer pass energy of 160 eV and a step of 0.4 eV. For the high-resolution spectra of S2p and Mo3d, the pass-energy was 20 eV with a step of 0.1 eV. The number of scans varied from 3 to 30 in order to ensure good signal to noise ratio. Charge neutralization was not required since the samples were conducting.

3.1.10 Temperature programmed oxidation (TPO)

Temperature programmed oxidation analysis was performed on an Autosorb-1 (Quantachrome Instruments, Florida, US). The spent catalysts were washed with toluene using Soxhlet extractor to remove the adsorbed oil and dried at 120 ℃ overnight. Approximately 50 mg of the spent catalyst powder was loaded in a U-shaped quartz tube and heated to 120 ℃ keeping for 60 minutes under a flow of 50 ml/min helium to remove any physisorbed water. Subsequently, the catalyst was heated at a rate of 10 ℃/min up to 750 ℃ under a flowing gas mixture of 5% oxygen in 100 ml/min helium. The eluting gas

was analyzed by a mass spectrometer (Residual gas analyzer, RGA200, Stanford Research Systems, Inc.).

3.2 Evaluation of catalyst performance

3.2.1 Hydrotreatment of LCO in batch reactor

The catalysts were evaluated with light cycle oil (LCO) in a 1 L batch reactor (Parker Autoclave Engineers). The properties and composition of LCO are listed in Table 3.1. The catalyst (0.6g) filtered through 200 mesh was first loaded in the 1 L autoclave reactor. The reactor was repeatedly evacuated and refilled with hydrogen to replace the air in the autoclave, and was heated up to 375 ℃. When the reactor reached the setting temperature, 120 g of preheated LCO (approximate 200 ℃) was then charged into the reactor through a feed charging tank on the top of the reactor. The weight ratio of catalyst to oil was 1:200. After that, the reactor was pressurized to 1500 psi. When the oil temperature was back to 375 ℃ (approx. 5 minutes), a liquid sample was taken from sampling tube marked as time zero. The reactor was refilled to 1500 psi after sampling. Other samples were taken during the reaction in an order of 20 min, 40 min, 1 h, 1.5 h, 2 h, 3 h, 4 h, 5 h, 6 h, 7 h, and 8 h. After that, the reactor was cooled down to room temperature with fan in about 1 hour. A stirring speed of 1000 rpm was used during the reaction.

At the beginning of the experiments, reproducibility of the process was evaluated by conduction of three parallel runs for one individual catalyst. Repeatability was also checked by the end of the experiments. Duplicate experiments on catalyst with optimal activity were conducted in particular. The standard deviation of rate constant is within 2%, which indicates a good reproducibility.

Table 3.1 Properties and composition of light cycle oil

Properties	
Density, (g/cm^3 @ 30 ℃)	0.9641
Sulfur components	*Sulfur content (ppmw)*
BT	210.1
1MBT	1528.0
2MBT	3024.8
3MBT	2854.9
4MBT	1575.3
BT-ABT	9193.2
DBT	713.8
1MDBT	2071.0
2MDBT	1653.3
3MDBT	933.3
DBT-ADBT	5371.5
Sum	14564.7
Nitrogen components	*Nitrogen content (ppmw)*
Alilines	10.3
Indoles	76.7
Carbazoles	67.2
Sum	159.2
Chemical composition (%)	
Saturates	22.61
Monoaromatics	12.89
Diaromatics	52.35
Polyaromatics	12.15
Boiling points (℃)	
Initial boiling point (IBP)	113.3
10%	227.0
20%	237.5
30%	254.9
40%	258.7
50%	273.5
60%	283.4
70%	293.8
80%	307.3
90%	328.4
Final boiling point (FBP)	376.4

3.2.2 Hydrotreatment of LCO in continuous reactor

The catalysts were evaluated in a 5 ml fixed-bed flow microreactor (Autoclave Engineer, BTR-Jr-PC). 1 g of catalyst powder was diluted with the same volume of glass beads, and then loaded in the reactor. To recover the possible activity lost due to oxidation by air, catalysts were re-sulfurized at 280 ℃ and 220 psi with a flow of 80 ml/min hydrogen and 0.1 ml/min dodecane solution containing 2% dimethyl disulfide (DMDS). The hydrotreatment was conducted at 375 ℃ and 1000 psi with a flow of 30 ml/min hydrogen and 0.05 ml/min LCO. Samples were taken for over 160 hours until the hydrodesulfurization conversion kept constant. The WHSV was 2.9 h^{-1}.

3.2.3 Hydrodeoxygenation of vegetable oils in batch reactor

The hydrodeoxygenation (HDO) activity of catalysts was evaluated in a batch reactor (Parker Autoclave Engineers). 0.6 g of unsupported catalysts and 120 g of waste cooking oil (WCO) or raw canola oil were added into the reactor, making the catalyst-to-oil ratio 1:200 by weight. The mixture was then heated to pre-set temperatures (300-375 ℃) and kept for 8 hours under a stirring speed of 1000 rpm. The pressure was maintained at 1300 psi at the reaction temperatures. Liquid samples were taken at different times (0.5 h, 1 h, 2 h, 3 h, 4 h, 5 h, 6 h, and 8 h) during the reaction. The gaseous products were collected after the reaction was completed and the reactor was cooled down to room temperature. In this experiment, the resistance of internal and external mass transfer was assumed to be negligible, since nanosized dispersed catalyst powders were applied.

3.3 Analysis of feedstock and hydrotreated products

3.3.1 Analysis of original and hydrotreated LCO

The total sulfur and nitrogen in original LCO and hydrotreated products were determined by Sulfur /Nitrogen analyzer (9000 series, Antek Instruments Inc) according to ASTM 5453 and ASTM 5462, respectively. The conversion of hydrodesulfurization and hydrodenitrogenation were calculated using Equation 3.9.

$$X = \frac{(C_{Feed} - C_{Product})}{C_{Feed}} \times 100\% \qquad \text{Equation 3.9}$$

where X stands for the HDS or HDN conversion; C_{Feed} and $C_{Product}$ represent sulfur or nitrogen content in the feed and products.

The kinetics for HDS and HDN were estimated based on pseudo-first-order reaction. The rate constant k was calculated from Equation 3.10.

$$-m\frac{dC}{dt} = kC \qquad \text{Equation 3.10}$$

where m, C, t, k stand for the catalyst weight, concentration of sulfur or nitrogen, hydrotreating time and reaction rate constant, respectively.

A detailed sulfur compounds composition was analyzed by a gas chromatograph (Varian 450) equipped with a non-polar VF-1ms capillary column (15 m x 0.25 mm x 0.25 μm, max temperature: 325 ℃) and a pulsed flame photometric detector (PFPD). The following temperature profile was used: 2 minutes at 120 ℃, followed by a linear

increase at 6 ℃/min to 170 ℃ and another increase at 20 ℃/min to 290 ℃, kept for 2 minutes. Benzothiophene (BT), dibenzothiophene (DBT), and 4,6-dimethyldibenzothiophene (4,6-DMDBT) were used as standards.

The nitrogen species in feed and products were quantified using a gas chromatography (GC-950, Shanghai Haixin Chromatographic Instrument Co. LTD) equipped with a nitrogen phosphorus detector (NPD). Anilines, indole, quinoline, tetrahydroquinoline, and carbazole were used to identify the peaks. The parameter setup was following the literature [169]. The column was heated up at 4 ℃/min from 40 ℃ to 265 ℃.

The aromatics distribution in the liquid samples was determined by high performance liquid chromatography (HPLC, Agilent 1200 series) according to ASTM 6591. Simulation distillation of the products was carried out using Shimadzu GC-2010 according to ASTM 2887. Density of the liquid oil was measured by portable density meter (DMA 35N, Anton Paar GmbH, Graz, Austria) following ASTM 4052.

3.3.2 Analysis of original and hydrotreated vegetable oils

The fatty acids of vegetable oils were analyzed following the procedure described by Simacek et al. [10]. The oil sample was added to a flask containing methanolic NaOH solution and heated until all WCO was completely dissolved. By introducing BF_3-methanol and boiling for 2 minutes complete esterification occurred. Petroleum ether and saturated NaCl solutions were then added to extract and separate the organic components. The resultant fatty acid methyl esters appeared in the top petroleum ether layer and were analyzed using a gas chromatography - mass spectrometry (Shimadzu GCMS-QP5000)

with a weak-polarity column (Agilent J&W HP-5). Temperature program was as follow: 2 minutes at 60 ℃, followed by a linear increase at 10 ℃ /min to 90 ℃, 30 ℃ /min to 180 ℃, 10 ℃ /min to 200 ℃, kept for 10 min, and another increase at 10 ℃/min to 290 ℃, kept for another 10 min. Except the solvent cut, full-scan mass spectra were acquired from 50 to 500 m/z. Identification of the peaks was based on the NIST (National Institute of Standards and Technology) 1998 library.

The hydrocarbons in liquid products were quantified using gas chromatography (Varian 450) equipped with a hydrogen flame ionization detector and a non-polarity capillary column (Agilent J&W VF-1 ms). The following temperature program was used: 5 minutes at 60 ℃, followed by a linear increase at 7 ℃ /min to 230 ℃ and another increase at 10 ℃/min to 300 ℃, kept for 5 min. Calibration curves were made using DB 2887 standards.

The total acidity number (TAN) was tested using ZD-2A Automatic potentiometric titrator (Saegmoter Company, Shanghai, China) according to ASTM-D664.

The components in the oil products were identified by GC-MS (Shimadzu GCMS-QP5000). The temperature program was as follow: 5 minutes at 60 ℃, followed by a linear increase at 10 ℃ /min to 180 ℃, kept for 5 min, then 8 ℃ /min to 240 ℃, maintained for 5 min, and another increase at 20 ℃/min to 300 ℃, kept for 2.5 min. The content of intermediate alcohols and aldehydes was estimated by the peak area (MS%)

and response factor to n-heptadecane of 1.3 and 1.4, respectively [170]. The unreacted glycerides were derived from the oxygen content, as shown in Equation 3.11.

$$C_g = 100\% - C_a - C_h - C_{alc} - C_{ald}$$ Equation 3.11

where C_g, C_a, C_h, C_{alc}, and C_{ald} stand for the oxygen content in glycerides, fatty acids, hydrocarbons, alcohols and aldehydes, respectively.

The original oil and the upgraded products were analyzed using a Fourier Transform Infrared Spectrometer (FTIR) (Nicolet 6700, Thermo Scientific, US). The spectra were collected for 32 scans at a resolution of 4 cm^{-1} in the range of 400-4000 cm^{-1}.

^1H nuclear magnetic resonance (NMR) spectra were recorded with a high-field multinuclear Agilent UNITY INOVA NMR spectrometer (Varian Unity 400) under standard acquisition conditions. The operating frequencies were 300 MHz. D-chloroform was used as solvent.

The elemental analysis for feedstock and upgraded products were conducted on CHNS-O 932 elemental analyzer (LECO Corporation, MI, US) following ASTM D5291. The oxygen content was calculated from the balance. The minimum measurability for carbon is 10 ppm and 100 ppm for hydrogen on the basis of a normal sample load (i.e. 2 mg).

CO and CO_2 generated during hydrotreatment were analyzed using a gas chromatography Varian 3400 equipped with a Thermal Conductivity Detector (TCD). Hydrocarbons, C_1–

C_6, were examined using a Shimadzu GC-17A equipped with a Flame Ionization Detector (FID). Calibration curves were made for quantitative analysis.

Chapter 4 Hydrothermal synthesis of nanocrystalline molybdenum sulfide

4.1 Introduction

Unsupported MoS_2 is a good candidate for deep hydrodesulfurization [14]. It is a great challenge to synthesize an unsupported MoS_2 catalyst of high catalytic activity with low-cost precursors and using a simple method. In this paper, commercially available MoO_3 and Na_2S were used as the precursors for the catalyst synthesis. A novel hydrothermal technique was introduced to synthesize a well-dispersed unsupported nanocrystalline molybdenum sulfide. Under subcritical water condition, a series of highly dispersed nanosized MoS_2 catalysts with high surface area and nanocrystalline structure were prepared. The textural and chemical structures of synthesized catalysts were extensively characterized by various techniques, e.g. TEM, BET, XRD, XPS, TPR, and XAFS. The hydrodesulfurization (HDS) and hydrodenitrogenation (HDN) activities were evaluated using light cycle oil (LCO). Efforts were also made to illustrate the relationship between the synthesis conditions, catalyst properties and the catalytic activity.

4.2 Catalyst synthesis

A series of molybdenum sulfide catalysts were synthesized by the hydrothermal method, using MoO_3 (STEM Scientific) and Na_2S $9H_2O$ (Fisher Scientific) as precursors. MoO_3 and Na_2S $9H_2O$ were first dissolved in deionized water, and HCl was slowly added into the solution. The mixture was then put into an autoclave and reacted for 2h at 320 ˚C at 500rpm. Two experimental runs were also conducted at higher pressure atmospheres of 200psi hydrogen or nitrogen. The precursors were mixed at synthesis temperature in

these two runs. The synthesis conditions are listed in Table 4.1. The resultant black solid and liquid were separated by filtration. The solid product was further washed by deionized water and ethanol, and dried under nitrogen protection at 150 ℃ for 4 hours.

Table 4.1 Synthesis conditions at 320 ℃

Factors	Conditions
Na_2S-to-MoO_3 molar ratio	2.0, 2.5, 3.0, 3.75, 4.5,5.0
HCl-to-MoO_3 molar ratio	0, 2.25, 4.5
Gas atmosphere	H_2 (200psi), N_2 (200psi), N_2 (1atm)

The catalyst recovery was calculated based on the theoretical MoS_2 yield (Equation 4.1). The prepared MoS_2 catalysts at different Na_2S to MoO_3 molar ratio (HCl/MoO_3 molar ratio 4.5) are denoted as CAT–x (where x is Na_2S to MoO_3 molar ratio), e.g. CAT-3.75. The pH of filtrate was tested by a pH meter (AB 15, Fisher Scientific). The concentration of sulfur anions $S_2O_3^{2-}$ and SO_4^{2-} in the filtrate was measured by ion chromatography (DIONEX, DX-120).

$$\text{Recovery} = \frac{Actual\ W_{product}}{Theorectical\ W_{MoS_2}} \times 100\% \qquad \text{Equation 4.1}$$

4.3 Results and discussion

4.3.1 Synthesis of nanocrystalline MoS_2

The crystal structure is essential to the MoS_2 catalyst to perform catalytic activity. Inappropriate synthesis conditions, however, may result in amorphous MoS_2 which is catalytically inert or may fail to produce MoS_2. Thus, a set of pre-testing reactions were conducted to investigate the formation of crystallized MoS_2 (Table 4.2). MoO_3 and Na_2S

were employed as molybdenum and sulfur sources, respectively. XRD was used to reveal the structures of the products, indicating the success or the failure of synthesis of crystallized MoS_2 (Figure 4.1). When the two precursors were mixed alone, no solid was obtained other than a dark yellowish solution. Since MoO_3 is an acidic oxide and dissolves in basic solutions, H^+ is required to provide an acidic environment and help form MoS_3. When increasing the HCl/MoO_3 ratio to 2.25, amorphous MoS_x was detected, indicated by the single 002 diffraction peak in XRD spectrum (Figure 4.1). Nanocrystal MoS_2 peaks were produced when the HCl/MoO_3 ratio increased to 4.5, which indicates a certain amount of H^+ was required for the MoS_2 formation. Possible reactions at room temperature are shown below (Reaction 4.1-Reaction 4.4).

$$S^{2-} + H_2O \leftrightarrow HS^- + OH^- \qquad \text{Reaction 4.1}$$

$$MoO_3 + 2OH^- \leftrightarrow MoO_4^{2-} + H_2O \qquad \text{Reaction 4.2}$$

$$MoO_4^{2-} + 8H^+ + 4S^{2-} \leftrightarrow MoS_4^{2-} + 4H_2O \qquad \text{Reaction 4.3}$$

$$MoS_4^{2-} + H^+ \leftrightarrow MoS_3 + HS^- \qquad \text{Reaction 4.4}$$

Table 4.2 Reaction conditions and products

Run No.	Reaction Conditions			Products		
	Na_2S/MoO_3 Ratio	HCl/MoO_3 Ratio	Gas Atmosphere	Solid Product	Solid Recovery (%)	Filtrate pH
1	2.50	0	N_2 (1atm)	Little solid	<1.0	13.29
2	2.50	2.25	N_2 (1atm)	Amorphous MoS_x	---	12.92
3	2.50	4.50	N_2 (1atm)	Nano MoS_2	96.2	2.61
4	5.00	4.50	N_2 (1atm)	Little solid	<1.0	12.25
5	2.00	4.50	N_2 (1atm)	MoS_2, MoO_2, MoS_x (x<<2)	---	
6	2.50	4.50	N_2 (200psi)	Nano MoS_2	~100	2.53
7	2.50	4.50	H_2 (200psi)	MoO_2	---	9.85

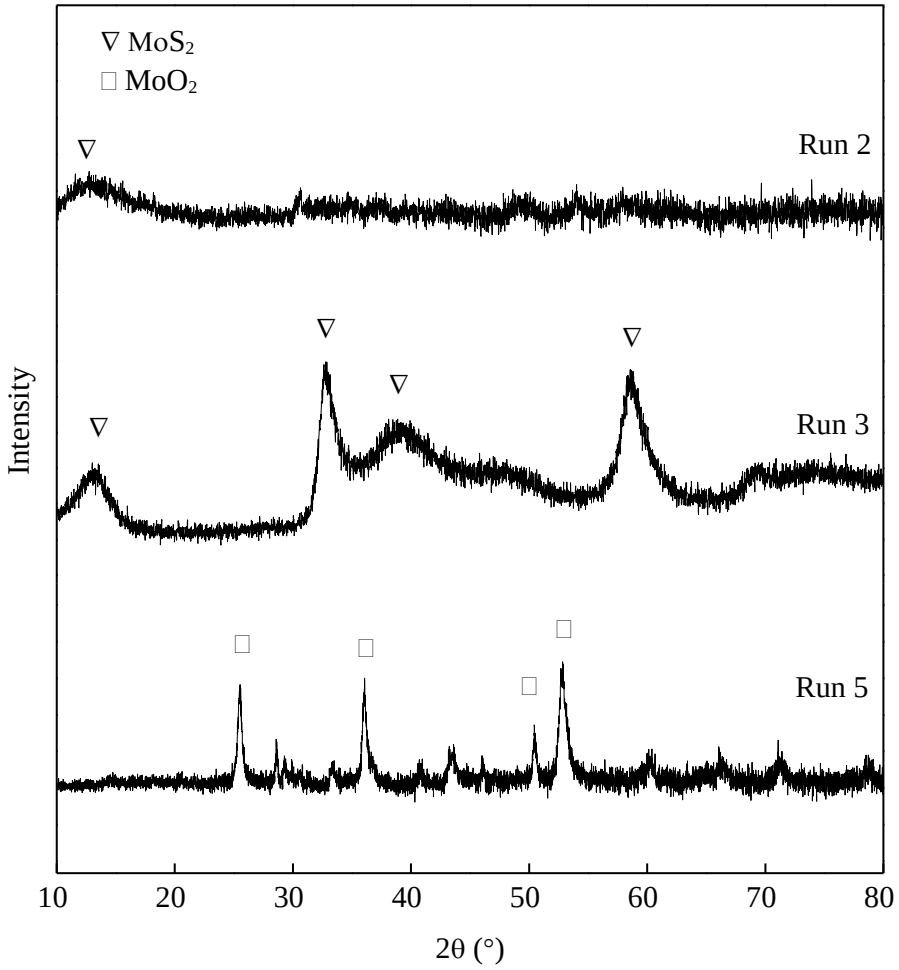

Figure 4.1 XRD spectra of products at different HCl/MoO_3 and Na_2S/MoO_3 ratios

The sulfur/molybdenum atomic ratios in the feedstock are controlled by adjusting the amount of Na_2S. Six ratios were prepared in a large range from 2 to 5. Since a portion of S in the reaction is acting as a redox mediator, the low S/Mo precursor ratio, e.g. 2, inevitably leads to an excess of MoO_3. Consequently, molybdenum-dominant solid particles are generated and embed themselves in the layered MoS_2, resulting in poor uniformity (Figure 4.2). On the other hand, solids are barely discernable at high S/Mo precursor ratio, e.g. 5, indicating that the overdose of Na_2S may also cause the failure of

synthesis. The proper range of Na_2S/MoO_3 for the synthesis of crystallized MoS_2 is between 2.5 and 4.5, revealed by the typical MoS_2 XRD diffraction peaks and electron diffraction rings (Figure 4.3 and Figure 4.4).

Gas environment is another factor that influences the conversion from MoO_3 to MoS_2. In inert gas (nitrogen), Na_2S (S^{2-}) acts as a reduction agent and crystallized MoS_2 is successfully synthesized. By contrast, in a reductive gas atmosphere, hydrogen works as the reduction agent, leading to the generation of MoO_2 (Figure 4.3). MoO_3 is reduced to MoO_2 instead of sulfidation to MoS_3 and further to MoS_2. It confirms that crytallized MoS_2 cannot be formed in reductive gas environment.

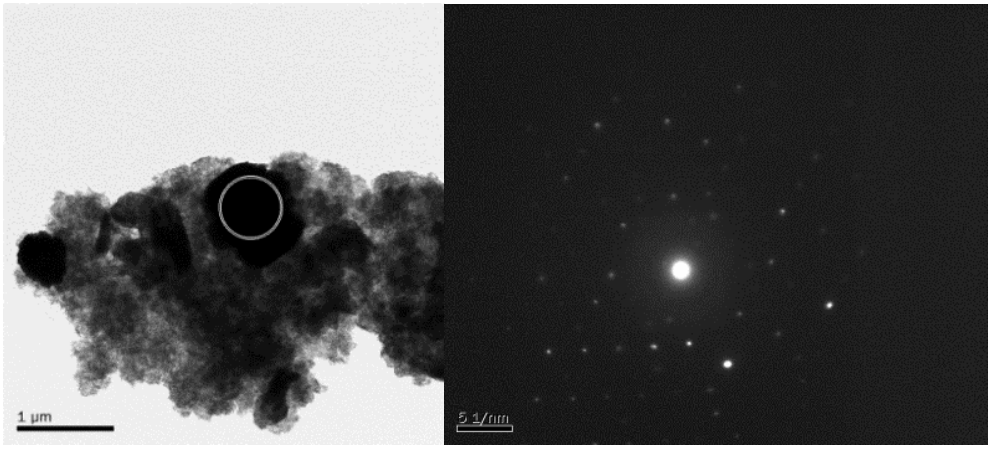

Figure 4.2 TEM image and diffraction pattern

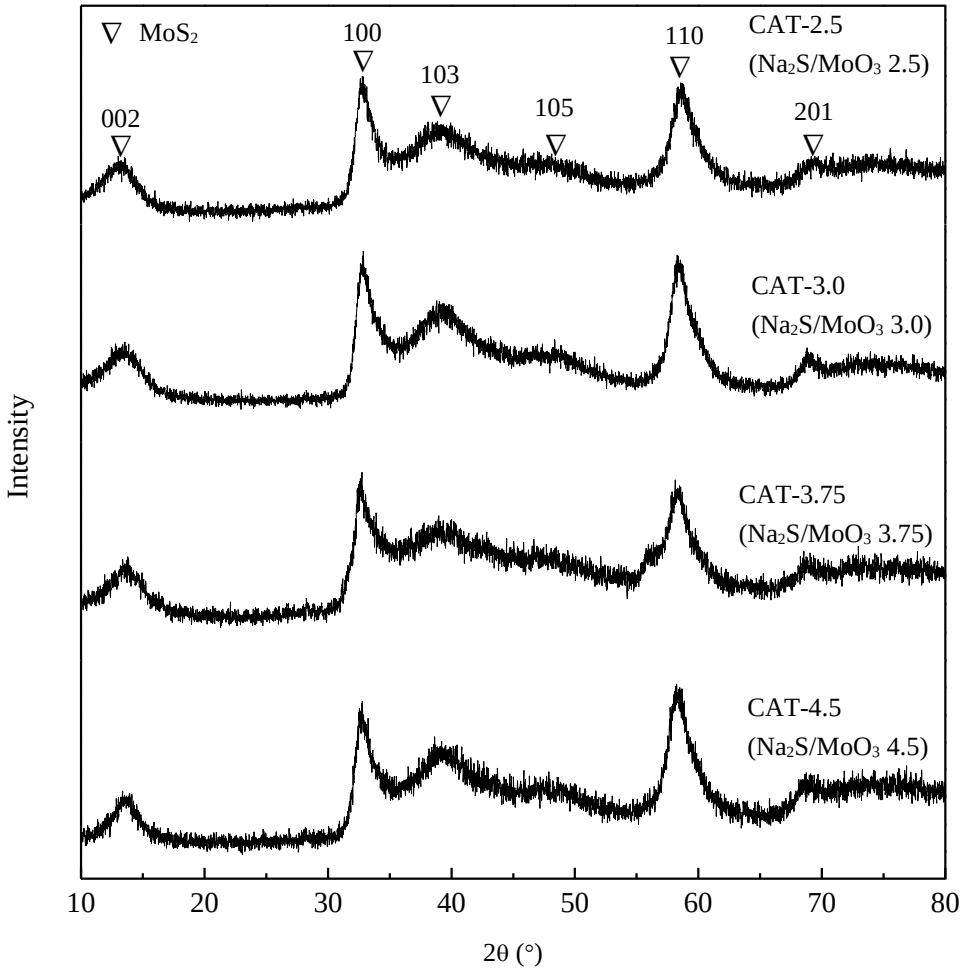

Figure 4.3 XRD spectra of MoS_2 synthesized at different Na_2S/MoO_3 ratios

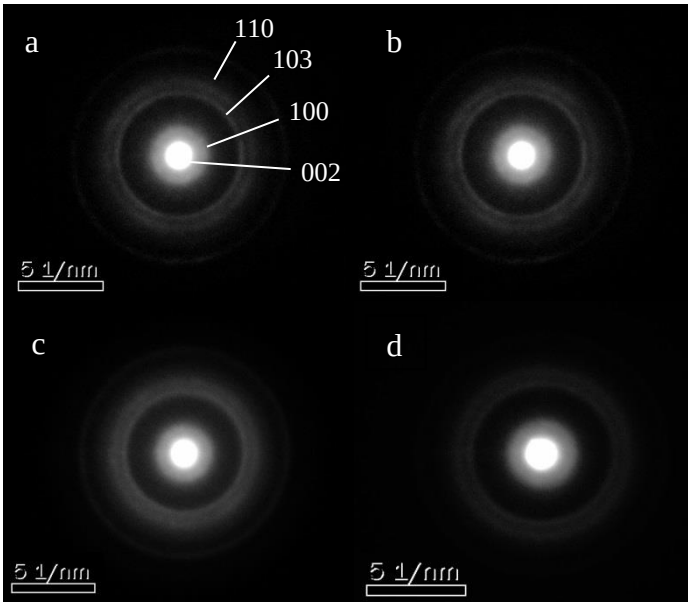

Figure 4.4 Diffraction rings of MoS_2 at different Na_2S /MoO_3 ratios
a: CAT-2.5; b: CAT-3.0; c: CAT-3.75; d: CAT-4.5

Under the successful synthesis conditions, the yield of MoS_2 is inversely proportional to the media pH (Table 4.3). Thus, based on acidity, the media is divided into three situations: acidic environment (pH 2-5), medium acidity (pH 8-10), and basic environment (pH >10). In the acidic environment, the yield of MoS_2 approaches 100%. Different sulfur valences exist, as seen from Table 4.3. In the basic medium, only a small amount of $S_2O_3^{2-}$ is produced, and most of sulfur may be in forms of unreacted S^{2-} or polysulfide S_x^{2-}. When increasing hydrogen ion concentration, the production of $S_2O_3^{2-}$ is enhanced. Further increase of hydrogen ion concentration facilitates the redox reaction with the generation of higher valence S form-SO_4^{2-} in the medium acidity atomsphere. A full conversion to SO_4^{2-} occurs in acidic environment. With the decrease of medium pH, the redox reaction moves forwards, as $S^{2-} \rightarrow S_x^{2-} \rightarrow S_2O_3^{2-} \rightarrow SO_4^{2-}$. Thus, more Mo^{6+} will be reduced to Mo^{4+}, leading to higher MoS_2 yield. The total reactions are shown in

Reaction 4.5 and Reaction 4.6 with $S_2O_3^{2-}$ and SO_4^{2-} as main oxidized product, respectively.

$$4MoO_3 + 9Na_2S + 16HCl \rightarrow 4MoS_2 + Na_2SO_4 + 16NaCl + 8H_2O \quad \text{Reaction 4.5}$$

$$4MoO_3 + 10Na_2S + 18HCl \rightarrow 4MoS_2 + Na_2S_2O_3 + 18NaCl + 9H_2O \quad \text{Reaction 4.6}$$

Table 4.3 Effect of Na_2S/MoO_3 molar ratio on MoS_2 recovery and filtrate pH

Catalysts	Initial pH	Filtrate pH	MoS_2 Yield (%)	$S_2O_3^{2-}$ Conc. (g/L)	SO_4^{2-} Conc. (g/L)
CAT-2.5	5.7	2.6	96.2	0.1	3.1
CAT-3.0	8.3	9.9	55.1	1.7	1.3
CAT-3.75	10.0	10.4	25.6	1.5	0.3
CAT-4.5	12.3	10.9	11.8	1.2	0.1
CAT-5.0	12.4	12.2	<1.0	0.2	0

4.3.2 Characterization of nanocrystalline MoS_2

The bulk and surface chemical states of catalysts are identified by XANES and XPS spectra. The S K-edge (a) and Mo L_3-edge (b) XANES spectra are displayed in Figure 4.5. The spectra acquired simultaneously in total electron yield (TEY) with an estimated 100 nm in probing depth are more bulk sensitive. The peak (whiteline) at 2471eV (peak A) is due to the S 1s to 3p dominated transitions of S in -2 oxidation state [171]. According to the typical periodic slab model [172], two types of S coordination are noticed on the MoS_2 surface. Thus, two broad peaks (B and C) located at 2478-2484eV and 2489-2495eV may be attributed to S pyramidal coordination on basal planes and S hexogen structure, respectively. The Mo L_3-edge (whiteline) observed at 2524eV with the shoulder peak (2532eV) is associated with the electron transition from Mo $2p_{3/2}$ to vacant 4d [173, 174] and the trigonal prismatic coordination of Mo atoms, respectively [173,

175]. Apparently, all spectra exhibit identical vacancy state as the reference, indicating a high purity of MoS_2.

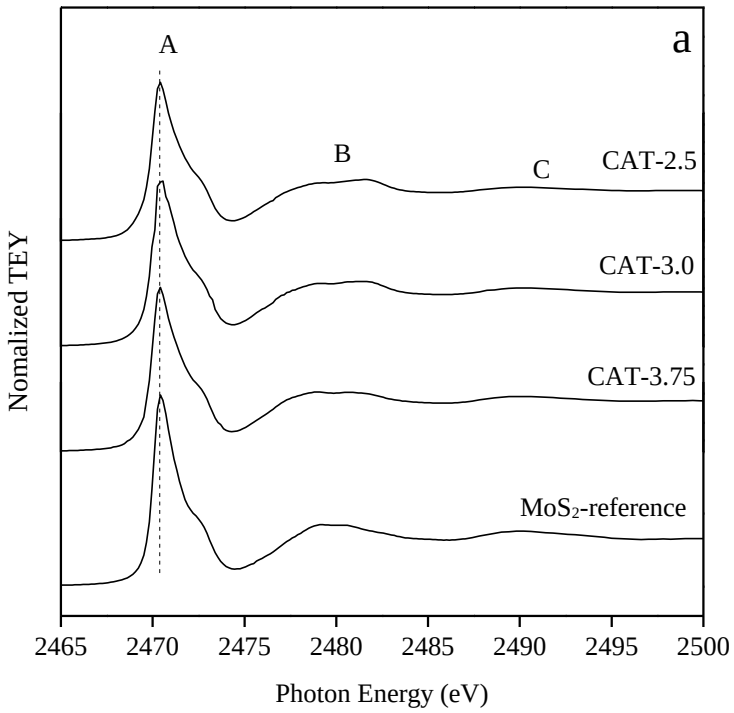

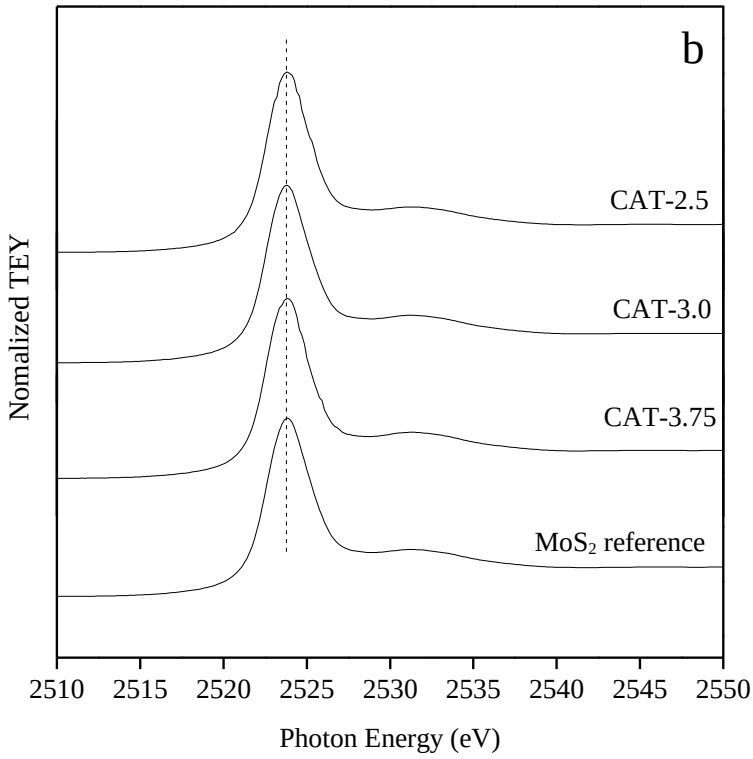

Figure 4.5 S K-edge (a) and Mo L_3-edge (b) XANES spectra of unsupported MoS_2

Typical XPS spectra of S 2p core level region of as-prepared MoS_2 catalysts are shown in Figure 4.6. All the spectra exhibit typical profiles of pure MoS_2 with strong S and Mo peaks. The S 2p spectra contain the S $2p_{3/2}$ (161.8 eV) and the S $2p_{1/2}$ (163.0 eV) spin-orbit doublet with intensity ratio of around 2:1 (Figure 4.6), which are indexed to a typical spectrum of sulfide S^{2-} ion [176]. No other S valences were detected. Small but clear differences in chemical shift are also observed among the catalysts. S $2p_{3/2}$ peak of CAT-2.5 slightly shifts to lower energy, whereas the peak of CAT-3.0 shifts to higher energy (circled), giving the electron binding energy order of CAT-2.5< CAT-3.75< CAT-3.0.

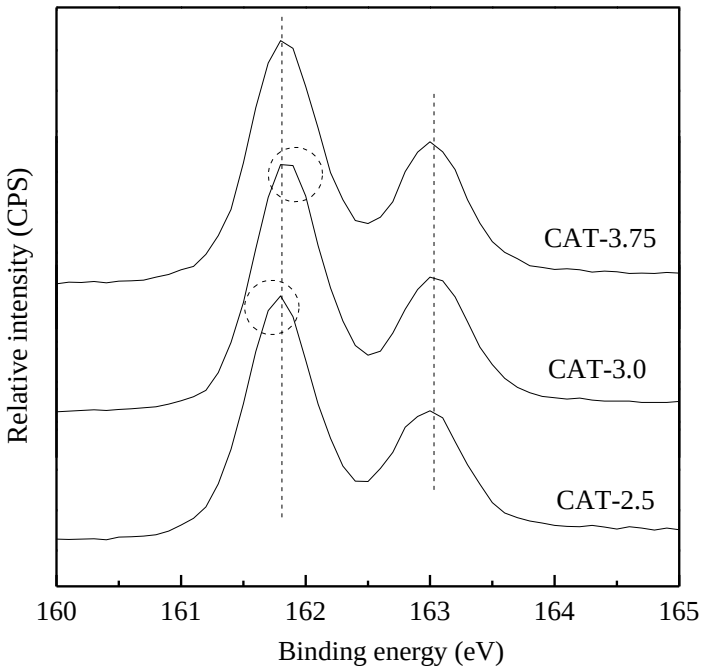

Figure 4.6 S 2p XPS spectra of unsupported MoS_2

The morphologies of the three unsupported catalysts with different MoO_3/Na_2S molar ratios are revealed by TEM (Figure 4.7). The dark thread-like lines shown in the fringes are the reflection of (0 0 2) lattice plane of the crystalline MoS_2, representing the stacked slabs. All the catalysts show dendritic morphologies and layered nanocrystallines. It is noticed that a large number of curved slabs are observed on the catalysts (circled in Figure 4.7), which may result in the creation of more defects on the basal plane [96].. Table 4.4 shows narrow ranges of 15.8-17.9 nm and 2.3-2.6 nm, for the average slab length and thickness, respectively. The average lengths obtained are significantly shorter than the crystallized MoS_2 synthesized by Li et al., with a slab of 50 nm in length [21]. The catalysts are in a similar range (10-20 nm) with those using $(NH_4)_2MoS_4$ (ATM) as precursors [18, 20].

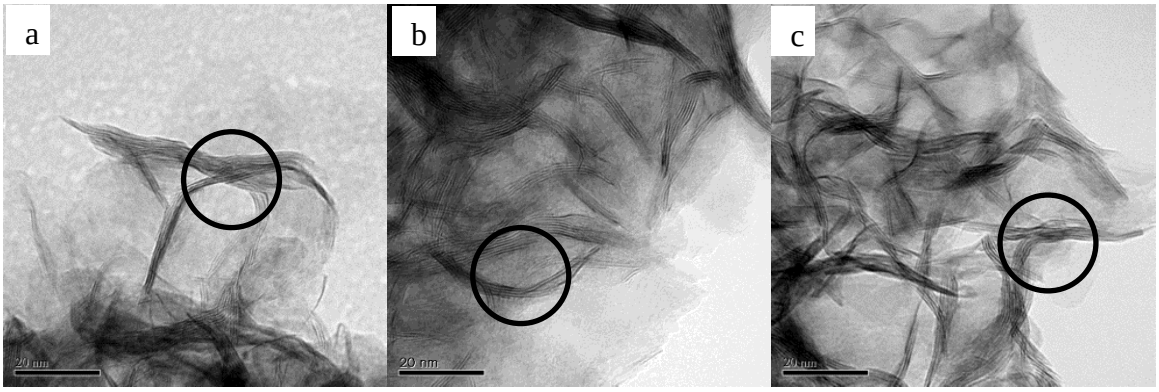

Figure 4.7 TEM images of MoS_2 at different Na_2S /MoO_3 ratios
a: CAT-2.5; b: CAT-3.0; c: CAT-3.75.

Table 4.4 Texture properties and elemental composition of unsupported MoS_2

Catalysts	Slab length (nm)	Slab thickness (nm)	BET surface area (m^2/g)	Total pore volume (m^3/g)	S/Mo ratio on the catalysts
CAT-2.5	17.4±0.9	2.3±0.2	231.1	2.276	1.85
CAT-3.0	15.8±0.7	2.6±0.1	262.2	1.607	2.05
CAT-3.75	17.9±0.8	2.5±0.2	198.9	0.945	2.10

Figure 4.8 shows SEM images of unsupported MoS_2. For both catalysts, thread-like MoS_2 crystals are associated in bundles and twisted together forming a flower-like morphology. The images exhibit nanosized particles with an average size of 100-200 nm. Mesopores over 10 nm are formed in between the crystals, as shown in the grey part surrounded by white MoS_2 layers. A slight difference observed is that CAT-2.5 looks more dendritic, while CAT-3.75 crystal favors growth on the boundary of particles.

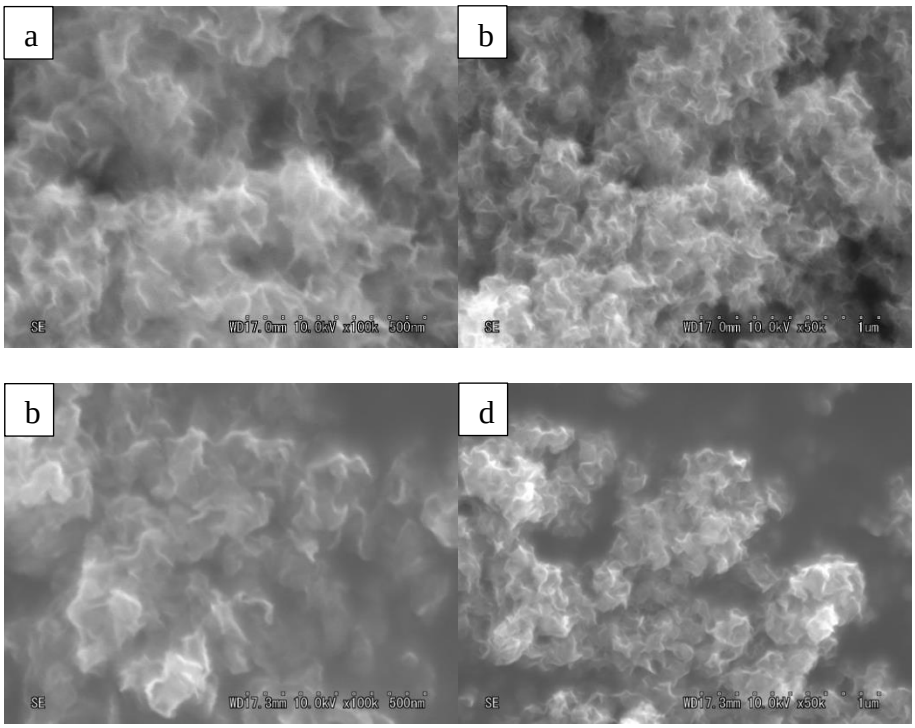

Figure 4.8 SEM images of unsupported MoS_2
a,b: CAT-2.5; c,d: CAT-3.75

The series of catalysts synthesized by the current hydrothermal method exhibit high surface area in the range of nearly 200 to 262 m^2/g (Table 4.4). A high pore volume of 0.95 to 2.28 m^3/g is also observed, which is much higher than that of other catalysts [98]. From the isotherm curves (Figure 4.9a), Type I adsorption isotherms are considered for all the MoS_2 catalysts and the hysteresis loop between adsorption and desorption isotherms is associated with mesoporosity. Catalysts also show similar pore size distribution with bimodal mesopore peaks at around 2.5 nm and over 10 nm (Figure 4.9b). A small shoulder is also seen at around 4 nm. The smaller pores are considered within the primary particles, whereas the larger pores are assumed to form in between the particles.

Both types of pores provide sufficient surface for catalytic application. The larger-size pores contribute to the substantial large pore volume of the catalysts.

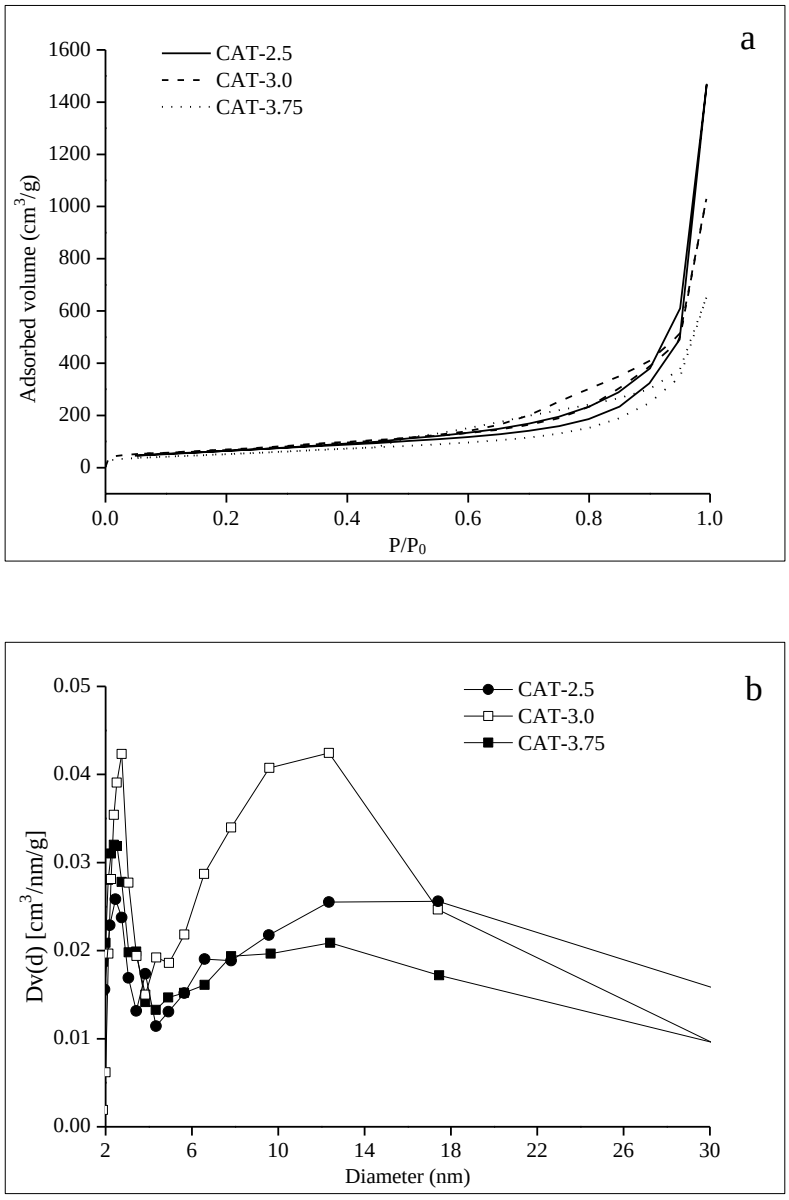

Figure 4.9 Isotherms (a) and pore size distribution (b) of MoS_2

Varying Na_2S/MoO_3 ratios from the precursors inevitably leads to the change of S/Mo ratios in the catalysts. The results from microprobe analysis show that S/Mo ratios are

1.85, 2.05 and 2.10 for the CAT-2.5, CAT-3.0, and CAT-3.75, respectively (Table 4.4). The lack or excess of sulfur might be related to the deformation of the crystal structure and defects on the catalysts. When S/Mo ratio is lower than the stoichiometric atom ratio of MoS_2 (2), defect sites might be already generated due to the deficiency of S. The lower S/Mo ratio was also observed on the hydrogen treated catalysts [84]. On the other hand, over-stoichiometric sulfur may exist in the form of S_2^{2-} species, which can form –HS species under hydrogen atmosphere and enhance hydrotreating reaction [84].

The TPR traces of sulfide catalysts are shown in Figure 4.10, illustrating the consumption of H_2 and the production of H_2S in the temperature range of 100-500 ℃. For H_2 consumption, typical peaks for weakly bonded sulfur are observed in the low temperature range of 200-370 ℃. It is commonly accepted that the consumption of H_2 can reflect the number of weakly bonded sulfur on the surface of catalysts [172, 177]. Dinter et al. described the model of this process: H_2 is firstly dissociatively adsorbed on two sulfur dimers that are bonded on adjacent Mo sites, creating two S-Mo-SH groups. Then one hydrogen atom transfers from one group to another to form a SH-Mo-SH group. Finally, H_2S is released from an active site of *-Mo-S, where * refers to the sulfur vacancy [172]. However, one assumption is that two sulfur dimers exist on the same Mo atom. If not, the SH-Mo-SH group cannot be formed properly, in which case, the system would be stabilized by a state of two *-Mo-SH groups, releasing no H_2S. Therefore, the contrast between H_2 consumption and a H_2S production in the TPR spectrum may distinguish the number of active sites that are already formed, from the active sites that can be formed. For catalyst CAT-2.5, the TPR spectrum shows a large H_2 consumption but no H_2S

production (Figure 4.10). The absence of a H_2S peak suggests a high deficiency of S on the surface. For the CAT-3.0 and CAT-3.75, the H_2S content is associated with the H_2 consumption, indicating the high coverage of S on the surface.

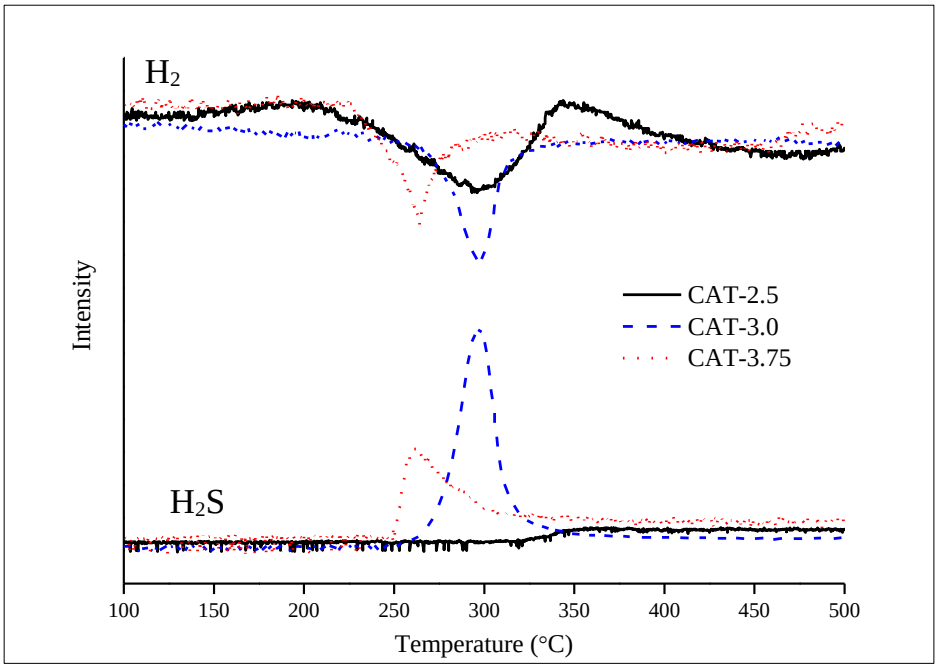

Figure 4.10 H_2 consumption and H_2S production during TPR treatment

Figure 4.11 shows the Fourier transform of the Mo K absorption edge for all the three catalysts. All the spectra exhibit two notable peaks corresponding to Mo-S (peak A) and Mo-Mo (peak B) [175]. The first largest peak at 1.90Å (phase shift uncorrected) arises from sulfur atoms in the first coordination sphere around Mo atoms, while the second peak at 2.86Å (phase shift uncorrected) is due to the nearest neighbor Mo atoms. The EXAFS results exhibit a similar MoS_2 structure. The only difference noticed is that the Mo-Mo bond for CAT-2.5 is lower than the other two catalysts. The calculated coordination number (CN) from the Fourier transform is shown in

Table 4.5. It is noticed that all the three catalysts exhibit lower CN than the MoS_2 in bulk. Similar to the spectra, the smallest CN of Mo-Mo is observed with CAT-2.5, indicating more disordered matrix on the surface.

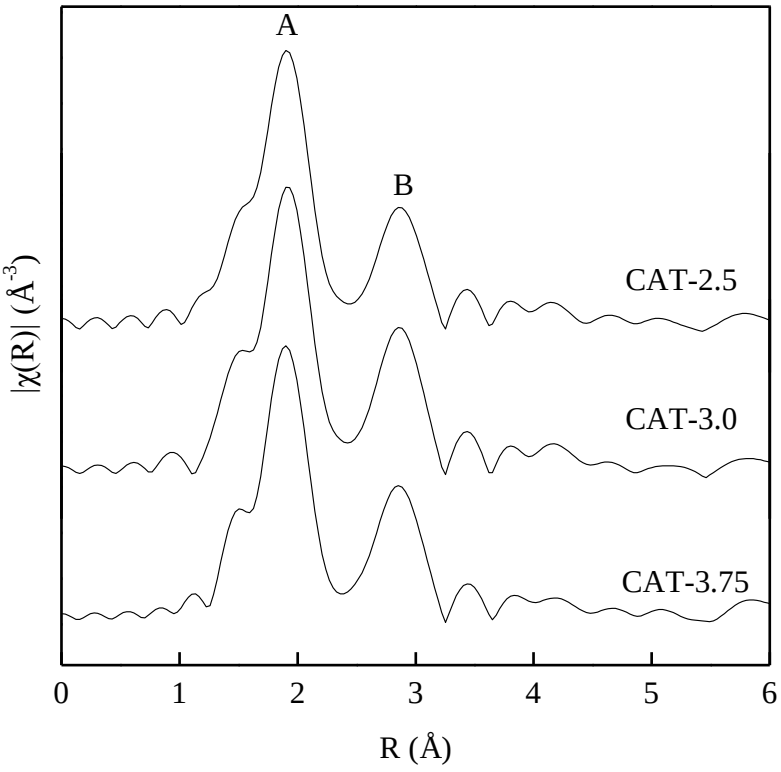

Figure 4.11 Fourier transformed EXAFS spectra of unsuppoted MoS_2

Table 4.5 Structural parameters resulting from the Mo K-edge Fourier-filtered k_3-weighted EXAFS functions of catalysts

Sample	Path	CN	R x100 (Å)	E_0 (eV)	R_f
MoS_2	Mo-S	6	241.3	-	-
	Mo-Mo	6	316.6		
CAT-2.5	Mo-S	5.0±0.1	240.8±0.3	2.2±0.6	0.0047
	Mo-Mo	4.0±0.3	316.4±0.4		
CAT-3.0	Mo-S	5.0±0.2	241.5±0.4	2.7±0.7	0.0053
	Mo-Mo	4.7±0.3	317.3±0.4		
CAT-3.75	Mo-S	4.8±0.2	240.6±0.5	1.7±0.9	0.0071
	Mo-Mo	4.6±0.4	3.171±0.006		

Estimated error: $\sigma^2_{Mo\text{-}S} \pm 0.002$ Å^2, $\sigma^2_{Mo\text{-}Mo} \pm 0.004$ Å^2.

4.3.3 Catalytic activities

Catalysts synthesized using the hydrothermal method with Na_2S and MoO_3 precursors were subjected to a performance test on HDS, HDN, and hydrocracking activities using LCO (Figure 4.12, Figure 4.13 and Figure 4.14). The initial HDS rate constants in the first hour for all catalysts are over 2×10^{-4} s^{-1} g $cata^{-1}$. The highest HDS activity is found with CAT-2.5, with a decreasing order of CAT-2.5>CAT-3.75> CAT-3.0. It needs to be noted that the decrease of reaction rate along with time is due to the complex sulfur composition in LCO (Table 3.1). CAT-2.5 also exhibits the highest HDN (Figure 4.12) and hydrocracking ability (seen from the product density in Figure 4.14).

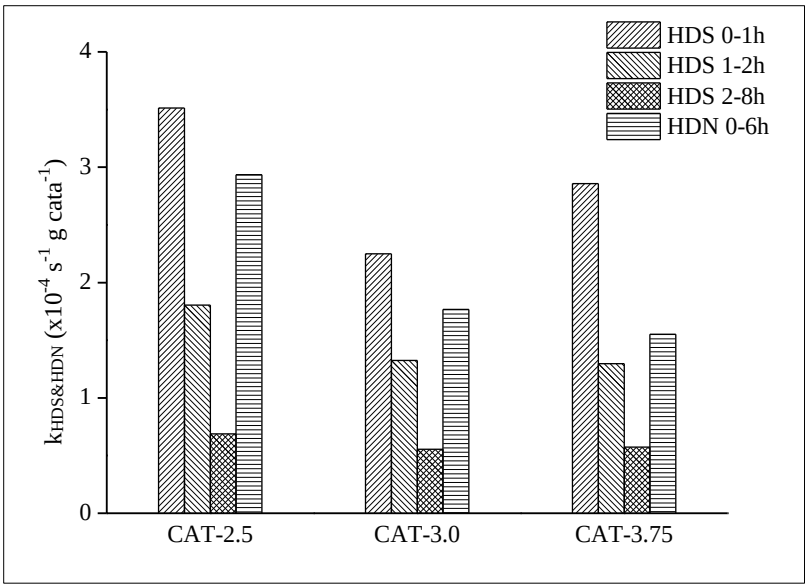

Figure 4.12 HDS and HDN activities of unsupported MoS_2 catalysts at different Na_2S/MoO_3 ratios

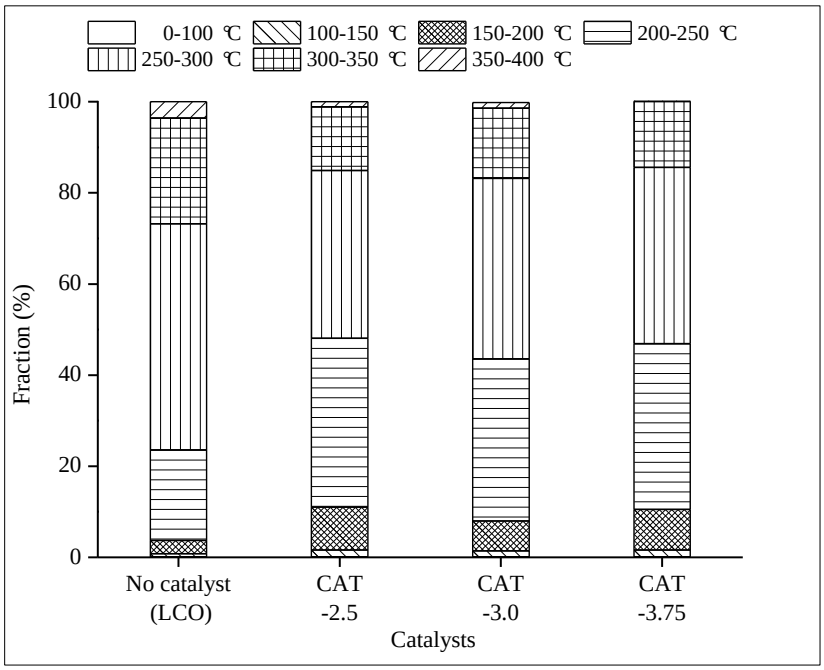

Figure 4.13 Boiling point distribution of LCO and hydrotreated product

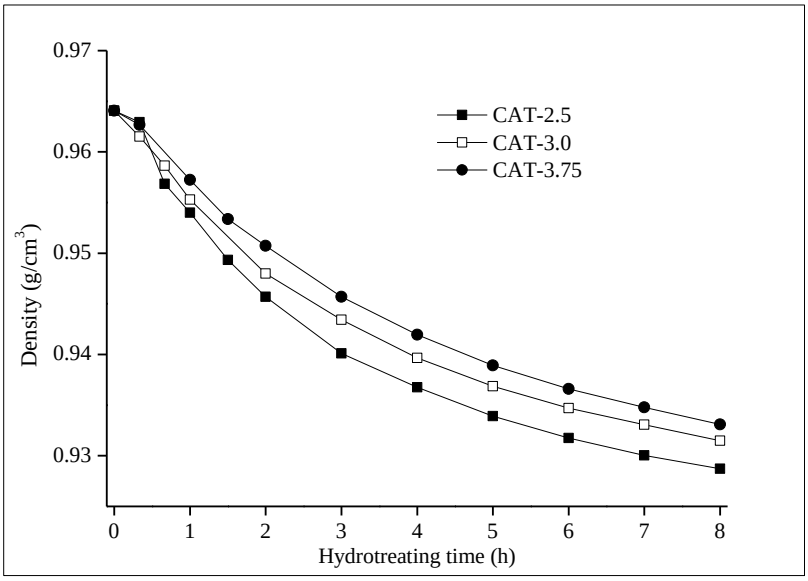

Figure 4.14 Density of hydrotreated LCO over unsupported MoS_2 catalysts (hydrocracking)

The hydrotreating activity can be interpreted by catalyst properties. Active sites are generally located on the edge and curved basal plane. The fraction of edge Mo atoms are proportional to the slab length [178]. Due to the similar slab length, the edge sites are similar on all three catalysts. The imperfect basal plane is also important for the activities, and defects are also largely located on the curved or twisted basal plane. This can be verified with TEM images that all the catalysts show highly curved morphologies. In particular, CAT-2.5 exhibits more blurred slabs, indicating more imperfect crystalline structure, which explains its highest activity of the three.

This phenomenon can be seen from S/Mo atomic ratio macroscopically. As more defects are created during the synthesis, the MoS_2 would deviate further from the perfect crystal, in other words, S/Mo ratio would further deviate from the stoichiometric number 2. This

is consistent with the results that MoS_2 with the highest difference from 2 exhibits the highest activity. The different types of active sites, i.e. S deficiency and overabundance are identified by TPR spectra. No H_2S is produced with CAT-2.5 of lower S/Mo ratio, while H_2S is generated corresponding the H_2 consumption with CAT-3.0 and CAT-3.75 of higher S/Mo ratio.

Relationships also can be observed between catalyst activities and other properties, e.g. binding energy, coordination number, disorder. However, no clear relationship is observed between activity and surface area. This observation was stated by several researchers [18]. Certain surface area is essential to provide more accessible active sites, however, the effect gets infinitesimal when sufficient exposed area are provided. Most of the calculated area is inert to the reaction.

4.4 Conclusions

Several novel nanocrystalline unsupported MoS_2 catalysts were successfully synthesized via hydrothermal method using commercially available MoO_3 and Na_2S. Results show that the H^+ is essential to the successful synthesis. The ratio of reactants, MoO_3 and Na_2S, is important to the nanocrystal structure and the yield. Excess or insufficient Na_2S/ MoO_3 ratio may result in poor purity of MoS_2 or low yield, respectively. Addition of other reduction agents, i.e. H_2, may fail to produce sulfide catalyst. Various characterization techniques were employed to assess the structure of synthesized catalysts. Results indicate that the catalysts are pure MoS_2 without any impurity substances. All catalysts synthesized at the proper range of Na_2S/MoO_3 (from 2.5 to 3.75 in the current case), have

nanosized structure, large surface area, and high pore volume (mesopores). HDS activity of hydrotreating LCO also exhibits a decreasing order of CAT-2.5>CAT-3.75> CAT-3.0.

Chapter 5 Effect of synthesis temperature and initial temperature on hydrothermal synthesis of a nanocrystal MoS_2

5.1 Introduction

In hydrothermal synthesis, temperature plays a significant role in determining MoS_2 catalyst qualities [21, 22]. However, comprehensive study of the effect of temperature from a catalysis standpoint has not been reported yet. The present work focuses on determining the effect of temperature on MoS_2 properties and activities. The effect of both synthesis temperature (sTemp) and initial temperature (iTemp) on catalyst characteristics were investigated. The properties of MoS_2 synthesized at different temperatures were extensively characterized by TEM, BET, XRD, XPS, TPR and XAFS, etc.; the hydrotreatment activities were evaluated using light cycle oil (LCO).

5.2 Catalyst synthesis

A series of molybdenum sulfide was synthesized by the hydrothermal method in a 1000 ml stainless steel autoclave (Parker Autoclave Engineers). 5.436 g of MoO_3 (STEM Scientific) and 33.989g of $Na_2S \cdot 9H_2O$ (Fisher Scientific) were first dissolved in 300 ml deionized water and slowly added with 42.5 ml of 4 M HCl solution (Fisher Scientific). The molar ratio of MoO_3, Na_2S and HCl was 1:3.75:4.5. The synthesis reaction was heated to different temperatures in the range of 200-350 ℃. For the synthesis temperature of 320 ℃, two initial temperatures of 20 ℃ and 270 ℃ were investigated. A special heating protocol was applied for the higher initial temperature (270 ℃). The reactor containing 300 ml water was first preheated to 270-280 ℃ and then 60 ml of concentrated precursor solution were instantaneously injected into reactor by nitrogen to

achieve the high-temperature start-up. For a special run, an immediate shutdown was applied once the reactor hit the setting temperature 320 ℃. All the other synthesis runs lasted for 2 hours under the stirring of 500 rpm unless indicated. After each run, the reactor was immediately cooled down with cooling water. Black solid resulted from synthesis was filtered and carefully washed with distilled water and ethanol. Catalysts prepared at different temperatures were denoted as CAT-initial temperature-synthesis temperature, e.g. CAT-20-200 stands for catalysts prepared at 200 ℃ starting heating from 20 ℃ (room temperature). A suffix "*" was used to indicate immediately suspended run at time zero, e.g. CAT-270-320*. The conditions are listed in Table 5.1.

Table 5.1 Synthesis conditions and textural structure of synthesized catalysts

Catalysts	Synthesis conditions		Slab length L (nm)	Slab thickness T (nm)	L/T[c] ratio	BET surface area (m^2/g)
	iTemp[a] (℃)	sTemp[b] (℃)				
CAT-20-200	20	200	10.2±0.3	5.1±0.2	2.0	84.5
CAT-20-270	20	270	13.4±0.6	1.9±0.1	7.1	218.4
CAT-20-320	20	320	17.9±0.8	2.5±0.2	7.2	198.9
CAT-20-350	20	350	11.3±0.4	2.0±0.1	5.7	155.9
CAT-270-320	270	320	12.3±0.6	1.7±0.1	7.2	236.3
CAT-270-320*	270	320	7.9±0.3	1.1±0.1	7.2	261.9

[a]: iTemp: Initial Temperature at which the heating starts.

[b]: sTemp: Synthesis Temperature at which synthesis is maintained.

[c]: L/T ratio: Ratio of slab length to slab thickness.

5.3 Results and discussion

5.3.1 Effect of synthesis temperature

5.3.1.1 Chemical state and crystallinity

The effect of synthesis temperature on the properties of the catalysts is first revealed from the chemical states of Mo and S atoms, using XANES spectra of S K-edge and Mo L_3-edge (Figure 5.1). For S (Figure 5.1a), the peak shown at 2471 eV in MoS_2 reference spectrum is attributed to the dominant electron transitions of S^{2-} valence state from 1s orbital to 3p orbital [171]. The broad peak presented at 2478-2484 eV and 2489-2495 eV is due to the S pyramidal coordination and S hexagon structure [172]. For Mo (Figure 5.1b), whiteline can be observed at 2524 eV for MoS_2 reference, which is due to the electron transition of Mo^{4+} oxidation state from $2p_{3/2}$ to vacant 4d orbital [173, 174]. The shoulder peak at 2532 eV is associated with the trigonal prismatic coordination of Mo atoms [173, 175]. Compared to the references, at a low sTemp of 200 ℃, a higher oxidation state of sulfur (S^{6+}) was indicated by the appearance of a small peak at 2483 eV. When inadequate temperature is imposed, oxygen is involved in the catalyst structure correlated with high valent sulfur. From the Mo spectra (Figure 5.1b), a complete reduction of Mo^{6+} was evidenced by the emergence of Mo^{4+} and absence of Mo^{6+}. For catalysts synthesized at elevated temperatures (270-350 ℃), MoS_2 profiles similar to the reference, indicating a pure MoS_2.

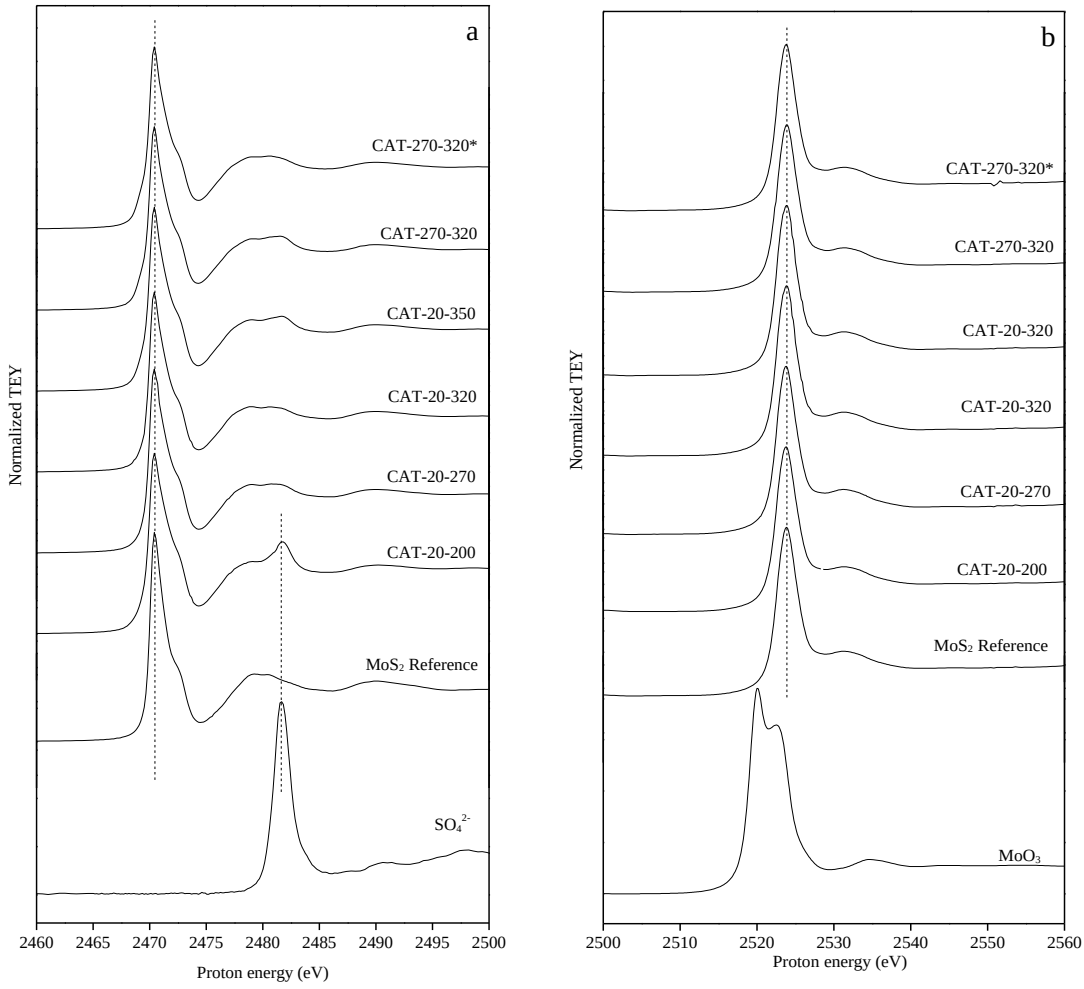

Figure 5.1 XANES spectra of unsuppoted MoS_2 a: S K-edge; b: Mo L_3-edge

The crystallinity of catalysts was identified by XRD spectra (Figure 5.2). At 200 ℃, the emergence of a 002 peak indicates a typical layered structure, whereas no discernible peaks are observed in the range of 33-58 ° except a board bulge, which may be derived from the merging of 100 and 103 faces. A small peak appears at 56.6 °, seen as left shift of 110 lattice facet. The spectra indicates a more amorphous-like MoS_2 (a-MoS_2) at low temperature. When the sTemp increases to 270 ℃, crystalline structure (denoted as c-

MoS_2 hereafter) starts to appear, manifested by the characteristic peaks for 002, 100, 103 and 110 facets (Figure 5.2). The broad peaks, on the other hand, also reveal poor crystallite structure, which cannot be further distinguished from XRD. Detailed comparison in crystallinity is revealed by EXAFS spectra with Fourier transform of the Mo K-edge adsorption for all the three MoS_2 catalysts at elevated temperatures (Figure 5.3). Each spectrum exhibits two notable peaks corresponding to Mo-S (peak A at 1.90 Å, phase shift uncorrected) and Mo-Mo (peak B at 2.86 Å, phase shift uncorrected) [175], which arise from S atoms in the first coordination sphere around the Mo atoms, and the nearest neighbor Mo atoms, respectively. Detailed curve fitting with bulk MoS_2 provides Mo–S and Mo–Mo structural parameters (Figure 5.2).

The Mo-S and Mo-Mo bond distances of all the catalysts are close to bulk MoS_2 standard. Mo-S and Mo-Mo coordination numbers (CN) at three temperatures are lower than six, similar to other literature results [121]. The deviation of CN from bulk MoS_2 is attributed to the disorder of the atomic arrangement. The CN is increasing with the elevation of sTemp, indicating that the catalyst crystallite structure is better developed at higher temperature, being more close to bulk MoS_2 phase [179].

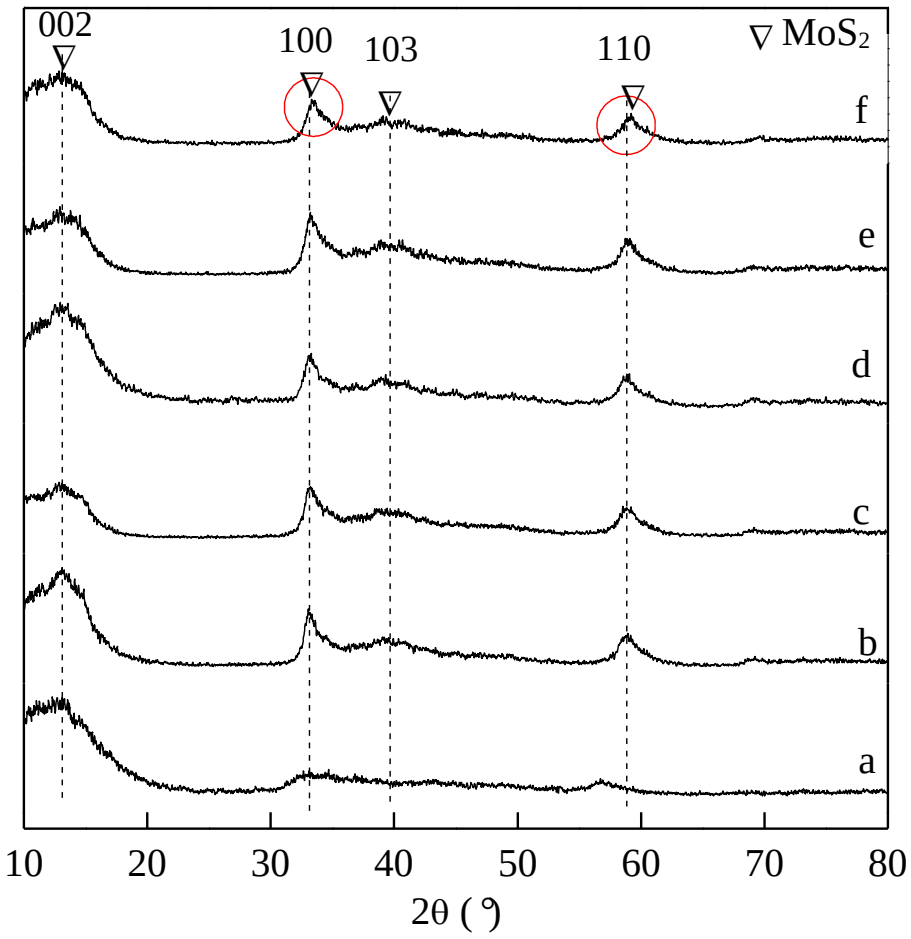

Figure 5.2 XRD spectra of synthesized MoS_2
a: CAT-20-200; b: CAT-20-270; c: CAT-20-320; d: CAT-20-350; e: CAT-270-320; f: CAT-270-320*.

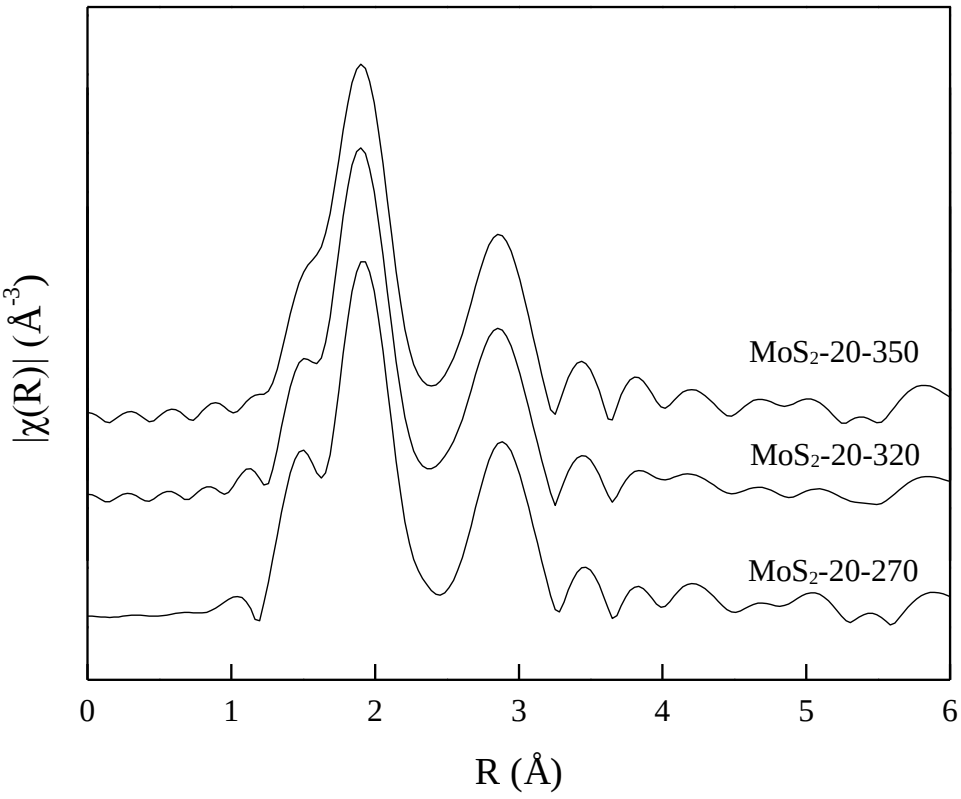

Figure 5.3 Fourier transformed EXAFS spectra of unsupported MoS_2

Table 5.2 Structural parameters from the Mo K-edge Fourier-filtered k_3-weighted EXAFS of unsupported MoS_2 catalysts

Samples	Path	CN	R ×100 (Å)	E_0 (eV)	R_f
MoS_2 reference	Mo-S	6	241.3	-	-
	Mo-Mo	6	316.6		
CAT-20-270	Mo-S	4.5 ±0.2	241.9 ±0.4	3.3 ±0.7	0.0053
	Mo-Mo	4.3 ±0.3	318.4 ±0.4		
CAT-20-320	Mo-S	4.8 ±0.2	240.6 ±0.5	1.7 ±0.9	0.0071
	Mo-Mo	4.6 ±0.4	317.1 ±0.6		
CAT-20-350	Mo-S	5.2 ±0.2	240.8 ±0.6	1.2 ±1.0	0.0103
	Mo-Mo	4.9 ±0.4	317.1 ±0.6		

Estimated error: $\sigma^2_{Mo\text{-}S} \pm 0.002$ Å^2, $\sigma^2_{Mo\text{-}Mo} \pm 0.004$ Å^2.

The development of crystallinity with temperature can be interpreted from the production process of MoS_2. The formation of MoS_2 crystallite from oxide precursor is a reactive crystallization, which is controlled by reaction and crystallization. At a low temperature of 200 ℃, a low reaction rate and thus a low supersaturation are expected. Sufficient supersaturation and temperature are required to overcome the maximum energy barrier for nucleation and crystal growth. Since the formation of amorphous material is more kinetically favorable [180], without adequate driving force molybdenum sulfide tends to grow in a less ordered manner to due to lowered growth resistance. In this case, the growth leads to a more amorphous-like MoS_2. This might be the reason for the existence of high valent sulfur S^{6+}. Without an ordered atomic arrangement, oxygen has an increased tendency to situate in the distorted structure as stated with Figure 5.1. When the temperature is elevated, atoms with sufficient energy to overcome the potential barrier will grow in a more ordered pattern. Continuous increase in temperature will increase the kinetic energy of atoms for the movement to the lowest energy position, and thus create a better crystal.

5.3.1.2 Textural structure and morphology

The size and morphology of synthesized catalysts is revealed by electron microscopy techniques. Both catalyst particles are in nano scale with an average size lower than 200 nm (Figure 5.4). CAT-20-200 seems having smaller size (50-100 nm) than that of CAT-20-320 (100-200 nm). An apparent difference was observed from the particle morphologies. No wirelike structure was generated at lower synthesis temperature (CAT-20-200), and the outer contour is more close to a sphere, whereas SEM images of CAT-20-320 show flower-like structure with associated needle-like MoS_2 crystalline.

Corresponding to the different morphology, distinct pore size distribution is observed. Two main pore size centered at 2-3 nm and 12-15 nm are shown for the catalysts synthesized at temperature 270-350 ℃ and only one broad peak appears at 2-3 nm for CAT-20-200. The smaller pores at 2-3 nm are the fine intra-aggregated pores from the material and the broad peak at larger size of 12-15 nm is attributed to the secondary pores from the combination of primary particles. The lack of large pores for CAT-20-200 is attributed to the smooth appearance of primary particles. Correspondingly, a-MoS_2 (CAT-20-200) shows a low BET surface area of 84.5 m^2/g (Table 5.1). c-MoS_2 (catalysts prepared at higher synthesis temperature), on the other hand, with dendritic structure, has great tendency to form secondary pores and exhibit high surface area in the range of 155.9-261.9 m^2/g.

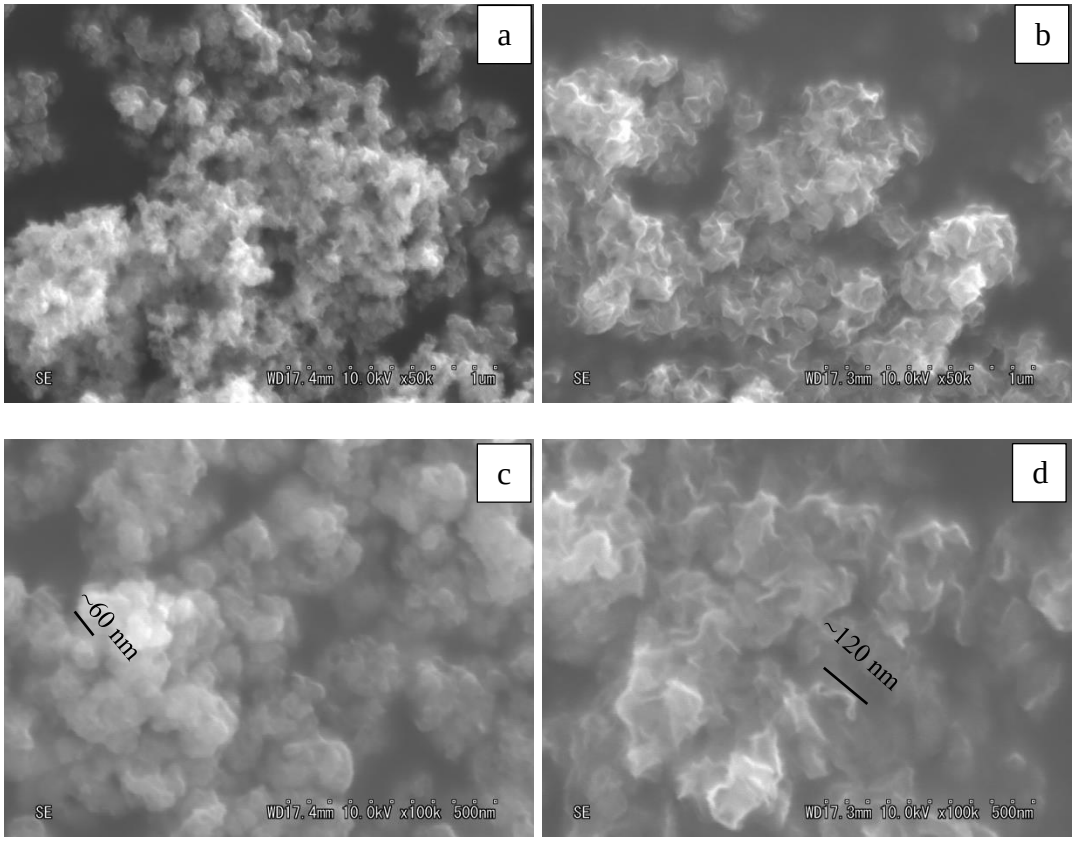

Figure 5.4 SEM images of unsupported catalysts
a,c, CAT-20-200; b,d, CAT-20-320

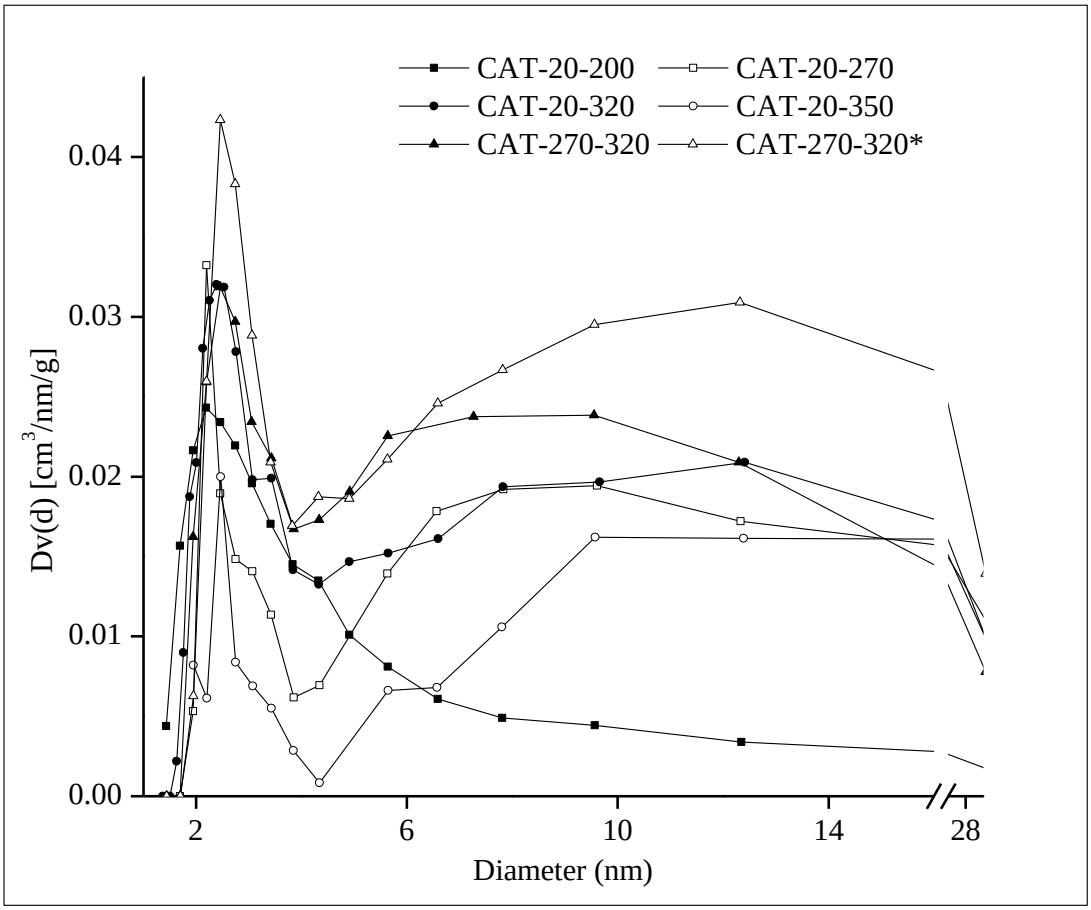

Figure 5.5 Pore size distribution of unsupported catalysts

Crystal structure was observed from TEM images (Figure 5.6). At 200 ℃, short MoS_2 slabs can be seen in the bulk of amorphous MoS_2 with an average length of 10.2 nm (Figure 5.6a). The full conversion of a-MoS_2 to c-MoS_2 occurs at a higher temperature (≥ 270 ℃) (Figure 5.6b-d). Catalysts synthesized at 270 ℃ and 320 ℃ both present highly dispersed dendritic morphologies and layered nanocrystallines. Clear crystal in the TEM images indicates the high purity of c-MoS_2, which is consistent with the XRD results. An increasing trend of length with the increase of temperature in the range of 200-320 ℃ is found. Similar phenomenon was also observed on other studies when synthesizing

nanocrystalline MoS_2 using ammonium tetrathiomolybdate as the precursor in a temperature range of 200-225 ℃ [181].

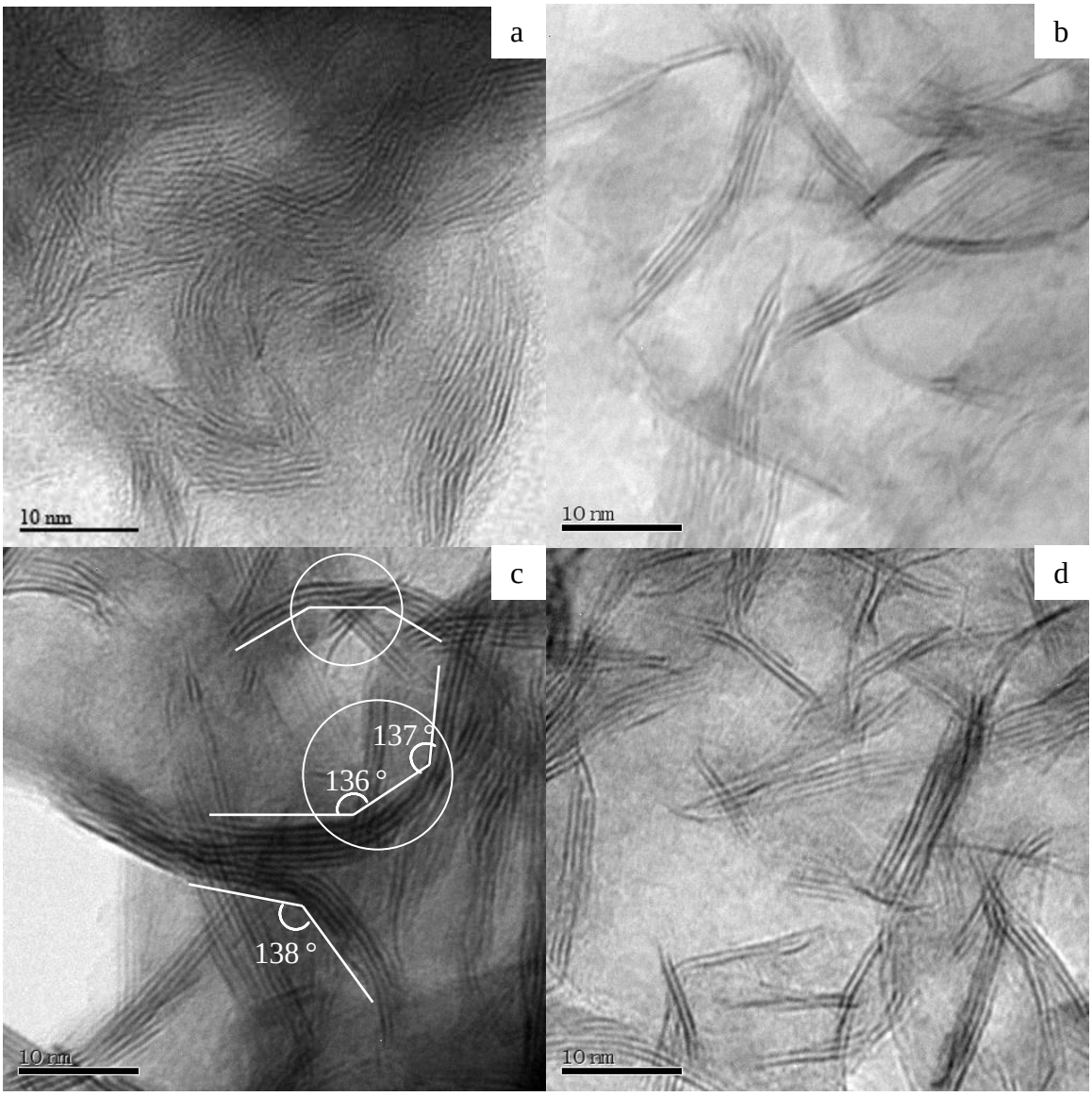

Figure 5.6 TEM images of unsupported catalysts
a. CAT-20-200; b: CAT-20-270; c: CAT-20-320; d: CAT-20-350

Further increasing the temperature to near-critical temperature 350 ℃, on the other hand, shortens the length of the c-MoS_2 from 17.9 nm to 11.3 nm (Figure 5.6d). The odd phenomenon indicates temperature is not merely functional in overcoming the activation energy. Furthermore, the properties of water are dramatically altered when approaching

the critical point. At or near critical point, specific characteristics are present, e.g. low dielectric constant, low surface tension, low solubility, high reaction rate and diffusivities, etc. [143, 182, 183]. At 350 ℃, the water would partially possess the characteristics of supercritical water. With these properties, such as low surface tension, the interfacial energy will be dramatically decreased and a large supersaturation will be generated leading to a higher nucleation rate (secondary nucleation) competing with the growth of MoS_2 slab. Smaller crystallites are consequently produced.

As well known, MoS_2 is a highly anisotropic layered material and the crystal growth occurs in parallel (length) and perpendicular directions (stacking) [14]. In the perpendicular direction, stacked multiple layers are bonded by weak Van der Waals forces. From Table 5.1, it can be seen that growth preferences are distinct for catalysts prepared at different synthesis temperatures. At low temperature of 200 ℃, growth of each face is more balanced, shown as a low L/T ratio. The priority of growth in a certain direction depends on the interfacial energy of each lattice plane. Growth is feasible when the energy barrier of a certain crystallographic face is overcome. In the perpendicular direction to the basal plane, superposition of layers with Van der Waals forces requires less energy than development of basal plane (002). Thus, CAT-20-200 crystals are thick and short.

At elevated temperature (≥270 ℃), when adequate energy is provided, the growth of 002 face becomes dominant, evidenced by the high L/T ratio (Table 5.1). Once the potential barrier is overcome, the ratio of growth rate of each face near constant (L/T:

around 7), which only depends on atomic planar density according to Bravais Law [184]. In the development of the basal plane at 320 ℃, it is also noted that the curvature of MoS_2 slab is significantly higher than of at 270 ℃, as seen from Figure 5.6c with a bending angle of 136-138 ° (circled). As the increase of growing rate with temperature, morphological instability would occur on the growing rough interface, which led to branching and curving [21]. The specialty of CAT-20-350 (L/T 5.61) is due to the characteristics of water in near-critical region, where advanced nucleation competes with the growth of MoS_2 basal plane.

5.3.2 Effect of initial temperatures

The initial temperature (iTemp) is the starting point for the synthesis of a crystalline catalyst. It becomes an important factor for the synthesis of a good catalyst as it determines the initial energy status of the synthesis environment. The effect of iTemp on the chemical state of the molybdenum and sulfur species of catalysts was examined using XANES and XPS techniques. In XANES spectra, no other Mo or S valences are detected except Mo^{4+} and S^{2-} as compared to the typical MoS_2 profile (Figure 5.1). Similar conclusions can also be drawn from XPS spectra. The profiles of S 2p orbital and Mo 3d orbital are exhibited in Figure 5.7. Typical peaks for S^{2-} ion and Mo^{4+} are observed at 161.8 eV and 163.0 eV for S 2p core, and at 229.0 eV and 232.1 eV for Mo 3d core, respectively [126, 176, 185]. Results indicate that the iTemp does not affect the molybdenum and sulfur state as long as sufficient synthesis temperature is applied. Typical MoS_2 diffraction peaks are observed from XRD spectra for catalysts under different iTemp with no significant differences noticed. It indicates the crystal structures can be generated once the minimum sTemp is exceeded (Figure 5.2).

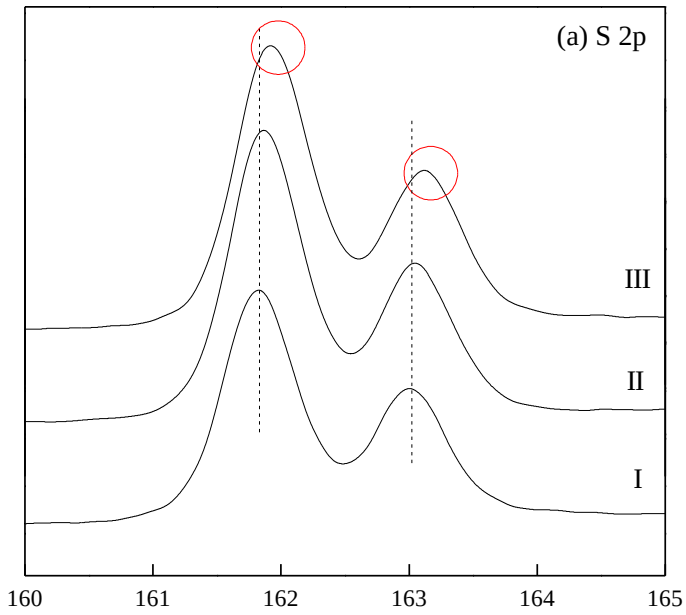

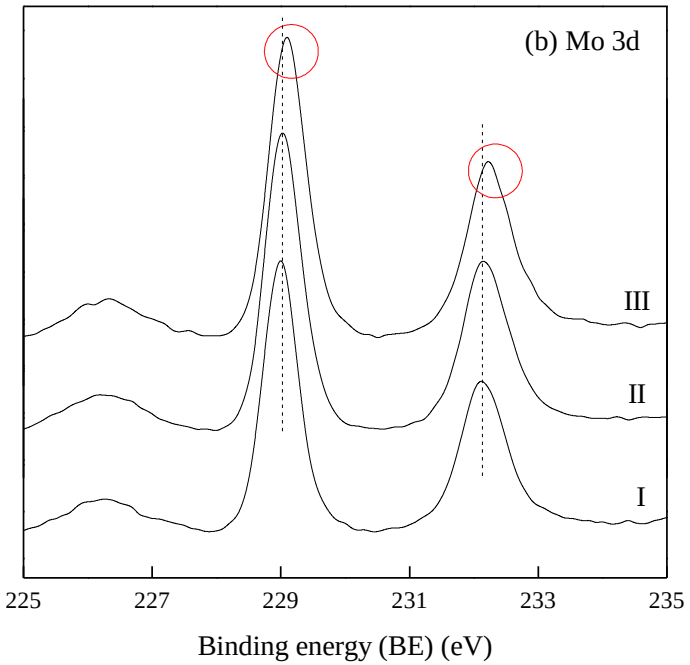

Figure 5.7 XPS spectra in the binding energy (BE)
a, S 2p; b, Mo 3d. Spectra I, II, III refer to CAT-20-320, CAT-270-320, and CAT-270-320*, respectively

TEM pictures clearly show high purity of c-MoS_2 structures for different iTemp. The effect of iTemp on crystalline structure can be found from the average slab length and thickness (Table 5.1). The statistical slab length and thickness are both decreased significantly with the increase of iTemp from 20 to 270 ℃. This is probably because more crystal nuclei are generated. At a high initial temperature of 270 °C, formation of MoS_2 occurs at an extremely high reaction rate. A high degree of supersaturation is generated simultaneously, which largely decrease the nucleation energy barrier according to the nucleation theory [135]. In addition, higher iTemp provides sufficient heat to overcome the potential barrier for the creation of nuclei leading to a high nucleation rate. The domination of nuclei formation leads to the formation of smaller particles, accompanying larger overall edge to basal ratio. In the situation of gradual increase of temperature, chemical reaction occurs in a moderate circumstance resulting in a relative low supersaturation state. Compared to the quick heating process, the nuclei of MoS_2 crystal are formed progressively, leading to the continuous growth of crystal in length, which results in a relatively large MoS_2 crystal.

The rapid crystallization not only leads to short slabs, but also largely influences the crystal morphology. At a high initial temperature, the growth following nucleation also occurs at an exceedingly high rate. Compared to the gradual heating protocol of CAT-20-320, more local defects are created on CAT-270-320 (Figure 5.8a,b), e.g. curvatures with sharper angles (circle 1), crystalline separation or merging (circle 2), slab growing together and lattice distance variation (circle 3) and rough edges (circle 4).

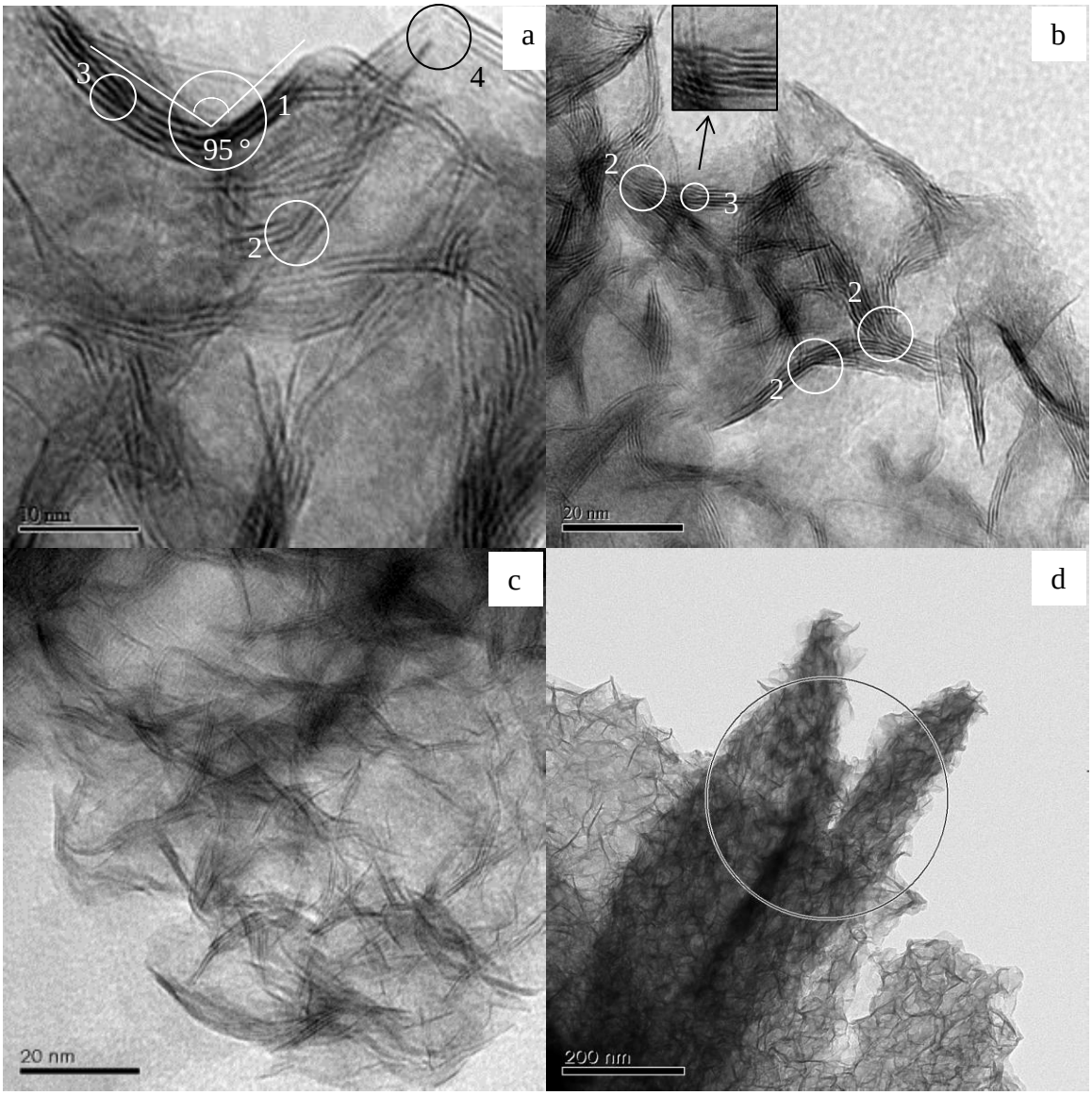

Figure 5.8 TEM images of unsupported catalysts
a, b: CAT-270-320; c, d: CAT-270-320*

5.3.3 Time–dependent crystal growth

To better understand the speciality of enhanced initial temperature, the time evolution of crystalline development was studied. The synthesis of CAT-270-320a* is forced to stop as soon as the setting sTemp is reached. Incomplete-sulfided stick-like MoO_x was observed from TEM images (Figure 5.8d, circled) and evidenced by EDX spectra with

the presence of oxygen peak and lowered sulfur peak compared to CAT-270-320 (Figure 5.9). Since only Mo^{4+} is detected in XANES and XPS spectra without the appearance of any other Mo oxide state (Figure 5.1, Figure 5.7), MoO_x is more likely to be in the form of MoO_2 instead of MoO_3. A further observation shows identical spectra in XANES but difference in XPS. An evident right shift in Mo and S peaks of CAT-270-320* is noticed compared to CAT-270-320 (Figure 5.7), indicating a higher binding energy of inner electrons (Table 5.3). The existence of polysulfide S_x^{2-} might be one of the possible reasons [176]. The different observations from XPS and XANES indicate the changing of chemical state is mainly on the surface, since XPS is more surface sensitive with a probing depth of 2-4 nm, while XANES with the estimated probing depth of 100 nm is more bulk sensitive [171]. When the reaction proceeds, MoO_x is fully sulfided and pure MoS_2 is generated.

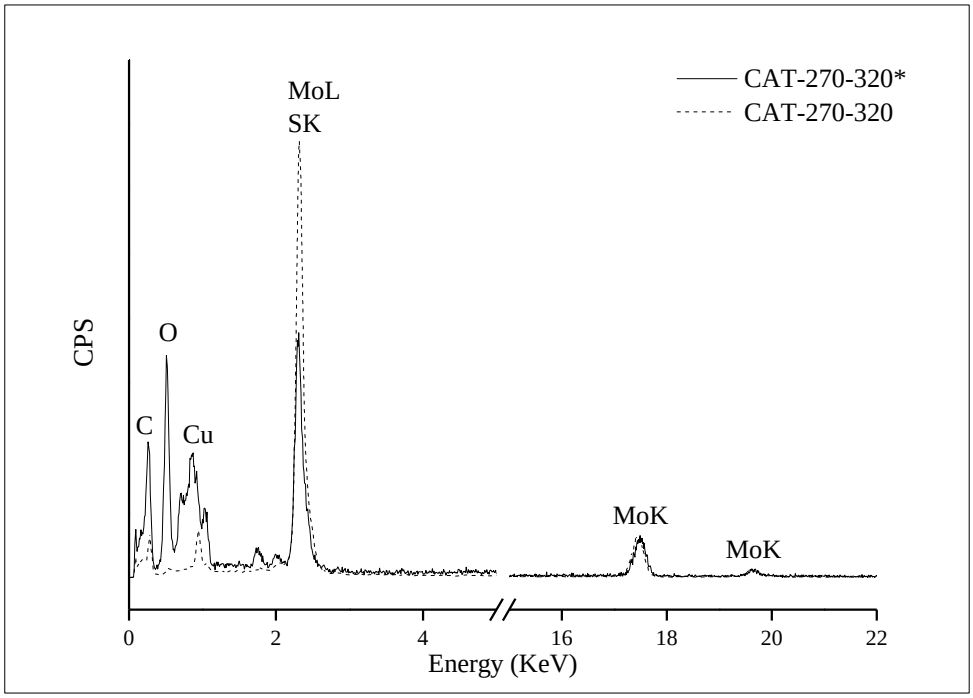

Figure 5.9 EDX spectra of CAT-270-320* (in the circle of Figure 5.8d) and CAT-270-320 (for comparison)

Table 5.3 XPS Binding Energies for unsupported MoS_2

Catalysts	Binding energy BE (eV)				BEs difference (eV)
	S $2p_{3/2}$	S $2p_{1/2}$	Mo $3d_{5/2}$	Mo $3d_{3/2}$	Mo $3d_{5/2}$-S $2p_{3/2}$
CAT-20-320	161.8	163.0	229.0	232.1	67.2
CAT-270-320	161.8	163.0	229.0	232.1	67.2
CAT-270-320*	161.9	163.1	229.1	232.2	67.2

From XRD results, the lattice distance at time zero (when iTemp is reached) is altered from the mature crystalline. The 100 and 110 peaks shift to the left and the distance d is correspondingly smaller (Figure 5.2, Table 5.4). In a quick nucleation and growth process, the formation of nuclei and deposition of monomers proceed at an enormous rate. Crystallization is forced to stop before atoms move to the lattice. With the passing of synthesis time, the crystal is further developed in crystallinity. The variation of thermal vibration continues to provide energy to atoms to overcome the surface potential and move to the lattice position, thus improve the crystal structure. This is evidenced by the rectified lattice distance after 2-hour reaction. It's worth noting that there are still more local defects on CAT-270-320 than the gradual heat-up (CAT-20-320), although the main lattice structure is identical.

Table 5.4 d values (Å) at different initial and synthesis temperatures

Catalysts	d values (Å)	
	(100)	(110)
CAT-20-320	2.71	1.57
CAT-270-320	2.71	1.57
CAT-270-320*	2.67	1.56

Higher initial temperature will provide more energy at the nucleation stage. As a result, a high metastable supersaturation will be formed, which not only generates nuclei, but

cause monomer deposition on the nuclei for consequent growth [186, 187]. As shown in Figure 5.10, crystal is quickly formed at time zero, and slowly developed with crystallization time. The initial growth into 7 nm at time zero occurs in a far-from-equilibrium region, and the crystalline is mainly due to the deposition of free monomers. Along with the growth, supersaturation decreases, leading to the decline of nucleation and growth rate. Thus the Gibbs-Thomson effect becomes significant. The growth of larger crystalline is then contributed by monomers from the dissolve of the smaller clusters, which leads to the slow increase of slab length from time zero to time 2 hours [134].

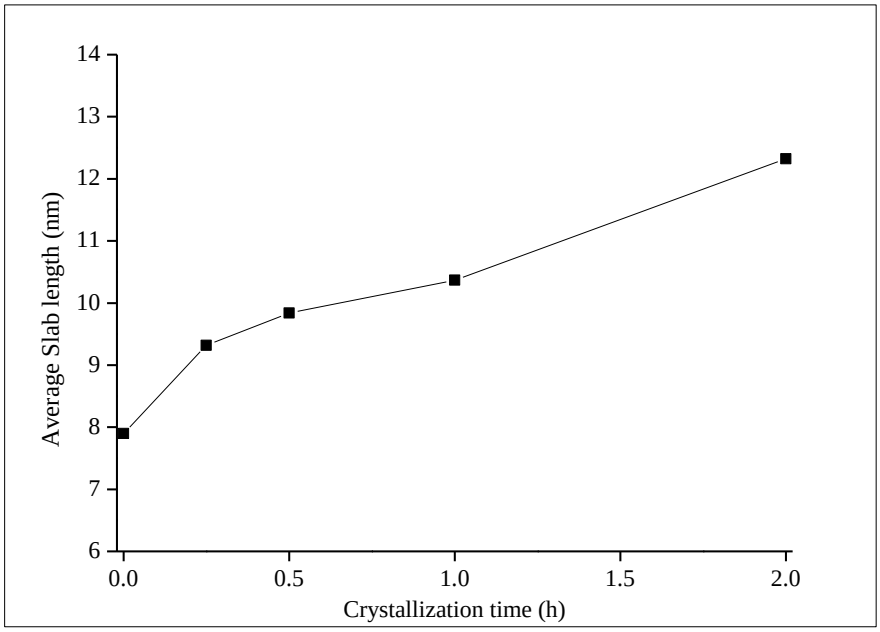

Figure 5.10 The development of crystalline length with crystallization time

5.3.4 Hydrotreating activity of MoS_2 on LCO

The synthesized MoS_2 catalysts were evaluated by hydrodesulfurization tests on LCO. Compared with model oil, the composition of LCO is more complex, containing both

easy (benzothiophene, alkyl-benzothiophene) and hard sulfur (dibenzothiophene, alkyl-dibenzothiophene) compounds, as well as nitrogen compounds (Table 3.1). Thus, the reaction is divided into two phases (0-1 hour and 1-8 hours) for the varied rate constants when eliminating S with different difficulties.

Table 5.5 shows the pseudo-first-order HDS and HDN activity of unsupported MoS_2 catalysts on LCO. Within all the catalysts prepared, the HDS kinetic rate constants vary in 19.3-54.9 and 5.3-11.4 $\times 10^{-5} s^{-1} g\ cata^{-1}$ in the first hour and following reaction, respectively. As the sTemp increases from 200 to 350 ℃, the initial HDS rate constant significantly increases from 19.3 to $45.2 \times 10^{-5}\ s^{-1} gcat^{-1}$. The effect of iTemp has the same trend with sTemp that the HDS increases significantly from 28.6 to $54.9 \times 10^{-5}\ s^{-1} gcat^{-1}$ when the iTemp increases. This indicates that a better catalyst may be generated by increasing the initial temperature. HDN activity follows the same trend with HDS. The hydrocracking ability is described by boiling point distribution obtained from simulated distillation, as shown in Figure 5.11. For each catalyst, the fraction of boiling point below 250 °C largely increases at the expense of fraction above 250 °C, indicating the occurrence of hydrocracking. Higher hydrocracking ability is obtained when increasing the synthesis temperature and initial temperature.

Table 5.5 Kinetic data for HDS activity on LCO at 375 ℃

Catalysts	Rate constant (10^{-5} $s^{-1}gcat^{-1}$)		
	HDS (0-1 hour)	HDS (1-8 hours)	HDN (0-8 hours)
CAT-20-200	19.3	5.3	3.2
CAT-20-270	23.3	5.9	9.9
CAT-20-320	28.6	6.6	15.5
CAT-20-350	45.2	6.8	30.0
CAT-270-320	54.9	11.4	47.0
CAT-270-320*	34.5	8.3	22.8

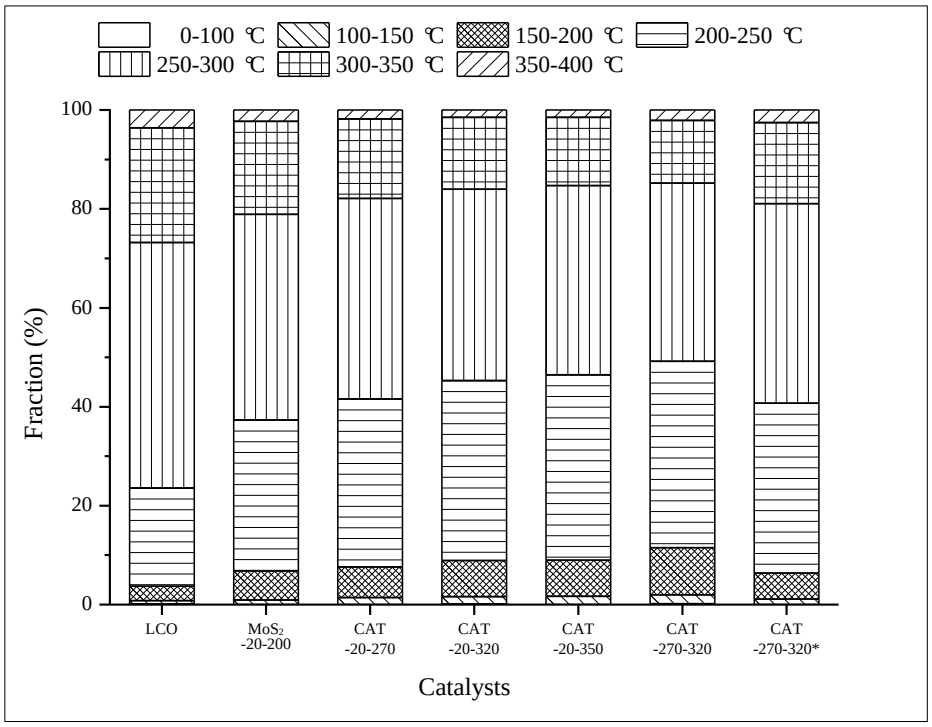

Figure 5.11 Distribution of boiling points of hydrotreated products

The catalytic activities of MoS_2 are highly influenced by synthesis temperature and initial temperature through the impact of crystal properties which, in our case, are crystal structure, crystal size and morphology. Crystal is essential to provide suitable structure and to create active sites and high surface areas, which can be evidenced by the low

hydrotreating performance of CAT-20-200 that do not have a crystal structure. It is also observed that the activity is increased with the improvement of crystallinity after crystal structure is generated. A possible reason may be related to the ability of providing structural sulfur. When the crystallinity is low, amorphous structure are generally exhibited on the edge sites, since the fully saturated basal plane is expected to be better arranged. Consequently, amorphous structure on the edge may decrease the efficiency of creating accessible structural sulfur deficiency.

Crystal size and morphology play an important role in generating sufficient amount of active sites. Based on the characterization and HDS evaluation, it is found that catalytic activity is enhanced with shorter slab and larger curvatures, regardless of the sTemp or iTemp. For instance, better performance is observed with catalysts of the shorter (CAT-20-350) or curved (CAT-20-320) slabs. The highest activity is obtained from CAT-270-320 that possesses both characteristics. This observation is consistent with the other statements that the active sites are located on the edge and curved basal plane [26, 28]. The exception of a lower activity of CAT-20-320* with shortest slabs compared to CAT-270-320 is mainly due to the impurity of MoO_x and distorted structure. However, it is worth noting, in spite of impurity, CAT-20-320* still exhibits a fair activity due to extensive sites on the edge and basal plane.

The relationship between the catalysts properties and activities is further investigated by temperature programmed reduction (TPR) (Figure 5.12). In TPR spectrum, no obvious hydrogen adsorption on a-MoS_2 (CAT-20-200) is identified from 100 to 500 ℃

compared to high synthesis temperature (Figure 5.12). The profile confirms the amorphous structure of the catalyst and exhibits a poor H_2 adsorpability. For c-MoS_2 catalysts, large peaks are found in the reduction temperature of 200-300 ℃, which refers to the S coverage on the edges and rims. Other H_2 adsorption (on the right side of line) at higher temperatures represents the further depletion of S on defect sites of basal. CAT-20-270 and CAT-20-350 with less curved slabs only have one distinguishable peak with a tiny peak at higher temperature (over 300 ℃). Results indicate activity of these catalysts is mainly resulted from the edge active sites. On the other hand, besides the distinct peak at low temperature range (on the left side of line), TPR spectra of CAT-20-320, CAT-270-320, and CAT-270-320* show a unique H_2 consumption shape at high temperature, which is hardly distinguished as a "peak, but a flat area. This H_2 consumption is attributed to the defect sites on the basal plane. Unlike more uniformed edge structure, which requires similar energy showing a shape peak on TPR spectra, the active sites on the basal plane are in a large variety due to the different degrees of curvature, leading to broad adsorption area in terms of temperature. It is also observed that the H_2 adsorption capability over 300-500 °C is largely increased for the catalysts synthesized at high iTemp, corresponding to the higher fraction of defects on the basal plane.

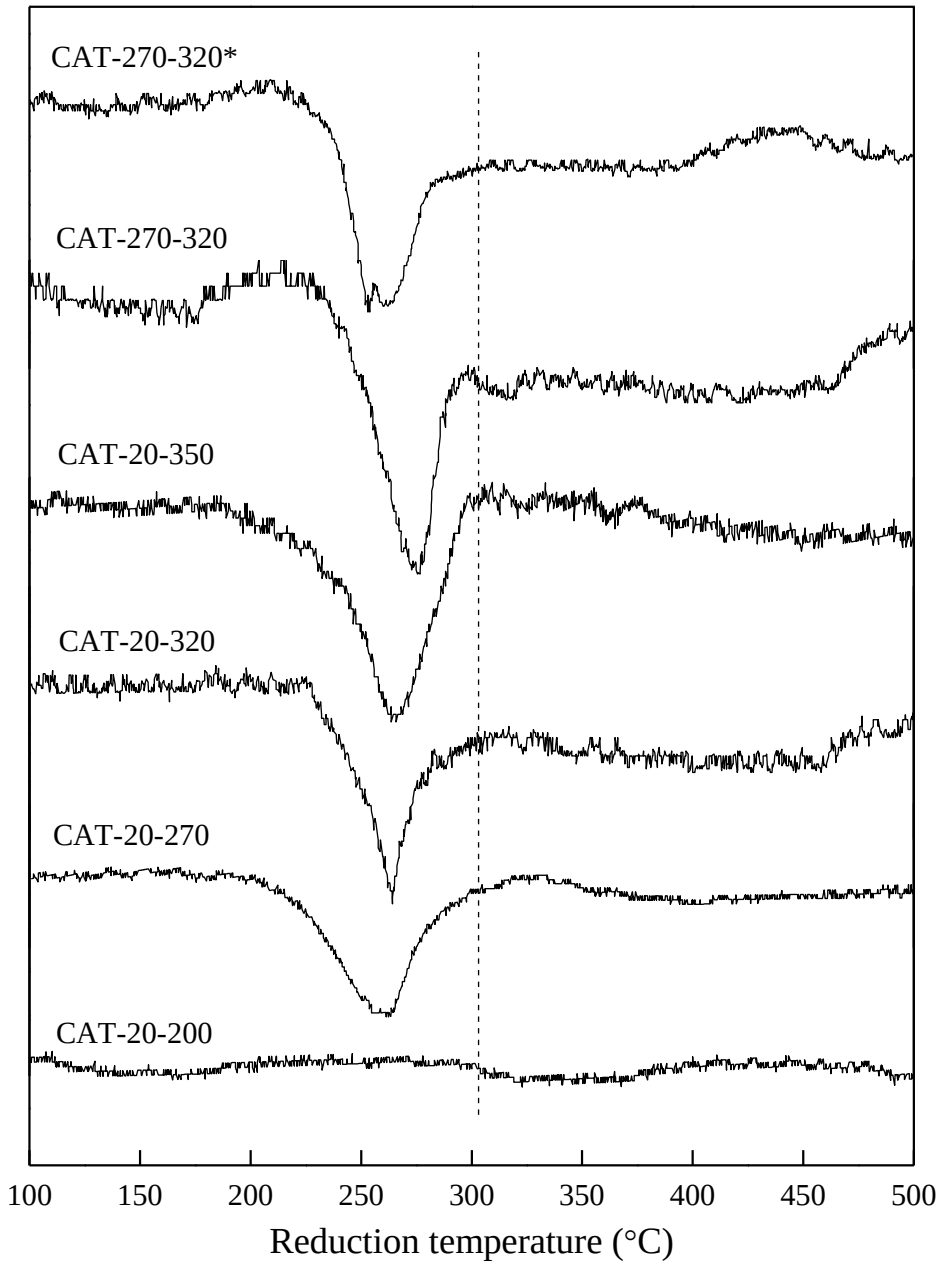

Figure 5.12 H_2 consumption during TPR treatment for catalysts synthesized with different synthesis temperatures and initial temperatures

In summary, crystalline structure is essential to provide the structural sulfur for potential active sites. To increase the active sites, more active sites are expected from the edge sites and local defects within the basal plane. The attempt to shorten slab length and

increase local deformation in the basal plane will thus benefit the hydrotreating performance.

5.4 Conclusions

A series of unsupported MoS_2 catalysts were synthesized via a novel hydrothermal method. Commercially available Na_2S and MoO_3 were employed as precursors. The synthesis temperature and initial temperature show a strong influence on catalyst properties and activities. MoS_2 prepared at higher synthesis temperature and initial temperature exhibits higher HDS and HDN activities. The HDS (BTs) rate constant of MoS_2 synthesized at 350 ℃ (CAT-20-350) is more than 2 times of that at 200 ℃ (CAT-20-200), and HDN rate constant of CAT-20-350 is nearly 10 times of the latter one. Similarly, the HDS and HDN rate constant of MoS_2 prepared from 270 ℃ is nearly 2 times of the one starting at 20 ℃.

There are two molybdenum sulfide states detected: amorphous a-MoS_2 and nanocrystalline MoS_2 (c-MoS_2). At low temperature of 200 ℃, the presence of amorphous a-MoS_2 and inadequate sulfidation largely decrease catalyst activity. The full conversion to c-MoS_2 was achieved after 270 ℃. The further increase of c-MoS_2 activity with temperature is attributed to the curved and shortened MoS_2 slabs. With the increase of synthesis temperature from 270 ℃ to 320 ℃, the slabs tend to grow longer and to curve; further increase of temperature to near critical temperature 350 ℃ results in a decrease in the curved slabs. Results are confirmed by TEM and TPR. Higher initial temperature increases the nucleation rate, which in turn would lead to more defects and short slabs, and further enhance the hydrotreating activities. The attempt of synthesis of a

catalyst with no reaction time to limit the crystal growth is not feasible due to the inadequate sulfidation. This prepared catalyst shows lower activities compared to fully sulfide MoS_2 synthesized for 2h in spite of its shorter slab length.

Chapter 6 Increase of curvature in the MoS_2 basal plane with organic solvent

6.1 Introduction

Recent studies discovered that active sites can be generated from the curved points on MoS_2 basal planes [19, 28, 29]. The generation of this potential active site (curvature) can be enhanced by adding organic solvent that can isolate the continuous water phase and orient the growth on the curved interfaces. In the present study, decalin was introduced to the synthesis system. The enhancement was evaluated by the HDS activity of catalysts in different decalin to water ratios. The effect of mixing energy on the isolation was also studied, since the dispersion of immiscible decalin and water highly depends on the agitation energy inserted. In addition, the study extends to supercritical fluid because of its higher ability of breaking the solution into droplets.

6.2 Experimental

Unsupported MoS_2 catalysts were synthesized by a hydrothermal method with MoO_3, $Na_2S \cdot 9H_2O$, and HCl as precursors. The precursors with the molar ratio of 1: 2.5: 4.5 were first dissolved in distilled water and then mixed with different amounts of the organic solvent decalin. After decalin was introduced to a batch reactor, the mixture was heated up to 320 ℃ and kept for 2h under different agitation speeds. For the synthesis with supercritical heptane, the precursors were introduced after the temperature over the critical temperature of heptane (267.1 ℃) to ensure the crystallization started in the supercritical condition. The obtained catalysts were denoted as CAT-fraction of solvent, solvent type-stirring speed, e.g. CAT-80D-500 represents the catalyst synthesized in the

media of 80 vol. % decalin (20 vol. % water) under 500 rpm stirring. D stands for decalin, while SC stands for supercritical fluid. The detailed synthesis conditions are listed in Table 6.1.

To quantify the effect of organic solvent (or supercritical fluid) on MoS_2 morphology, the degree of curvature for an individual slab (i) is defined and calculated by Equation 6.1 [188].

$$\kappa_i = \frac{\Delta\varphi_i}{\Delta s_i}|_{i=1,2,3...} \qquad \text{Equation 6.1}$$

where, κ, Δφ, and Δs denote the mean curvature of a stacked slab, the change of angles in radian, and the length of arc, respectively. The average curvature $\bar{\kappa}$ is represented by the mean of κ_i based on at least 100 measurements from different particles. The standard deviation was calculated based on particles.

Table 6.1 Synthesis condition of unsupported MoS_2

Catalysts	Additives	Solvent fraction vol.%	Stirring speed (rpm)
CAT-500	-	-	500
CAT-10D-500	decalin	10	500
CAT-20D-500	decalin	20	500
CAT-80D-500	decalin	80	500
CAT-80SC-500	supercritical heptane	80	500
CAT-80D-100	decalin	80	100
CAT-100	-	-	100

6.3 Results and discussion

6.3.1 Characterization

From a catalytic point of view, the activity of MoS_2 depends on the relative amount of defect sites where sulfur vacancies can be easily formed. Currently, MoS_2 synthesized by

the hydrothermal method usually forms long flat slabs (10-over 20 nm) with fewer defect sites, due to the efficient mass transport in the aqueous phase [14]. In this study, efforts were made to divide bulk media into small reaction cells to limit the growth of crystalline, by adding organic decalin and supercritical heptane in the solution.

The chemical state of Mo and S in synthesized catalysts is determined by XANES spectra. Figure 6.1 displays the S K-edge (a) and Mo L_3-edge (b) XANES spectra for the synthesized catalysts. At S K-edge, the whiteline at 2471 eV is attributed to the S 1s to 3p dominated transitions. The broad peak in 2478-2484 eV is probably due to S pyramidal coordination on basal planes. At the Mo L_3-edge, the whiteline is observed at 2524 eV, which is attributed to the electron transition from Mo $2p_{3/2}$ to vacant 4d [173, 174]. All the catalysts exhibit similar structures as the MoS_2 standard. No other sulfur or Mo^{6+} is detected. The addition of organic solvent does not affect the chemical state of MoS_2.

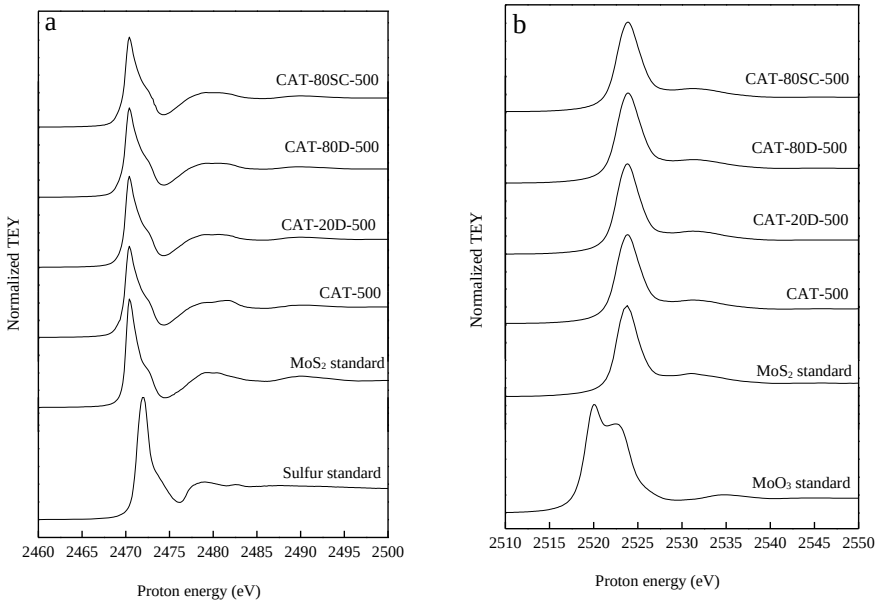

Figure 6.1 S K-edge (a) and Mo L_3-edge (b) XANES spectra of MoS_2 catalysts

The XRD patterns for the synthesized catalysts are shown in Figure 6.2. Crystalline MoS_2 is clearly identified with the characterized peaks at 2θ=13.3, 33, 40, and 57 for 002, 100, 103, and 110 Bragg planes, respectively. For CAT-500, CAT-10D-500 and CAT-20D-500, the XRD spectra are almost identical, indicating the same crystalline structures. For catalysts synthesized in the media with the majority of organic solvent (CAT-80D-500 and CAT-80SC-500), crystalline MoS_2 is also generated, but the reflections for 100, 103, and 110 are significantly smaller than those of other catalysts, indicating shorter crystalline slabs in length. The sizes of the crystalline domains for all the catalysts are calculated by the Scherrer Equation from 002 and 110 planes (Equation 3.8) [24]. Since the Scherrer Equation calculates the ordered crystalline domains along the corresponding planes, the estimated length and thickness may be significantly shorter than the slab length and thickness viewed from TEM (Table 6.2). With the increase of decalin fractions in the solution, the average length seems to decrease. In addition, the slab length is further decreased when changing the solvent to supercritical heptane.

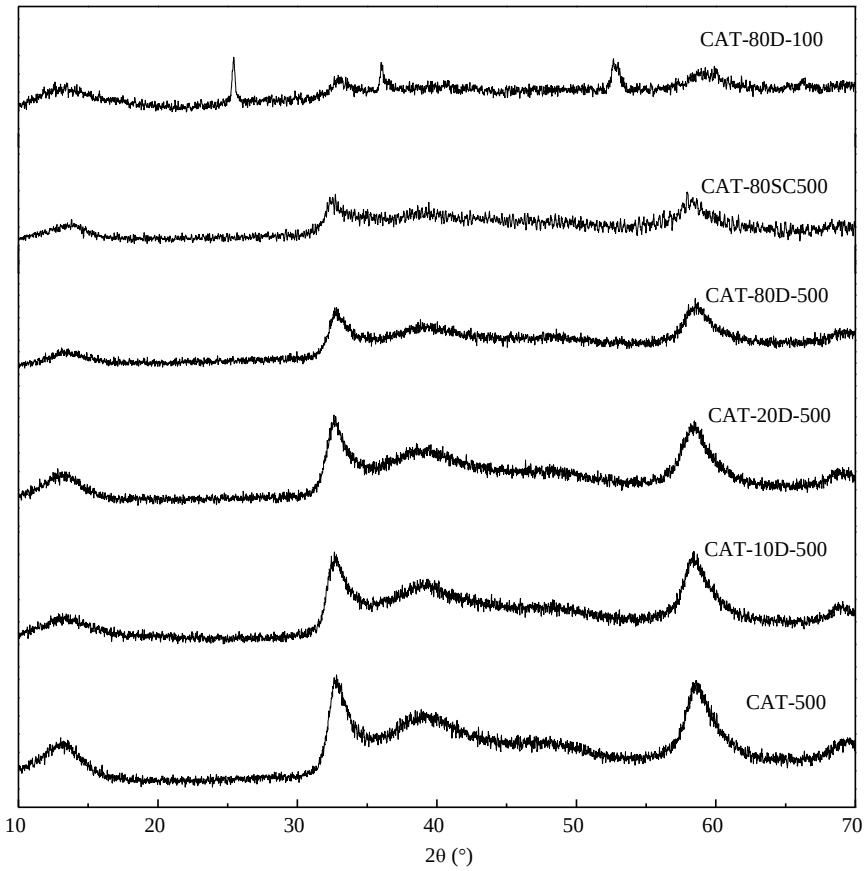

Figure 6.2 XRD spectra of MoS_2 catalysts

Table 6.2 BET surface area and average crystal size of MoS_2

Catalysts	BET surface area (m^2/g)	Length (nm)[a]	Thickness (nm)[a]	Length (nm)[b]	Thickness (nm)[b]	$\bar{\kappa} \times 100$ (nm^{-1})
CAT-500	231.1	3.5	1.6	17.4 ±0.8	2.3±0.2	2.2±0.1
CAT-10D-500	251.7	2.8	1.5	18.3±0.5	2.4±0.1	2.3±0.2
CAT-20D-500	312.4	2.5	1.4	21.2±0.7	2.5±0.2	2.5±0.1
CAT-80D-500	280.5	2.3	1.4	15.4±0.4	1.9±0.1	3.8±0.2
CAT-80SC-500	199.5	2.2	1.3	14.7±0.2	1.4±0.1	5.7±0.3
CAT-80D-100[c]	88.1	-	-	7.4±0.1[c]	1.2±0.1[c]	---

[a]: Measured from TEM images

[b]: Calculated from XRD spectra

[c]: Average length and thickness of CAT-80D-100 was calculated from the particles with short slabs.

The synthesized catalysts (expect CAT-80D-100) present high BET surface areas in a range of 231.1-312.4 m^2/g. The pore size distributions are shown in Figure 6.3. Bimodal peaks were observed for MoS_2 with or without the presence of decalin. The first peak at around 2.5 nm with a shoulder between 3-5 nm may be attributed to the pore formed from the twisted slabs within primary particles, while the broad peak around 11 nm is mainly attributed to secondary pores from the aggregation of primary particles. It is found that more pores are formed in small sizes with the increase of decalin amount. This indicates that more curved structures appear on the crystalline slabs. The addition of supercritical heptane also shows a higher amount of small pores in spite of a lower surface area.

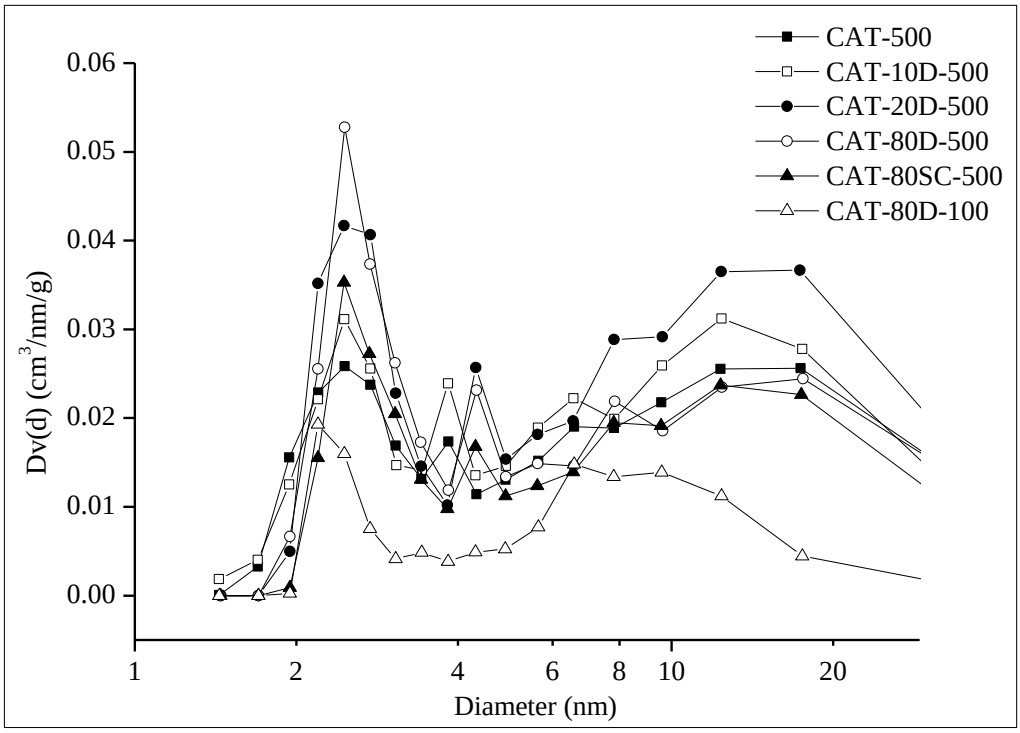

Figure 6.3 Pore size distribution of MoS_2 catalysts

The morphologies of the synthesized catalysts are revealed by TEM. The average length, thickness, and curvature are listed in Table 6.2. Thread-like crystalline structures are observed for all the catalysts (Figure 6.4). For CAT-500, stacked slabs are visualized and the slabs are distributed uniformly with slight interlacing (Figure 6.4b, circled). Since no organic solvent is applied, this can be treated as the blank sample for further comparison. When decalin is added in the solution in a fraction of 20%, it exists as droplets in the aqueous phase. The catalyst appears to be gathered and curved (Figure 6.4d, circled). This behaviour is probably because the growth of the crystal is blocked by the phase interface. The average length for CAT-20D-500 is 21.2 nm from the TEM image, which is larger than that of CAT-500. This result indicates that the organic solvent can only curve the slabs by changing their growth direction, instead of limiting the growth. When

the decalin/water ratio increases to 80%, merged slabs can be visualized with clear characteristic fringes (Figure 6.4f, circled). Careful observation of the catalysts shows that the slabs are significantly curved under the high decalin to water ratio (CAT-80D-500), when compared to CAT-20D-500 and CAT-500. An increase of average curvature from 0.022 nm^{-1} to 0.038 nm^{-1} is observed when the decalin/water ratio increases from 0 to 80% (Table 6.2). Additionally, the increase of curvature may result in the decrease of the stability along the basal plane by increasing the strain effect. When the curvature angle of the catalyst is sufficiently high, the strain effects may continue to increase and eventually cause the slabs to break [189]. Statistical results from TEM confirm that CAT-80D-500 has a shorter average length (15 nm) than CAT-20D-500 (21 nm) and CAT-500 (17 nm). This is in agreement with the calculation from the XRD spectra, which shows that CAT-80D-500 has the lowest ordered crystalline domains.

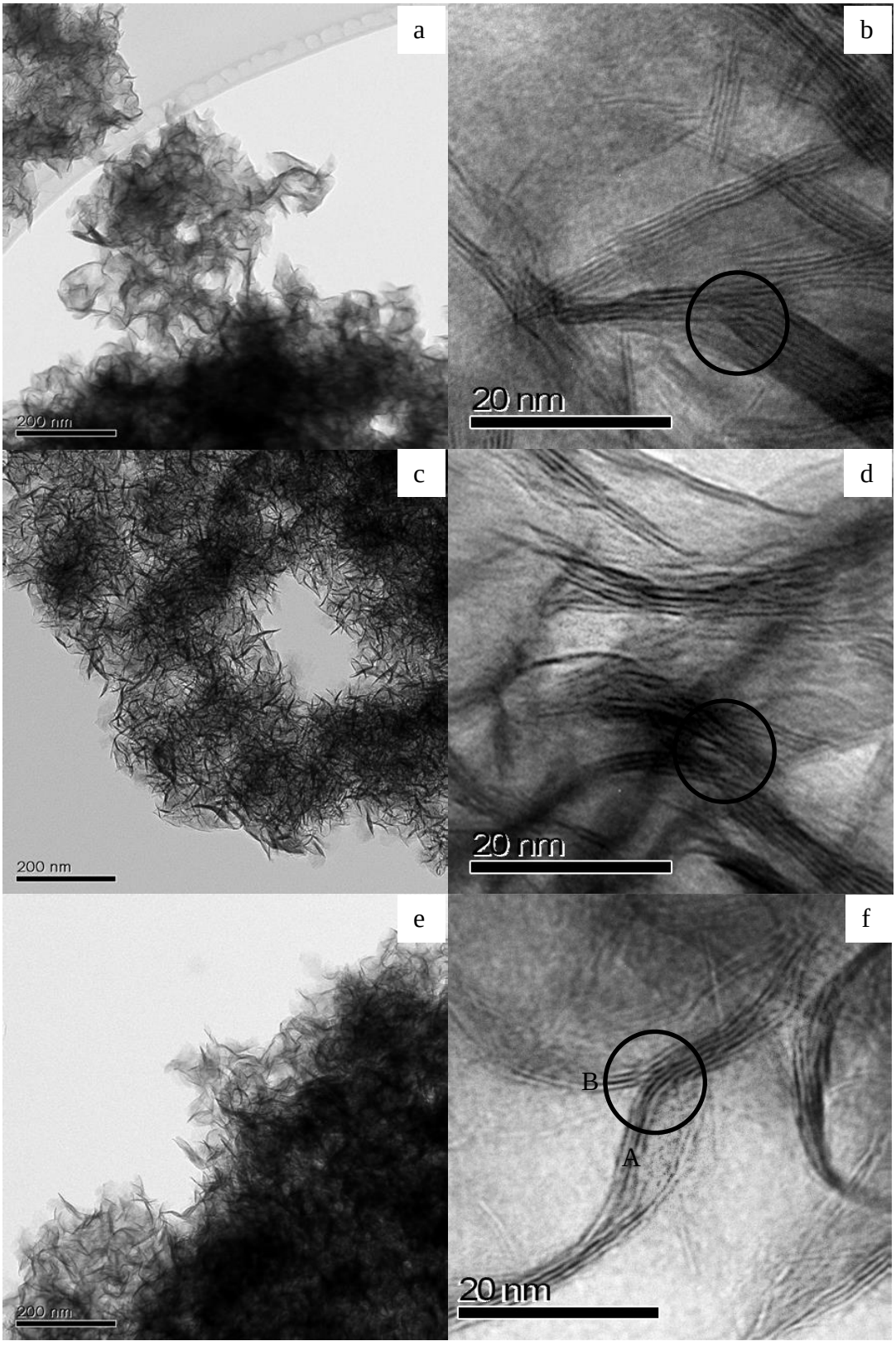

Figure 6.4 TEM images of MoS_2 catalysts at different decalin/water ratios a,b, CAT-500; c,d,CAT-20D-500; e,f, CAT-80D-500.

The bending effect of CAT-80D-500 may be attributed to two possibilities. As the isolated phase and continuous phase are determined by the organics to water ratio, water will be isolated into small droplets when the decalin to water is sufficiently high. In this situation, crystal growth is limited in isolated aqueous regions where the phase boundaries are highly curved. When the slabs meet the decalin-water interface, they tend to bend and grow along the interface with a higher curvature (e.g. slab A in Figure 6.4f). Additionally, the phase boundary will prevent the catalyst from dispersing, which increases the interruption among the catalysts and forces the slabs to bend. One of the examples can be observed in Figure 6.4f, which shows that the growth of slabs (e.g. slab B) changes direction by the blocking of other slabs (e.g. slab A).

6.3.2 Effect of supercritical heptane as water droplet separator

To further decrease the sizes of water droplets, supercritical heptane (SC-heptane) is applied to substitute decalin as separator. Due to the high dispersing and low density nature of supercritical heptane, it will disperse precursor-containing water into homogeneous nanosized reaction cells. Figure 6.5 shows the morphology of the catalyst synthesized in the presence of supercritical fluid. Compared to other circumstances without SC-heptane, CAT-80SC-500 exhibits significantly greater curvature angles. This is expected since water is highly dispersed in the heptane continuous phase under the supercritical condition, and it will break into small droplets. As the droplet size decreases, the interface of the two solvents is more curved. Thus, the catalyst slabs will be more bended when growing along the phase boundary (Figure 6.5b circled). Full observation of the slabs shows that CAT-80SC-500 is uniformly distributed (Figure 6.5a). This is probably because the number of water droplets is significantly increased as the size

decreased. So the nucleation process can start in more droplet cells, which leads to uniform dispersion. The crystalline slabs of CAT-80SC-500 (from TEM) exhibit only a slightly shorter length than that of CAT-500 and CAT-80D-500, indicating that the mass transfer among the water droplets is not obstructed by the SC-heptane.

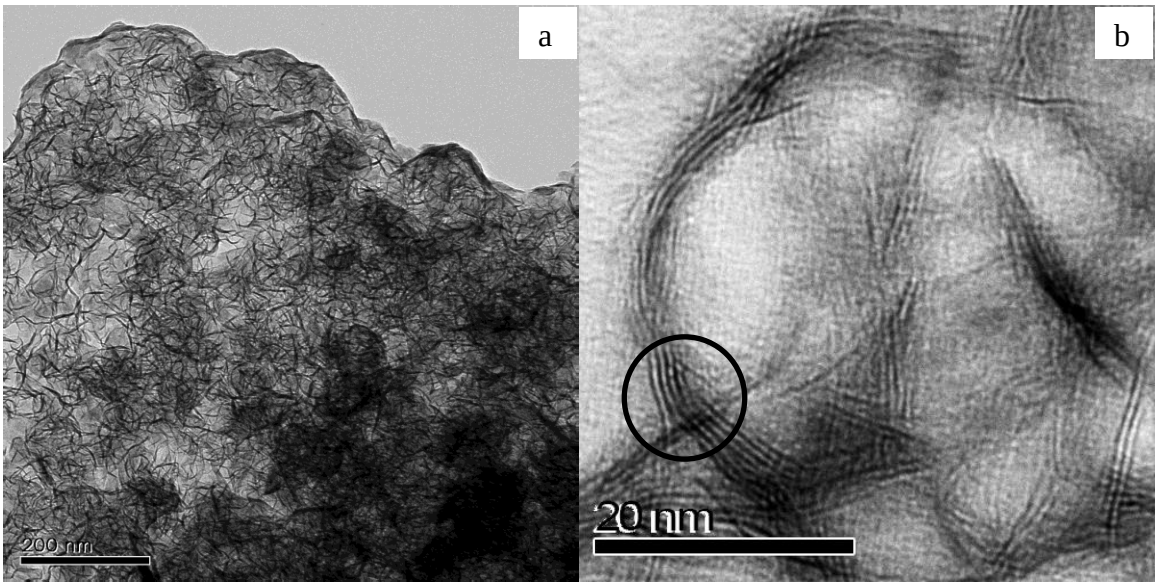

Figure 6.5 TEM images of CAT-80SC-500

6.3.3 The isolation effect

One of the effects of adding organic solvent in the hydrothermal process is that the continuous water phase breaks into droplets. Since water and decalin are insoluble in each other, the dispersion of these two solvents depends strongly on the agitation energy. With a high decalin to water ratio and low agitation speed, the precursors tend to be trapped and isolated in water droplets. In order to study this isolation effect, two catalysts are purposely synthesized under low stirring speed. Without the addition of decalin, the catalyst (CAT-100) shows a homogenous crystalline structure, indicating no isolation effect is applied. When the decalin to water ratio is increased to 80%, the TEM pictures

of CAT-80D-100 show the three different morphologies on the catalyst: large aggregates, small crystallines (short and thin slab), and long curved slab (similar with the case of CAT-80D-500) (Figure 6.6). The different appearances clearly indicate that the growth of catalysts is highly inhomogeneous in water phase. This statement is verified by XRD with impurity peaks besides MoS_2 (Figure 6.2). A distinct pore size distribution is also observed showing a shift to smaller pore size (Figure 6.3).

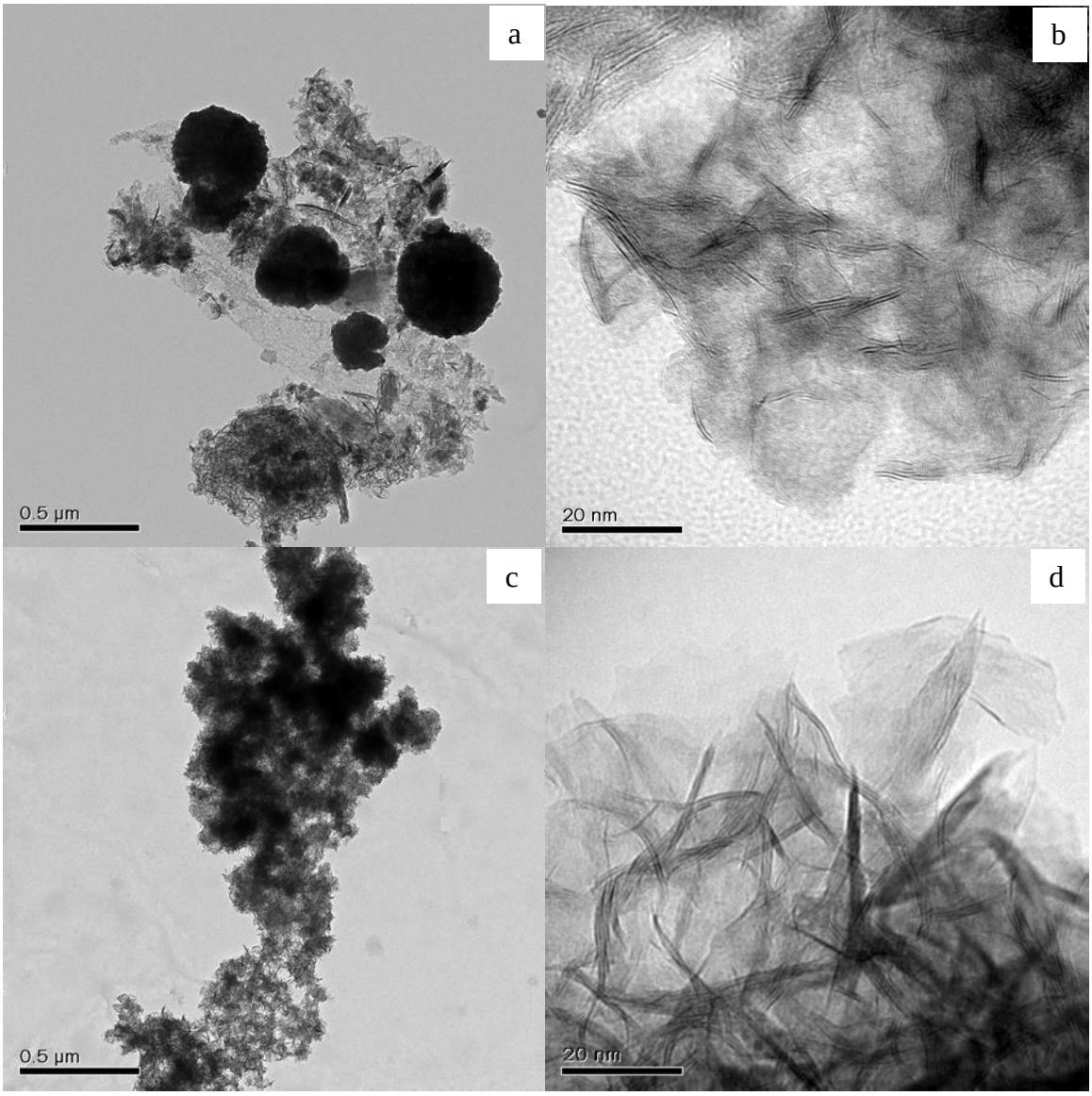

Figure 6.6 TEM images of MoS_2 catalysts
a,b, CAT-80D-100; c,d, CAT-100.

One possible reason for the distingushing structure is that different amounts of precusors are trapped in the water droplets. When the amount of precursors is insufficent in a particular water droplet, shorter slabs are formed due to the lack of precursor supply. On the other hand, if the precusors are over-dosed in a water droplet, the catalysts will aggregate together to form large blocks. When increasing the mixing speed to 500 rpm, the inhomogeneity disappears. The small-size crystals vanish as well as the aggregates. The vigorous agitation makes the water droplets collide together and in the incessant breakup and recombination, which enhances precursor mass transfer and creates a uniform environment. During the continual collision of water droplets, crystalline growth would be highly changed. The observation from the TEM images concludes the existense of the isolation effect and indicates that this effect is only applied with a high decalin to water ratio and a low agitation energy.

6.3.4 HDS performance

The performances of synthesized MoS_2 catalysts with/without the addition of decalin or supercritical heptane on LCO were evaluated and compared. The feedstock contains a total amount of 1.5% w.t. sulfur. The HDS results are listed in Table 6.3. All the catalysts show high HDS activities, with a minimum conversion of 52.9% after the 1 hour of reaction and 76.4% after 4 hours. CAT-80SC-500 exhibits the highest HDS performance (85.6% after 1 hour), indicating a significant improvement of catalytic activity when supercritical heptane is applied. Compared to the one without decalin addition, the catalysts with decalin addition are more efficient. CAT-80D-500 shows 73.9% (after 1 hour) HDS conversion, which is 13% and 21% higher than that of CAT-20D-500 and

CAT-500, respectively. This indicates that higher decalin/water ratio may benefit the catalytic activities.

Table 6.3 Evaluation results of MoS_2 catalysts

Catalysts/oil	Density (g/cm^3) (4 hours)	HDS conversion (%)	
		1 hour	4 hours
LCO	0.9641	-	-
CAT-500	0.9368	52.9	76.4
CAT-10D-500	0.9349	56.3	78.9
CAT-20D-500	0.9328	60.6	81.8
CAT-80D-500	0.9242	73.9	87.0
CAT-80SC-500	0.9137	85.6	93.0

An attempt to correlate HDS performance with the corresponding crystalline structures is conducted using temperature program reduction. For CAT-500, the first peak of adsorbed H_2 below 350 ℃ corresponds to the depletion of S on the rim and edge (Figure 6.7). One or two broad peaks are detected in between 350 and 600 ℃, which can be interpreted as the adsorption of hydrogen for the elimination of sulfur on curved points and other defects on basal. The third peak can be found at a higher temperature range, which is due to the decomposition of bulk MoS_2 (not shown). As the presence of the curvature, the stacked layers will be stretched inward, which will weaken the Mo-S bond strength on the outside and the create defect sites on the curved basal [28]. Thus, the existence of curvatures decreases the reduction energy of S atoms on the curved basal, and makes them accessible active sites under hydrotreating conditions. The enhanced HDS activity with the increasingly added decalin then can be attributed to the increase of curvatures, evidenced by the augmented area of the second temperature region (350-600 ℃). It is worth noting that such behaviour may only have a moderate effect on the HDS activity

since the reduction temperature of sulfur on the curved basal is in a relatively high temperature region compared to normal HDS reactions.

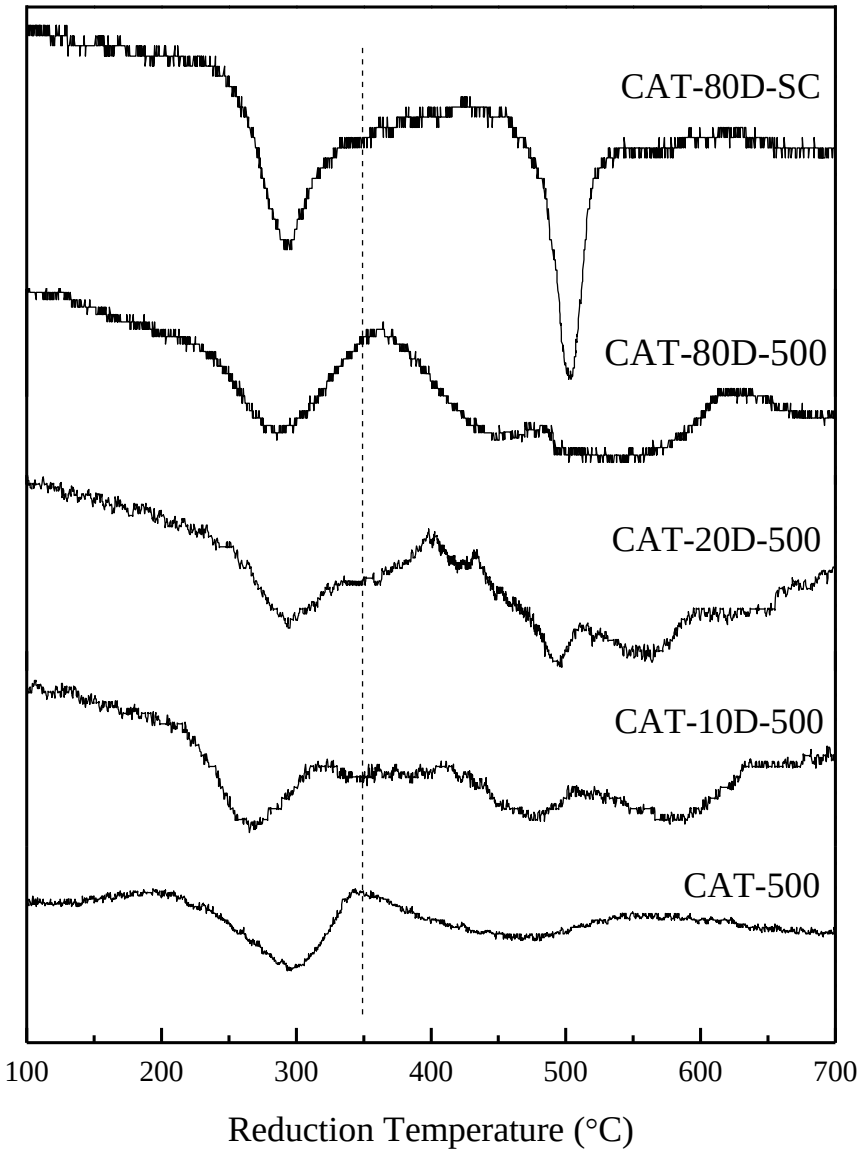

Figure 6.7 Tempreature program reduction profile

For CAT-80SC-500, TPR shows a bimodal profile below 600 ℃. The interpretation of the first peak is the same as other catalysts because of the similar reduction temperature.

The second peak is significantly sharper than that of other catalysts, indicating a high order of consistency on the curvature structure. Additionally, the onside and maxima of the second peak are significantly changed, compared to the catalysts without supercritical heptane. One possible reason is that the strong bending effect presenting on the curved slabs leads to an exposure of rim-like edges, which have similar reducible sulfur atoms with those on the rims. It is concluded that the increase of curvature angles on the bulk surface contributes the HDS activities.

6.4 Conclusions

In this study, a novel approach for the synthesis of high curvatures on MoS_2 slabs by adding organic solvents in the hydrothermal synthesis is demonstrated. The addition of decalin can disperse the precursor-contained water droplets into small reaction cells, which leads to a high bending effect during the growth of catalysts. XRD and XANES confirm the successful synthesis of crystalline MoS_2 structures. TEM images show that the dispersed water droplets would not affect the average length of MoS_2 slabs under a high stirring speed, but curve them to generate more defect sites on the bulk surface. Supercritical heptane exhibits a higher ability to form high curved slabs than the common organic fluid. The HDS activity test shows that the S conversion is increased from 76.4% to 87.0%, when decalin concentration is increased from 0 to 80 vol. %. The catalyst synthesized with supercritical heptane possesses the highest catalytic capability among all the prepared catalysts, with S conversion of 93.0% after 4 hours of hydrotreatment.

Chapter 7 Promotion effect of cobalt on unsupported MoS_2 for upgrading light cycle oil

7.1 Introduction

Mo based catalysts are commonly used as hydrotreating catalysts [190, 191]. It is widely accepted that the addition of cobalt can largely enhance the hydrotreating performance of MoS_2 [103, 104]. The ability to enhance the catalytic activity and the optimal cobalt addition differ from case to case. In this work, CoMoS was synthesized by a hydrothermal synthesis reaction. Different Co to Mo molar ratios were investigated, as well as medium acidity, which was adjusted by the variation of Na_2S to HCl ratio. The promotion effect of cobalt was evaluated by the upgrading of light cycle oil in comparison with unpromoted MoS_2 (CAT-2.5 in Chapter 4).

7.2 Catalyst synthesis

CoMoS catalysts were synthesized by the hydrothermal method using MoO_3 (STEM Scientific), $Co(NO_3)_2$ $6H_2O$,Na_2S $9H_2O$, and HCl (Fisher Scientific) as precursors. MoO_3 was first dissolved in the Na_2S solution before $Co(NO_3)_2$ was introduced to the solution forming the cobalt-molybdenum complex. The mixture was then transferred into a 1000 ml autoclave, which reacted for 2 hours at 320 °C under a stirring speed of 500 rpm. The resultant black solid was filtered and washed with distilled water and ethanol. As seen from Table 7.1, two parameters were varied in this experiment, including the cobalt to molybdenum ratio and HCl to Na_2S molar ratio, which was done to adjust the synthesis pH. Catalysts synthesized at different cobalt addition levels were denoted in a form of

"CAT-Co fraction", e.g. CAT-30, while CoMoS prepared at different Na_2S to HCl ratios (different acidic/basic media) was expressed by suffix (a, b1, or b2).

Table 7.1 Hydrothermal synthesis condition

Catalysts	Precursor Co/(Co+Mo) atomic ratio	HCl/Na_2S molar ratio	Filtrate pH
CAT-0	0	1.8	2.6
CAT-30a	30	1.8	2.6
CAT-43a	43	1.8	3.1
CAT-50a	50	1.8	2.9
CAT-57a	57	1.8	2.9
CAT-43b1	43	1.4	8.4
CAT-43b2	43	1	10.2

7.3 Results and discussion

7.3.1 Effect of cobalt to total metal ratio

The successful synthesis of high performance CoMoS requires the careful control of the operation parameters, such as Co/Mo ratio and media acidity. In this study, a series of unsupported CoMoS catalysts with different dosages of cobalt were synthesized in acidic media. The filtrate pH after the reaction is in the range of 2-4 (Table 7.1). The catalysts exhibit crystalline structures that were identified by TEM diffraction patterns in Figure 7.1. The d spaces calculated from the TEM diffraction rings exhibits the key characteristic peaks for 002, 100, 103, and 110 planes (Table 7.2). The results are in agreement with the reference MoS_2.

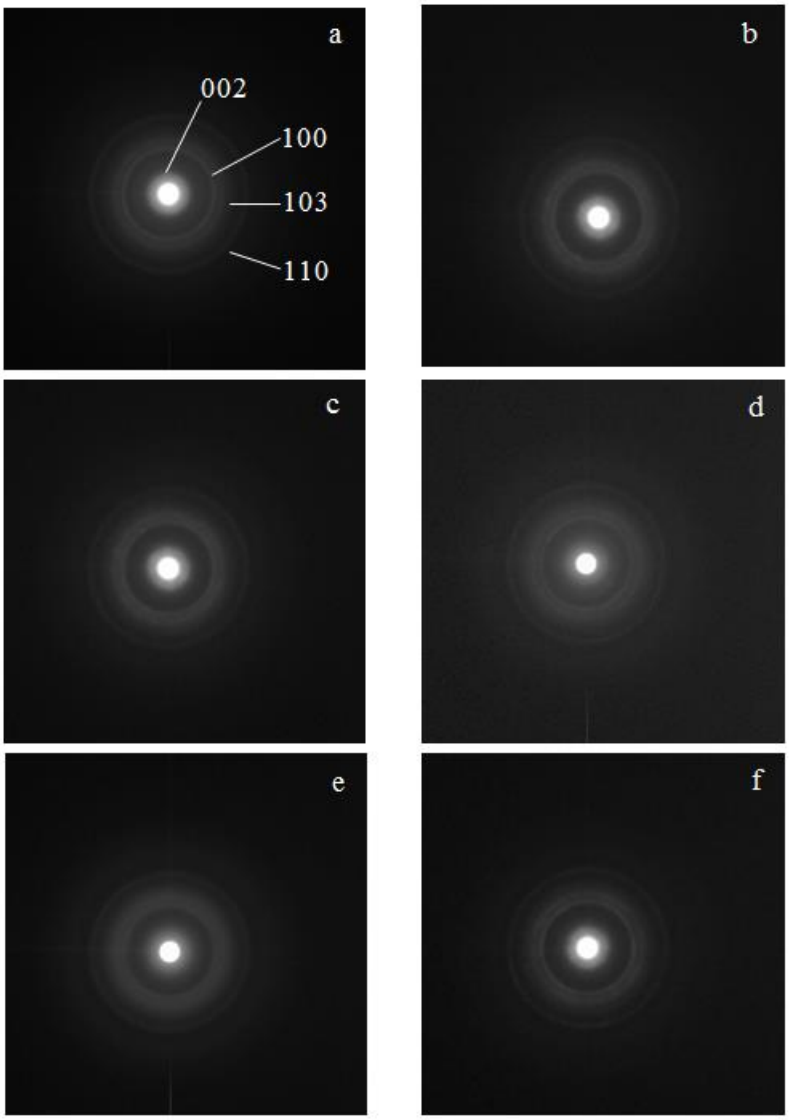

Figure 7.1 Selected area electron diffraction.
a: CAT-0; b: CAT-30a; c: CAT-43a; d:CAT-50a; e: CAT-43b1; f: CAT-43b2

Table 7.2 d-value of MoS_2 at different Co ratio and media pH

h k l	Standards	CAT-0	CAT-30a	CAT-43a	CAT-50a	CAT-57a	CAT-43b1
	d (nm)						
0 0 2	0.616	---	---	---	---	---	---
1 0 0	0.274	0.268	0.267	0.268	0.267	0.269	0.267
1 0 3	0.228	0.225	0.225	0.226	0.226	0.225	0.226
0 0 6	0.205						
1 1 0	0.158	0.156	0.157	0.158	0.159	0.158	0.157
0 0 8	0.154						

The crystalline morphology of CoMoS can be observed from TEM images (Figure 7.2). Compared to unpromoted MoS_2, the average length and layer numbers of CoMoS are dramatically decreased (Table 7.3). This is probably because the heteroatom cobalt interrupts the extending of crystalline planes by changing the local structure on the growth interface. This is also consistent with previous research in which the transit metals are more likely to be present on the edges [22].

Table 7.3 BET surface area of CoMoS and Co/Mo relative ratios

Catalysts	Slab length L_a (nm)[a]	Layer number n[b]	Edge metal fraction a	BET surface area (m^2/g)	Co/Mo intensity ratio[c]
CAT-0	17.4±0.9	4.5±0.4	0.071	231.1	0
CAT-30a	9.4±0.4	2.9±0.1	0.128	141.2	0.312
CAT-43a	10.0±0.3	3.0±0.1	0.120	62.4	0.217
CAT-50a	9.5±0.3	3.3±0.2	0.126	55.4	0.306
CAT-57a	--	--	--	3.3	---
CAT-43b1	7.8±0.2	2.9±0.1	0.151	82.2	0.410
CAT-43b2	10.1±0.3	2.9±0.1	0.119	40.5	0.203

[a]: L_a, crystallite size of MoS_2 in the plane of layers;
[b]: n, the number of layers perpendicular to the plane;
[c]: Co/Mo in MoS_2 layers

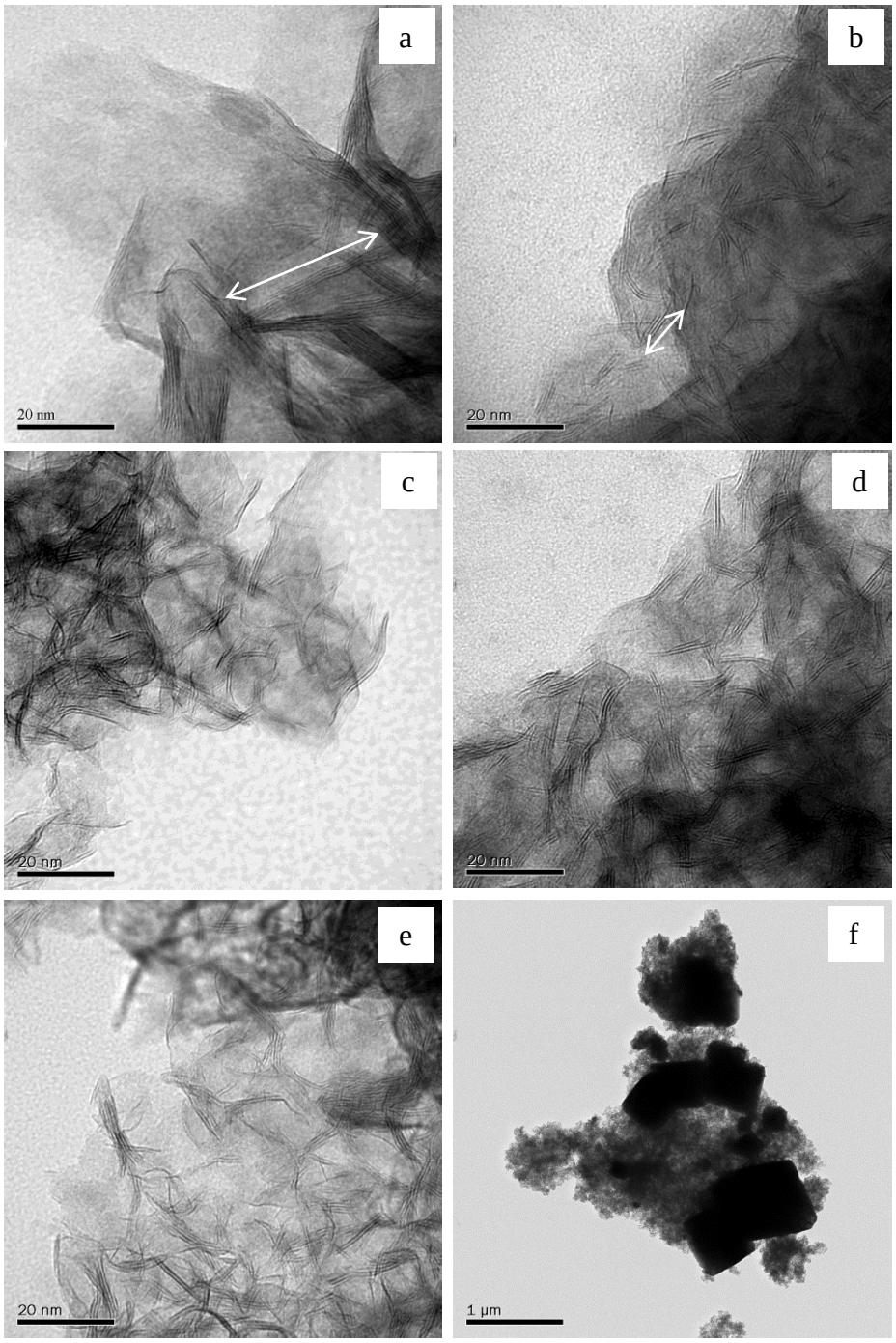

Figure 7.2 TEM images of CoMoS
a: CAT-0; b:CAT-30a; c: CAT-43a; d: CAT-50a; e,f: CAT-43b1

The shortened slabs will increase the edge areas that are considered as potential active sites. The ratio of edge-to-total metal can be calculated according to Equation 3.4-Equation 3.7, assuming the structure of Co-promoted MoS_2 is the same as that of bulk MoS_2 in a hexagonal shape with the Mo-Mo distance of 0.316 nm [167]. Compared to reference MoS_2, the edge-to-total metal ratios for CoMoS catalysts are almost doubled. No significant difference is noticed among the CoMoS catalysts.

The pore size distribution and BET surface areas of the synthesized catalysts are shown in Figure 7.3 and Table 7.3, respectively. The BET surface area decreases significantly with the increase of the cobalt content, which was also observed by other research [22]. Correspondingly, fewer small and medium-size pores are observed in the higher cobalt containing MoS_2. This phenomenon could be attributed to the impurity of the catalysts. With more cobalt involved, cobalt sulfide is more likely to form instead of active binary metal phase Co-Mo-S. One of the samples can be spotted in Figure 7.2. Different to the short stacked MoS_2 slabs, Co_9S_8 is presented as large chunks with non-nano structures, which decreases the BET surface areas and pore sizes.

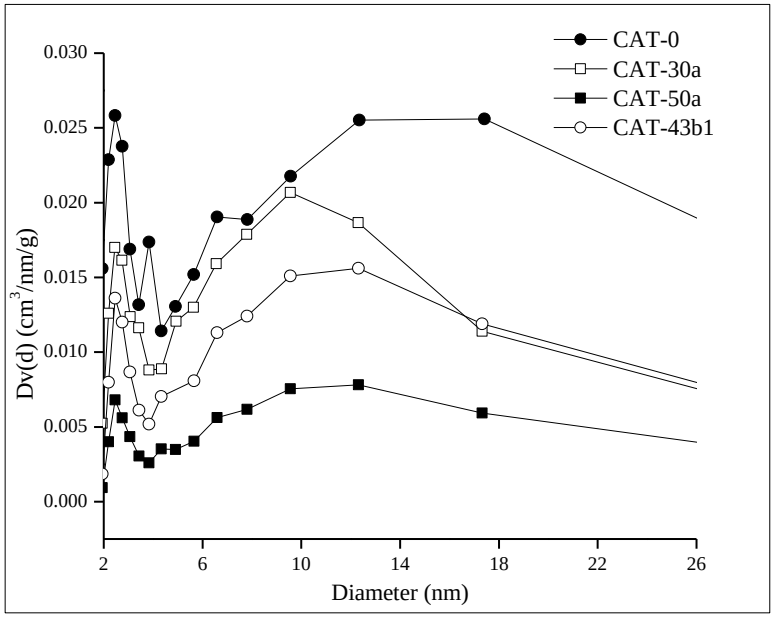

Figure 7.3 Pore size distribution of CoMoS

Despite the presence of some large cobalt sulfide crystals, CoMoS still demonstrated higher hydrotreating activities (Figure 7.4). It is observed that the HDS rate is promoted from 3.77 to 13.25 ($\times 10^{-4}$ g^{-1} $cata^{-1}$) in the first 20 min, when the cobalt content is increased from 0 to 30%. This indicates that more active sites could be generated with the presence of Co metal on the edges. Catalysts with Co loading between 30-50% exhibit similar activities (Figure 7.6). Continuously adding Co into the system dramatically decreases the catalyst activity. When the Co/Co+Mo is 57%, the HDS activity for the CoMoS is even lower than the reference MoS_2 (CAT-0). The decreased performance may be due to the increased large CoS_x. The results indicate that the activities of CoMoS are closely related to the formation of the Co-Mo-S phase. Nevertheless, the HDS tests show that CoMoS catalysts generally possess higher activity than MoS_2 does as long as the Co content is between 30-50%.

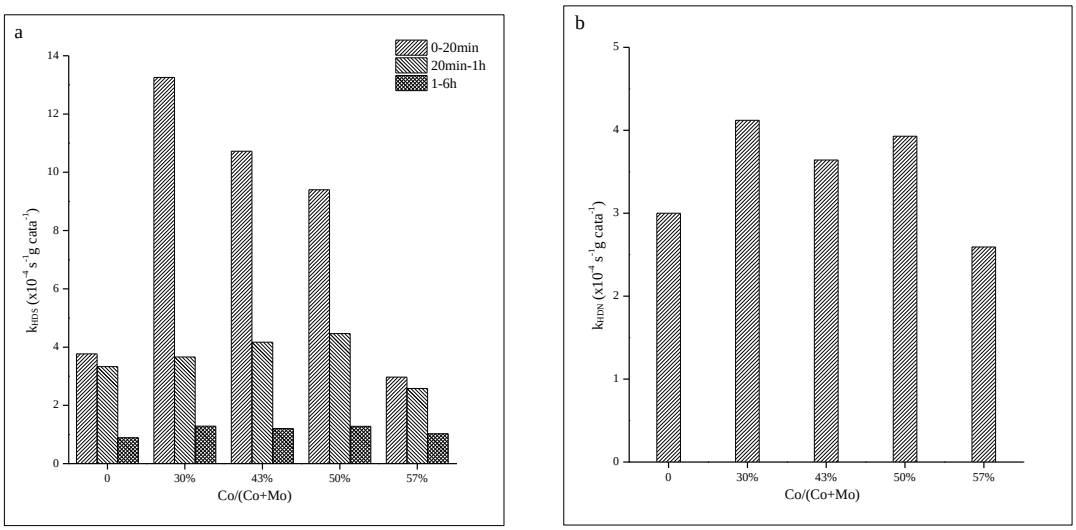

Figure 7.4 HDS and HDN reaction rate constant at different cobalt content
a, HDS; b, HDN

7.3.2 Effect of media acidity

Previous studies have concluded that the acidity of the solution plays an important role in the successful synthesis of crystalline MoS_2. A similar method was applied to the CoMoS, in which the acidity was also investigated by varying the HCl/Na_2S ratios. Since the binary metal compounds are more complicated than the single metal, the Co/(Co+Mo) ratio was kept at 43% in this study for simplification. Possible reactions for the Co-Mo-S complex are listed in Reaction 7.1-Reaction 7.4. Hydrogen ion (H^+) is essential for the formation of MoS_4^{2-} ions. Lack of H^+ may result in forming a Co-Mo complex without involving sulfur (Reaction 7.5). On the other hand, precipitation of MoS_3 would occur upon over dosage of H^+. In this case, CoS is expected due to the insufficient Mo anions (Reaction 7.6 and Reaction 7.7). The segregation of cobalt sulfide and molybdenum sulfide would result in a poor Co-Mo combination structure. Consequently, it is suggested that an optimal acidity exists for the synthesis of a desirable catalyst.

Three HCl/ Na_2S ratios were selected for the investigation of media acidity. Among the three pH values selected, CAT-43b1 is of the highest BET surface area and also performs the best hydrotreating results. CAT-43b1 shows more cobalt in the Co-Mo-S phase than CAT-43a and CAT-43b2, which is consistent with the previous statement that higher hydrotreating activities were obtained when more cobalt was present in the Co-Mo-S. The evaluation results of HDS and HDN are shown in Figure 7.5 and Figure 7.6, respectively. All the catalysts exhibited a high initial reaction rate for LCO. Hard sulfur, such as DMDBT contributed to a smaller k value in the following reactions.

$$S^{2-} + H_2O \leftrightarrow HS^- + OH^-$$ Reaction 7.1

$$MoO_3 + 2OH^- \leftrightarrow MoO_4^{2-} + H_2O$$ Reaction 7.2

$$MoO_4^{2-} + 8H^+ + 4S^{2-} \leftrightarrow MoS_4^{2-} + 4H_2O$$ Reaction 7.3

$$MoS_4^{2-} + Co^{2+} \leftrightarrow CoMoS_4$$ Reaction 7.4

$$MoO_4^{2-} + Co^{2+} \rightarrow CoMoO_4$$ Reaction 7.5

$$MoS_4^{2-} + H^+ \rightarrow MoS_3 + HS^-$$ Reaction 7.6

$$Co^{2+} + S^{2-} \rightarrow CoS$$ Reaction 7.7

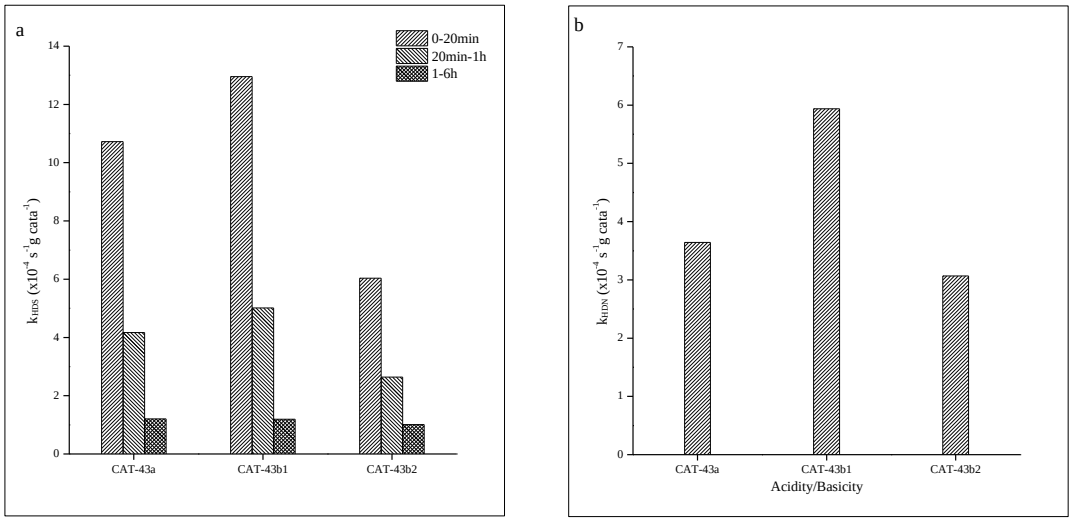

Figure 7.5 HDS and HDN reaction rate constant at different media
a, HDS; b, HDN

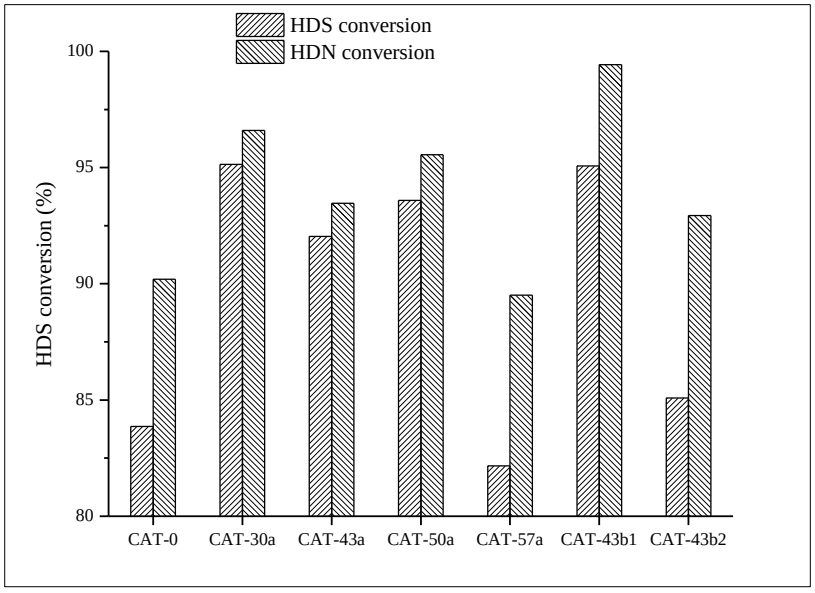

Figure 7.6 HDS/HDN conversions for the CoMoS catalysts

7.4 Conclusions

In this study, CoMoS was successfully synthesized under different operating conditions. It is noticed that catalyst structure depends on the medium acidity and the cobalt content. TEM results show that the addition of cobalt contributes to shorter slab length compared to unpromoted MoS_2. Weakly basic medium is likely to assist in the adopting of Co on the MoS_2 surface. There is an optimal Co amount for the synthesis of CoMoS catalysts, which is in the range of 30% to 50%. The HDS and HDN results confirm that the introduction of cobalt on MoS_2 can significantly improve the activity.

Chapter 8 Kinetics of hydrotreatment of light cycle oil over a dispersed MoS_2 catalyst

8.1 Introduction

Light cycle oil from the fluid catalytic cracking (FCC) is a blend of straight run gas oil for diesel production [45, 46]. So far, there is little work conducted on the kinetics of LCO over a dispersed catalyst. In this work, LCO was hydrotreated by nano catalyst MoS_2 (CAT-2.5 in Chapter 4). The feed oil and liquid products were extensively analyzed. The total sulfur and nitrogen in the original LCO and hydrotreated products were determined to evaluate the HDS and HDN activity. In addition, the composition of sulfur and nitrogen compounds was analyzed to demonstrate the HDS and HDN kinetics. The hydrogenation ability was illustrated by the variation of aromatic compounds. The distribution of boiling point and liquid density was also determined as evidence of the hydrocracking reaction.

8.2 Results and discussion

8.2.1 Hydrodesulfurization activity

The total sulfur conversion versus hydrotreating time is shown in Figure 8.1. Three catalyst to oil ratios (COR) were investigated to determine the effect of catalyst concentration on the HDS performance. The results show a similar 3-step trend for all the CORs. The conversion increases dramatically in the first half an hour, followed by a gentle increase from the 0.5^{th} hour to approximately 2^{nd} hour. The final step is a smooth increase where the reaction speed is significantly reduced. From the 2^{nd} hour to the 8^{th} hour, the conversion only increases approximately 10% for all CORs. However,

differences are noticed among the catalysts to oil ratios. Higher COR possesses higher initial reaction speed. The conversion reaches almost 60% at the 0.5th hour at COR=1:100 while the conversion for 1:200 and 1:800 are 30% and 15%, respectively. This indicates that a higher catalyst concentration increases the initial reaction rate by quickly removing easy sulfur containing compounds. After the second step, the conversion differences among the three CORs appear constant along with the hydrotreating time. This shows that the different catalyst to oil ratios have similar reaction rates for hard sulfurs. At the end of the reaction (8th hour), the higher COR exhibits higher HDS conversion. The reason is probably because the higher catalyst concentration reduces the time required for the depletion of easy sulfur components. Therefore, more time is gained to remove hard sulfurs.

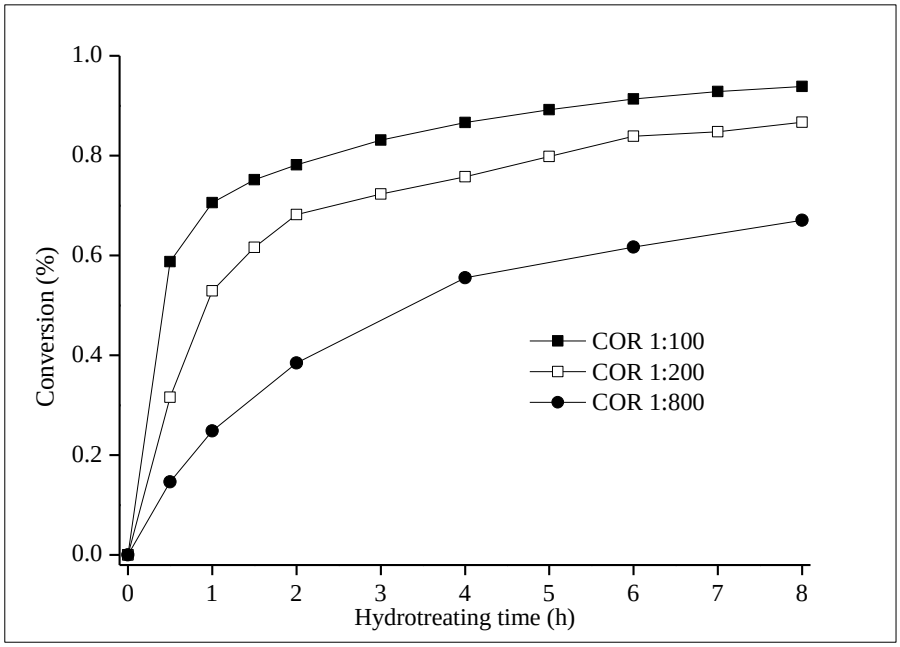

Figure 8.1 HDS conversion over dispersed MoS_2 at different catalyst-to-oil ratios (COR, w.t.)

Sulfur species in the LCO feed were identified. Several types of sulfur were detected, including benzothiophene (BT), methyl-benzothiophene (1MBT-4MBT), dibenzothiophene, and methyl-dibenzothiophene (1MDBT-3MDBT), as shown in Figure 8.2. At the 2nd hour, the easy sulfurs such as BT and 1MBT-4MBT are almost removed, while hard sulfurs are largely preserved. This is consistent with the reaction rate observation that only easy sulfurs are quickly removed within the first 2 hours of reaction. At the end of the reaction, easy sulfur compounds are not detected in the final products. The amount of hard sulfurs are greatly reduced but not totally removed. This indicates that the hard sulfur components require significantly longer reaction time. The detailed kinetics for each detected sulfur-containing compound with hydrotreating time is shown in Figure 8.3, and the calculated rate constant is listed in Table 8.1. The substances are catalogued into 2 groups, easy sulfur compounds (Figure 8.3a) and hard sulfur compounds (Figure 8.3b). In Figure 8.3a, BT and 1MBT possess the highest reaction rates, and they are totally removed within the first 2 hours of reaction. Other compounds from 2MBT to 4MBT show slightly lower reaction speeds, but still, more than 90% of these substances are converted at the 2nd hour of reaction. A trend is noticed that the reaction rate decreases with the increase of the complexity of the compounds. With more alkyls on the aromatic ring, the reaction becomes more difficult. In Figure 8.3b, all compounds exhibit similar reaction speeds as a function of time, indicating that the steric effect is not significant among these compounds.

There are generally two desulfurization pathways, with one being direct desulfurization (DDS) route where sulfur is removed without hydrogenation of the adjacent aromatic ring;

the other being hydrogenation (HYD) route where sulfur is eliminated after neighboring olefinic bond or aromatic ring have been saturated (Figure 2.8, Figure 2.9) [152, 154]. The former route depends on hydrogenolysis reactivity and the hydrogenation route is associated with electronic characteristics of the benzene ring or olefinic bond adjacent to the S atom [192, 193]. Both reaction pathways are considered for the interpretation of reactivity difference of easy sulfur (BT type) and hard sulfur (DBT type). Reaction through DDS route is expected comparable on both easy and hard sulfur compounds due to their similar electron density (5.739-5.758) [193]. The HYD pathway is closely related to the difficulty in hydrogenation of unsaturated bonds. Once the double bonds are saturated the electron density on sulfur atoms shall be largely enhanced, leading to a high hydrogenolysis reaction rate of sulfur atoms. Due to the difference of bond order, BT-type sulfur compounds tend to adopt HYD routes than DBT-type compounds. Similarly, within the BT-type compounds, the decrease in the reactivity of 1MBT and 2MBT compared to BT may due to the substituents at C2 and C3 positions, which reduce C2-C3 bond order. Further increase of the methyl substitutes on BT at other positions does not affect their activity, as seen from the similar rate constant (Table 8.1). For hard sulfur (DBT-type compounds), under the current hydrotreating condition, the reaction mainly goes through DDS routes due to the difficulty in saturation of benzene rings. The introduction of alkyl groups does not influence the electron density on sulfur atoms, but will increase the steric hindrance, e.g. alkyl substituents at 4 or/and 6 positions. Thus the desulfurization of alkyl-DBT will go via HYD route, which can remove the steric hindrance through the molecular puckering. In such case, the reactivity of alkyl-DBT will be much lower than DBT. This phenomenon is observed in literatures using

supported catalysts [149]. However, in this study, all the alkyl-DBTs show the same reaction rate, which indicates they are going through the same reaction route as DBT, i.e. DDS instead of HYD. The steric hindrance arisen from alkyl substitution does not influence the activity. These results suggest that compared to supported catalysts, nanosized unsupported catalysts are easier to get contact with hindered sulfur and desulfurize the most refractory sulfur compounds.

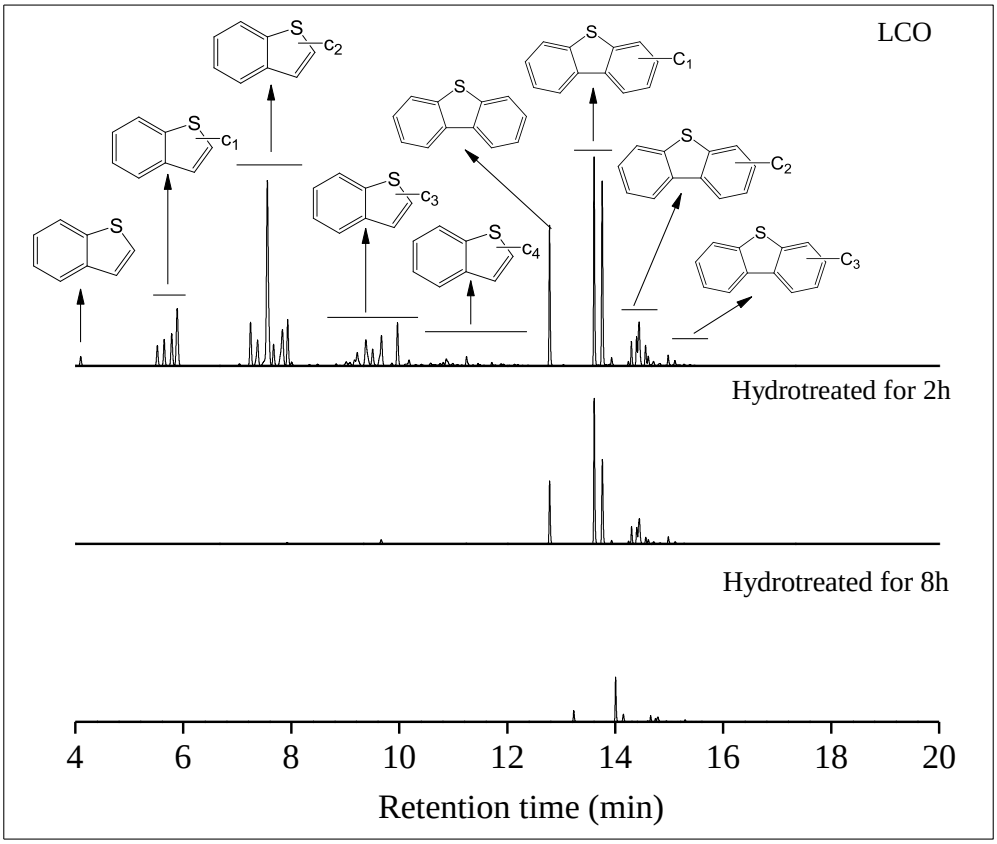

Figure 8.2 Major sulfur compounds composition of LCO and hydrotreated products COR=1:200

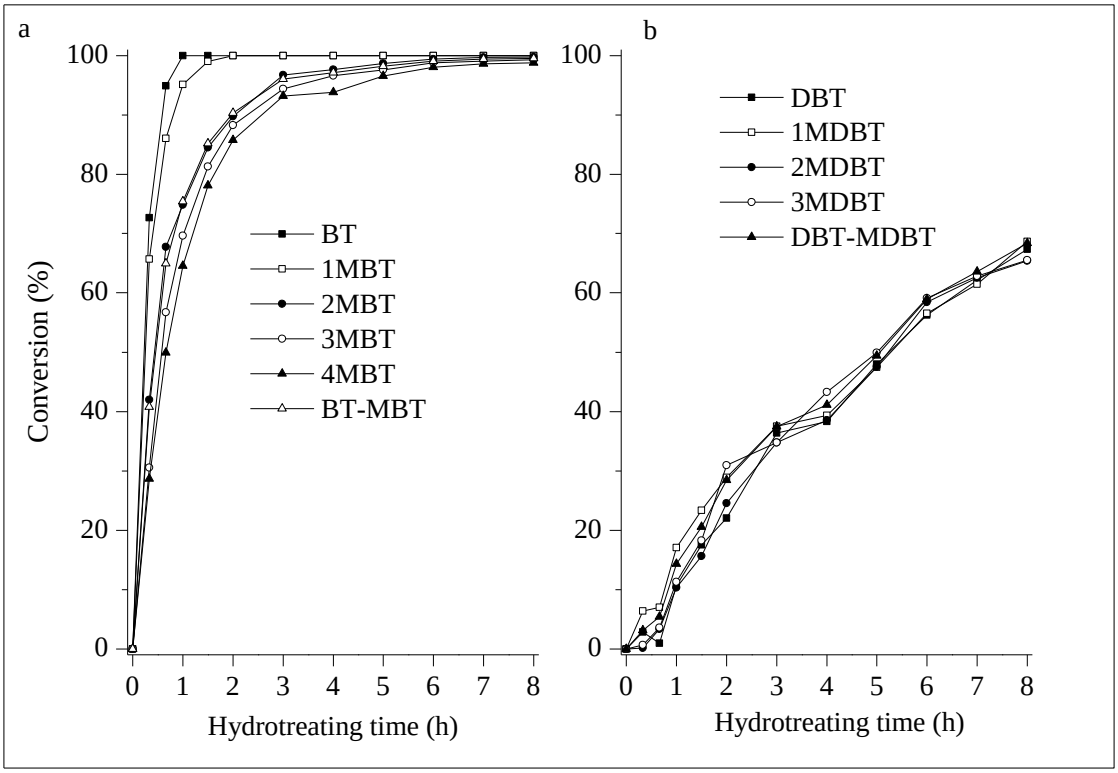

Figure 8.3 HDS conversion of single sulfur component

Table 8.1 Reaction rate constant for different sulfur components

Sulfur components	k_{HDS} ($x10^{-4}$ s^{-1} g cata $^{-1}$)
BT[a]	20.65
1MBT[b]	14.15
2MBT[c]	5.14
3MBT[c]	4.98
4MBT[c]	4.54
DBT	0.65
1MDBT	0.63
2MDBT	0.65
3MDBT	0.65

[a]: Calculated based on the first 40 minutes of reaction
[b]: Calculated based on the first 1.5 hours of reaction
[c]: Calculated based on the first 2 hours of reaction

8.2.2 Hydrodenitrogenation activity

The LCO feedstock contains a small amount of nitrogen compounds, which are categorized into 3 species: anilines, indoles, and carbazoles. The detailed composition of

nitrogen components in feed and product stream was identified by GC-NPD (Figure 8.4). In the feedstock, the content of indole is significantly higher than its alkyl substitutes. The concentration of the alkyl substituted indoles increases with the increase of the number of substitutes. For carbazoles, the highest peak refers to C1 carbazole and the content decreases with the increase of substitution numbers. The figure shows that all the anilines and a majority of indoles and carbazoles are removed within the 6 hour hydrotreating. The unreacted N containing compounds in the product stream mainly consist of C4 indoles and C1-C2 carbazoles. The nitrogen distribution at different reaction time is listed in Table 8.2. It is observed that anilines are quickly removed within the first 2 hours, indicating anilines are the easiest N compounds in LCO. Compared to carbazoles, indoles can be more efficiently removed as the concentration drops from 76.7 ppm to 20.2 ppm within 2 hours. Carbazoles are the most refectory N compounds in the LCO, which are reduced only ~50% in the first 2 hours. Additionally, the dynamics of different nitrogen types are simulated by pseudo-first-order rate constants, which are listed in Table 8.3. Only indole and carbazole are provided since the anilines are not detectable after 2 hours. The rate of elimination of nitrogen compounds is determined following this trend: anilines> indoles> carbazoles.

As the order of the HDN difficulty is associated with the reactant, it is of importance to distinguish the structural differences among anilines, indoles, and carbazoles. Aniline has one benzene ring with an attached NH_2 group. With a pair of lone electrons on N atom, it denote electrons and show basicity. For indole and carbazole, the lone-pair electrons will be delocalized around the aromatic ring(s) and therefore unable to denote electron to

Lewis acid [153]. The electron density on N atom of indole and carbazole is significantly decreased. As a result, the electron density on N atom decreases in the order of aniline, indole and carbazole [194]. Shiraishi et al. reported that the reactivity of nitrogen containing compounds linearly increased with the electron density on N atom [195]. This explains the observation that the three nitrogen-containing components lies in the same decreasing order as their electron density.

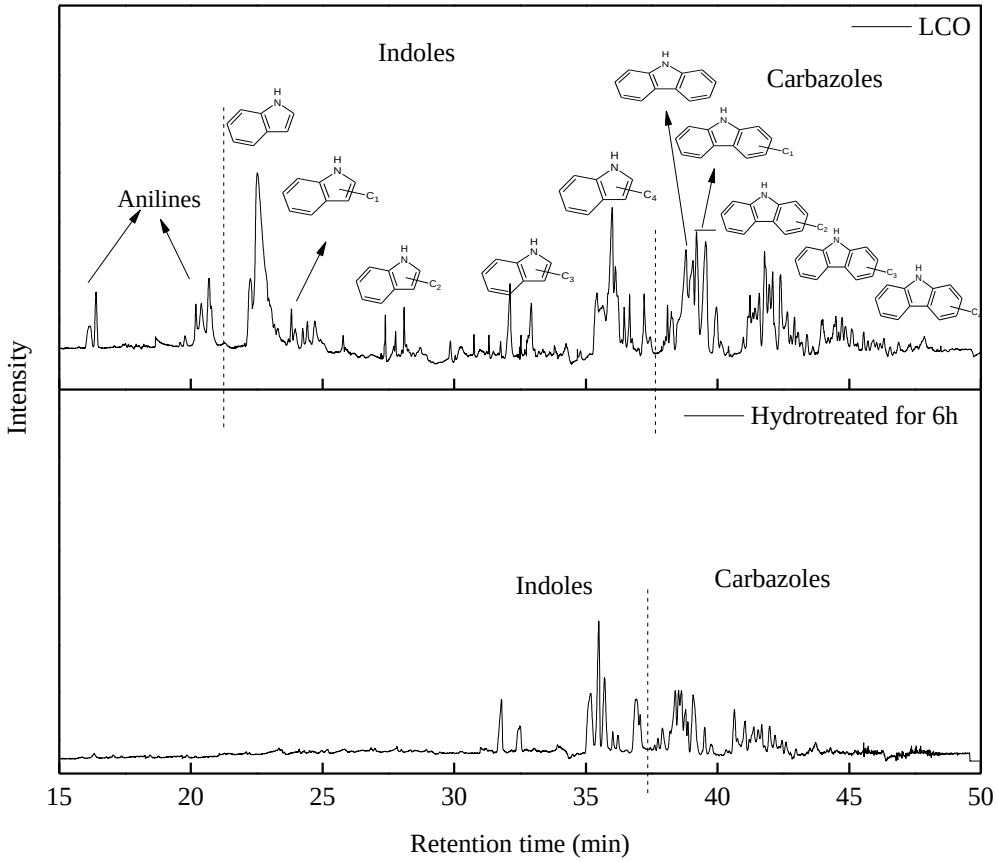

Figure 8.4 Major nitrogen compounds composition of LCO and hydrotreated products (GC-NPD)

Table 8.2 Nitrogen distribution in feed and hydrotreated products

Hydrotreating time (h)	N in Alilines (ppm)	N in Indoles (ppm)	N in carbazoles (ppm)	Total N (ppm)
0 (LCO)	10.3	76.7	67.2	159.2
2	0	20.2	34.4	54.6
6	0	6.9	9.8	16.7

Table 8.3 Reaction rate constant for different nitrogen type

Nitrogen components	$k_{HDN}(x10^{-4}\ s^{-1}\ g\ cata^{-1})$
Indole types	1.60
Carbazole types	1.29

8.2.3 Hydrogenation and hydrocracking activities

During the HDS process, a series of by-reactions occur, including hydrogenation and hydrocracking. The variations of aliphatic and aromatic hydrocarbons along with the hydrotreating time are shown in Figure 8.5. The content of aliphatic hydrocarbons is almost unchanged during HDS, indicating that the ring opening conversion from aromatic to aliphatic hydrocarbons is not significant. The main by-reaction is the conversion of diaromatics to monoaromatics. The diaromatics decrease from 52.3% to 10.3%, and the monoaromatics increase from 12.9% to 59.6%. The results indicate the hydrogenation reaction mainly occurred on bicyclic aromatics and only one of the aromatic rings can be saturated. The polycyclic aromatics are also refractory components, and the difficulty of their saturation may be attributed to the steric hindrance.

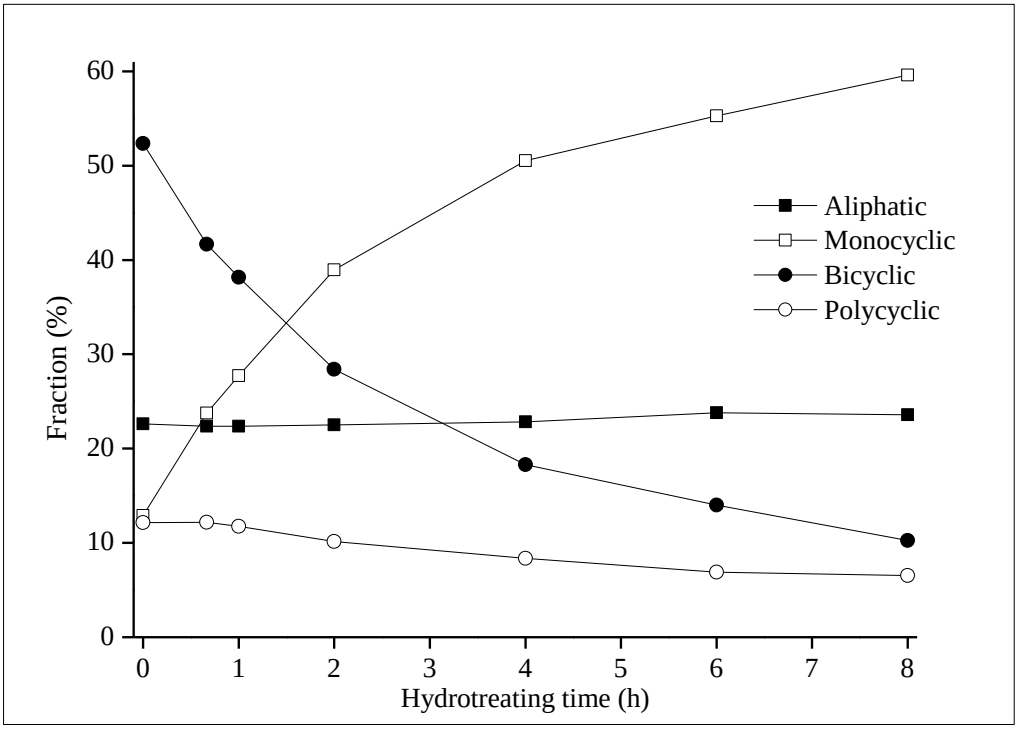

Figure 8.5 Hydrogenation along with hydrotreating time

The hydrocracking activity is revealed by simulated distillation (Figure 8.6). During the process of reaction, heavy components (> 250 ℃) are gradually consumed and the 200-250 ℃ fraction is increased significantly, which exhibits the occurrence of hydrocracking reaction on heavier components. It is noticed that the total fraction below 300 ℃ is barely changed within the first 6 hours, indicating that the main hydrocracking is the conversion 250-300 ℃ fraction to 200-250 ℃ fraction in the first several hours. However, the hydrocracking on components greater than 300 ℃ can eventually happen in long hydrotreating processes, which can be evidenced by the drop of >300 ℃ fraction after the 6^{th} hour. The fractions lighter than 200 ℃ are also slightly increased during the reaction, but they are not the main products of hydrocracking. The hydrocracking

reaction can also be verified by the continuous decrease in density, as shown in Figure 8.7.

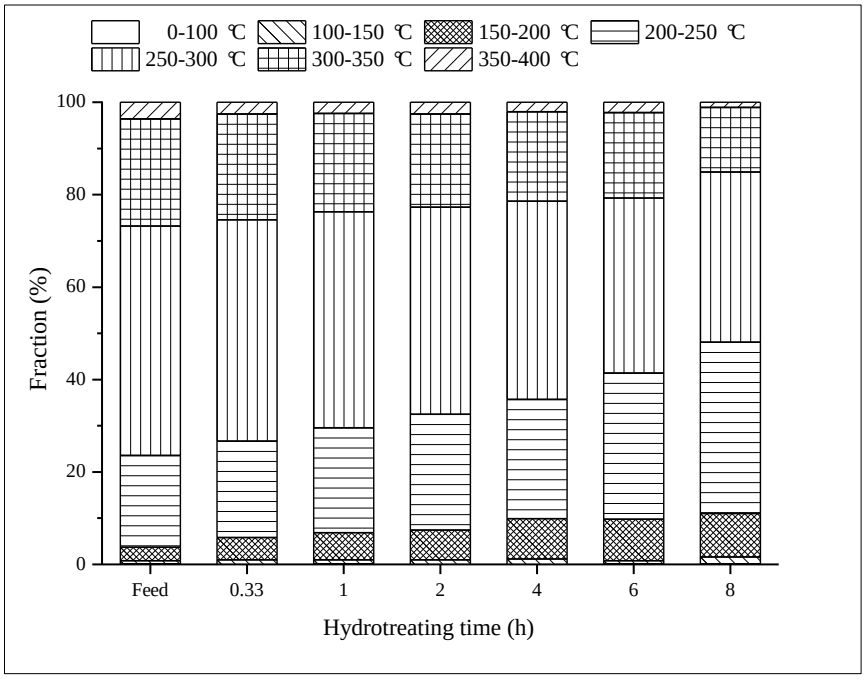

Figure 8.6 Boiling point distribution of LCO and hydrotreated products

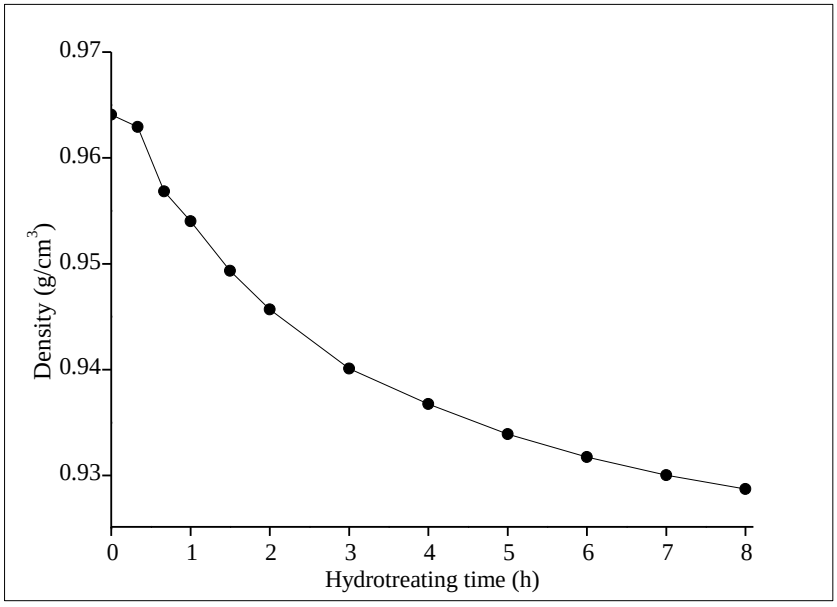

Figure 8.7 Variation of density of the product with the hydrotreating time

8.3 Conclusions

Light cycle oil is a complex middle distillate, containing different kinds of sulfur, nitrogen, and aromatic compounds. Hydrotreatment of this complex feedstock was carried out over an unsupported MoS_2 in a batch reactor, and conclusions were drawn based on the extensive analysis of hydrotreated products. The reactivity of different sulfur-containing compounds over the dispersed nano catalyst takes place in the following order of BT>1MBT>>2MBT>3MBT>4MBT>>DBT≈1MDBT≈2MDBT≈ 3MDBT. The rate of elimination of nitrogen compounds is determined in the following trend of Anilines> Indoles> Carbazoles. The change of aromatics demonstrates the presence of hydrogenation. From detailed analysis, the hydrogenation reaction mainly occurs on bicyclic aromatics to produce monocyclic compounds. The monocyclic and polycyclic aromatics are barely hydrogenated. The hydrocracking activity is revealed by the distribution of boiling points and the variation of liquid density. The boiling points' peak shifts to lower temperature after hydrotreatment, and the product density decreases with reaction time. Both results indicate the existence of hydrocracking reactions.

Chapter 9 Investigation of long-term HDS performance and deactivation mechanism of unsupported MoS_2

9.1 Introduction

Catalysts experience deactivation during the hydrotreating process. The main reason for deactivation is the loss of active sites, which can be attributed to different causes, including coke deposition, sintering or decomposition of active phase, poisoning, etc. [196-198]. In the present work, a deactivation study was carried out over an unsupported MoS_2 catalyst (CAT-2.5 in Chapter 4) on a fixed-bed microreactor. Unlike other studies using gas phase thiophene [197, 199, 200], LCO was employed in this work for better translation of the results to industrial conditions. Spent catalyst (160 hour of time-on-stream) was extensively characterized by XRD, TEM, XANES, Autosorb, etc. to evaluate the deactivation mechanisms. A comparative study was also performed on supported catalysts to elucidate the specificity of unsupported catalysts.

9.2 Experimental

The spent catalysts were washed with toluene using a Soxhlet extractor to remove the adsorbed feed before analysis. The carbon content on the spent catalyst was analyzed on a CHNS-O 932 elemental analyzer (LECO Corporation, MI, US). Extensive characterization was conducted on the spent catalyst, including nitrogen adsorption and desorption, TEM, XANES, microprobe analysis, and elemental analysis. The detailed procedure was described in Chapter 3. Supported catalyst CoMoS loaded on a combined acidic support of alumina and zeolite, denoted as CoMo/AZ, was used for comparison.

9.3 Results and discussion

9.3.1 Activity analysis

Investigation of the variation of catalytic activity as a function of reaction time is of importance to the practical application of a catalyst, since a catalyst inevitably approaches inactivation after long-term use. The resistance to deactivation is a critical criterion for a suitable catalyst. Figure 9.1 shows the variation of the catalytic activity of CAT-2.5 as a function of time-on-stream. At the earlier stage of hydrotreating, the catalyst shows a high activity with over 98% sulfur conversion. The conversion decreases during the following 60 hours of time-on-stream, which indicates the occurrence of deactivation. After 60 h, the activity reaches a steady state and HDS conversion is maintained at 86% to the end of the run (160 h). The results indicate that unsupported catalysts are stable in the long run once the steady state is reached.

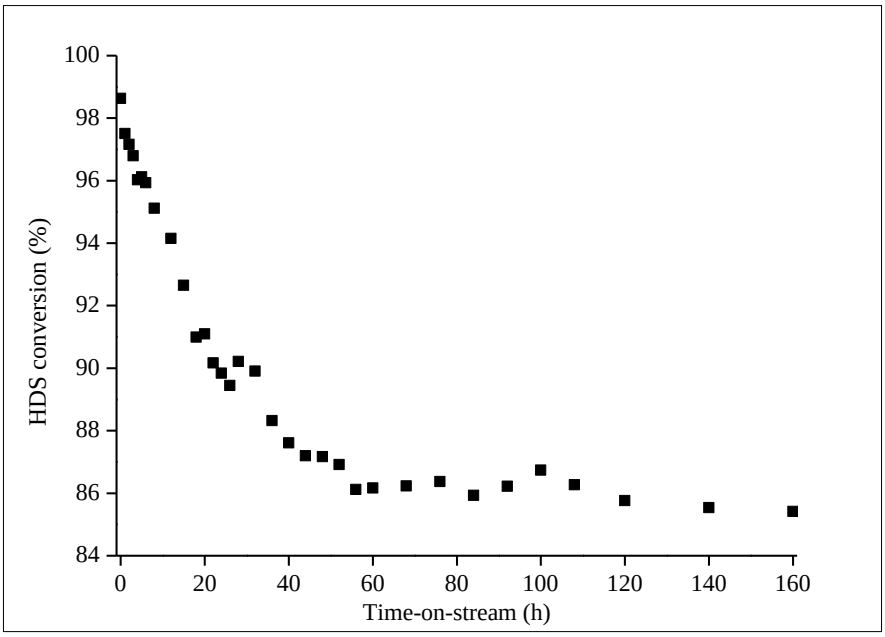

Figure 9.1 The variation of HDS conversion over unsupported MoS_2

9.3.2 Characterization of spent catalysts

In order to reveal the reasons for deactivation, the differences between the spent catalyst and fresh catalyst should be first identified. For such reason, the spent catalyst was characterized and compared with the fresh catalyst to illustrate changes in the crystalline structure and morphologies.

The XANES spectra of S K-edge and Mo L_3-edge are displayed in Figure 9.2. The spectra were acquired simultaneously in total electron yield (TEY) with an estimated 100 nm in probing depth. Detailed interpretation of the spectra can be found in Chapter 4. Compared to the reference MoS_2, fresh and spent catalysts exhibit identical spectra with the reference, indicating no bulk reduction of active sites after hydrotreatment. This is also evidenced by microprobe analysis that sulfur content only slightly decreases in S/Mo ratio after the long-time exposure to hydrogen (Table 9.1). XRD spectra also verify that no obvious changes in MoS_2 crystalline structure (Figure 9.3). The results indicate that the long term HDS reaction has a trivial effect on changing the chemical states and crystalline structure, which may contribute to the high stability of unsupported MoS_2.

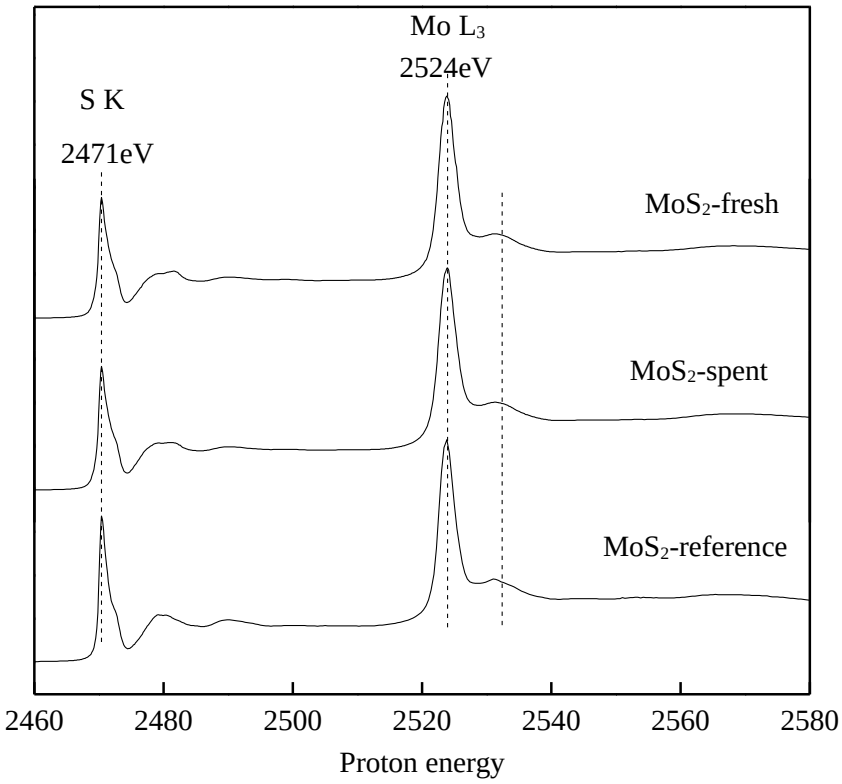

Figure 9.2 S K-edge and Mo L_3-edge XANES spectra of fresh and spent MoS_2

Table 9.1 Carbon and sulfur content

Catalysts	Carbon content (%)[a]	ΔS/Mo[b]
MoS_2-spent	7.36	(-)2.7
CoMo/AZ-spent	14.67	(-)37.3

[a]: tested from elemental analyzer

[b]: tested from microprobe analyzer

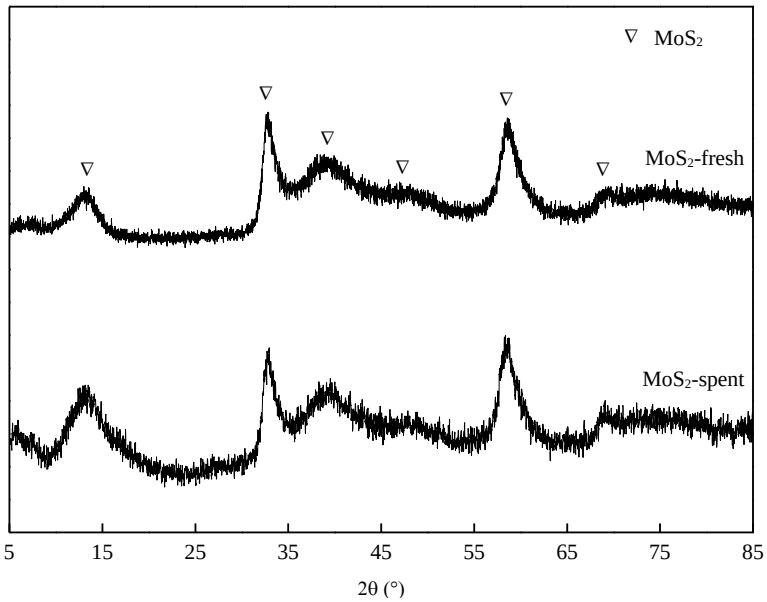

Figure 9.3 XRD spectra of fresh and spent catalysts

Compared to fresh catalysts, no distinct difference was observed in the dispersion and morphology of the catalysts (Figure 9.4). The average length of spent MoS_2 slabs increases from 17.43 nm to 18.93 nm, indicating a small degree of sintering (Table 9.2). One possible reason is that crystal slabs are rearranged and re-grow during the HDS process. This result is consistent with other studies conducted with unsupported MoS_2 [200]. No obvious change is observed in terms of layer numbers, indicating no re-stacking happens. This is probably because MoS_2 is anisotropic; thus, it may behave differently on the two directions [24].

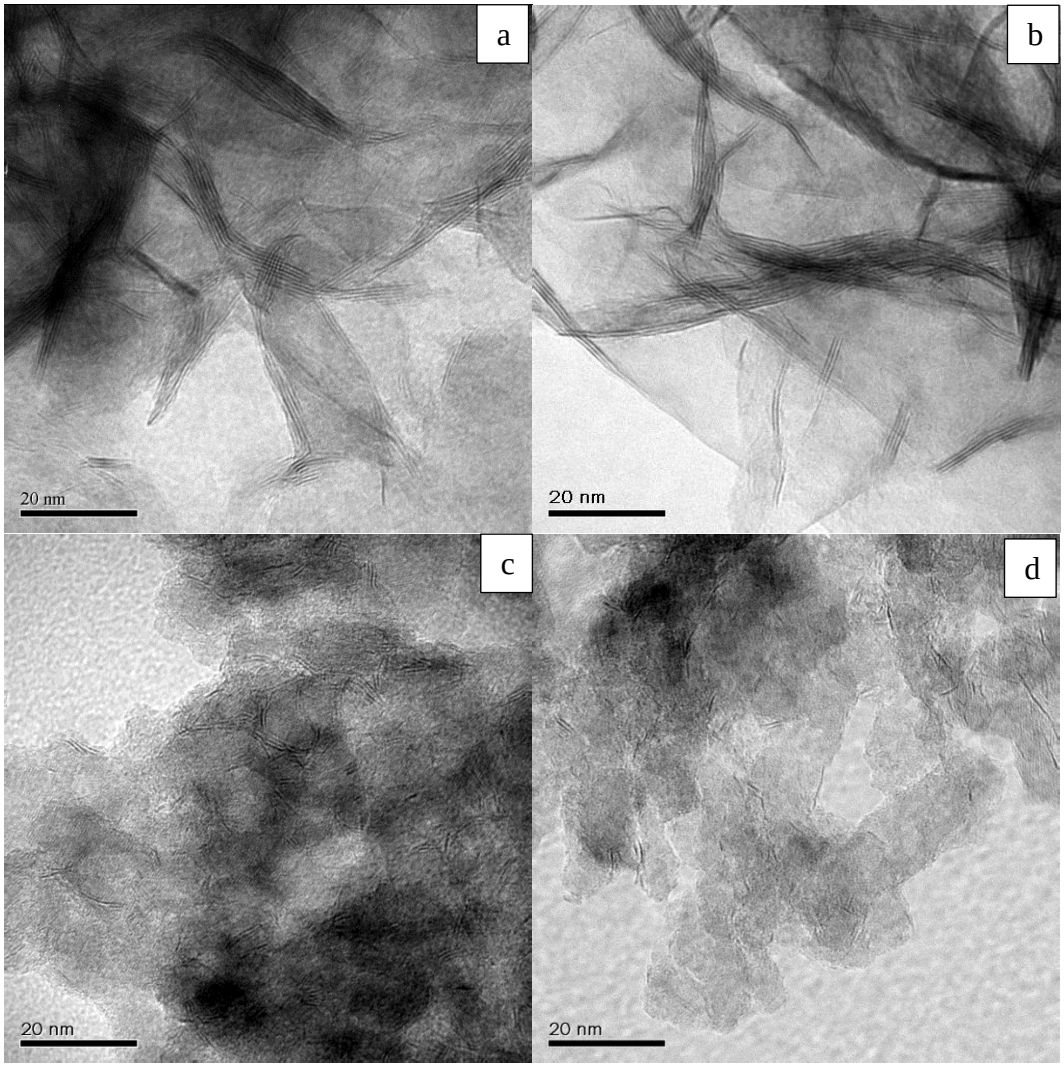

Figure 9.4 TEM images of fresh and spent catalysts
a: fresh MoS_2; b: spent MoS_2; c: fresh CoMo/AZ; d: spent CoMo/AZ.

Table 9.2 The variation of average slab length and layer number

Catalysts	Average slab length L(nm)	Average layer number n	ΔL (%)	Δn (%)
MoS_2-fresh	17.43	4.51		
MoS_2-spent	18.93	4.43	(+)8.6	(-)1.8
CoMo/AZ-fresh	6.07	2.15		
CoMo/AZ-spent	4.12	1.42	(-)33.8	(-)32.0

The fresh catalyst MoS_2 has a BET surface area of 231.1 m^2/g and a total pore volume of 2.276 cm^3/g (Table 9.3). Bimodal pore size distribution shows two peaks centered at 2.5

nm and 12 nm (Figure 9.5a). The smaller pores around 2.5 nm with a shoulder at 4-5 nm are the fine intra-aggregated pores from the material, and the broad peak at larger sizes is attributed to the secondary pores from the combination of primary particles. In Figure 9.5a, the mesopores at 2.5-5 nm of the fresh catalyst disappear and the corresponding pores shrink to less than 2 nm (micropore). Additionally, the secondary pores exhibit a significant smaller volume. As a consequence, a total decrease of 35-37% in both BET surface area and total pore volume is observed. The results indicate the occurrence of coke deposition on the catalyst, which blocks the pores from the reactants. The extent of carbonaceous deposition was measured via elemental analysis, which shows that 7.36% carbon was deposited on the spent catalyst (Table 9.1). The coke type was further analyzed through measurement of burn-off product CO and CO_2. As seen from Figure 9.6a, the majority of carbon is oxidized before 400 ℃, indicating that the coke is easy to remove.

Table 9.3 Comparison of textual structure of fresh and spent catalysts

Catalysts	BET surface area S_{BET} (m^2/g)	Total pore volume V_t (cm^3/g)	ΔS_{BET}[a] (%)	ΔV_t[b] (%)
MoS_2-fresh	231.1	2.276		
MoS_2-spent	148.2	1.421	(-)35.9	(-)37.6
CoMo/AZ-fresh	184.9	0.487		
CoMo/AZ-spent	96.0	0.242	(-)48.1	(-)50.3

[a]: ΔS_{BET}= (S_{BET} of spent catalyst- S_{BET} of fresh catalyst) /S_{BET} of fresh catalyst

[b]: ΔV_t= (V_t of spent catalys- V_t of fresh catalyst)/ V_t of fresh catalyst

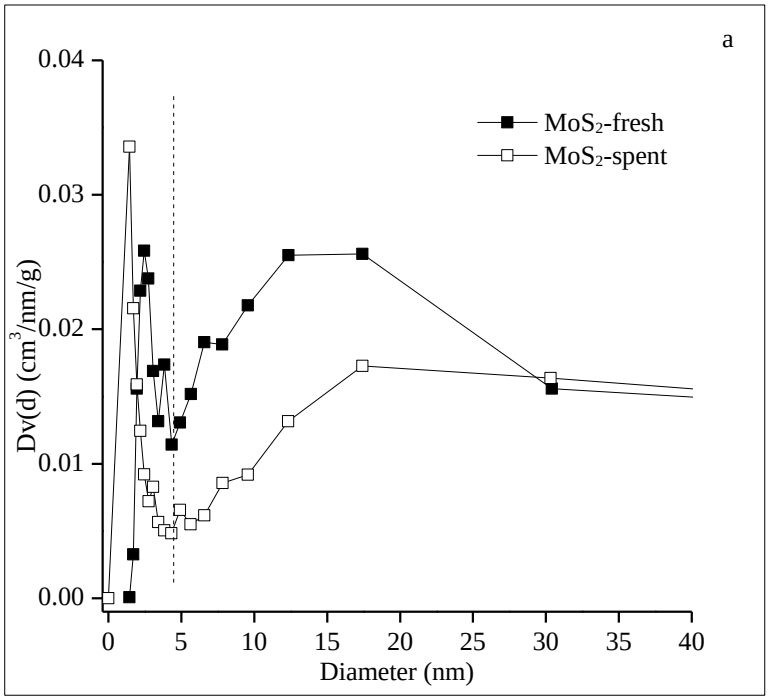

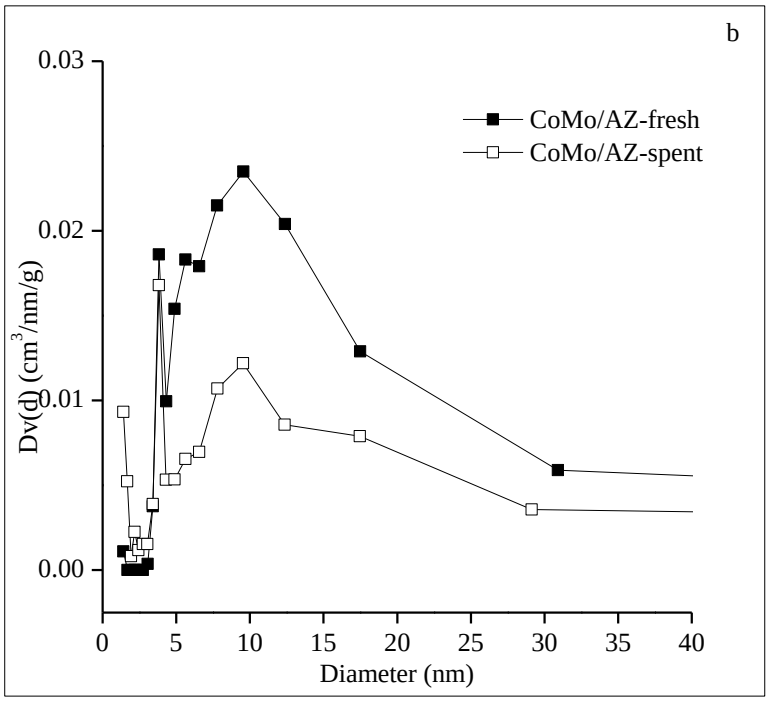

Figure 9.5 Pore size distribution of fresh and spent catalyst
a: MoS_2; b: CoMo/AZ

The comparison of fresh and spent catalysts indicates that the cause of deactivation may be attributed to coke deposition and active phase sintering. The former is considered to be the primary deactivation cause. As light cycle oil contains a large amount of aromatics, especially poly-aromatics, these compounds can be polymerized to asphaltenes and coke on the catalysts. Coke deposition will block the pores, both small pores and large pores, and consequently the accessibility of active sites will be decreased. Sintering consists in the decrease of the amount of active sites on the edges. During the enlarging of the slabs, some active sites will vanish due to the decreased edge to basal ratio, which will eventually result in the deactivation of the catalyst. Such phenomenon was also observed by other research [199, 200].

9.3.3 Comparison with supported catalysts

To reveal the deactivation behaviour of unsupported catalyst, a comparative study was conducted with the supported catalyst loaded on alumina and zeolite (AZ). The evaluation follows the same HDS conditions. For supported CoMo/AZ, a significant decrease in surface area and pore volume is observed. The pore structure is well maintained with similar distribution. The smaller pore sizes slightly decrease, while a significant drop is observed on the secondary pores centered at 10nm (Figure 9.5b). The decrease of pore volume is mainly due to carbon deposition, as seen from the high carbon content of 14.67% (Table 9.1). Further analysis of carbon type shows that the main coke type on supported catalysts is hard coke, which cannot be burned until 400 ℃ (Figure 9.6b). Another reason for the deactivation is the decomposition of active sites (Reaction 9.1), as indicated by the large loss of sulfur (37.3%, Table 9.1) and the decrease of MoS_2 slab length and layer numbers (Figure 9.4, Table 9.2).

$$MoS_2 + 2H_2 \rightarrow Mo + 2H_2S$$ Reaction 9.1

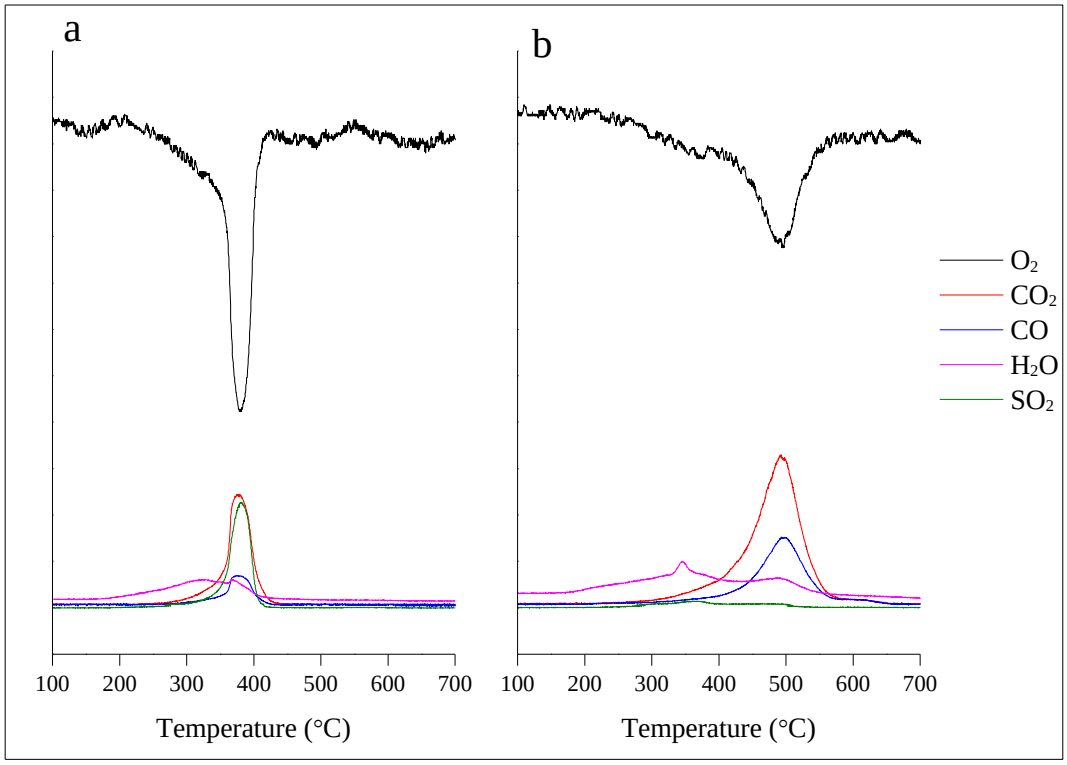

Figure 9.6 TPO spectra of spent catalysts
a: MoS_2; b: CoMo/AZ

Comparison with supported catalysts shows a significant difference on deactivation mechanisms. Although coke deposition is still one of the deactivation causes, without acidic support, only easy coke is generated. The activity of the catalysts is easy to recover by washing the catalysts with strong solvent or low temperature burning. Additionally, active sites on unsupported MoS_2 are mainly located on certain areas, e.g. edge sites and curved basal plane. Without support, the structure is more stable as seen from the slight decrease of sulfur content, in comparison with the supported catalyst CoMo/AZ, which is easier to be reduced and loses a large proportion of structural sulfur when exposed to

hydrogen. Such results tend to show that acid support may have a negative effect on catalyst stability.

9.4 Conclusions

The deactivation behaviour of the unsupported MoS_2 has been studied through a 160 hours of HDS reaction. The result shows that the activity of the catalyst dropped gradually within the first 60 h, after which the activity of the catalyst is maintained to the end of the run. Compared with the fresh catalyst, the spent catalyst exhibits differences on the slab length and pore volume, due to the sintering and coke deposition, respectively. The catalyst was compared with the supported catalysts, and the results show that the high stability of the unsupported catalyst may be derived from less coke deposition and the higher resistance to structure decomposition.

Chapter 10 The role of cobalt and nickel in deoxygenation of vegetable oils

10.1 Introduction

Recently, nickel (Ni)/cobalt (Co)-promoted molybdenum (Mo)-based catalysts have been applied to hydrodeoxygenation processes in the elimination of oxygen from plant oils [158, 201]. In the present work, unsupported CoMoS and NiMoS were synthesized using the hydrothermal method described in Chapter 7. Emphasis was given on the differences of deoxygenation ability and selectivity over these two unsupported catalysts. Reaction schemes were proposed on both Co and Ni promoted catalysts based on the experimental results. Other selectivity was also defined to discuss the role of Co/Ni in hydrogenation, hydrocracking, and polymerization.

10.2 Product analysis

The catalyst activity was expressed in terms of glycerides conversion and oxygen removal rate, as shown in Equation 10.1 and Equation 10.2, respectively.

$$Glycerides\ conversion = 1 - \frac{Glycerides\ in\ liquid\ product}{Glycerides\ in\ canola\ oil} \qquad \text{Equation 10.1}$$

$$Oxygen\ removal\ rate = 1 - \frac{oxygen\ in\ liquid\ product}{oxygen\ in\ canola\ oil} \qquad \text{Equation 10.2}$$

Comparison of different oxygen elimination reactions, hydrodeoxygenation (HDO) and hydrodecarbonylation/decarboxylation (HDC), was presented by the ratio of generated C_{18}/C_{17} hydrocarbons (Equation 10.3).

$$C_{18}/C_{17}\ ratio = \frac{Mass\ of\ C_{18}\ hydrocarbons}{Mass\ of\ C_{17}\ hydrocarbons} \quad \text{Equation 10.3}$$

The hydrocracking and polymerization degree was calculated by Equation 10.4 and Equation 10.5, respectively.

$$Hydrocracking\ \deg ree = \frac{Mass\ of\ \sum C_i (i<15)}{Mass\ of\ total\ hydrocarbons} \quad \text{Equation 10.4}$$

$$Polymerization\ \deg ree = \frac{Mass\ of\ \sum C_i (i>18)}{Mass\ of\ total\ hydrocarbons} \quad \text{Equation 10.5}$$

Hydrogenation activity was reflected by paraffin selectivity (Equation 10.6).

$$Paraffin\ selectivity = \frac{Mass\ of\ Paraffins}{Mass\ of\ total\ hydrocarbons} \quad \text{Equation 10.6}$$

10.3 Results

10.3.1 Unsupported catalyst

The crystalline structures of nanosized unsupported CoMoS and NiMoS catalysts are identified by TEM images (Figure 10.1). CoMoS crystalline shows well dispersed small particles (Figure 10.1a) and short slabs (Figure 10.1c), while NiMoS appears to be more agglomerative (Figure 10.1b) and longer in length (Figure 10.1d). The main properties of the catalysts are listed in Table 10.1. The average layer number and slab length for CoMoS are 2.9 and 7.8 nm, respectively, while they are 4.8 and 10.4 nm for NiMoS. Using the method described by Calais et al. [167], the fraction of edge metal atoms on

catalysts were calculated, which shows that Co-promoted catalyst has more edge sites than Ni-promoted catalyst does. EDX results show that the atomic ratios of Co and Ni to total metals are 25% and 24%, respectively. The S contents of spent CoMoS and NiMoS drop 3.3% and 6.8%, respectively, in comparison with the corresponding fresh catalysts. The loss of sulfur is probably caused by the oxygen replacement on the edge of sulfur sites. The surface area and pore volume of nickel and cobalt promoted catalysts are also shown in Table 10.1. CoMoS has larger surface area and pore volume than NiMoS does. In Figure 10.2, a bimodal pore size distribution is observed for CoMoS with a sharp peak at 2.5 nm and a broad peak at around 12 nm. Similar pore size distribution is also found for NiMoS but lower peak height. The TPR spectra shown in Figure 10.3 are quantitatively summarized in Table 10.2. As expected, the total consumption of H_2 by CoMoS is higher, which is consistent with more calculated edge sites of CoMoS (Table 10.1). However, H_2S was not generated over CoMoS until temperature is higher than 400 ℃. NiMoS behaves differently. H_2S is detected simultaneously with the consumption of H_2 and the amount of produced H_2S is similar to the consumption of H_2.

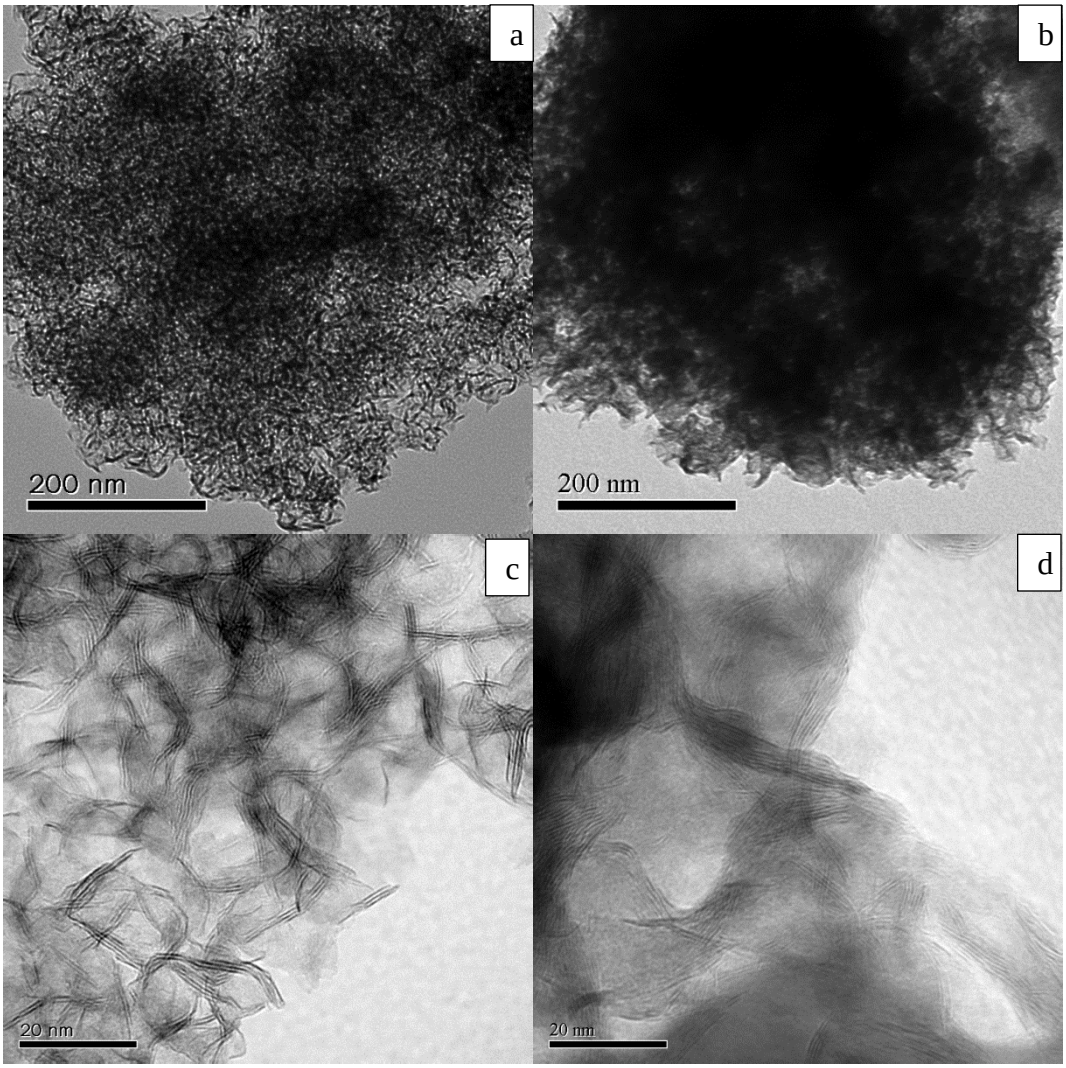

Figure 10.1 TEM images of unsupported catalysts
a.c CoMoS; b.d NiMoS

Table 10.1 Basic properties of NiMoS and CoMoS

Catalysts	NiMoS	CoMoS
Promoter/(promoter+Mo)	0.24	0.25
Slab length (nm)	10.4±0.6	7.8±0.2
Layer numbers	4.8±0.4	2.9±0.1
Fraction of edge metal atoms (%)	11.6	15.1
BET surface area (m^2/g)	37.8	82.2
Total pore volume (cm^3/g)	0.257	0.526
Fraction of S loss (%)[a]	6.8	3.3

[a]: Fraction of S loss is calculated from the difference of S content between fresh catalyst and spent catalyst.

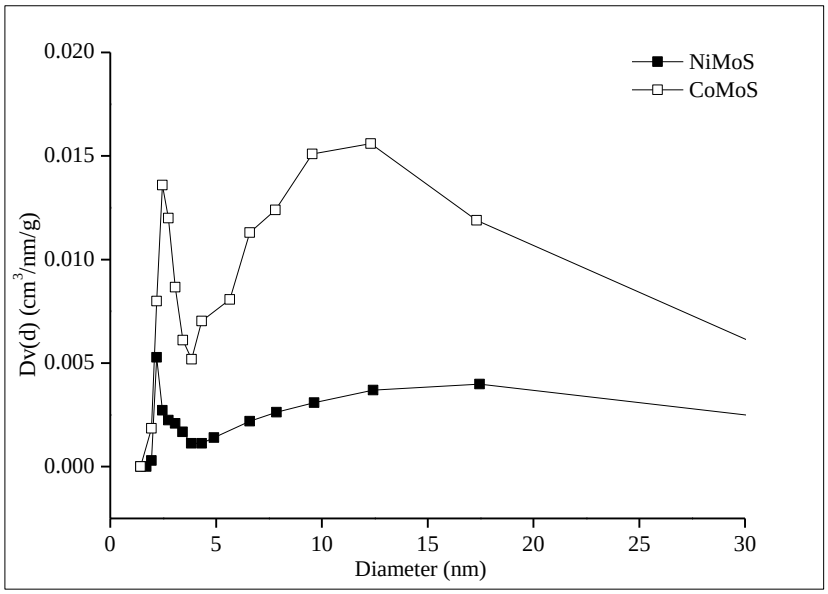

Figure 10.2 BJH pore size distribution of unsupported catalysts

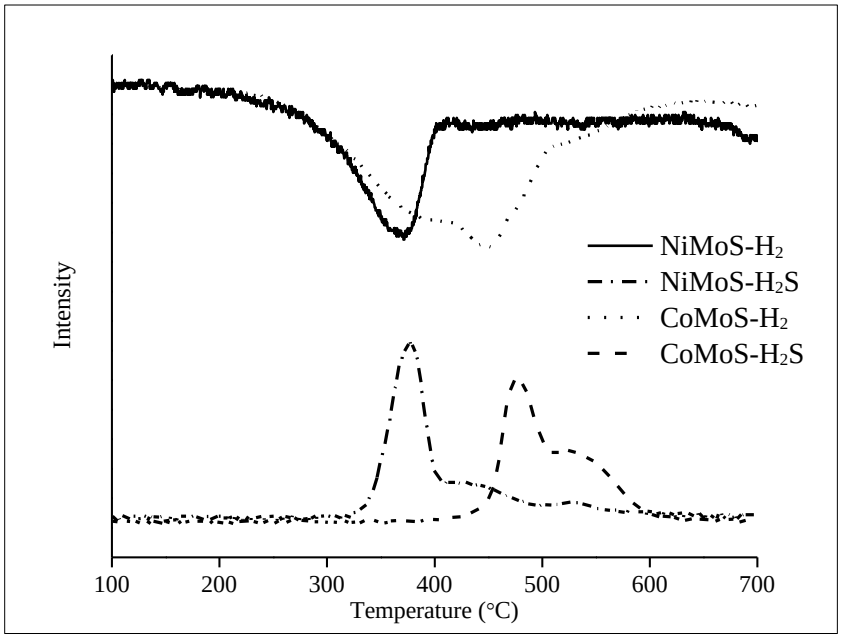

Figure 10.3 TPR spectra of unsupported catalysts CoMoS and NiMoS

Table 10.2 TPR data summary

Catalysts	H_2 consumption		Corresponding H_2S production	
	Peak temperature (℃)	Amount ($x10^{-3}$ mol/g cata)	Peak temperature (℃)	Amount ($x10^{-3}$ mol/g cata)
NiMoS	230-415	2.34	310-415	2.25
CoMoS[a]	230-430	2.56	402-510	1.26

[a]: Calculation based on the first peak

10.3.2 Deoxygenation activity

Triglycerides are the main components of canola oil with a small amount of free carboxylic acids at a total acidity number (TAN) of 2.89 (Table 10.3). The distribution of fatty acids is listed in Table 10.4, which shows that there are only acids with even-numbered carbon atoms. C_{18} fatty acids are dominant component of canola oil, most of which are unsaturated carbon chains. After 8 hours of hydrotreatment, the oxygen was completely removed over both catalysts. The TAN of hydrotreated liquid products are close to 0, indicating a complete conversion of carboxylic acids (Table 10.3).

Table 10.3 Properties of the feed and hydrotreated products (8 hours)

Oils	Density (g/cm^3) @25 ℃	TAN number (mgKOH/g)	Oxygen content (%)
Canola oil	0.9179	2.89	11.66
HCO 1[a]	0.7801	0	0
HCO 2[b]	0.8004	0.01	0

[a]: Hydrotreated canola oil over catalyst NiMoS
[b]: Hydrotreated canola oil over catalyst CoMoS

Table 10.4 Fatty acid composition of canola oil tested by GC-MS

Fatty acids (Cn:m)[a]	C16:0	C16:1	C18:0	C18:1	C18:2	≥C20:0
Content (w.t. %)	5.9	0.4	1.3	73.4	17.7	0.6

[a]: Cn:m: n, number of carbon atoms; m, number of C=C double bonds in fatty acids e.g. C16:1, fatty acid with 16 carbon atoms and 1 C=C double bond.

Under the hydrotreating condition, triglycerides are first converted to the corresponding fatty acids which will be further transformed to hydrocarbons through two main reaction pathways: hydrodeoxygenation and hydrodecarbonylation/decarboxylation. The development of deoxygenated products was observed by FTIR (Figure 10.4). For NiMoS, the two peaks characterizing the absorption of ester C=O and C-O-C are significantly smaller than that of feedstock at the first 0.5 hour of reaction, indicating a quick decomposition of triglycerides. After 2 hours, most of esters and fatty acids are transformed as the intensity of the peaks is significantly dropped. The complete conversion of triglycerides/fatty acids is reached after 8 hours because only the absorption for alkanes is observed (Figure 10.4a). On the other hand, a slow decomposition rate of triglycerides/fatty acids over CoMoS is noted. Strong adsorption spectra characterizing fatty esters and acids are observed at 0.5 hour of reaction (Figure 10.4b). Figure 10.5 and Figure 10.6 compare the glyceride conversion and oxygen removal rates over catalysts CoMoS and NiMoS. Within the first 3 hours of reaction, NiMoS exhibits higher glycerides conversion and oxygen removal rate than CoMoS. The maximum differences in glycerides conversion and oxygen removal rate are 8% and 34%, respectively.

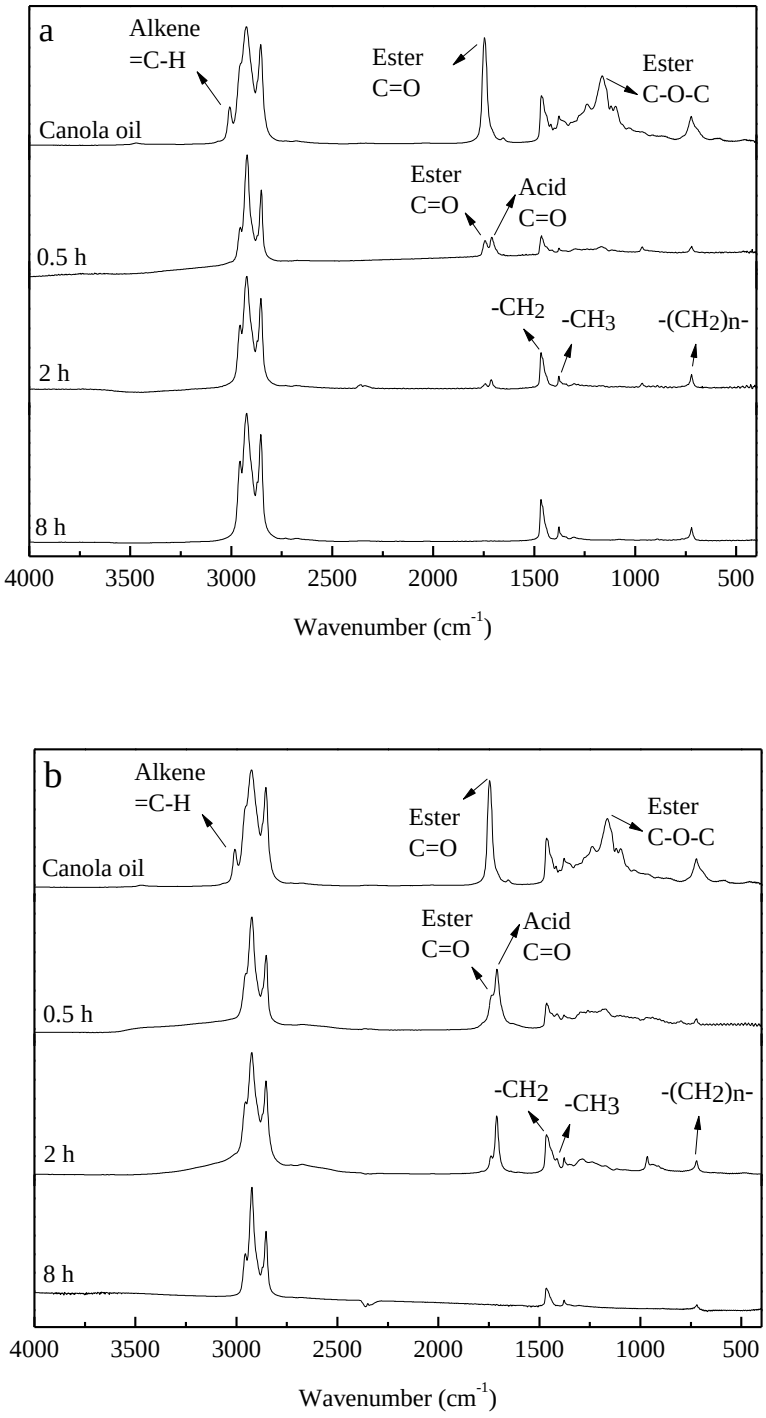

Figure 10.4 FTIR spectra of hydrotreated canola oil
Catalysts: a. NiMoS; b. CoMoS. Ester C=O: 1742 cm^{-1}; Ester C-O-C: 1170 cm^{-1}; Fatty acid C=O: 1711 cm^{-1} C=C: >3000 cm^{-1}; C-H: 3000-2800 cm^{-1}; CH_2 and CH_3: 1475-1300 cm^{-1}; $-(CH_2)_n-$:722 cm^{-1}.

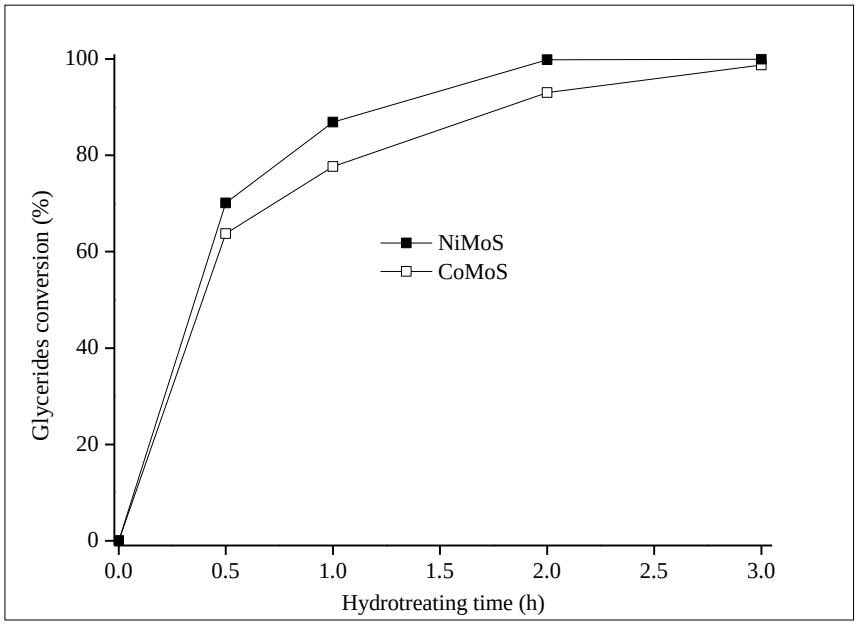

Figure 10.5 Comparison of glycerides conversion

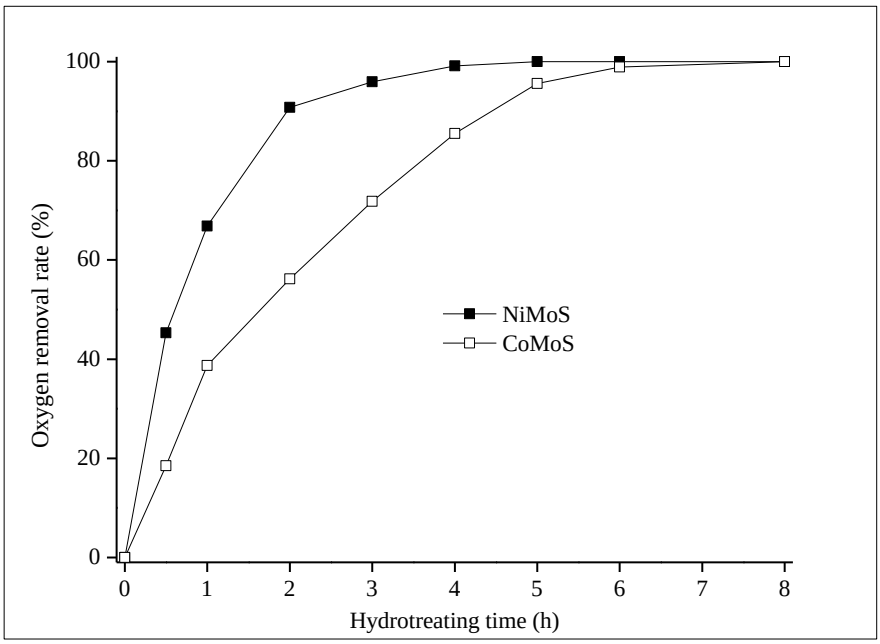

Figure 10.6 Comparison of deoxygenation activities

10.3.3 Product selectivity

C_{18}/C_{17} ratio

The mass balance for both catalysts was carried out after 8 hours of reaction (Table 10.5). The sums of gas and liquid products over CoMoS and NiMoS reach 96.2% and 96.7%, respectively. The C_{18}/C_{17} ratios are compared in Figure 10.7. It is noticed that the C_{18}/C_{17} ratio obtained with NiMoS (1.7) is much higher than that over CoMoS (0.5) in the entire course of the reaction. High C_{18}/C_{17} ratio over NiMoS suggests that HDO is the main \pathway. Oxygen is removed in the form of H_2O in the HDO route. On the other hand, HDC is favorable on CoMoS, with the formation of CO or CO_2 (Table 10.5). In addition, hydrodecarbonylation is more favored than decarboxylation on CoMoS, evidenced by the formation of more CO than CO_2. There is no obvious evidence of the formation of methane from the reduction of carbon oxide, as seen from the low methane content (Table 10.5).

Table 10.5 Product distribution

	Hydrotreated over NiMoS	Hydrotreated over CoMoS
Liquid (w.t. %)	90.3	86.0
CO (w.t. %)	3.4	6.1
CO_2 (w.t. %)	1.3	1.6
Methane C_1 (w.t. %)	0.1	0.2
C_2-C_6 (w.t. %) [a]	1.6	2.3
Mass balance (w.t. %)	96.7	96.2

Hydrogen was not considered in the mass balance calculation

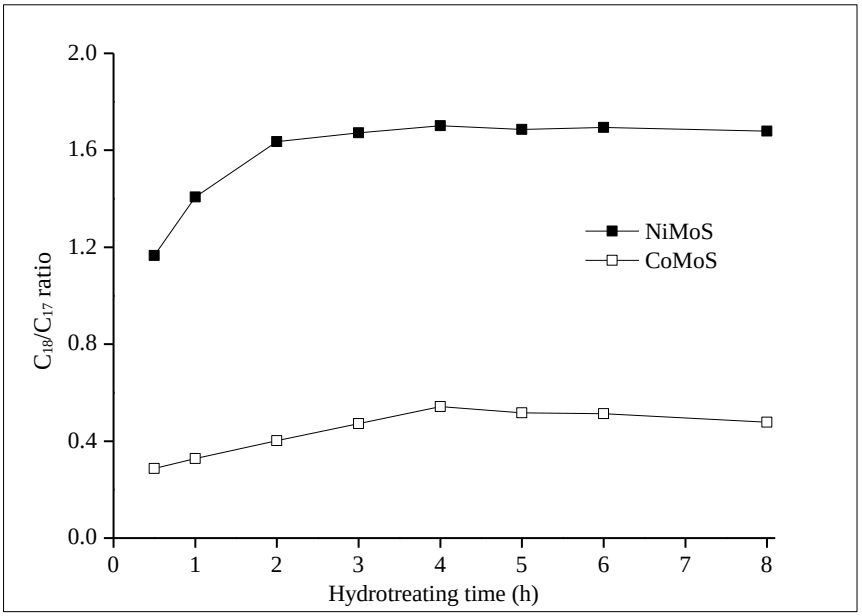

Figure 10.7 Comparison of C_{18}/C_{17} ratio

Hydrocracking and polymerization degree

Canola oil is composed of 99 w.t. % C_{16} and C_{18} fatty acids. C_{15} to C_{18} hydrocarbons are the corresponding hydrotreated products [9]. Therefore, hydrocarbons with number of carbon lower than 15 and higher than 18 are of the hydrocracking and the polymerization products. After 8 hours of hydrotreatment, approximately 14% of the canola oil is hydrocracked and polymerized on CoMoS. In contrast, less than 7% of feed is observed with NiMoS (Figure 10.8). Higher degree of hydrocracking and polymerization is observed over CoMoS. Simulated distillation results show a dramatic decrease of heavy components after hydrotreatment on both catalysts. NiMoS shows good performance with high selectivity to diesel-like hydrocarbons. In contrast, high yields of gasoline-like hydrocarbons and heavy components are obtained over CoMoS (Figure 10.9). It has been indicated that cobalt promotes the breakage and formation of C-C bonds.

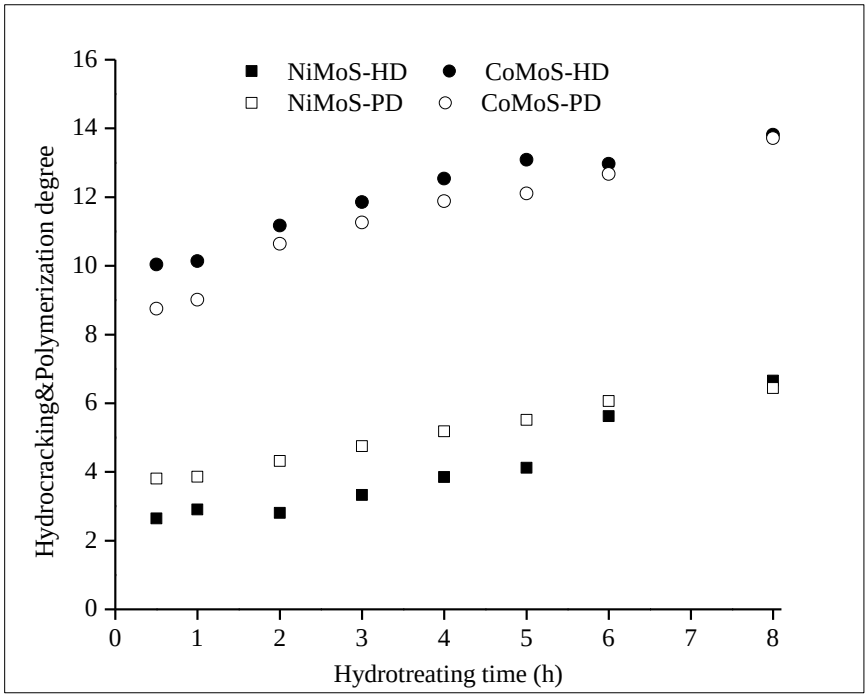

Figure 10.8 Comparison of hydrocracking and polymerization degree
HD: hydrocracking degree; PD: polymerization degree

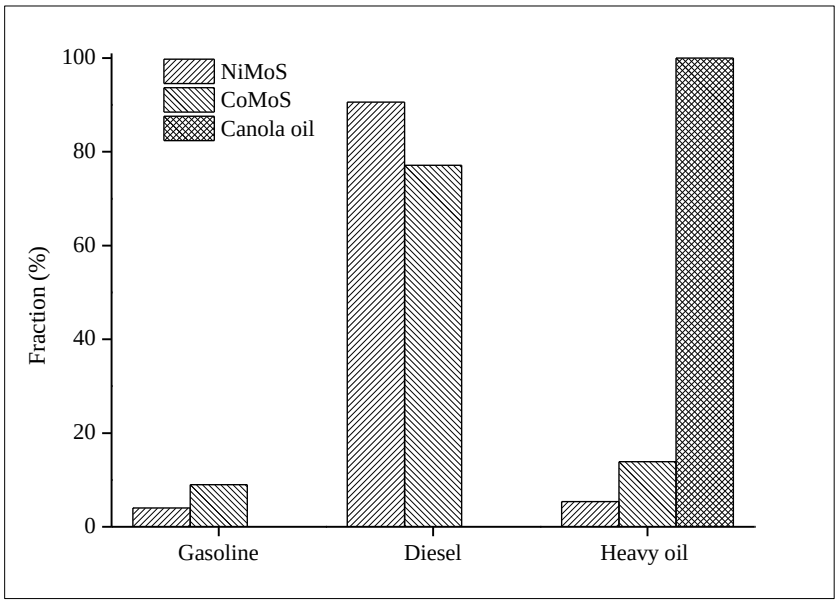

Figure 10.9 Distribution of hydrocarbon products from simulated distillation
Gasoline: boiling point (BP) <200 ℃; Diesel: BP 200-350 ℃; Heavy oil: BP>350 ℃

Paraffin selectivity

Figure 10.10 shows that, at the end of the reaction, over 90% hydrocarbons are saturated over NiMoS, while nearly 40% hydrocarbons still contain double bonds when using CoMoS. This suggests that NiMoS has higher hydrogenation activity than CoMoS. The observation is also supported by the H/C molar ratio (Figure 10.11). The H/C ratios increase with the conversion of oxygenates. Much higher H/C ratios are observed over NiMoS than over CoMoS. It confirms high hydrogenation activity of NiMoS.

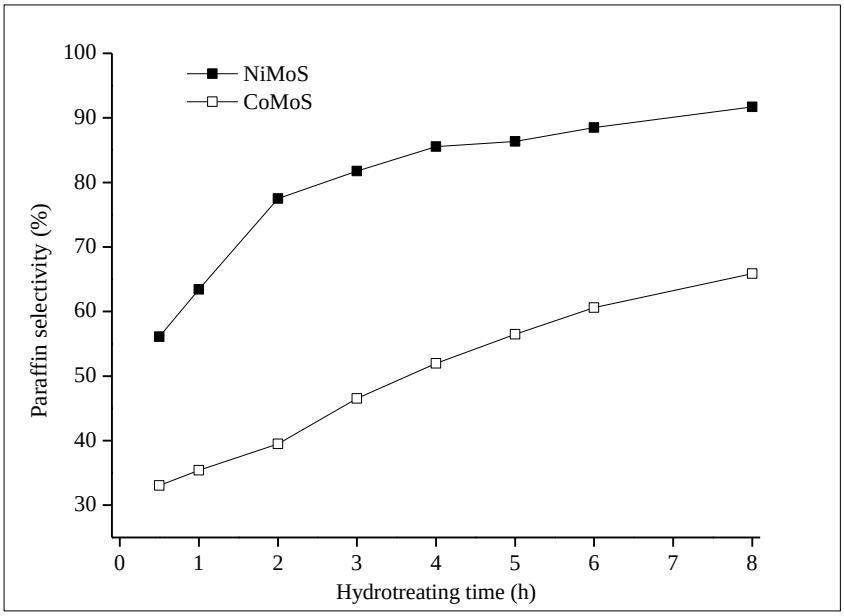

Figure 10.10 Comparison of paraffin selectivity

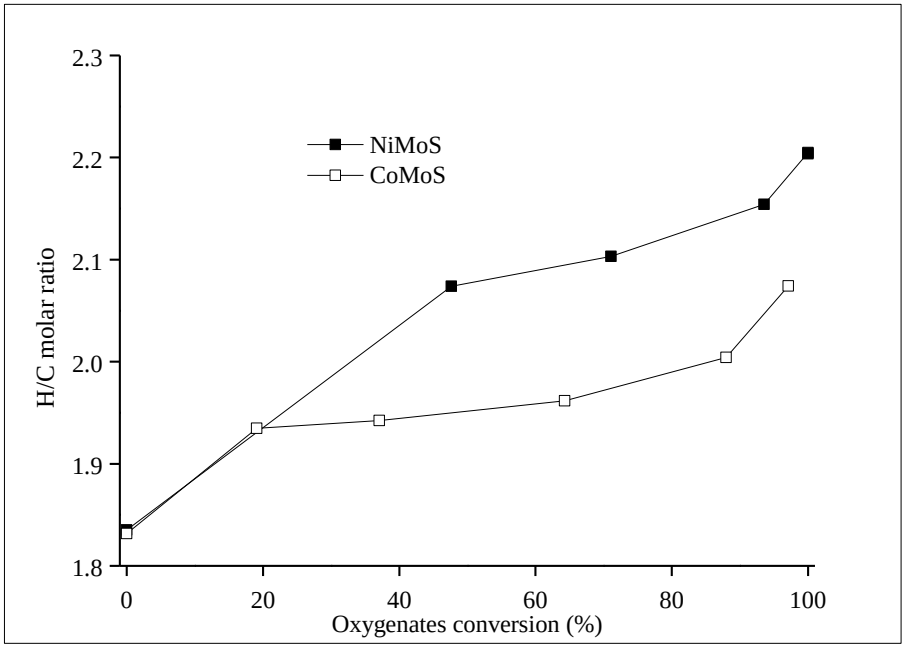

Figure 10.11 Comparison of H/C molar ratio

10.4 Discussion

Deoxygenation of plant oils (triglycerides) using conventional supported sulfide catalysts has been well studied [11, 68]. Disagreements in the main reaction pathways remain unsolved. Support materials of catalyst play a key role in reaction pathways [12, 77]. In this work, unsupported sulfided catalysts were used so that the interference by catalyst support was eliminated. It has been observed that Ni-doped MoS_2 catalyst promotes hydrodeoxygenation reaction, ending up with C_{18} hydrocarbons as the main liquid product. Co-promoted MoS_2 catalyst favors hydrodecarbonylation/decarboxylation reaction, resulting in more C_{17} hydrocarbons produced (Figure 10.7). The distinct roles of Ni and Co are attributed to the difference of their structures. Ni-promoted catalyst contains abundant sulfur vacancies, whereas CoMoS has none until 400 ℃, evidenced by the TPR results shown in Figure 10.3. Consequently, at the reaction temperature of

375 ℃, the main active sites of Ni-promoted catalyst are the unsaturated sites; on the contrary, saturated sites dominate the catalyst promoted by Co. The observation agrees with the density function theory (DFT) calculation that nickel favors to be on the Mo-edge of MoS_2 and cobalt tends to substitute the Mo on the S-edge [87, 202, 203]. Therefore, the reactions over Ni-promoted catalyst tend to occur on the unsaturated metal edge, while the reactions over Co-promoted catalyst are likely to take place on saturated sulfur edge. The distinct active sites of the catalysts may be responsible for different main reaction pathways. It's worth noting that unsaturated sites would be created on CoMoS in a prolonged hydrotreating reaction, and saturated sites are also present on NiMoS, especially at the beginning of the reaction. The following discussion only focuses on the main reaction pathways of both catalysts.

The main reaction mechanism of NiMoS at unsaturated metal edge is proposed in Scheme 10.1 (S1 hereafter). Firstly, hydrogen is dissociated and adsorbed on unsaturated Mo atom and S atom, forming S-H and Mo-H at the S vacancies (S1-B). Formation of the Mo-H and S-H pair is exothermal and requires the minimal dissociation energy [204]. The high electrophilic Mo atom tends to adsorb O atom in C=O bond as O tends to be more nucleophilic in C=O than in C-O-C. Introduction of Ni promotes disruption of π bond on O=C to form a -Mo-O-C-Ni- cycle (S1-C). This "synergy effect" displayed by NiMoS has been recently explained by the DFT theory. The presence of Ni can reduce the energy barriers for O=C bond [99]. S1-C is a critical step for Ni to realize its promoting effect on MoS_2 catalysts. S vacancies are essential in providing the sites for Mo and Ni to bond O and C atoms. With dissociative adsorbed H in the vicinity, Ni-C

scission proceeds readily. Dissociated H preferentially interacts with C and O to form C-H and O-H bonds (S1-D) [99, 205]. Surrounded by abundant dissociated H on Mo and S atoms, the C-O splitting is likely to take place with alcohol and water as products. Alcohol will undergo another C-O scission to form n-octadecane or n-octadecene. The generation of alcohol is essential for C_{18} production and determines the main deoxygenation. In terms of reactants, the C associated with C=O is partial oxidized since an electron transfers from C to Ni (S1-C in Scheme 10.1). This will lead to the formation of carbonic carbonium on C atom. The carbonic carbonium will then absorb H from the reactant to break the C-Ni bond to form C-H bond (S1-D). As another H attack the C atom, the C-O single bond is eventually broken with O atom removed, which leads to the reduction of fatty acid to form alcohol.

The main reaction mechanism over Co-promoted MoS_2 is demonstrated in Scheme 10.2 (referred as S2). High H_2 consumption over CoMoS in the TPR test indicates that cobalt can facilitate hydrogen adsorption on sulfur sites generating stable H-S bonds (S2-B). This phenomenon is consistent with the published DFT calculations that (Co-) SH group is the most stable hydrogen species on the Co-promoted S-edge [23, 24]. The weaker bonding between S and Co atoms opens the door to strong interaction between the terminal S and H atoms [115, 206]. The formed HS groups are highly nucleophilic and attractive to the electrophilic C atoms with or adjacent to a carboxyl group (S2-C). And then the scission of weakened C-C bond is followed by forming n-heptadecane or n-heptadecene and by-product formic acid, which can be easily decomposed to CO and

H_2O [207-209]. It is noted that saturated sulfur sites providing C atom adsorption sites essentially contribute to the HDC reaction route.

Scheme 10.1 suggests a deoxygenation mechanism for C=O over NiMoS. The compounds containing C=O bonds such as acids, aldehydes, etc. most likely undergo the same pathways over NiMoS in the elimination of oxygen. This finding is in agreement with the model compounds, e.g. ethyl heptanoate, heptanoic acid, etc. [205]. The compounds that do not have C=O bonds (e.g. phenol), the synergy effect (shown in Scheme 10.1) may not be able to be established. Scission of C-O may be achieved through hydrogenation. Yoosuk et al. observed that more hydrogenated products such as cyclohexane were produced than benzene when phenol was treated over a NiMoS catalyst [210]. With the same reactant, more benzene produced over CoMoS, which indicated direct C-O splitting was more favorable than C-O cleavage through hydrogenation [211]. For petroleum components, such as dibenzothiophene, similar trend was observed that selectivity in hydrogenation (HYD) pathway on NiMoS was higher than on CoMoS [18, 212].

The high hydrogenation ability of NiMoS was also observed in this work, where a high degree of saturation was observed (Figure 10.10). CoMoS exhibits higher hydrocracking activity (Figure 10.8, Figure 10.9). The TPR results obtained in this work lead to a conclusion that hydrocracking activity is facilitated by saturated active sites on sulfur edge while hydrogenation favors to take place at sulfur vacancies located at the edges of active metal sites. The findings are in good agreement with the literature, where it was

reported that SH groups promoted hydrogenolysis and hydrogenation took place on the unsaturated metal sites [213, 214].

In a common practice, MoS_2 is loaded onto porous materials, such as Al_2O_3. Comparing our results to the supported catalysts reported in the literature may lead a way to understand the role of support in deoxygenation. The hydrocarbons generated over most supported Co(Ni)MoS catalysts show higher C_{18}/C_{17} ratios than the ratio obtained over their unsupported counterparts [68, 160]. There is no distinct performance difference observed between supported CoMoS and NiMoS [162]. It is generally accepted that the Lewis acid sites on Al_2O_3 supports increases the activity of hydrogenation and dehydration reactions, which indicates catalyst support, e.g. Al_2O_3, enhances the HDO pathway [12]. It suggests that catalyst support plays a role in deoxygenation and the presence of catalyst support covers the different behaviours of active phases-NiMoS and CoMoS.

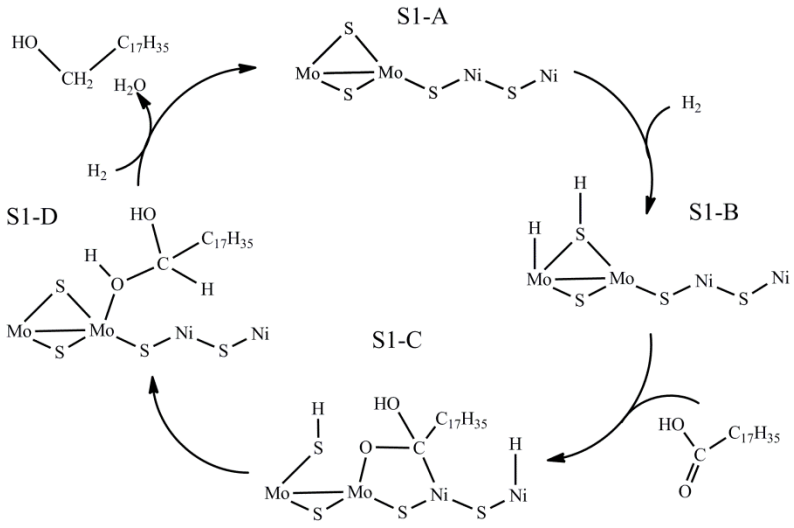

Scheme 10.1 Main deoxygenation mechanism on NiMoS

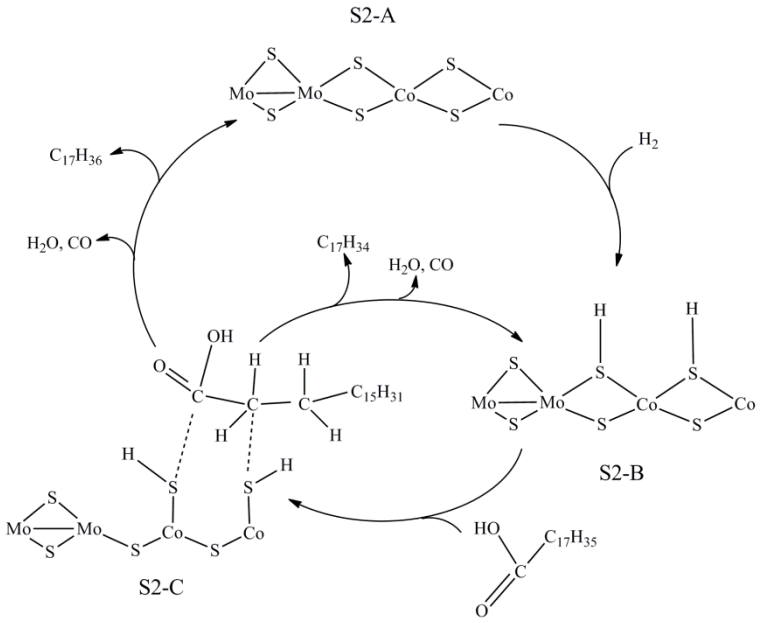

Scheme 10.2 Main deoxygenation mechanism on CoMoS

10.5 Conclusions

Unsupported Ni and Co-promoted MoS_2 catalysts were studied in the deoxygenation of raw canola oil. The TEM images show that CoMoS has more edge sites; the TPR results indicate that Co-promoted catalyst has high ability to adsorb H_2. Sulfur vacancies can be barely observed until 400 ℃. Compared to CoMoS, NiMoS exhibits lower amount of edge sites but higher ability to create sulfur vacancy at low temperatures. Different properties lead to their distinct performances in hydrotreatment of canola oil in terms of activity and selectivity. NiMoS presents a higher deoxygenation activity than CoMoS. NiMoS exhibits high selectivity towards C_{18} (HDO product) with a C_{18}/C_{17} ratio of 1.7, generates low hydrocracking and polymerization side reactions and produces more paraffins over olefins.

The promoter Ni primarily functions through the synergy effect of Mo and Ni on unsaturated metal sites while Co facilitates HDC reaction routes by activating the saturated sulfur sites. The higher hydrocracking (C-C hydrogenolysis) activity of CoMoS indicates that hydrocracking tends to occur on the saturated sites; the high hydrogenation capacity of NiMoS implies that sulfur vacancies are likely to be involved in hydrogenation reactions.

Chapter 11 Kinetics study on hydrodeoxygenation of waste cooking oil over unsupported CoMoS

11.1 Introduction

Waste cooking oil (WCO) is accepted as a second generation resource for biofuel production [162, 215, 216]. Its main component, triglycerides, can be easily converted to combustible biofuel. In this work, WCO was hydrotreated using unsupported CoMoS (CAT-43b1). A comprehensive kinetics analysis was carried out to understand the deoxygenation process. Reaction mechanisms and catalyst deactivation were investigated using kinetic modeling based on a proposed reaction network. The calculated rate constants indicate dominant reactions and rate-limiting steps in a series of parallel and consecutive reactions. Other reactions including hydrocracking, polymerization, hydrogenation, and cyclization were also studied as well as the reaction temperature effect. The comprehensive analysis of deoxygenation process would provide valuable information on the mechanism study of vegetable oil type feedstock with unsupported catalysts.

11.2 Results and discussion

11.2.1 Overall description of WCO and hydrotreated product

The composition of fatty acid in WCO was determined by GC-MS (Table 11.1). Most fatty acids detected are present in the form of triglycerides, in addition that the total acid number (TAN) of WCO is low (0.65). Triglycerides are identified by FTIR and ^{1}H-NMR spectra, with the presence of the large peaks of esters at 1740 and 1163 cm^{-1} and peaks 2,3,5 and 7 for protons related to ester and carboxylic groups [217], respectively (Figure

11.1, Figure 11.2). In Table 11.1, it is noted that the fatty acids having even number of carbon atoms exist in WCO and over 90 wt% are C_{18} fatty acids, most of which are unsaturated with one or two C=C double bonds.

Table 11.1 Composition of fatty acids in WCO

Fatty acids (n:m)[a]	≤14:0	16:0	18:0	18:1	18:2	≥20:0
Content (% w.t.)	0.3	5.8	1.3	73.9	17.6	1.1

[a]: n, number of carbon atoms in fatty acids; m, number of C=C double bonds in fatty acids

e.g. 18:1: a fatty acid with 18 carbon atoms and one C=C double bond

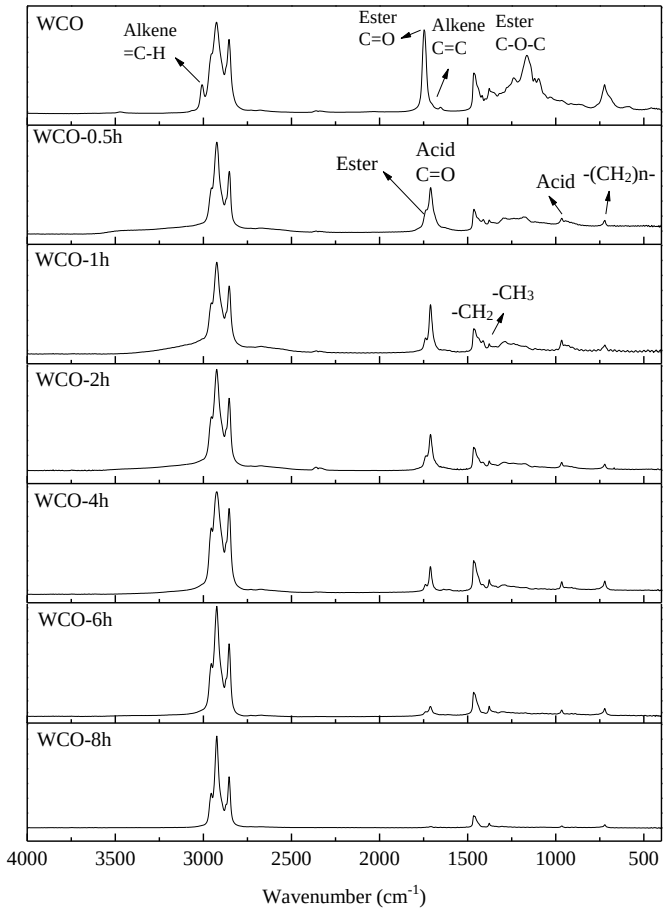

Figure 11.1 FTIR spectra of original and hydrotreated WCO (375 ℃)

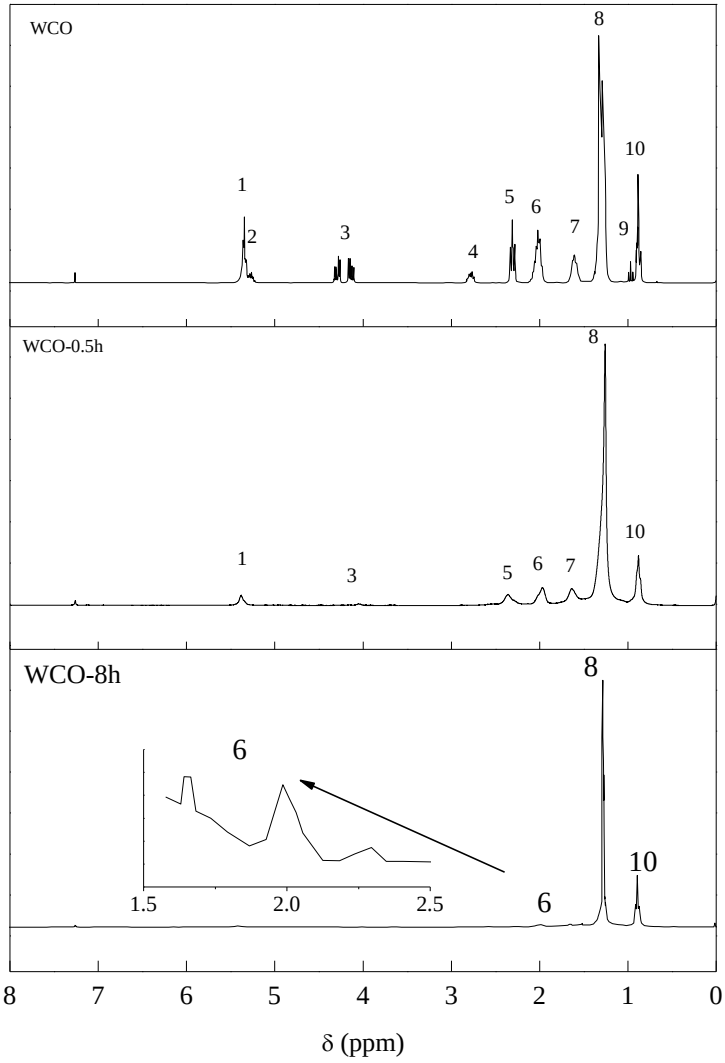

Figure 11.2 H-NMR spectra for original and hydrotreated WCO (375 ℃)
Peaks 1-10 (**H** in bold): 1. C**H**=CH, 2. C**H**-OCOR, 3. C$\mathbf{H_2}$-OCOR, 4. CH=CH-C$\mathbf{H_2}$-CH=CH, 5. C$\mathbf{H_2}$-COOH, 6. C$\mathbf{H_2}$-CH=CH, 7. C$\mathbf{H_2}$-CH_2COOH, 8. $(C\mathbf{H_2})_n$, 9. CH=CH-CH_2-C$\mathbf{H_3}$, 10. $CH_2CH_2CH_2$-C$\mathbf{H_3}$ [217]

The waste cooking oil was hydrotreated in a batch autoclave reactor, allowing sampling at different time intervals during the hydrotreating reaction. Due to small amounts of sampling (1.0 g/sample), the effect of sampling is reasonably assumed to be negligible to the hydrotreating reaction. The reactor was oxidized before each hydrotreating test in order to minimize the influence of the reactor wall. For comparison purpose, a blank experiment (without catalyst) was carried out under the same hydrotreating condition at 375 ℃. Table 11.1 shows low glycerides and oxygen conversions compared to the situation with catalyst. Therefore, the thermal effect was not considered in the kinetics studies.

The variation of glycerides and fatty acids along with reaction is identified by the FTIR and NMR as shown in Figure 11.1 and Figure 11.2. The sharp FTIR peak centered at 1740 cm^{-1} - representing esters in WCO- noticeably diminishes and shifts to 1711 cm^{-1}, a characteristic peak of fatty acids, after half an hour of hydrotreatment. The peaks centered at 1163 cm^{-1} standing for C-O-C of esters also dramatically decreases (Figure 11.1). The peaks at 1711 cm^{-1} and 965 cm^{-1} characterizing the absorption of fatty acids weaken with the reaction until disappearing after 8 hours of hydrotreating. In NMR spectra, peaks 2 and 3 representing protons in ester group of triglycerides vanish in half an hour and peaks 5 and 7 assigned to the protons on the acyl chains associated with carboxylic group diminishes and finally disappears at 8 h. These variations along the reaction process are further illustrated in Figure 11.3. It is seen that triglycerides are quickly decomposed to fatty acids in the initial reaction, and then the decomposition rate slows down gradually. Within the first half an hour of the reaction, more than 70% of

triglycerides are converted to fatty acids. Correspondingly, the acid number of the hydrotreated products increase abruptly from 0.65 of the feed WCO to 110 mg KOH/g oil when a majority of triglycerides are decomposed, this value then steadily declines to a minimum at the end of the reaction (Figure 11.3). This confirms that fatty acids are intermediate products of de-esterification of triglycerides. Fatty acids are the main cause of the acidity of the WCO and hydrotreated products; this finding is consistent with the literature [9].

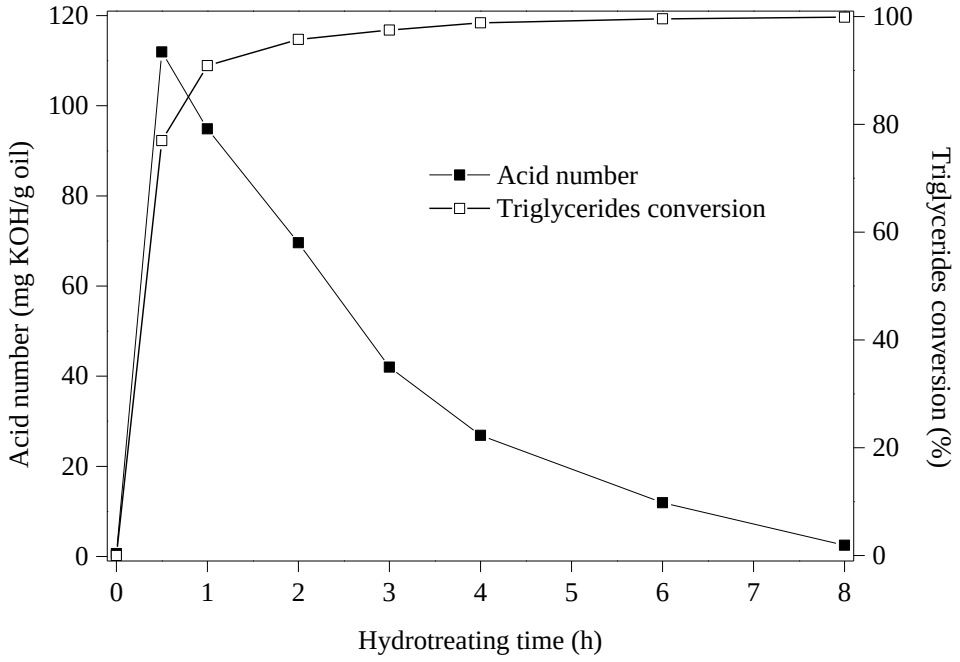

Figure 11.3 Acid number and triglycerides conversion (375 ℃)

The WCO contains even-numbered-carbon-atom acids only as discussed previously and shown in Table 11.1. After hydrotreatment, both odd- and even-numbered-carbon-atom hydrocarbons can be observed in the liquid hydrotreated products. Figure 11.4 shows the distribution of hydrocarbons in the liquid products at different hydrotreating times. Hydrocarbons with odd-numbered-carbon-atoms appear at higher concentrations than the

even-numbered-carbon-atom counterparts. In particular, hydrocarbons, C_{17}, reach approximately 40% in the final liquid product. Generation of odd-numbered-carbon-atom hydrocarbons suggests the existence of decarbonization reaction.

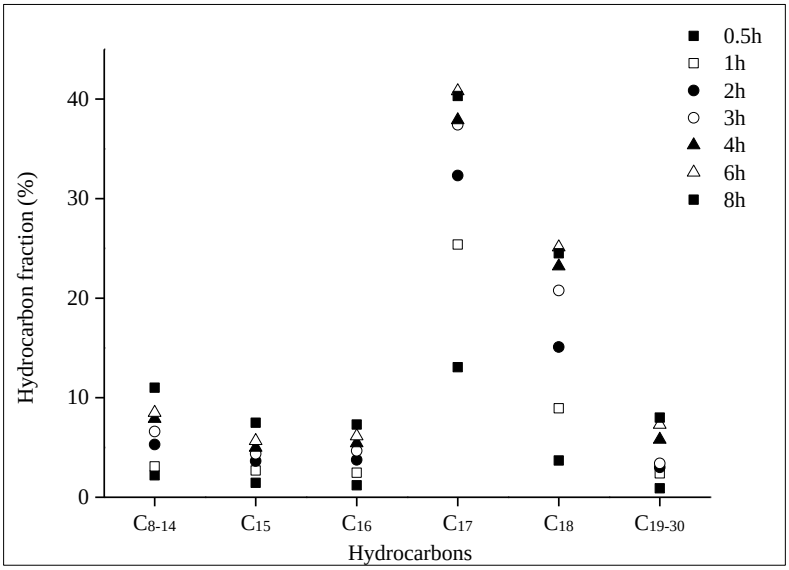

Figure 11.4 Hydrocarbon distribution at different hydrotreating times (375 ℃)

In comparison with the feed WCO (Table 11.1), the hydrotreated products have a wider range of hydrocarbons and the distribution becomes more diversified with hydrotreating time (Figure 11.4). Hydrocarbons lighter than C_{14} increase from approximate 0.3 wt% initially to 2.2 wt% in the liquid product after only half an hour of hydrotreatment. A detailed comparison was made between WCO feed and hydrotreated WCO at the completion of the reaction (Figure 11.5). A decrease of C_{17} and C_{18} is clearly seen and a corresponding increase of other components can also be seen. 27% of C_{17} and C_{18} is converted to lighter hydrocarbons, of which 11% falls in the range of C_8 and C_{14}, 9% between C_{15} and C_{16}, and 7% between C_{19} and C_{30}. The lighter alkanes are derived due to hydrocracking, whereas the long-chain hydrocarbons are the products of polymerization.

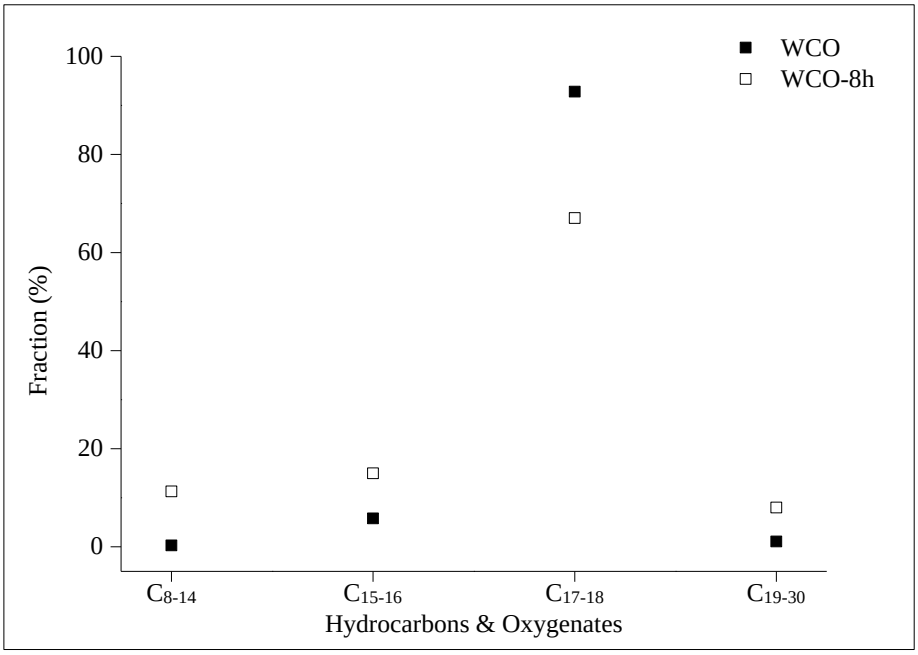

Figure 11.5 Comparison of different carbon-number compounds (hydrocarbons and oxygenates)
WCO: triglycerides, WCO-8h: hydrocarbon and fatty acids (375 ℃)

The hydrogenation reaction can be evidenced by the fatty acid distribution. The WCO feed contains high contents of unsaturated fatty acids including 17.6% linoleic (18:2) and 73.9% linolenic acids (18:1) (Table 11.1). In Figure 11.6, free $C_{18}^{==}$ (18:2) fatty acids are not detected in the hydrotreated products, indicating that all the linoleic acids have been hydrogenated to linolenic ($C_{18}^{=}$) or saturated acids (C_{18}) before the hydrolysis of triglycerides. In addition, linolenic acids also decrease dramatically with reaction time from 37% after 0.5 hours of reaction to 10% after 2 hour of reaction. Saturated acids (C_{18}) increased from 1.3% in the feed to the highest value 19% at 2 h. The increment of saturated acids is attributed to the saturation of linoleic and linolenic acids. The hydrogenation reaction can be further evidenced by the FTIR and ^{1}H-NMR spectra

shown in Figure 11.1 and Figure 11.2. Disappearance of the FTIR peaks at 3007.3 cm^{-1} (assigned to =C-H) and at 1654 cm^{-1} (assigned to C=C) demonstrates hydrogenation of double bonds. Similarly, saturation of double bonds is also seen from the decreased or vanished peaks of 1, 4, 6 and 9 in NMR spectra. The disappearance of peak 4, specifically, after 30 minutes implies the quick saturation of linoleic compounds (Figure 11.2). Note that a small peak at chemical shift of 2.00 observed in Figure 11.2 suggests the presence of unsaturated acyl chain after 8 h, indicating an incomplete saturation. In addition, –CH is not detected in the product, which suggests a nearly pure straight-chain structure (Figure 11.2).

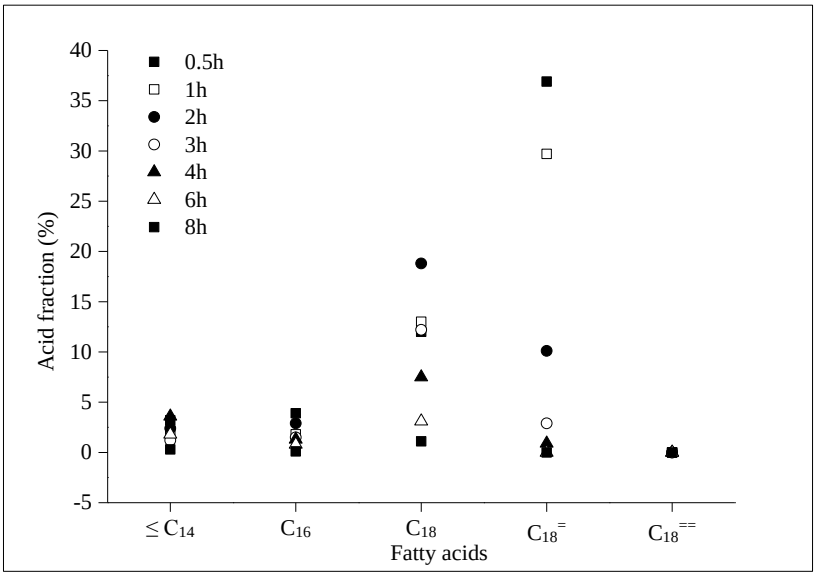

Figure 11.6 Fatty acids distribution at different hydrotreating times (375 ℃)
C_{14}, C_{16}, C_{18}: saturated fatty acids; $C_{18}^{=}$: with one C=C double bond; $C_{18}^{==}$: with two C=C double bonds

Figure 11.7 shows the instant rate constants of the generation of C_{17}, C_{18}. Equation 11.1 defines the instant rate constants at reaction time t. It is noticed that the rate constant k_t of

C_{17} decreases while the rate constant for C_{18} is kept constant during the reaction. It indicates that the catalyst deactivates over the HDC activity only.

$$\frac{dC_{Cn,t}}{dt} = k_t C_{a,t} \qquad \text{Equation 11.1}$$

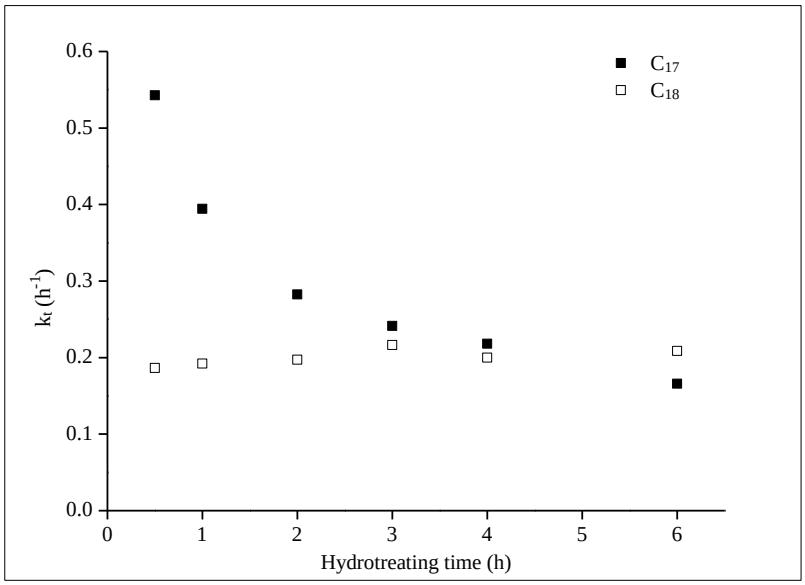

Figure 11.7 Instant rate constants (k) variation during the reaction (375 ℃)

11.2.2 Kinetics studies

11.2.2.1 Sketched reaction routes and deactivation of catalyst

To understand the reaction pathways of oxygen removal process, a kinetic model of hydrotreatment is proposed on the basis of the findings described in Section 3.2. The simplified hydrotreating pathways are presented in Scheme 11.1. Decomposition of glycerides to fatty acids is a very fast reaction and its rate constant is denoted as k_1. Glycerol, a by-product of the decomposition, can be quickly converted to propane and

propene over the catalyst, which is confirmed by Figure 11.8. Thus, decomposition of glycerides to fatty acids is assumed to be an irreversible reaction. Fatty acids are then further transferred to hydrocarbons through different routes since CO, CO_2, and H_2O are detected in gas and liquid products. Given sufficient hydrogen gas, the reaction that fatty acids are hydrodeoxygenated to C_{18} is assumed to be pseudo-first-order-kinetics. Its reverse reaction is neglected due to the fact that low oxygenation activity of MoS_2 and sufficient hydrogen atmosphere. The HDC reaction is also considered as an irreversible reaction to be consistent with the previous reports [218, 219]. The rate constants for HDO and HDC products are denoted as k_2 and k_3, respectively. Deactivation of catalyst is taken into account for both HDO and HDC reactions. A commonly used second-order decay law is applied on both routes. The corresponding specific decay constants are denoted as k_{d1} and $k_{d2.}$

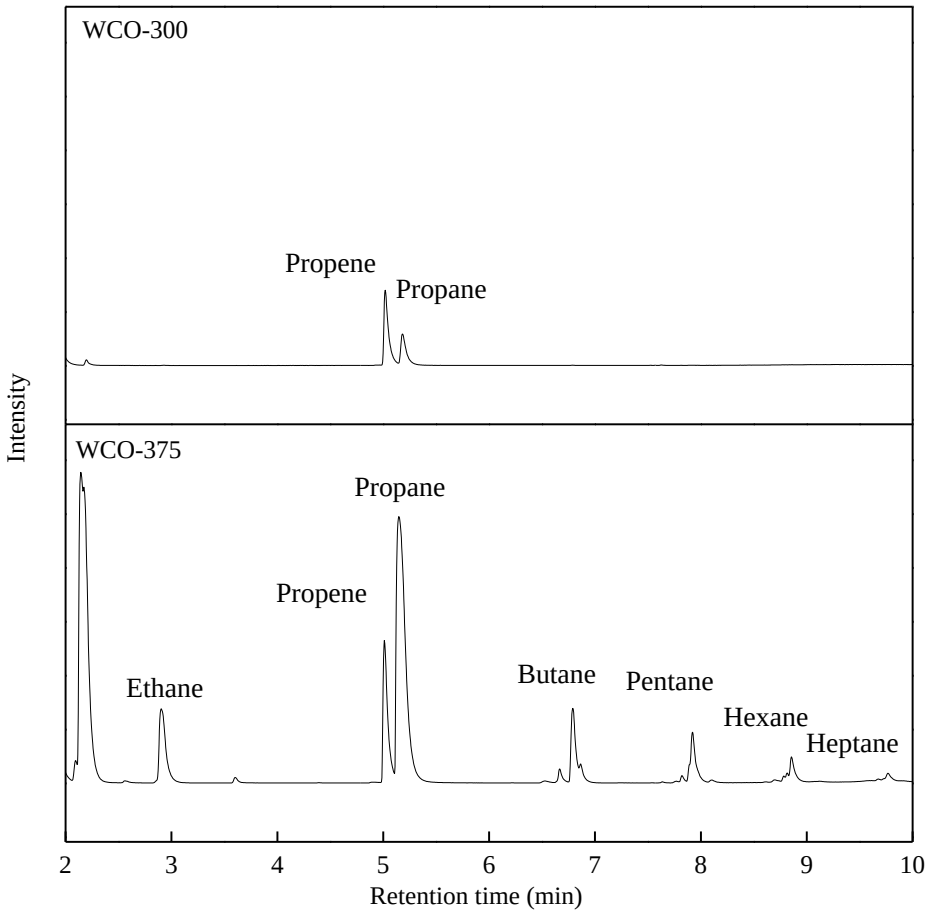

Figure 11.8 Organic gas analysis of hydrotreated WCO (8 hours)

Equation 11.2-Equation 11.7 show mass balance, reaction kinetics, and catalyst deactivation. The Runge-Kutta method and trust-region-reflective optimization algorithm with least squares as objective function were applied, and the confidence intervals of the rate constants were estimated under 0.95 confidence level based on an asymptotic normal distribution. The resulted k values with their confidence intervals are shown at their corresponding reaction routes. For an instant, rate constant k is denoted as $k = m \pm \Delta$, where m is the estimated value of k and Δ is the upper bound of the confidence interval,

that is, 95% possibility of the true k value falls in between m - Δ and m + Δ. It is seen that the estimation of rate constants is reliable due to low deviations of the estimates.

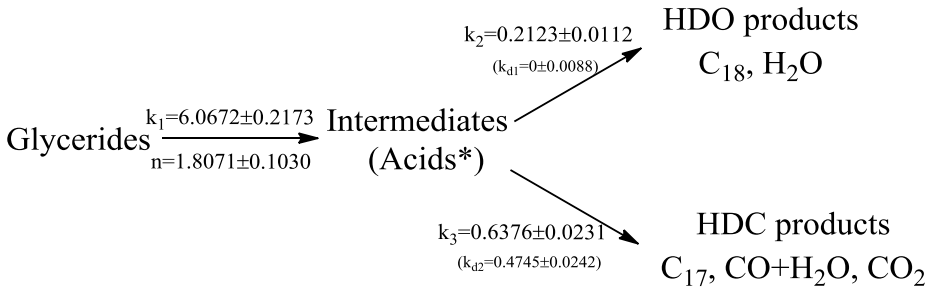

Scheme 11.1 Simplified reaction pathways

* A small amount of other oxygenate intermediates are detected.

$$\frac{dc_g}{dt} = -k_1 c_g^n \qquad \text{Equation 11.2}$$

$$\frac{dc_a}{dt} = k_1 c_g^n - a_1 k_2 c_a - a_2 k_3 c_a \qquad \text{Equation 11.3}$$

$$\frac{dc_{C_{18}}}{dt} = a_1 k_2 c_a \qquad \text{Equation 11.4}$$

$$\frac{dc_{C_{17}}}{dt} = a_2 k_3 c_a \qquad \text{Equation 11.5}$$

$$\frac{da_1}{dt} = k_{d1} a_1^2 \qquad \text{Equation 11.6}$$

$$\frac{da_2}{dt} = k_{d2}\, a_2^2 \qquad \text{Equation 11.7}$$

where c_g represents the mass fraction of total glycerides (mono-, di- tri-).; c_a stands for the total concentration of intermediate fatty acids; c_{C18} and c_{C17} are the total mass fraction of HDO and HDC produced hydrocarbons, respectively. a_1 and a_2 showing the catalyst activities of HDO and HDC, are defined as the ratio of a reaction rate at t=t to the initial reaction rate at t=0. Catalyst deactivation occurs when the value of *a* is less than 1.

Comparison of the estimated results and the experimental data is shown in Figure 11.9. R^2 is calculated by Equation 11.8, where c_{exp} and c_{est} stand for the experimental data and estimated values, respectively. A good agreement can be seen.

$$R^2 = 1 - \frac{(c_{exp} - c_{est})^2}{(c_{exp} - \bar{c}_{exp})^2} \qquad \text{Equation 11.8}$$

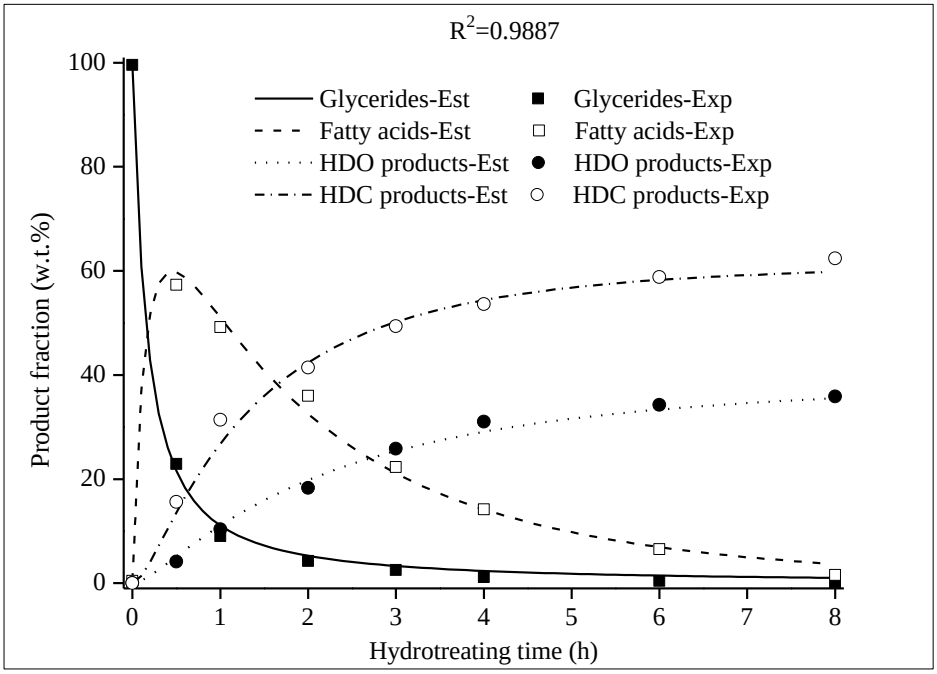

Figure 11.9 Comparison of experimental data and modeling results of sketched reaction routes (375 ℃)
Est: estimates; Exp: experimental data.

From Scheme 11.1, one may note that HDC reaction is the predominant reaction pathway because the rate constant of HDC is 3 times as high as that of HDO. The total deactivation rate (TDR) of catalysts can be revealed by the sum of k_{d1} and k_{d2}, which

leads to a remarkable 80% activity lost by the end of the reaction. A possible reason may be gradual loss of sulfur on the catalyst surface, which is evident by the significant increase of sulfur content in the hydrotreated products (140 ppm comparing to the feed 30 ppm, about 3% of the catalyst sulfur). Comparing k_{d1} to k_{d2} suggests that the catalyst deactivation is primarily contributed by the HDC reaction (k_{d2}=0.4745) while the HDO activity is well maintained during the entire reaction course (k_{d1}=0). It indicates a different reaction mechanism between the HDO and the HDC over catalyst CoMoS. HDO takes place at the active sites that are unsaturated and oxygen is removed by the sulfur vacancy on the catalyst surface. HDC involves the steps occurring on the sulfur saturated sites. Sulfur is continuously lost during the reaction, which lowers the sulfur saturated sites and thus reaction rates of HDC are reduced significantly. On the other hand, the activity of HDO is retained due to maintenance of a similar amount of active sites, which is a combined result of new vacancy sites created by hydrogen reduction and loss of active sites due to oxygen occupation. This is consistent with the report given by D. Kubicka and J. Horacek [220].

11.2.2.2 Detailed kinetics for the oxygen elimination process

Possible reaction routes for the deoxygenation of C_{18} fatty acid are proposed in Diagram 11.1. Prior to the simulation, the significance of each reaction pathway was equally treated and dominant reaction pathways were determined by the simulation results. The Runge-Kutta method was used in the simulation, the same algorithms used for derivation of Scheme 11.1. Confidence intervals for each k were estimated at confidence level of 0.95.

In Diagram 11.1, C_{18} and C_{17} hydrocarbons are the two main components of the final liquid product, while aldehydes and alcohols are intermediates. C_{17} hydrocarbons are the products of HDC reactions through different reaction pathways. Saturated hydrocarbon C_{17} can either be produced from fatty acid through decarboxylation with by-product of CO_2 [12, 207] or from aldehyde via decarbonylation with CO as by-product [218]. Unsaturated C_{17} is derived directly from fatty acid with by-products of H_2O and CO [69] or from aldehydes through decarbonylation reaction with by-product of CO [221]. The C_{18} hydrocarbons are obtained via the hydrodeoxygenation, primarily from alcohols with H_2O as the by-product [64, 70]. For intermediates, aldehydes were reduced from acids, and alcohols can either be formed by further reduction of aldehydes or directly from fatty acids. As seen in Diagram 11.1, deviations of the estimates are low, indicating reliable results. The estimated results are compared to the experimental data as shown in Figure 11.10.

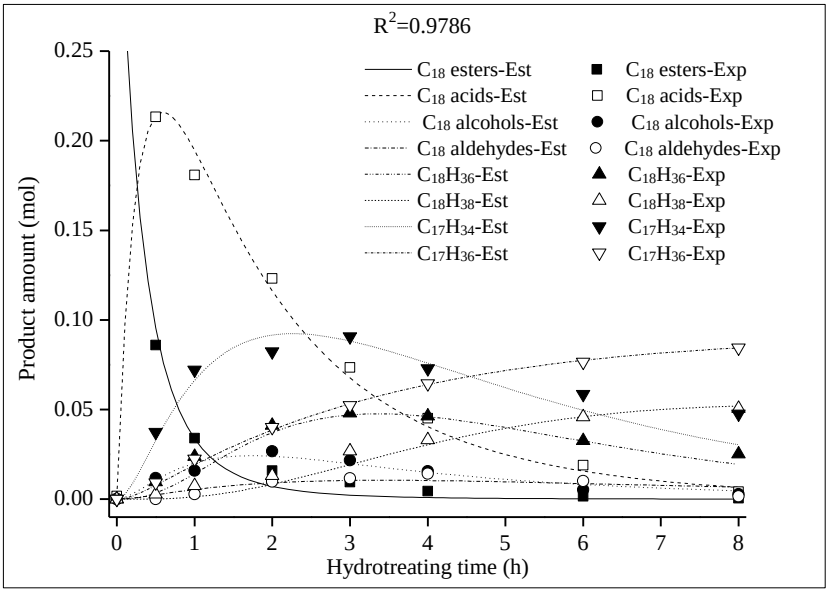

Figure 11.10 Comparison of experimental and modeling data of detailed kinetics (375 ℃) Est: estimates; Exp: experimental data.

The simulation results suggest that direct decarbonylation is a main pathway, due to the highest rate constant (k_2 =0.502). k_1 (0.116) is significantly lower than k_2, indicating that direct decarbonylation primarily produces C_{17}-alkenes and CO. The final product, C_{17}-alkanes is resulted from the hydrogenation of C_{17}-alkenes. This can be evidenced by the ratio CO to CO_2 of 10:1. This finding supports previous reports, in which hydrogen enhanced the decarbonylation selectivity over decarboxylation [222].

Reduction of fatty acids is carried out through a series of reactions. The simulation result indicates that direct deoxygenation of acids to produce alcohol is a key pathway since k_4 (0.214) is approximately 5 folds of k_3 (0.041). This is consistent with the experimental results shown in Figure 11.10, where the concentration of alcohol is much higher than that of aldehydes. A similar mechanism was demonstrated with metal ion/oxygen vacancy created in the reducible oxide in the presence of platinum [223]. However, there is an argument that the formation of alcohol is essentially correlated to decomposition of aldehydes [218]. In this work, catalyst CoMoS was used. The unsaturated sulfur vacancies on CoMoS catalysts have a strong capability to capture oxygen atoms from carbon-oxygen double bonds and the double bonds can be fully broken to form alcohols. It supports the simulation result. With a high dehydration ability (k_8, 1.267), the reduction of fatty acids is the limiting step in the HDO pathway.

After the kinetics analysis, the main deoxygenation reaction routes are summarized in Scheme 11.2. Three main routes are identified, direct decarbonylation and decarboxylation from fatty acids and hydrodeoxygenation to generate alcohols. The

deoxygenation rate constants follow in the order of decarbonylation> hydrodeoxygenation>decarboxylation.

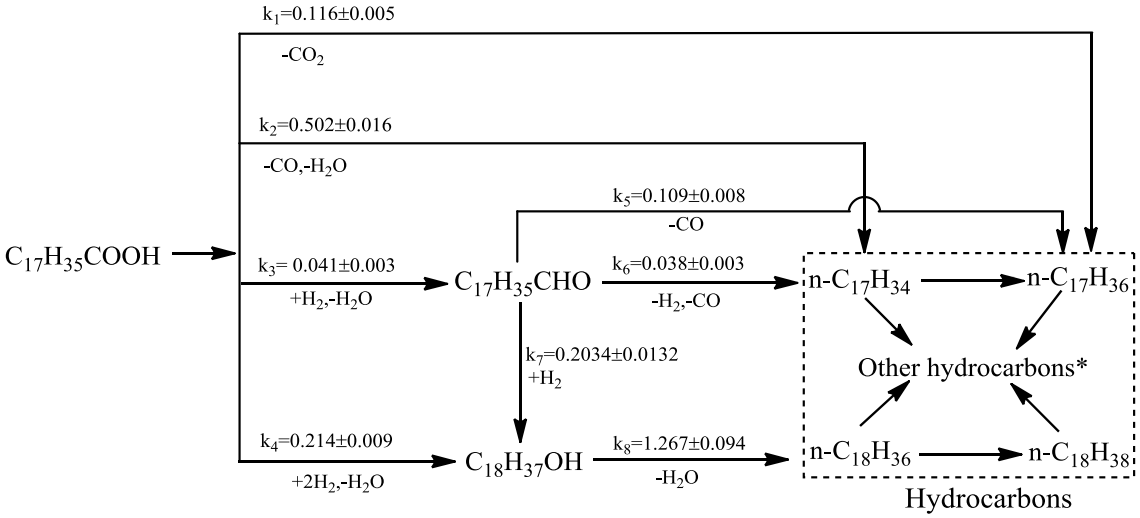

Diagram 11.1 Proposed reaction routes for the consumption of carboxylic acid
*Other hydrocarbons include products from hydrocracking, polymerization, and the cyclization.
The reactants H_2 and by-products are listed under the arrow.

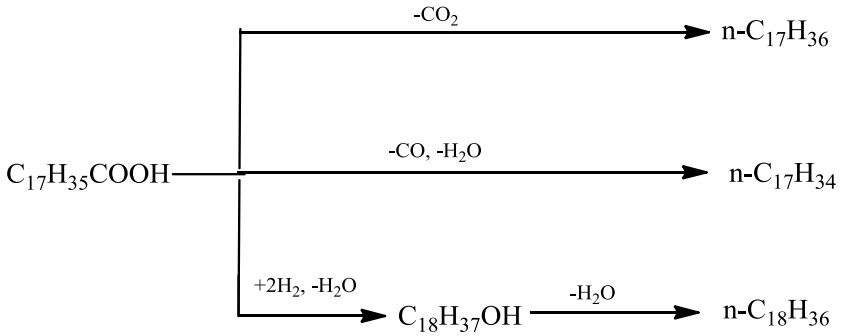

Scheme 11.2 Main deoxygenation reaction routes

11.2.2.3 Hydrogenation, hydrocracking, polymerization, and cyclization

Besides oxygen elimination reactions, hydrogenation also occurs so that the unsaturated bonds become saturated. The degree of hydrogenation is revealed by the degree of unsaturation, i.e. the number of double bonds (NDB) in the products. For component i, NDB_i can be calculated by Equation 11.9 [224], in which C is the number of carbon, and H is the number of hydrogen. The total NDB is expressed as the sum of NDB of each component i based on 1 mole of feed oil (Equation 11.10). Figure 11.11 shows the number of double bonds (NDB) and H/C atomic ratio varying with the reaction. It is seen that the NDB decreases with increasing reaction time, indicating a continuous saturation of double bonds. A quick drop from 2.1 to 1.5 occurs in the first half an hour of reaction and then it slows down. A corresponding observation is shown for the variation of H/C atomic ratio. The H/C ratio increases from 1.81 to 1.89 in the first 0.5 hour and reaches 2.04 after 8 hours of reaction. The dramatic decrease of NDB at the beginning of reaction is caused by a rapid hydrogenation of the double bonds of unsaturated fatty acids. This decrease may be attributed to the saturation of the C=C generated during the reaction.

$$NDB_i = C + 1 - \frac{H}{2} \quad i: hydrocarbons\ and\ oxygenates \qquad \text{Equation 11.9}$$

$$NDB = \frac{\sum_{i=1,2\ldots n}^{n} NDB_i \times n_i}{n_{tot,0}} \quad n_{tot,0}: initial\ feed\ moles \qquad \text{Equation 11.10}$$

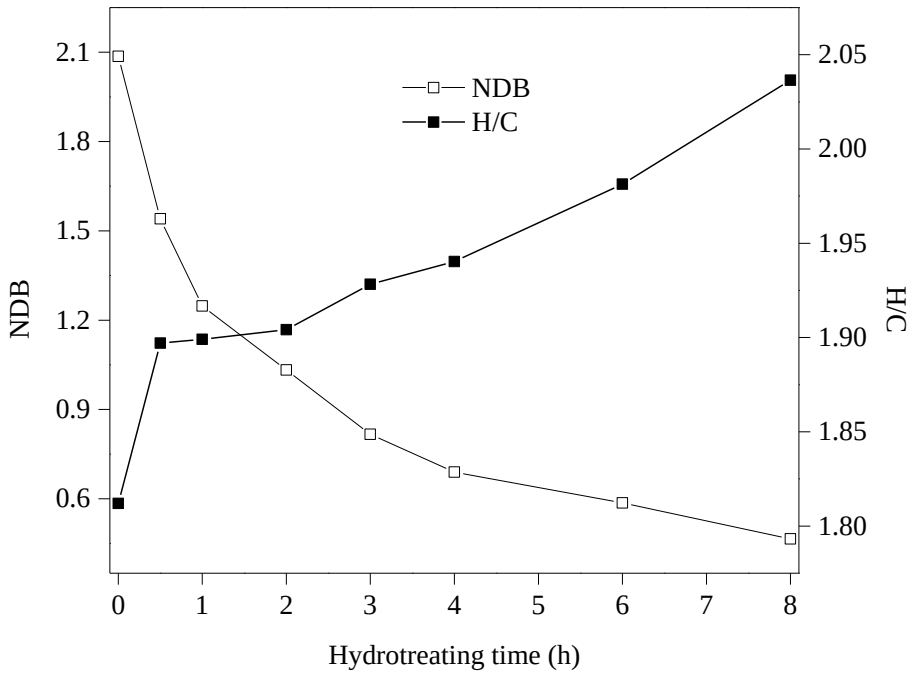

Figure 11.11 The number of double bonds (NDB) and H/C atomic ratio (375 ℃)

Hydrocracking and polymerization are also observed, which are verified by the diversified hydrocarbons in the final liquid products (Figure 11.4, Figure 11.5) Hydrocracking degree (HCD) and polymerization degree (PMD) are defined as the number of C-C bond going through breakage and formation, respectively (Equation 11.11, Equation 11.12). In the Equations, the number of C-C bond breakage based on 1 unit weight is calculated as the ratio of moles of increased light molecules (carbon number lower than 17) to moles of cracked C_{17} and C_{18} minus 1. The actual mole of C-C breakage is the value multiplied by the total hydrocracking conversion of $C_{17\text{-}18}$ to $C_{8\text{-}16}$($x_{17,18\rightarrow 8\text{-}16}$); the PMD is calculated similarly. The HCD and PMD are plotted in Figure 11.12. It is shown that both values increase with reaction time, which indicates that

hydrocracking and polymerization proceed throughout the entire reaction. Comparing the HCD and PMD, it is noticed that hydrocracking is more intense than the polymerization.

$$Hydrocracking\,\deg ree\,(HCD) = \left(\frac{\sum_i \Delta n_{i(i=8,9...16)}}{\Delta_{HCD}(n_{17}+n_{18})} - 1\right) \times x_{17,18 \to 8-16} \qquad \text{Equation 11.11}$$

$$Polymerization\,\deg ree\,(PMD) = \left(\frac{\Delta_{PMD}(n_{17}+n_{18})}{\sum_j \Delta n_{j(j=19,20...30)}} - 1\right) \times x_{17,18 \to 19-30} \qquad \text{Equation 11.12}$$

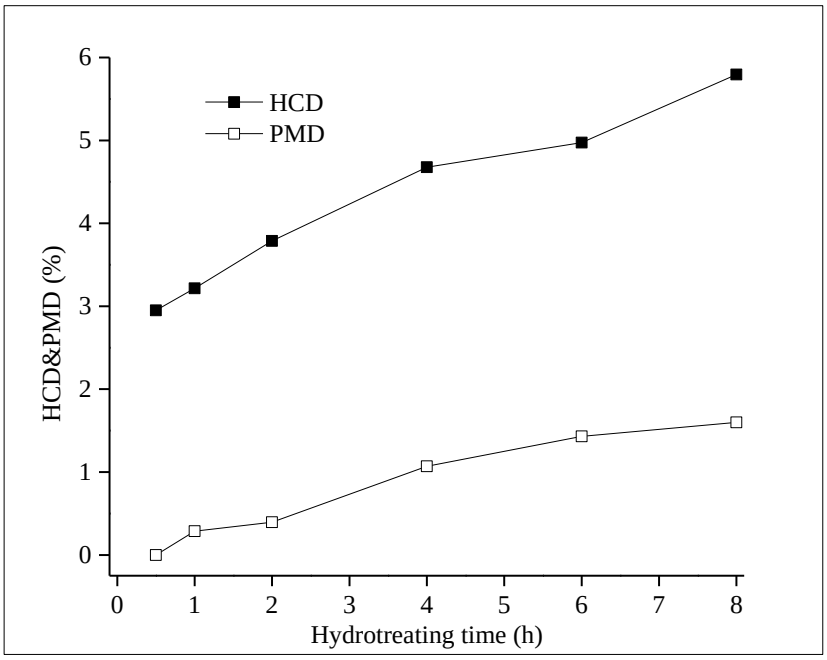

Figure 11.12 Hydrocracking and polymerization degree (HCD&PMD) (375 ℃)

Cyclization reactions are also observed by the formation of cyclohexane and cyclodecane, which are the two main cycloalkanes formed. As seen from Figure 11.13, the selectivity of cycloalkanes increases from 5% to 24% and n-alkane from 20% to 48% during the reaction, which compensates the decrease of selectivity of alkenes. The results suggest that cyclization is more common than the isomerization of alkenes rather than the

de-hydrogenation of n-alkanes. The high accumulation of alkenes facilitates the cyclization reaction. It is worth noting that aromatics are not detected in this work, which indicates that the reaction ceases at the production of cycloalkanes without further de-hydrogenation.

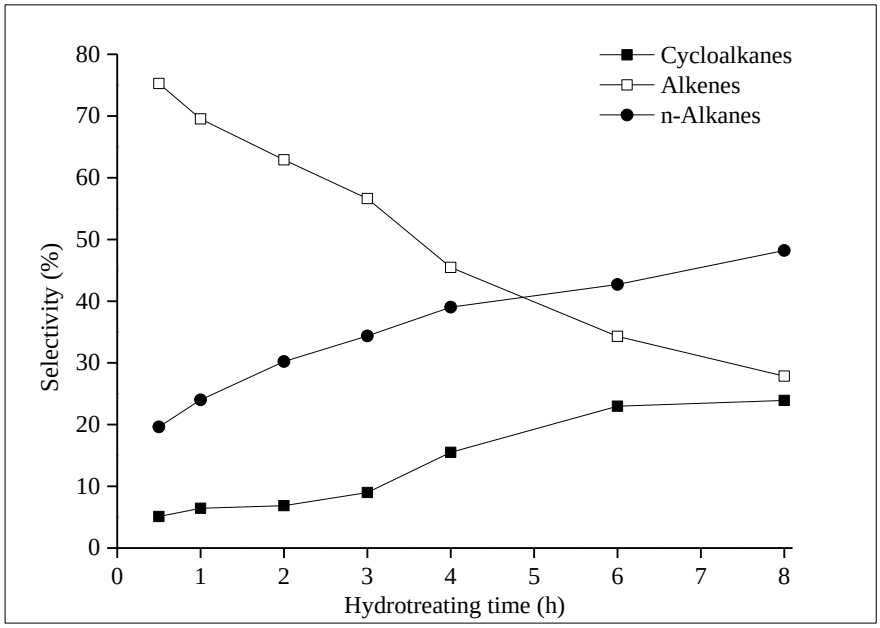

Figure 11.13 Selectivity of different type of hydrocarbons (375 ℃)

11.2.3 Comparison of the performances of supported and unsupported catalysts for HDO

The supported Co/NiMoS with Al_2O_3 have been widely used in the industry and laboratory settings. With supports, catalysts demonstrate significant difference on hydrotreating performance and the kinetics can be altered. In this work, the hydrotreating results with unsupported CoMoS were compared with other research using supported catalysts. The product distribution shows that an unsupported catalyst has a significantly lower C_{18}/C_{17} ratio (0.6) than that of supported catalysts (Table 11.2).

Mathematically, the lower C_{18}/C_{17} may be attributed to either the decrease of C_{18} or the increase of C_{17}. However, there is lack of evidence to support the hypothesis that unsupported catalyst tends to promote the decarbonation process. Our results show that the decarbonation mainly occurred on the sulfur saturated active sites on Co-Mo catalysts and it suffers from catalyst deactivation. The discussion may indicate that production of C_{18} is low over unsupported catalyst due to lack of acidity. This is consistent with the research conducted by Ryymin et al., which stated that large amount of Lewis acid sites on Al_2O_3 supports can benefit the hydrogenation and dehydration reactions [12]. In addition, comparing to the performance of supported catalysts, higher hydrocracking and polymerization are noticed when dealing with unsupported catalysts [160, 162] , as indicated by HCD and PMD values (Table 11.2). Due to the lack of acidic support, lower hydrocracking is expected to obtain. The higher C-C breakage and formation may be due to the high reaction temperature. Therefore, a support with Lewis acid sites may play an

important role in the selectivity for the hydrodeoxygenation pathways and promoting the final product quality.

Table 11.2 Comparison of HDO/HDC product ratios on supported and unsupported catalyst

Feed oils	Catalysts	Hydrotreating temperature (℃)	C_n/C_{n-1} ratio	HYD (%)	HCD /PMD (%)	ISO (Branched)
Methyl heptanoate [218]	$CoMoS/Al_2O_3$ $NiMoS/Al_2O_3$	250	1.7-2.0	14.1 80.6	---	---
Rapeseed oil [160]	$NiMoS/Al_2O_3$	360	2.1	100	1.2/1.4	13.4
Sunflower oil [9]	$NiMoS/Al_2O_3$	300-450	1.0-2.3	100	2-22/--	4-12
Waste cooking oil [162]	$CoMoS/B_2O_3$-Al_2O_3 $NiMoS/B_2O_3$-Al_2O_3	350	1.5-3 1.5-4	--- 99.0	--- 4.3[a]	--- 7.5
Waste cooking oil	CoMoS	375	0.6	63.5	11.1/8.2	<0.1

[a]: Sum of HCD and PMD.
Hydrogenation: HYD=alkanes/ (alkenes+alkanes) ×100%
Hydrocracking: HCD= cracked hydrocarbons/total hydrocarbons ×100%
Polymerization: PMD= polymerized hydrocarbons/total hydrocarbons ×100%
Isomerization: ISO=branched hydrocarbons/total hydrocarbons ×100%

11.2.4 Temperature effect on reaction degree

Temperature is an important factor influencing the overall reaction rate. In this study, experiments were conducted at three different temperatures, 300, 340 and 375 ℃. The FTIR spectra for original and hydrotreated WCO are shown in Figure 11.14. At the lowest temperature of 300 ℃, the main products are mono-/di-glycerides and carboxylic acid converted from triglyceride, as evidenced by the large characteristic peaks of ester and fatty acid at 1742 and 1711 cm^{-1}. A brown wax, as oppose to a liquid product, was

produced when the reactor was cooled down to room temperature (20 ℃). Propane and propene are detected in gas phase, which are obtained from the hydrotreating of the resultant glycerol through de-esterification (Figure 11.8). At the highest temperature, 375 ℃, fatty acid triglycerides in WCO are almost fully converted into hydrocarbons. The characteristic peaks of esters at 1742 and 1170 cm^{-1} disappear, only the peaks standing for C-H bond in alkanes are observed. The main product is a mixture of alkanes and alkenes with small amount of acid (<1%).

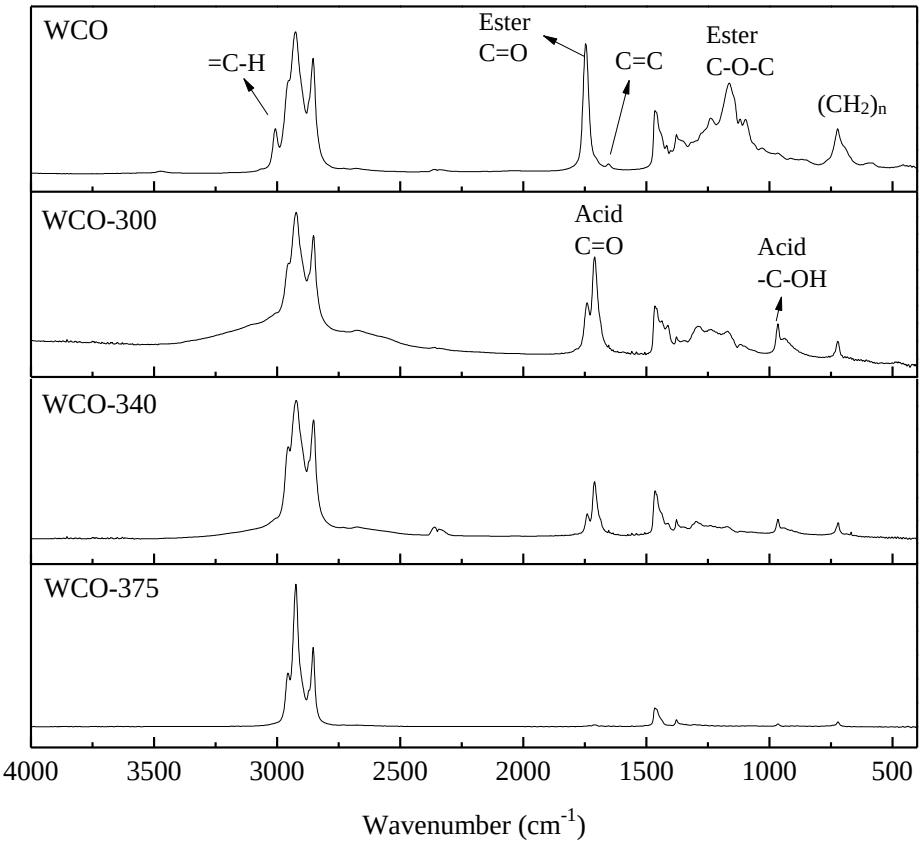

Figure 11.14 FTIR spectra of original and hydrotreated WCO (8 hours)

Gas chromatography and elemental analysis were used to determine product distributions and oxygen conversion rate at all three temperatures (Figure 11.15). At 300 ℃, 67.6% of

glycerides are consumed to form fatty acids with 14% hydrocarbons generated, which implies that the deoxygenation from fatty acids are the rate limiting step and degradation of triglycerides is the predominant reaction at this temperature. When increasing temperature to 340 ℃, hydrodeoxygenation and hydrodecarbonylation /decarboxylation take place to a larger extent, indicated from the dramatic increase of oxygen conversion. At 375 ℃, the oxygen conversion approached 100%, which indicates that hydrocarbon is generated quickly compared to the performance at the lower temperatures. However, lower diesel yields are produced at higher temperatures; the yield of $C_{15\text{-}18}$ upon total hydrocarbon is 81%, comparing to 94.6% and 94.1% for 300 ℃ and 340 ℃, respectively (Table 11.3). Increased paraffin selectivity and H/C atomic ratio also indicate that temperature can facilitate hydrogenation reactions (Table 11.3).

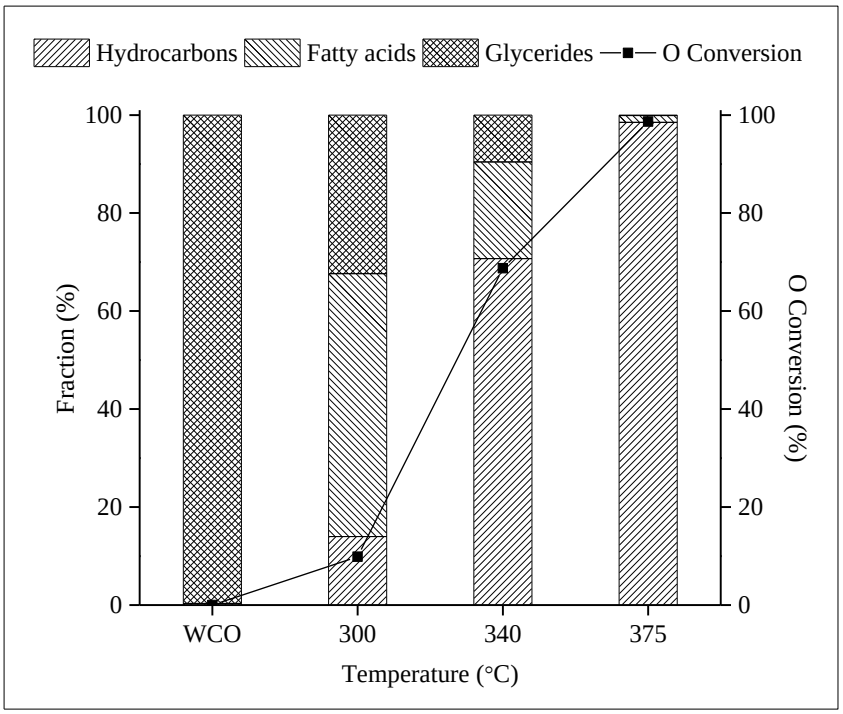

Figure 11.15 Temperature effect on product distribution (8 hours)

Table 11.3 Properties and hydrocarbon distribution of original and hydrotreated WCO at different temperatures (8 hours)

	WCO	WCO-300	WCO-340	WCO-375
Density (g/cm^3)	0.9184	0.8935	0.8661	0.8138
C_{18}/C_{17} mass ratio	---	0.70	0.64	0.62
C_{8-14} selectivity (%)	---	2.4	3.5	11.1
C_{15-18} selectivity (%)	---	94.6	94.1	81.0
C_{19-30} selectivity (%)	---	2.0	2.4	7.9
Paraffin selectivity (%)	---	18.5	38.4	65.0
C/H atomic ratio	1.81	1.93	1.98	2.04

All the density was calibrated to the value at 30 ℃

Kinetics modeling for deoxygenation reactions at 300 and 340 ℃ was performed according to Scheme 11.2. The same reaction order and deactivation constants were assumed as 375 ℃ for better comparison. The estimated rate constants are shown in Table 11.4. For all three temperatures, the rate constant for decomposition of glycerides (k_1) is much higher than the deoxygenation steps (k_2 and k_3), indicating that deoxygenation is rate-limiting step for all the investigated temperatures. In addition, similar to 375 ℃, HDC is also the dominant deoxygenation route at 300 and 340 ℃, as seen from the larger k_3. With increase in reaction temperature, all the rate constants are increased. The rate constant for HDO pathway (k_2) increases by a factor of 8.0 from 300 to 375 ℃, whereas the rate constant for HDC route (k_3) increases by a slightly higher factor of 8.5 in the same temperature range. This indicates the effect of temperature is similar on HDO and HDC pathways over this unsupported CoMoS, while HDC is slightly more favorable at higher temperature.

Table 11.4 Estimated parameters at different temperatures

Parameters	WCO-300	WCO-340	WCO-375
k_1	0.301 ± 0.013	1.563 ± 0.060	6.067 ± 0.217
k_2	0.027 ± 0.002	0.103 ± 0.007	0.212 ± 0.011
k_3	0.075 ± 0.006	0.301 ± 0.020	0.638 ± 0.023

11.3 Conclusions

Hydrodeoxygenation of waste cooking oil on unsupported CoMoS catalysts was investigated in a batch reactor. Analysis of WCO and hydrotreated products shows that the oxygen containing compounds (glycerides) are mainly converted to C_{17} and C_{18} hydrocarbons, while acids, aldehydes and alcohols are identified as major intermediates. Accompanying the deoxygenation reaction, side reactions, such as hydrogenation, hydrocracking, polymerization, and cyclization also take place.

Reaction schemes are proposed on the deoxygenation process according to the kinetic modeling results. The estimation indicates that the total HDC reaction routes (hydrodecarbonylation and decarboxylation) are the predominant pathways to eliminate oxygen, with the rate constant 3 times as high as HDO. Direct hydrodecarbonylation from fatty acids is the main HDC reaction route with the highest rate constant. HDO consists of a series of reactions, transferring fatty acids to aldehydes/alcohols and then to final C_{18} hydrocarbon products. Direct reduction to alcohols from fatty acids is dominant over the pathway from fatty acids to aldehydes, suggesting that alcohols are the more important intermediates than aldehydes for the HDO process. The higher dehydration rate constant indicates that the reduction of fatty acids is the rate limiting step. From a finalized scheme, three main reaction pathways are determined and the order of their rate constants from high to low is decarbonylation of fatty acid, hydrodeoxygenation to produce alcohols, and decarboxylation of fatty acids.

Selective deactivation is observed on the HDC route, with 80% of activity lost in 8 h, while HDO maintains the initial activity during the whole reaction process. The loss in catalyst activity is attributed to the gradual loss of sulfur from the catalyst surface. It indicates that HDC mainly occurs on saturated sites, which is highly related to the sulfur coverage, and HDO happens on the sulfur vacancies.

Based on the product distribution, side reactions of hydrogenation, hydrocracking, polymerization, and cyclization occur continuously along the reaction. Analyzing the results shows that hydrogenation is more intense in the first half an hour since the total number of double bonds decreases dramatically from 2.1 to 1.5. Hydrocracking is more intense than the polymerization as the degree of hydrocracking is 6 times that of polymerization after 8 hours of reaction. Cyclization is more commonly developed from the isomerization of alkenes as oppose to the de-hydrogenation of n-alkanes.

Temperature is another key factor for the reaction rate. At low temperature of 300 ℃, the main products are mono-/di-glycerides and carboxylic acids, indicating insufficient hydrodeoxygenation. At high temperature 375 ℃, fatty acid triglycerides in WCO are almost fully converted into hydrocarbons but with lower diesel selectivity due to a higher hydrocracking and polymerization.

Chapter 12 Conclusions and recommendations

12.1 Conclusions

The preparation of unsupported MoS_2 with high hydrodesulfurization activity and affordable cost is still a challenge. In this thesis, a novel hydrothermal method was successfully established using commercial available Na_2S and MoO_3 as precursors. The effects of ratio of precursors, synthesis temperature, initial temperature, solvents, and promoters on the performance of synthesized catalysts were carefully investigated. Several results were achieved from the analysis of the various characterization techniques, such as XRD, TEM, SEM, XANES, EXAFS, Auto-sorb, TPR, and XPS, etc.

Results show that the acidic medium is essential to the successful synthesis of the catalyst. The ratio of reactants, MoO_3 and Na_2S, is important to the nanocrystalline structure and the catalyst yield. Excess or insufficient MoO_3/Na_2S ratio may result in poor purity of MoS_2 or low yield, respectively. All catalysts synthesized at the proper range of Na_2S/MoO_3 (from 2.5 to 3.75 in the current case), have nanosized structure, large surface area, and high pore volume (mesopores).

Temperature is a key factor for the synthesis of MoS_2 with high catalytic activity by the hydrothermal method. The nucleation and ripening process of formation of crystalline MoS_2 depend on the temperature introduced. There exists a minimum sTemp for the formation of crystalline MoS_2. Lower than the minimum sTemp results in amorphous structure. Increasing sTemp does not alter the lattice structures but change the curvatures and lengths of the slabs. Higher iTemp is beneficial to the fast nucleation, which leads to

shorter slabs and more defects. The curved and shortened slabs formed at higher synthesis temperature (320 and 350 ℃) contributed to higher catalytic activity, due to more exposed active sites. The highest activity (HDS constant: 54.9 $x10^{-5}$ $s^{-1}gcat^{-1}$) was obtained at higher initial temperature (270 °C).

Introducing organic solvent or supercritical heptane into the system can dramatically change the status of the aqueous solution. The results show that the MoS_2 slabs could be bent with the addition of decalin and exhibits higher HDS conversion. Increasing the decalin to water ratio and stirring speed would benefit to form uniform MoS_2 with large curvature angles, thus enhancing the HDS activity. Evaluation results show that the S conversion is increased from 76.37% to 86.97%, when decalin concentration is increased from 0 to 4:1. Supercritical heptane shows a great potential to generate highly curved slabs and substantially gains better HDS performance, with 92.95% S conversion.

Cobalt plays an important role in promoting the HDS performance of MoS_2. With the introduction of cobalt, significantly shorter slabs are observed compared to the unpromoted counterpart. HDS and HDN results indicate that the optimal Co/(Co+Mo) ratio is in the range of 0.3-0.5. Weakly basic media is beneficial to the adopting of Co on the MoS_2 edge sites to form Co-Mo-S phase. It is discovered that catalysts with higher Co-Mo-S phase concentration exhibit higher hydrotreating activity.

A comprehensive kinetics study was conducted on the hydrotreatment of light cycle oil over a dispersed MoS_2 catalyst. The performance was evaluated in terms of

hydrodesulfurization, hydrodenitrogenation, hydrogenation of aromatics, and hydrocracking. The reactivity of different sulfur compound over the dispersed nano catalyst is in the order of BT>1MBT>>2MBT>3MBT>4MBT>>DBT≈1MDBT≈ 2MDBT≈3MDBT. The easy sulfur components, BT and its derivatives, are easily eliminated and the difficulty increases with the methyl substitutes. DBTs experience a much lower conversion than BTs. Further increase of methyl groups on DBT does not decrease the reactivity on the dispersed catalyst, indicating the steric hindrance is not as significant as that on the supported catalysts.

The stability of unsupported catalysts MoS_2 is investigated in long-term hydrotreatment process (160 hours on stream). Results show the HDS conversion gradually decreases in the first 60 hours from 98.6% to 86% at which level the activity can be maintained. Study on the deactivation mechanism indicates that the activity loss is mainly attributed to coke deposition and the slight sintering of active phase. Compared with supported catalyst, unsupported MoS_2 exhibits much less coke deposition and structure decomposition.

The catalytic roles of nickel/cobalt promoted MoS_2 catalysts were studied in hydrodeoxygenation of vegetable oils. Without the influence of catalyst supports, the inherent impact of nickel and cobalt on the main hydrodeoxygenation route has been investigated. Ni-promoted catalyst exhibits higher selectivity for direct deoxygenation (DDO) reaction over hydrodecarboxy(ny)lation (HDC), while Co-promoted catalyst prefers HDC. A new insight was proposed to interpret the impact of catalysts structure on hydrodeoxygenation pathways. NiMoS creates abundant sulfur vacancies that improve

the hydrogenation ability; CoMoS catalyst shows saturated edge sites in hydrogen atmosphere, facilitating hydrocracking (C-C hydrogenolysis). The enhancement of DDO reaction by Ni is primarily realized through the synergy effect of Mo and Ni on unsaturated sites of metal edge. By contrast, the HDC reaction is facilitated by Co-promoted MoS_2 through adsorption of C atoms on the S edge that is adjacent to Co.

The kinetics of hydrodeoxygenation over CoMoS catalysts was investigated using waste cooking oil. A kinetic model was established and a comprehensive analysis of each reaction pathway was carried out. Hydrodecarbonylation/decarboxylation routes are the predominant reaction pathways in the elimination of oxygen, with the rate constant 3 times as high as that of hydrodeoxygenation. However, the HDC activity of the CoMoS catalyst deactivates due to the gradual loss of sulfur from the catalyst. HDO process is insensitive to sulfur deficiency. The kinetic modeling shows that direct hydrodecarbonylation of fatty acids dominates the HDC routes. In the HDO route where fatty acids are transferred to C_{18} hydrocarbons through intermediates aldehydes/alcohols, the reduction of acids is the rate limiting step. The HDO route via alcohols is dominant over aldehydes due to a significantly higher reaction rate constant.

12.2 Recommendations for future work

Synthesis of high active unsupported MoS_2 through hydrothermal technique using affordable MoO_3 and Na_2S has been proved feasible. One of advantages of this synthesis technique is a variety of controllable parameters. The current study mainly focuses on the variation of the factors that are most important. Further investigation can be extended to

other factors, such as agitation speed, precursor concentration, and the interaction between the factors for the production of better catalysts.

Organic solvent and supercritical fluid were proved beneficial to the catalyst performance. Introduction of surfactant along with organic solvent/ supercritical fluid may help to form microemulsions and thus further separate the aqueous phase into even smaller droplets. It is worth noting that surfactant needs to be carefully selected with certain features, e.g. high stability at hydrothermal temperature.

This thesis mainly focuses on the synthesis of MoS_2. The study of promoted catalyst (Co) is not systematic. More investigation can be carried out on the improvement of the synthesis procedure, e.g. precursor type, ratios, and adding protocol, and illustration of reaction mechanism. Study can also be extended to Ni promoted catalyst.

Kinetics study of hydrotreatment of light cycle oil and vegetable oil over an unsupported catalyst provided valuable information on the intrinsic characteristics of the active phase. Further HDS study on model sulfur substances can be complemented in comparison with the same components in LCO to elucidate their different behaviours with/without the presence of nitrogen compounds or aromatics. The deoxygenation investigation can be extended to phenol-type substances.

Appendix A: Synthesis procedure of MoS_2

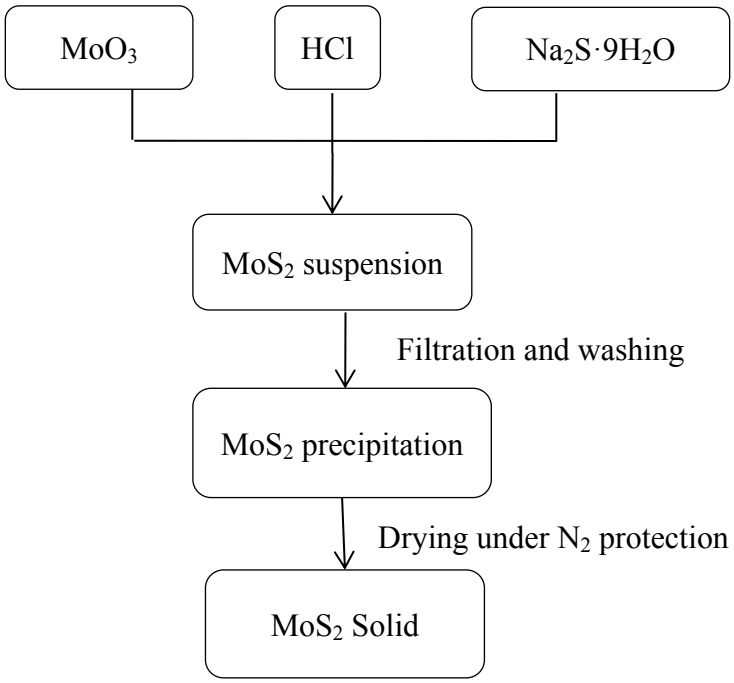

Appendix B: Flowchart of 1 L stirred autoclave reactor

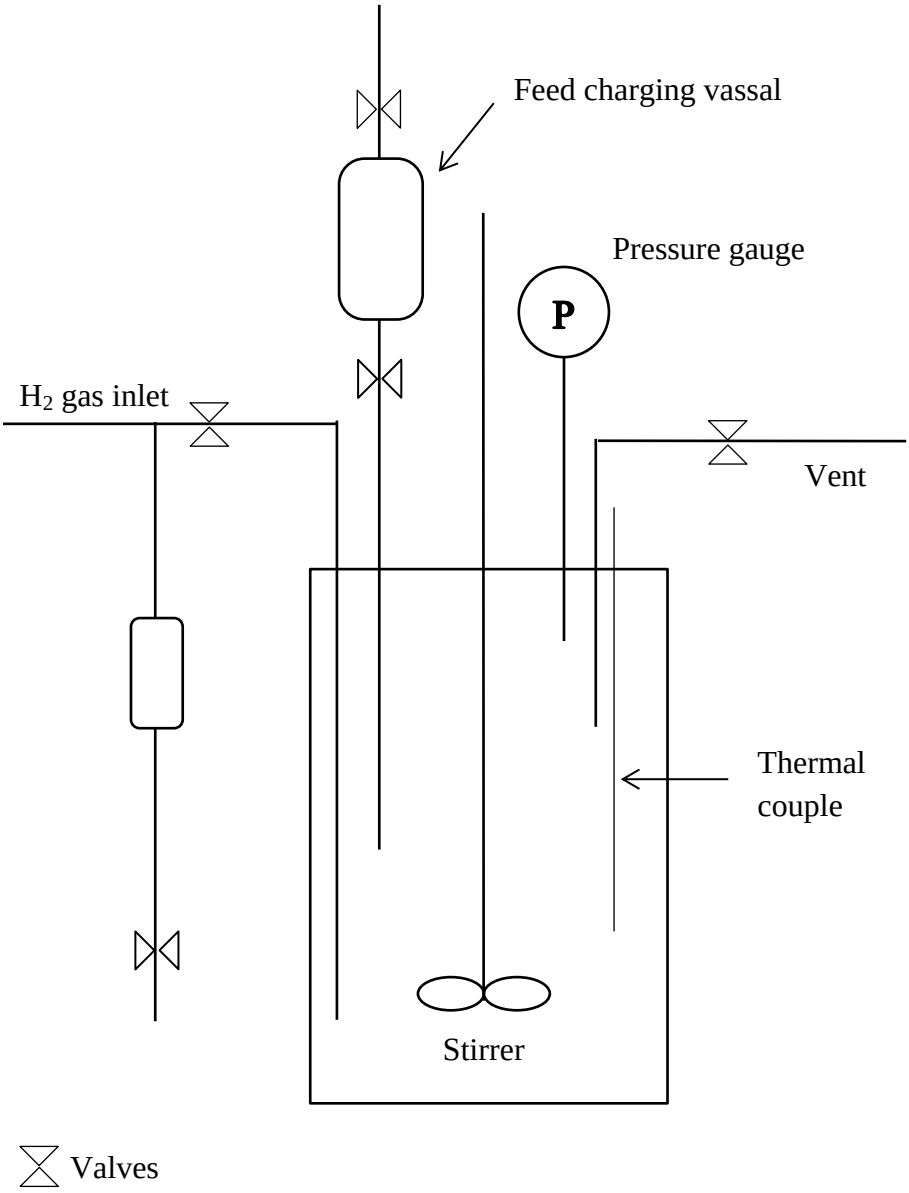

Appendix C: Flowchart of 25 ml microreactor

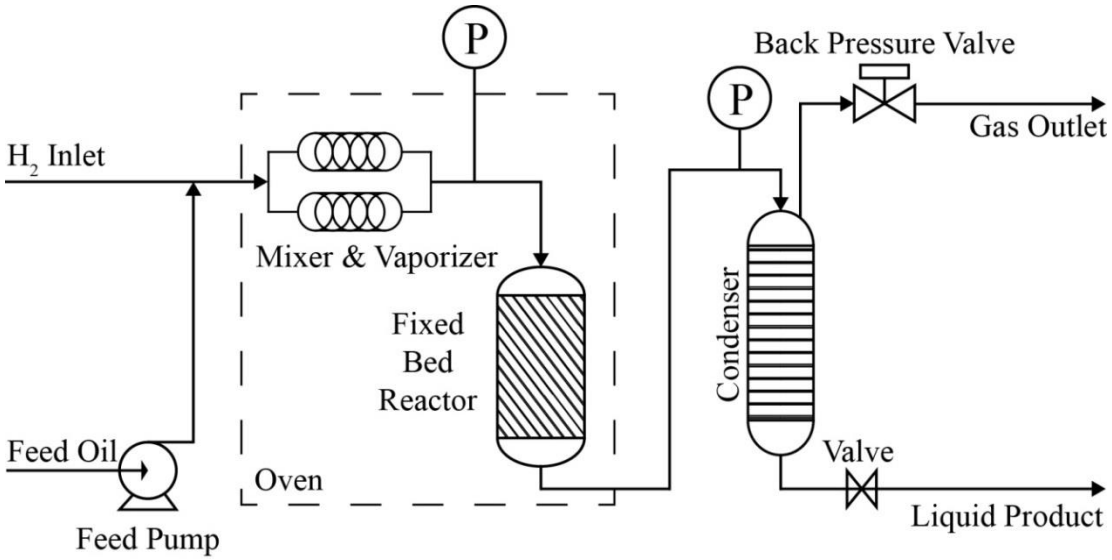

Appendix D: Mass balance for hydrotreatment of light cycle oil

For MoS_2-2.5 in Chapter 4

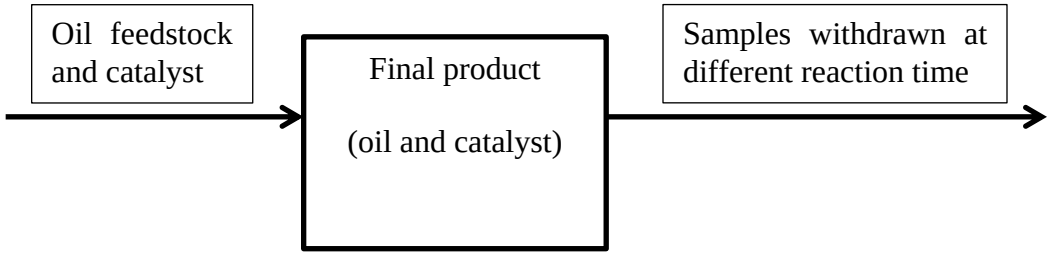

Input:
Oil: 120.2 g
Catalyst: 0.6 g

Output:
Samples withdrawn at different time: 18.5 g
Final product: 100.4 g
Total output oil: 118.2

Liquid oil recovery=Input oil/total output oil=98.4%

Bibliography

[1] J.M. Marchetti, V.U. Miguel, A.F. Errazu, Renewable Sustainable Energy Rev. Possible methods for biodiesel production, 11 (2007) 1300.
[2] S. Bezergianni, A. Dimitriadis, A. Kalogianni, P.A. Pilavachi, Bioresour. Technol. Hydrotreating of waste cooking oil for biodiesel production. Part I: Effect of temperature on product yields and heteroatom removal, 101 (2010) 6651.
[3] D.Y.C. Leung, X. Wu, M.K.H. Leung, Appl. Energy A review on biodiesel production using catalyzed transesterification, 87 (2010) 1083.
[4] S. Zheng, M. Kates, M.A. Dube, D.D. McLean, Biomass Bioenergy Acid-catalyzed production of biodiesel from waste frying oil, 30 (2006) 267.
[5] M. Lopez Granados, M.D. Zafra Poves, D. Martin Alonso, R. Mariscal, F. Cabello Galisteo, R. Moreno-Tost, J. Santamaria, J.L.G. Fierro, Appl. Catal., B Biodiesel from sunflower oil by using activated calcium oxide, 73 (2007) 317.
[6] T. Kalnes, T. Marker, D.R. Shonnard, Int. J. Chem. Reactor Eng. Green diesel: A second generation biofuel, 5 (2007) A48.
[7] B. Donnis, R.G. Egeberg, P. Blom, K.G. Knudsen, Top. Catal. Hydroprocessing of Bio-Oils and Oxygenates to Hydrocarbons. Understanding the Reaction Routes, 52 (2009) 229.
[8] E. Furimsky, Appl. Catal., A Catalytic hydrodeoxygenation, 199 (2000) 147.
[9] G.W. Huber, P. O'Connor, A. Corma, Appl. Catal., A Processing biomass in conventional oil refineries: Production of high quality diesel by hydrotreating vegetable oils in heavy vacuum oil mixtures, 329 (2007) 120.
[10] P. Simacek, D. Kubicka, G. Sebor, M. Pospisil, Fuel Hydroprocessed rapeseed oil as a source of hydrocarbon-based biodiesel, 88 (2009) 456.
[11] T.M. Sankaranarayanan, M. Banu, A. Pandurangan, S. Sivasanker, Bioresour. Technol. Hydroprocessing of sunflower oil-gas oil blends over sulfided Ni-Mo-Al-zeolite beta composites, 102 (2011) 10717.
[12] E.M. Ryymin, M.L. Honkela, T.R. Viljava, A.O.I. Krause, Appl. Catal., A Competitive reactions and mechanisms in the simultaneous HDO of phenol and methyl heptanoate over sulphided NiMo/gamma-Al2O3, 389 (2010) 114.
[13] S. Eijsbouts, S.W. Mayo, K. Fujita, Appl. Catal., A Unsupported transition metal sulfide catalysts: From fundamentals to industrial application, 322 (2007) 58.
[14] P. Afanasiev, C.R. Chim. Synthetic approaches to the molybdenum sulfide materials, 11 (2008) 159.
[15] M. Soto-Puente, M. Del Valle, E. Flores-Aquino, M. Avalos-Borja, S. Fuentes, J. Cruz-Reyes, Catal. Lett. Synthesis, characterization and cyclohexene hydrogenation activity of high surface area molybdenum disulfide catalysts, 113 (2007) 170.
[16] R. Romero-Rivera, A. Del Valle, G. Alonso, E. Flores, F. Castillon, S. Fuentes, J. Cruz-Reyes, Catal. Today Cyclohexene hydrogenation with molybdenum disulfide catalysts prepared by ex situ decomposition of ammonium thiomolybdate-cetyltrimethylammonium thiomolybdate mixtures, 130 (2008) 354.
[17] I. Bezverkhy, P. Afanasiev, M. Lacroix, Inorg. Chem. Aqueous Preparation of Highly Dispersed Molybdenum Sulfide, 39 (2000) 5416.
[18] B. Yoosuk, J.H. Kim, C. Song, C. Ngamcharussrivichai, P. Prasassarakich, Catal. Today Highly active MoS2, CoMoS2 and NiMoS2 unsupported catalysts prepared by

hydrothermal synthesis for hydrodesulfurization of 4,6-dimethyldibenzothiophene, 130 (2008) 14.
[19] Y. Araki, Y. Iwata, Y. Miki, K. Honna, N. Matsubayashi, H. Shimada, in: B. Delmon, G. F. Froment, P. Grange (Eds.) Hydrotreatment and Hydrocracking of Oil Fractions, Elsevier Science B.V., The Netherlands, 1999, p. 69.
[20] E. Devers, P. Afanasiev, B. Jouguet, M. Vrinat, Catal. Lett. Hydrothermal syntheses and catalytic properties of dispersed molybdenum sulfides, 82 (2002) 13.
[21] W.J. Li, E.W. Shi, J.M. Ko, Z.Z. Chen, H. Ogino, T. Fukuda, J. Cryst. Growth Hydrothermal synthesis of MoS2 nanowires, 250 (2003) 418.
[22] B. Yoosuk, C. Song, J.H. Kim, C. Ngamcharussrivichai, P. Prasassarakich, Catal. Today Effects of preparation conditions in hydrothermal synthesis of highly active unsupported NiMo sulfide catalysts for simultaneous hydrodesulfurization of dibenzothiophene and 4,6-dimethyldibenzothiophene, 149 (2010) 52.
[23] N.M.D. Brown, N. Cui, A. McKinley, Appl. Surf. Sci. An XPS study of the surface modification of natural MoS2 following treatment in an RF-oxygen plasma, 134 (1998) 11.
[24] W.Z.Q.J.W.W.L.W. Wang Shanmin, Mater. Chem. Phys. Nanocrystalline MoS2 through directional growth along the (0 0 2) crystal plane under high pressure, 130 (2011) 170.
[25] K.-I. Tanaka, T. Okuhara, Catalysis Reviews Regulation of Intermediates on Sulfided Nickel and MoS2 Catalysts, 15 (1977) 249.
[26] M. Daage, R.R. Chianelli, J. Catal. Structure-Function Relations in Molybdenum Sulfide Catalysts: The "Rim-Edge" Model, 149 (1994) 414.
[27] M.Y. Sun, J. Adjaye, A.E. Nelson, Appl. Catal., A Theoretical investigations of the structures and properties of molybdenum-based sulfide catalysts, 263 (2004) 131.
[28] A. Nogueira, R. Znaiguia, D. Uzio, P. Afanasiev, G. Berhault, Appl. Catal., A Curved nanostructures of unsupported and Al2O3-supported MoS2 catalysts: Synthesis and HDS catalytic properties, 429 (2012) 92.
[29] H. Farag, A.-N.A. El-Hendawy, K. Sakanishi, M. Kishida, I. Mochida, Appl. Catal., B Catalytic activity of synthesized nanosized molybdenum disulfide for the hydrodesulfurization of dibenzothiophene: Effect of H2S partial pressure, 91 (2009) 189.
[30] B. Guichard, M. Roy-Auberger, E. Devers, B. Rebours, A.A. Quoineaud, M. Digne, Appl. Catal., A Characterization of aged hydrotreating catalysts. Part I: Coke depositions, study on the chemical nature and environment, 367 (2009) 1.
[31] M.R. Khan, J.G. Reynolds, Chem. Tech. Formulating a response to the Clean Air Act, 26 (1996) 56.
[32] C. Song, X.L. Ma, Appl. Catal., B New design approaches to ultra-clean diesel fuels by deep desulfurization and deep dearomatization, 41 (2003) 207.
[33] K.-H. Choi, Y. Sano, Y. Korai, I. Mochida, Appl. Catal., B An approach to the deep hydrodesulfurization of light cycle oil, 53 (2004) 275.
[34] H. Farag, I. Mochida, J. Colloid Interface Sci. A comparative kinetic study on ultra-deep hydrodesulfurization of pre-treated gas oil over nanosized MoS2, CoMo-sulfide, and commercial CoMo/Al2O3 catalysts, 372 (2012) 121.
[35] Small Entity Compliance Guide for "Control of Emissions from Nonroad Diesel Engines and Fuel", in, EPA 420-B-05-009, September 2005.

[36] K. Tawara, T. Nishimura, H. Iwanami, T. Nishimoto, T. Hasuike, Ind. Eng. Chem. Res. New hydrodesulfurization catalyst for petroleum-fed fuel cell vehicles and cogenerations, 40 (2001) 2367.
[37] I.e.a.o.m. report.
[38] Z. Liu, Y. Zheng, W. Wang, Q. Zhang, L. Jia, Appl. Catal., A Simulation of hydrotreating of light cycle oil with a system dynamics model, 339 (2008) 209.
[39] L.H. Ding, Z.S. Zhang, Y. Zheng, Z. Ring, J.W. Chen, Appl. Catal., A Effect of fluorine and boron modification on the HDS, HDN and HDA activity of hydrotreating catalysts, 301 (2006) 241.
[40] A. Delbianco, N. Panariti, S. Dicarlo, J. Elmouchnino, B. Fixari, P. Leperchec, Appl. Catal., A Thermocatalytic hydroconversion of heavy petroleum cuts with dispersed catalyst, 94 (1993) 1.
[41] US EPA Clean Air Act Tier, (1999).
[42] K.G. Knudsen, B.H. Cooper, H. Topsoe, Appl. Catal., A Catalyst and process technologies for ultra low sulfur diesel, 189 (1999) 205.
[43] Y. Yi, B. Zhang, X. Jin, L. Wang, C.T. Williams, G. Xiong, D. Su, C. Liang, J. Mol. Catal. A: Chem. Unsupported NiMoW sulfide catalysts for hydrodesulfurization of dibenzothiophene by thermal decomposition of thiosalts, 351 (2011) 120.
[44] C. Wang, Z. Wu, C. Tang, L. Li, D. Wang, Catal. Commun. The effect of nickel content on the hydrodeoxygenation of 4-methylphenol over unsupported NiMoW sulfide catalysts, 32 (2013) 76.
[45] Z. Đukanović, S.B. Glišić, V.J. Čobanin, M. Nićiforović, C.A. Georgiou, A.M. Orlović, Fuel Process. Technol. Hydrotreating of straight-run gas oil blended with FCC naphtha and light cycle oil, 106 (2013) 160.
[46] J. Ancheyta-Juárez, E. Aguilar-Rodríguez, D. Salazar-Sotelo, G. Betancourt-Rivera, M. Leiva-Nuncio, Appl. Catal., A Hydrotreating of straight run gas oil–light cycle oil blends, 180 (1999) 195.
[47] P.D. Costa, C. Potvin, J.-M. Manoli, B. Genin, G. Djega-Mariadassou, Fuel Deep hydrodesulphurization and hydrogenation of diesel fuels on alumina-supported and bulk molybdenum carbide catalysts, 83 (2004) 1717.
[48] Y. Saih, A. Nagata, T. Funamoto, Y. Masuyama, K. Segawa, Appl. Catal., A Ultra deep hydrodesulfurization of dibenzothiophene derivatives over NiMo/TiO2-Al2O3 catalysts, 295 (2005) 11.
[49] G.A. Camacho-Bragado, J.L. Elechiguerra, A. Olivas, S. Fuentes, D. Galvan, M.J. Yacaman, J. Catal. Structure and catalytic properties of nanostructured molybdenum sulfides, 234 (2005) 182.
[50] D. Mahajan, C.L. Marshall, N. Castagnola, J.C. Hanson, Appl. Catal., A Sono synthesis and characterization of nano-phase molybdenum-based materials for catalytic hydrodesulfurization, 258 (2004) 83.
[51] T.C. Ho, J.M. McConnachie, J. Catal. Ultra-deep hydrodesulfurization on MoS2 and Co0.1MoS2: Intrinsic vs. environmental factors, 277 (2011) 117.
[52] M. Kouzu, K. Uchida, Y. Kuriki, F. Ikazaki, Appl. Catal., A Micro-crystalline molybdenum sulfide prepared by mechanical milling as an unsupported model catalyst for the hydrodesulfurization of diesel fuel, 276 (2004) 241.

[53] P.A.G. O'Hare, E. Benn, F.Y. Cheng, G. Kuzmycz, J. Chem. Thermodyn. A fluorine bomb calorimetric study of molybdenum disulfide. The standard enthalpies of formation of the di- and sesquisulfides of molybdenum, 2 (1970) 797.
[54] F. Morel, S. Kressmann, V. Harle, S. Kasztelan, in: G. F. Froment, B. Delmon, P. Grange (Eds.) Hydrotreatment and Hydrocracking of Oil Fractions, Elsevier Science Bv, Amsterdam, 1997, p. 1.
[55] S. Peureux, S. Bonnamy, B. Fixari, F. Lambert, P. Leperchec, B. Pepindonat, M. Vrinat, Bull. Soc. Chim. Belg. Deep hydroconversion of heavy oil residues with dispersed catalysts - analysis of the transformation, 104 (1995) 359.
[56] Y. Iwata, Y. Araki, K. Honna, Y. Miki, K. Sato, H. Shimada, Hydrogenation active sites of unsupported molybdenum sulfide catalysts for hydroprocessing heavy oils, in, Elsevier Science Bv, 2001, pp. 335.
[57] C.E. Galarraga, C. Scott, H. Loria, P. Pereira-Almao, Ind. Eng. Chem. Res. Kinetic models for upgrading Athabasca bitumen using unsupported NiWMo catalysts at low severity conditions, 51 (2012) 140.
[58] Y. Iwata, K. Sato, T. Yoneda, Y. Miki, Y. Sugimoto, A. Nishijima, H. Shimada, Catal. Today Catalytic functionality of unsupported molybdenum sulfide catalysts prepared with different methods, 45 (1998) 353.
[59] H. He, T. Wang, S. Zhu, Fuel Continuous production of biodiesel fuel from vegetable oil using supercritical methanol process, 86 (2007) 442.
[60] K. Nie, F. Xie, F. Wang, T. Tan, J. Mol. Catal. B: Enzym. Lipase catalyzed methanolysis to produce biodiesel: Optimization of the biodiesel production, 43 (2006) 142.
[61] M. Di Serio, R. Tesser, M. Dimiccoli, F. Cammarota, M. Nastasi, E. Santacesaria, J. Mol. Catal. A: Chem. Synthesis of biodiesel via homogeneous Lewis acid catalyst, 239 (2005) 111.
[62] I. Sebos, A. Matsoukas, V. Apostolopoulos, N. Papayannakos, Fuel Catalytic hydroprocessing of cottonseed oil in petroleum diesel mixtures for production of renewable diesel, 88 (2009) 145.
[63] J. Holmgren, C. Gosling, R. Marinangeli, T. Marker, G. Faracii, C. Perego, Hydrocarb. Process. New developments in renewable fuels offer more choices - Vegetable oil-based diesel can offer better integration within crude-oil refineries for fuels blending, 86 (2007) 67.
[64] L. Boda, O. Gyorgy, H. Solt, L. Ferenc, J. Valyon, A. Thernesz, Appl. Catal., A Catalytic hydroconversion of tricaprylin and caprylic acid as model reaction for biofuel production from triglycerides, 374 (2010) 158.
[65] T.T. Pham, L.L. Lobban, D.E. Resasco, R.G. Mallinson, J. Catal. Hydrogenation and Hydrodeoxygenation of 2-methyl-2-pentenal on supported metal catalysts, 266 (2009) 9.
[66] E.W. Ping, J. Pierson, R. Wallace, J.T. Miller, T.F. Fuller, C.W. Jones, Appl. Catal., A On the nature of the deactivation of supported palladium nanoparticle catalysts in the decarboxylation of fatty acids, 396 (2011) 85.
[67] T.V. Choudhary, C.B. Phillips, Appl. Catal., A Renewable fuels via catalytic hydrodeoxygenation, 397 (2011) 1.
[68] M. Krar, S. Kovacs, D. Kallo, J. Hancsok, Bioresour. Technol. Fuel purpose hydrotreating of sunflower oil on CoMo/Al2O3 catalyst, 101 (2010) 9287.

[69] J. Gusmão, D. Brodzki, G. Djéga-Mariadassou, R. Frety, Catal. Today Utilization of vegetable oils as an alternative source for diesel-type fuel: hydrocracking on reduced Ni/SiO2 and sulphided Ni-Mo/γ-Al2O3, 5 (1989) 533.
[70] D. Kubicka, L. Kaluza, Appl. Catal., A Deoxygenation of vegetable oils over sulfided Ni, Mo and NiMo catalysts, 372 (2010) 199.
[71] H.Y. Zhao, D. Li, P. Bui, S.T. Oyama, Appl. Catal., A Hydrodeoxygenation of guaiacol as model compound for pyrolysis oil on transition metal phosphide hydroprocessing catalysts, 391 (2011) 305.
[72] B. Phuong, J. Antonio Cecilia, S.T. Oyama, A. Takagaki, A. Infantes-Molina, H. Zhao, D. Li, E. Rodriguez-Castellon, A. Jimenez Lopez, J. Catal. Studies of the synthesis of transition metal phosphides and their activity in the hydrodeoxygenation of a biofuel model compound, 294 (2012) 184.
[73] I. Tyrone Ghampson, C. Sepulveda, R. Garcia, L.R. Radovic, J.L. Garcia Fierro, W.J. DeSisto, N. Escalona, Appl. Catal., A Hydrodeoxygenation of guaiacol over carbon-supported molybdenum nitride catalysts: Effects of nitriding methods and support properties, 439 (2012) 111.
[74] J. Monnier, H. Sulimma, A. Dalai, G. Caravaggio, Appl. Catal., A Hydrodeoxygenation of oleic acid and canola oil over alumina-supported metal nitrides, 382 (2010) 176.
[75] A.L. Jongerius, R.W. Gosselink, J. Dijkstra, J.H. Bitter, P.C.A. Bruijnincx, B.M. Weckhuysen, Chemcatchem Carbon nanofiber supported transition-metal carbide catalysts for the hydrodeoxygenation of guaiacol, 5 (2013) 2964.
[76] W. Zhang, Y. Zhang, L. Zhao, W. Wei, Energ. Fuel. Catalytic activities of NiMo carbide supported on SiO2 for the hydrodeoxygenation of ethyl benzoate, acetone, and acetaldehyde, 24 (2010) 2052.
[77] A. Centeno, E. Laurent, B. Delmon, J. Catal. Influence of the Support of CoMo Sulfide Catalysts and of the Addition of Potassium and Platinum on the Catalytic Performances for the Hydrodeoxygenation of Carbonyl, Carboxyl, and Guaiacol-Type Molecules, 154 (1995) 288.
[78] Y.-Y. Chen, M. Dong, Z. Qin, X.-D. Wen, W. Fan, J. Wang, J. Mol. Catal. A: Chem. A DFT study on the adsorption and dissociation of methanol over MoS2 surface, 338 (2011) 44.
[79] Y.V. Joshi, P. Ghosh, P.S. Venkataraman, W.N. Delgass, K.T. Thomson, J. Phys. Chem. C Electronic Descriptors for the Adsorption Energies of Sulfur-Containing Molecules on Co/MoS2, Using DFT Calculations, 113 (2009) 9698.
[80] V.M. Kogan, N.T. Dung, V.I. Yakerson, Bull. Soc. Chim. Belg. Comparative-study of sulfide Ni-Mo catalysts, supported on gamma-Al2O3 and activated carbon by using radioisotope S-35, 104 (1995) 303.
[81] P.J. Mangnus, A. Bos, J.A. Moulijn, J. Catal. Temperature-programmed reduction of oxidic and sulfidic alumina-supported NiO, WO3, and NiO-WO3 catalysts, 146 (1994) 437.
[82] S. Kasztelan, A. Wambeke, L. Jalowiecki, J. Grimblot, J.P. Bonnelle, J. Catal. Site structure sensitivity of diene hydrogenation and isomerization-reactions on MoS2-gamma-Al2O3 catalysts, 124 (1990) 12.
[83] I. Mochida, K.H. Choi, Sekiyu Gakkaishi An overview of hydrodesulfurization and hydrodenitrogenation, 47 (2004) 145.

[84] P. Afanasiev, J. Catal. The influence of reducing and sulfiding conditions on the properties of unsupported MoS2-based catalysts, 269 (2010) 269.
[85] T.S. Smit, K.H. Johnson, J. Mol. Catal. The importance of sulfur-sulfur bonding in the hydrodesulfurization process of thiophene, using transition-metal sulfide catalysts, 91 (1994) 207.
[86] M. Egorova, R. Prins, J. Catal. Competitive hydrodesulfurization of 4,6-dimethyldibenzothiophene, hydrodenitrogenation of 2-methylpyridine, and hydrogenation of naphthalene over sulfided NiMo/gamma-Al2O3, 224 (2004) 278.
[87] P.G. Moses, B. Hinnemann, H. Topsoe, J.K. Norskov, J. Catal. The hydrogenation and direct desulfurization reaction pathway in thiophene hydrodesulfurization over MoS2 catalysts at realistic conditions: A density functional study, 248 (2007) 188.
[88] J.V. Lauritsen, M. Nyberg, J.K. Norskov, B.S. Clausen, H. Topsoe, E. Laegsgaard, F. Besenbacher, J. Catal. Hydrodesulfurization reaction pathways on MoS2 nanoclusters revealed by scanning tunneling microscopy, 224 (2004) 94.
[89] B.M. Vogelaar, P. Steiner, T.F. van der Zijden, A.D. van Langeveld, S. Eijsbouts, J.A. Moulijn, Appl. Catal., A Catalyst deactivation during thiophene HDS: The role of structural sulfur, 318 (2007) 28.
[90] S. Eijsbouts, Appl. Catal., A On the flexibility of the active phase in hydrotreating catalysts, 158 (1997) 53.
[91] H. Topsoe, B.S. Clausen, F. Massoth, Hydrotreating catalysis, science and technology, Springer, Berlin, 1996.
[92] K.I. Tanaka, T. Okuhara, Cat. Rev.-Sci. Eng. Regulation of intermediates on sulfided nickel and MoS2 catalysts, 15 (1977) 249.
[93] S. Kasztelan, L. Jalowiecki, A. Wambeke, J. Grimblot, J.P. Bonnelle, Bull. Soc. Chim. Belg. Location and description of active-sites for cis-1,3-pentadiene isomerization and hydrogenation on mos2/gamma-Al2O3 catalysts, 96 (1987) 1003.
[94] K.-I. Tanaka, in: H. P. D.D. Eley, B. W. Paul (Eds.) Advances in Catalysis, Academic Press, 1985, p. 99.
[95] R.R. Chianelli, G. Berhault, P. Santiago, D. Mendoza, A. Espinosa, J.A. Ascencio, M.J. Yacaman, Mater. Technol. Synthesis, fundamental properties and applications of nanocrystals, sheets, nanotubes and cylinders based on layered transition metal chalcogenides, 15 (2000) 54.
[96] A.K. Datye, S. Srinivasan, L.F. Allard, C.H.F. Peden, J.R. Brenner, L.T. Thompson, J. Catal. Oxide Supported MoS2 Catalysts of Unusual Morphology, 158 (1996) 205.
[97] D. Le, T.B. Rawal, T.S. Rahman, J. Phys. Chem. C Single-Layer MoS2 with Sulfur Vacancies: Structure and Catalytic Application, 118 (2014) 5346.
[98] G. Alonso, G. Berhault, A. Aguilar, V. Collins, C. Ornelas, S. Fuentes, R.R. Chianelli, J. Catal. Characterization and HDS activity of mesoporous MoS2 catalysts prepared by in situ activation of tetraalkylammonium thiomolybdates, 208 (2002) 359.
[99] C. Dupont, R. Lemeur, A. Daudin, P. Raybaud, J. Catal. Hydrodeoxygenation pathways catalyzed by MoS(2) and NiMoS active phases: A DFT study, 279 (2011) 276.
[100] C. Fontaine, Y. Romero, A. Daudin, E. Devers, C. Bouchy, S. Brunet, Appl. Catal., A Insight into sulphur compounds and promoter effects on Molybdenum-based catalysts for selective HDS of FCC gasoline, 388 (2010) 188.
[101] D. Genuit, P. Afanasiev, M. Vrinat, J. Catal. Solution syntheses of unsupported Co(Ni)-Mo-S hydrotreating catalysts, 235 (2005) 302.

[102] L.S. Byskov, B. Hammer, J.K. Norskov, B.S. Clausen, H. Topsoe, Catal. Lett. Sulfur bonding in MoS2 and Co-Mo-S structures, 47 (1997) 177.
[103] R.R. Chianelli, Cat. Rev.-Sci. Eng. Fundamental-studies of transition-metal sulfide hydrodesulfurization catalysts, 26 (1984) 361.
[104] S. Harris, R.R. Chianelli, J. Catal. Catalysis by transition-metal sulfides - a theoretical and experimental-study of the relation between the synergic systems and the binary transition-metal sulfides, 98 (1986) 17.
[105] R.R. Chianelli, G. Berhault, B. Torres, Catal. Today Unsupported transition metal sulfide catalysts: 100 years of science and application, 147 (2009) 275.
[106] E. Krebs, A. Daudin, P. Raybaud, Oil & Gas Science and Technology-Revue D Ifp Energies Nouvelles A DFT study of CoMoS and NiMoS catalysts: from Nano-Crystallite morphology to selective hydrodesulfurization, 64 (2009) 707.
[107] I.K. Seo, I.W. Seong, Appl. Catal Effect of sulfiding temperatures on the formation of sulfides of Mo/Al2O3 and CoMo/Al2O3, 74 (1991) 109.
[108] S. Fuentes, M. Avalosborja, D. Acosta, F. Pedraza, J. Cruz, Z. Paal, R.P. Silvy, M. Ternan, Stud. Surf. Sci. Catal. High-resolution electron-microscopy characterization of the poorly crystalline-structure of molybdenum disulfide-based catalysts, 75 (1993) 611.
[109] C.B. Roxlo, M. Daage, A.F. Ruppert, R.R. Chianelli, J. Catal. Optical-absorption and catalytic activity of molybdenum sulfide edge surfaces, 100 (1986) 176.
[110] J.P.R. Vissers, V.H.J. Debeer, R. Prins, J. Chem. Soc. Faraday Trans. The role of Co in sulfidized Co-Mo hydrodesulfurization catalysts supported on carbon and alumina, 83 (1987) 2145.
[111] T.S. Smit, K.H. Johnson, Catal. Lett. A unified theory of periodic and promotion effects in transition-metal sulfide hydrodesulfurization catalysts, 28 (1994) 361.
[112] B. Delmon, Bull. Soc. Chim. Belg. Selectivity in HDS, HDN, HDO and hydrocracking contribution of remote-control and other new concepts, 104 (1995) 173.
[113] M. Karroua, H. Matralis, P. Grange, B. Delmon, J. Catal. Synergy between NiMoS and Co9S8 in the hydrogenation of cyclohexene and hydrodesulfurization of thiophene, 139 (1993) 371.
[114] D. Pirotte, J.M. Zabala, P. Grange, B. Delmon, Bull. Soc. Chim. Belg. The remote-control of the active-sites of hydrodesulfurization catalysts comparison of experimental results with the model, 90 (1981) 1239.
[115] A. Travert, H. Nakamura, R.A. van Santen, S. Cristol, J.-F. Paul, E. Payen, J. Am. Chem. Soc. Hydrogen Activation on Mo-Based Sulfide Catalysts, a Periodic DFT Study, 124 (2002) 7084.
[116] K. Inamura, R. Prins, J. Catal. The Role of Co in Unsupported Co-Mo Sulfides in the Hydrodesulfurization of Thiophene, 147 (1994) 515.
[117] M.L. Vrinat, L. De Mourgues, Appl. Catal On the role of cobalt in sulfided unsupported Co-Mo hydrodesulfurization catalysts: kinetic studies and scanning electron microscopic observations, 5 (1983) 43.
[118] R.C. Hoodless, R.B. Moyes, P.B. Wells, Bull. Soc. Chim. Belg. Temperature programmed reduction and desorption studies of Co-precipitated cobalt-molybdenum sulfide powders, 93 (1984) 673.
[119] K.C. Pratt, J.V. Sanders, N. Tamp, J. Catal. The role of nickel in the activity of unsupported Ni-Mo hydrodesulfurization catalysts, 66 (1980) 82.

[120] C. Gachet, R. Paulus, L. Demourgues, C. Durand, H. Toulhoat, Bull. Soc. Chim. Belg. Unsupported Ni-Mo sulfide catalysts - relation between the HDS and hydrogenation activities and some structural-properties, 93 (1984) 681.
[121] M. Polyakov, M.W.E. van den Berg, T. Hanft, M. Poisot, W. Bensch, M. Muhler, W. Gruenert, J. Catal. Hydrocarbon reactions on MoS2 revisited, I: Activation of MoS2 and interaction with hydrogen studied by transient kinetic experiments, 256 (2008) 126.
[122] J.L. Brito, M. Ilija, P. Hernandez, Thermochim. Acta Thermal and reductive decomposition of ammonium thiomolybdates, 256 (1995) 325.
[123] R.I. Walton, A.J. Dent, S.J. Hibble, Chem. Mater. In situ investigation of the thermal decomposition of ammonium tetrathiomolybdate using combined time-resolved X-ray absorption spectroscopy and X-ray diffraction, 10 (1998) 3737.
[124] B.R. Srinivasan, S.N. Dhuri, A.R. Naik, C. Naether, W. Bensch, Polyhedron Crystallographic and thermal investigations of organic ammonium tetrathiomolybdates, 27 (2008) 25.
[125] N. Rueda, R. Bacaud, M. Vrinat, J. Catal. Highly dispersed, nonsupported molybdenum sulfides, 169 (1997) 404.
[126] P. Afanasiev, G.F. Xia, G. Berhault, B. Jouguet, M. Lacroix, Chem. Mater. Surfactant-assisted synthesis of highly dispersed molybdenum sulfide, 11 (1999) 3216.
[127] S. Somiya, Hydrothermal reactions for materials science and engineering, Elsevier Applied Science, London, 1989.
[128] K. Byrapp, M. Yoshimura, Handbook of Hydrothermal Technology, Noyes Publications, New Jersey, U.S.A., 2001.
[129] K. Byrappa, J. Ceram. Soc. Jpn. Novel hydrothermal solution routes of advanced high melting nanomaterials processing, 117 (2009) 236.
[130] J.-X. Su, X.-P. Wang, Q. Pan, W. Qu, Chin. J. Inorg. Chem. Effect of hydrothermal conditions on the crystallization of Mg3Al-CO32- hydrotalcite, 23 (2007) 1015.
[131] J. Yu, G. Wang, B. Cheng, M. Zhou, Appl. Catal., B Effects of hydrothermal temperature and time on the photocatalytic activity and microstructures of bimodal mesoporous TiO2 powders, 69 (2007) 171.
[132] B. Akin, M. Oner, Res. Chem. Intermed. Aqueous pathways for formation of zinc oxide particles in the presence of carboxymethyl inulin, 38 (2012) 1511.
[133] G. Madras, B.J. McCoy, J. Chem. Phys. Temperature effects during Ostwald ripening, 119 (2003) 1683.
[134] G. Madras, B.J. McCoy, Chem. Eng. Sci. Temperature effects on the transition from nucleation and growth to Ostwald ripening, 59 (2004) 2753.
[135] G. Madras, B.J. McCoy, Acta Mater. Temperature effects for crystal growth: a distribution kinetics approach, 51 (2003) 2031.
[136] Y.M. Tian, X. Zhao, L.C. Shen, F.Y. Meng, L.Q. Tang, Y.H. Deng, Z.C. Wang, Mater. Lett. Synthesis of amotphous MoS2 nanospheres by hydrothermal reaction, 60 (2006) 527.
[137] J. Eastoe, M.J. Hollamby, L. Hudson, Adv. Colloid Interface Sci. Recent advances in nanoparticle synthesis with reversed micelles, 128 (2006) 5.
[138] Y. Yoneyama, C. Song, Energ. Fuel. Promoting effect of H2O addition on C-O bond cleavage and hydrogenation of dinaphthyl ether over MoS2 catalyst in situ generated from ammonium tetrathiomolybdate, 16 (2002) 767.

[139] C. Aymonier, A. Loppinet-Serani, H. Reveron, Y. Garrabos, F. Cansell, J. Supercrit. Fluids Review of supercritical fluids in inorganic materials science, 38 (2006) 242.
[140] Q. Xu, W. Ni, Progress in Chemistry Nanomaterials preparation in the supercritical fluid system, 19 (2007) 1419.
[141] E. Reverchon, R. Adami, J. Supercrit. Fluids Nanomaterials and supercritical fluids, 37 (2006) 1.
[142] B. Chehroudi, Combust. Sci. Technol. Supercritical fluids: Nanotechnology and select emerging applications, 178 (2006) 555.
[143] Y. Zhang, C. Erkey, J. Supercrit. Fluids Preparation of supported metallic nanoparticles using supercritical fluids: A review, 38 (2006) 252.
[144] U. Nylén, J.F. Delgado, S. Järås, M. Boutonnet, Fuel Process. Technol. Characterization of alkylated aromatic sulphur compounds in light cycle oil from hydrotreated vacuum gas oil using GC-SCD, 86 (2004) 223.
[145] R. Shafi, G.J. Hutchings, Catal. Today Hydrodesulfurization of hindered dibenzothiophenes: an overview, 59 (2000) 423.
[146] H. Yang, J.W. Chen, Y. Briker, R. Szynkarczuk, Z. Ring, Catal. Today Effect of nitrogen removal from light cycle oil on the hydrodesulphurization of dibenzothiophene, 4-methyldibenzothiophene and 4,6-dimethyldibenzothiophene, 109 (2005) 16.
[147] V. Vanrysselberghe, G.F. Froment, Ind. Eng. Chem. Res. Kinetic modeling of hydrodesulfurization of oil fractions: Light cycle oil, 37 (1998) 4231.
[148] T.C. Ho, Catal. Today Deep HDS of diesel fuel: chemistry and catalysis, 98 (2004) 3.
[149] M. Houalla, D.H. Broderick, A.V. Sapre, N.K. Nag, V. Beer, B.C. Gates, H. Kwart, J. Catal. Hydrodesulfurization of methyl-substituted dibenzothiophenes catalyzed by sulfided Co-Mo-gamma-Al2O3, 61 (1980) 523.
[150] D.D. Whitehurst, T. Isoda, I. Mochida, Advances in Catalysis, Vol 42 Present state of the art and future challenges in the hydrodesulfurization of polyaromatic sulfur compounds, 42 (1998) 345.
[151] F. Ronald, P.E. Colwell, Oil refinery processes: A brief overview, in.
[152] C.T. Tye, K.J. Smith, Catal. Today Hydrodesulfurization of dibenzothiophene over exfoliated MoS2 catalyst, 116 (2006) 461.
[153] M.J. Girgis, B.C. Gates, Ind. Eng. Chem. Res. Reactivities, reaction networks, and kinetics in high-pressure catalytic hydroprocessing, 30 (1991) 2021.
[154] V. Vanrysselberghe, R. Le Gall, G.F. Froment, Ind. Eng. Chem. Res. Hydrodesulfurization of 4-methyldibenzothiophene and 4,6-dimethyldibenzothiophene on a CoMo/Al2O3 catalyst: Reaction network and kinetics, 37 (1998) 1235.
[155] B.C. Gates, H. Topsoe, Polyhedron Reactivities in deep catalytic hydrodesulfurization: Challenges, opportunities, and the importance of 4-methyldibenzothiophene and 4,6-dimethyldibenzothiophene, 16 (1997) 3213.
[156] G. Pérot, Catal. Today Hydrotreating catalysts containing zeolites and related materials—mechanistic aspects related to deep desulfurization, 86 (2003) 111.
[157] T. Isoda, S. Nagao, X.L. Ma, Y. Korai, I. Mochida, Energ. Fuel. Hydrodesulfurization pathway of 4,6-dimethyldibenzothiophene through isomerization over Y-zeolite containing CoMo/Al2O3 catalyst, 10 (1996) 1078.
[158] E. Laurent, B. Delmon, Ind. Eng. Chem. Res. Influence of oxygen-containing, nitrogen-containing, and sulfur-containing-compounds on the hydrodeoxygenation of

phenols over sulfided CoMo/gamma-Al2O3 and NiMo/gamma-Al2O3 catalysts, 32 (1993) 2516.
[159] N.B. Van, D. Laurenti, P. Afanasiev, C. Geantet, Appl. Catal., B Hydrodeoxygenation of guaiacol with CoMo catalysts. Part I: Promoting effect of cobalt on HDO selectivity and activity, 101 (2011) 239.
[160] P. Simacek, D. Kubicka, G. Sebor, M. Pospisil, Fuel Fuel properties of hydroprocessed rapeseed oil, 89 (2010) 611.
[161] J. Walendziewski, M. Stolarski, R. Luzny, B. Klimek, Fuel Process. Technol. Hydroprocesssing of light gas oil - rape oil mixtures, 90 (2009) 686.
[162] M. Toba, Y. Abe, H. Kuramochi, M. Osako, T. Mochizuki, Y. Yoshimura, Catal. Today Hydrodeoxygenation of waste vegetable oil over sulfide catalysts, 164 (2011) 533.
[163] S. Bezergianni, A. Dimitriadis, T. Sfetsas, A. Kalogianni, Bioresour. Technol. Hydrotreating of waste cooking oil for biodiesel production. Part II: Effect of temperature on hydrocarbon composition, 101 (2010) 7658.
[164] I. Kubickova, M. Snare, K. Eranen, P. Maki-Arvela, D.Y. Murzin, Catal. Today Hydrocarbons for diesel fuel via decarboxylation of vegetable oils, 106 (2005) 197.
[165] O.I. Senol, T.R. Viljava, A.O.I. Krause, Catal. Today Hydrodeoxygenation of methyl esters on sulphided NiMo/gamma-Al2O3 and CoMo/gamma-Al2O3 catalysts, 100 (2005) 331.
[166] O.I. Senol, E.M. Ryymin, T.R. Viljava, A.O.I. Krause, J. Mol. Catal. A: Chem. Effect of hydrogen sulphide on the hydrodeoxygenation of aromatic and aliphatic oxygenates on sulphided catalysts, 277 (2007) 107.
[167] C. Calais, N. Matsubayashi, C. Geantet, Y. Yoshimura, H. Shimada, A. Nishijima, M. Lacroix, M. Breysse, J. Catal. Crystallite size determination of highly dispersed unsupported MoS2 catalysts, 174 (1998) 130.
[168] K.S. Liang, R.R. Chianelli, F.Z. Chien, S.C. Moss, J. Non-Cryst. Solids Structure of poorly crystalline MoS2 — A modeling study, 79 (1986) 251.
[169] D.L. Vassilaros, R.C. Kong, D.W. Later, M.L. Lee, J. Chromatogr. Linear retention index system for polycyclic aromatic compounds critical evaluation and additional indexes, 252 (1982) 1.
[170] R. Costa, B.d.A. Zellner, M.L. Crupi, M.R. De Fina, M.R. Valentino, P. Dugo, G. Dugo, L. Mondello, Flavour Frag. J. GC-MS, GC-O and enantio-GC investigation of the essential oil of Tarchonanthus camphoratus L, 23 (2008) 40.
[171] V.R. Surisetty, Y.F. Hu, A.K. Dalai, J. Kozinski, Appl. Catal., A Structural characterization and catalytic performance of alkali (K) and metal (Co and Rh)-promoted MoS2 catalysts for higher alcohols synthesis, 392 (2011) 166.
[172] N. Dinter, M. Rusanen, P. Raybaud, S. Kasztelan, P. da Silva, H. Toulhoat, J. Catal. Temperature-programed reduction of unpromoted MoS2-based hydrodesulfurization catalysts: Experiments and kinetic modeling from first principles, 267 (2009) 67.
[173] H. Aritani, T. Tanaka, T. Funabiki, S. Yoshida, K. Eda, N. Sotani, M. Kudo, S. Hasegawa, J. Phys. Chem. Study of the local structure of molybdenum-magnesium binary oxides by means of Mo L(3)-edge XANES and UV-vis spectroscopy, 100 (1996) 19495.
[174] H. Aritani, O. Fukuda, A. Miyaji, S. Hasegawa, Appl. Surf. Sci. Structural change of molybdenum on silica-alumina in contact with propene studied by ESR and Mo L-III-edge XANES, 180 (2001) 261.

[175] Y.V. Zubavichus, A.S. Golub, Y.N. Novikov, Y.L. Slovokhotov, A.N. Nesmeyanov, P.J. Schilling, R.C. Tittsworth, J. Phys. IV XAFS study of MoS2 intercalation compounds, 7 (1997) 1057.
[176] R.S. Smart, W.M. Skinner, A.R. Gerson, Surf. Interface Anal. XPS of sulphide mineral surfaces: Metal-deficient, polysulphides, defects and elemental sulphur, 28 (1999) 101.
[177] X.S. Li, Q. Xin, X.X. Guo, P. Grange, B. Delmon, J. Catal. Reversible hydrogen adsorption on MoS2 studied by temperature-programmed desorption and temperature-programmed reduction, 137 (1992) 385.
[178] M. Vrinat, M. Breysse, C. Geantet, J. Ramirez, F. Massoth, Catal. Lett. Effect of MoS2 morphology on the HDS activity of hydrotreating catalysts, 26 (1994) 25.
[179] H.-R. Seo, Y.-K. Lee, Journal of the Korean Physical Society EXAFS Studies on the Formation of MoS2 Nanoparticles, 59 (2011) 730.
[180] B.D. Fahlman, in: Material Chemistry, Springer, 2011.
[181] X. Bokhimi, J.A. Toledo, J. Navarrete, X.C. Sun, M. Portilla, Int. J. Hydrogen Energy Thermal evolution in air and argon of nanocrystalline MoS2 synthesized under hydrothermal conditions, 26 (2001) 1271.
[182] K. Byrappa, S. Ohara, T. Adschiri, Adv. Drug Delivery Rev. Nanoparticles synthesis using supercritical fluid technology - towards biomedical applications, 60 (2008) 299.
[183] A. Michailovski, G.R. Patzke, Chemistry-a European Journal Hydrothermal synthesis of molybdenum oxide based materials: Strategy and structural chemistry, 12 (2006) 9122.
[184] G. Dhanaraj, K. Byrappa, V. Prasad, M.e. Dudley, Handbook of Crystal Growth, Springer, Berlin Heidelberg, 2010.
[185] L.P. Nielsen, M. Schonning, S.V. Christensen, S.V. Hoffmann, Z.S. Li, P. Hofmann, F. Besenbacher, B.S. Clausen, Catal. Lett. Combined TPS, XPS, EXAFS, and NO-TPD study of the sulfiding of Mo/Al2O3, 73 (2001) 85.
[186] R.B. McClurg, R.C. Flagan, J. Colloid Interface Sci. Critical Comparison of Droplet Models in Homogeneous Nucleation Theory, 201 (1998) 194.
[187] B.J. McCoy, Ind. Eng. Chem. Res. Distribution Kinetics Modeling of Nucleation, Growth, and Aggregation Processes, 40 (2001) 5147.
[188] The Great Soviet Encyclopedia, 3rd ed., The Gale Group, Inc., 1970.
[189] M. Ramos, G. Berhault, D.A. Ferrer, B. Torres, R.R. Chianelli, Catalysis Science & Technology HRTEM and molecular modeling of the MoS2-Co9S8 interface: understanding the promotion effect in bulk HDS catalysts, 2 (2012) 164.
[190] P. Raybaud, J. Hafner, G. Kresse, S. Kasztelan, H. Toulhoat, J. Catal. Structure, energetics, and electronic properties of the surface of a promoted MoS2 catalyst: An ab initio local density functional study, 190 (2000) 128.
[191] M.J. Ledoux, B. Djellouli, Appl. Catal Comparative hydrodenitrogenation activity of molybdenum, Co–Mo and Ni–Mo alumina-supported catalysts, 67 (1990) 81.
[192] X. Ma, K. Sakanishi, T. Isoda, I. Mochida, Energ. Fuel. Quantum Chemical Calculation on the Desulfurization Reactivities of Heterocyclic Sulfur Compounds, 9 (1995) 33.
[193] X. Ma, K. Sakanishi, I. Mochida, Ind. Eng. Chem. Res. Hydrodesulfurization Reactivities of Various Sulfur Compounds in Vacuum Gas Oil, 35 (1996) 2487.

[194] Y. Shiraishi, K. Tachibana, T. Hirai, I. Komasawa, Ind. Eng. Chem. Res. A novel desulfurization process for fuel oils based on the formation and subsequent precipitation of S-alkylsulfonium salts. 5. Denitrogenation reactivity of basic and neutral nitrogen compounds, 40 (2001) 4919.
[195] Y. Shiraishi, K. Tachibana, T. Hirai, I. Komasawa, Ind. Eng. Chem. Res. A novel desulfurization process for fuel oils based on the formation and subsequent precipitation of S-alkylsulfonium salts. 3. Denitrogenation behavior of light oil feedstocks, 40 (2001) 3390.
[196] E. Furimsky, F.E. Massoth, Catal. Today Deactivation of hydroprocessing catalysts, 52 (1999) 381.
[197] L. Elst, S. Eijsbouts, A.D. van Langeveld, J.A. Moulijn, J. Catal. Deactivation of MoS2/Al2O3 in thiophene hydrodesulfurization: An infrared spectroscopic analysis by adsorbed CO, 196 (2000) 95.
[198] S. Eijsbouts, A.A. Battiston, G.C. van Leerdam, Catal. Today Life cycle of hydroprocessing catalysts and total catalyst management, 130 (2008) 361.
[199] B.M. Vogelaar, P. Steiner, A.D. van Langeveld, S. Eijsbouts, J.A. Moulijn, Applied Catalysis a-General Deactivation of Mo/Al2O3 and NiMo/Al2O3 catalysts during hydrodesulfurization of thiophene, 251 (2003) 85.
[200] F. Pedraza, S. Fuentes, M. Vrinat, M. Lacroix, Catal. Lett. Deactivation of MoS2 catalysts during the HDS of thiophene, 62 (1999) 121.
[201] V.N. Bui, D. Laurenti, P. Afanasiev, C. Geantet, Appl. Catal., B Hydrodeoxygenation of guaiacol with CoMo catalysts. Part I: Promoting effect of cobalt on HDO selectivity and activity, 101 (2011) 239.
[202] J.F. Paul, E. Payen, J. Phys. Chem. B Vacancy formation on MoS2 hydrodesulfurization catalyst: DFT study of the mechanism, 107 (2003) 4057.
[203] M. Brorson, A. Carlsson, H. Topsoe, Catal. Today The morphology of MoS2, WS2, Co-Mo-S, Ni-Mo-S and Ni-W-S nanoclusters in hydrodesulfurization catalysts revealed, 123 (2007) 31.
[204] I. Borges, Jr., A.M. Silva, A.P. Aguiar, L.E.P. Borges, J.C.A. Santos, M.H.C. Dias, J. Mol. Struc-Theochem Density functional theory molecular simulation of thiophene adsorption on MoS2 including microwave effects, 822 (2007) 80.
[205] M.R. de Brimont, C. Dupont, A. Daudin, C. Geantet, P. Raybaud, J. Catal. Deoxygenation mechanisms on Ni-promoted MoS2 bulk catalysts: A combined experimental and theoretical study, 286 (2012) 153.
[206] M.Y. Sun, A.E. Nelson, J. Adjaye, J. Catal. Ab initio DFT study of hydrogen dissociation on MoS2, NiMoS, and CoMoS: mechanism, kinetics, and vibrational frequencies, 233 (2005) 411.
[207] S. Brunet, D. Mey, G. Perot, C. Bouchy, F. Diehl, Appl. Catal., A On the hydrodesulfurization of FCC gasoline: a review, 278 (2005) 143.
[208] O.I. Senol, T.R. Viljava, A.O.I. Krause, Appl. Catal., A Effect of sulphiding agents on the hydrodeoxygenation of aliphatic esters on sulphided catalysts, 326 (2007) 236.
[209] S. Czernik, A.V. Bridgwater, Energ. Fuel. Overview of applications of biomass fast pyrolysis oil, 18 (2004) 590.
[210] B. Yoosuk, D. Tumnantong, P. Prasassarakich, Fuel Amorphous unsupported Ni-Mo sulfide prepared by one step hydrothermal method for phenol hydrodeoxygenation, 91 (2012) 246.

[211] B. Yoosuk, D. Tumnantong, P. Prasassarakich, Chem. Eng. Sci. Unsupported MoS2 and CoMoS2 catalysts for hydrodeoxygenation of phenol, 79 (2012) 1.
[212] J.H. Kim, X.L. Ma, C.S. Song, Y.K. Lee, S.T. Oyama, Energ. Fuel. Kinetics of two pathways for 4,6-dimethyldibenzothiophene hydrodesulfurization over NiMo, CoMo sulfide, and nickel phosphide catalysts, 19 (2005) 353.
[213] B. Delmon, Catal. Lett. New technical challenges and recent advances in hydrotreatment catalysis. A critical updating review, 22 (1993) 1.
[214] A.Y. Bunch, U.S. Ozkan, J. Catal. Investigation of the Reaction Network of Benzofuran Hydrodeoxygenation over Sulfided and Reduced Ni–Mo/Al2O3 Catalysts, 206 (2002) 177.
[215] S. Bezergianni, A. Kalogianni, A. Dimitriadis, Fuel Catalyst evaluation for waste cooking oil hydroprocessing, 93 (2012) 638.
[216] S. Bezergianni, A. Kalogianni, Bioresour. Technol. Hydrocracking of used cooking oil for biofuels production, 100 (2009) 3927.
[217] G. Vigli, A. Philippidis, A. Spyros, P. Dais, J. Agric. Food. Chem. Classification of edible oils by employing (31)P and (1)H NMR spectroscopy in combination with multivariate statistical analysis. A proposal for the detection of seed oil adulteration in virgin olive oils, 51 (2003) 5715.
[218] O.I. Senol, E.M. Ryymin, T.R. Viljava, A.O.I. Krause, J. Mol. Catal. A: Chem. Reactions of methyl heptanoate hydrodeoxygenation on sulphided catalysts, 268 (2007) 1.
[219] A.S. Berenblyum, T.A. Podoplelova, E.A. Katsman, R.S. Shamsiev, V.Y. Danyushevsky, Kinet. Catal. Kinetics and mechanism of the deoxygenation of stearic acid in the presence of palladium catalysts on alumina, 53 (2012) 595.
[220] D. Kubicka, J. Horacek, Appl. Catal., A Deactivation of HDS catalysts in deoxygenation of vegetable oils, 394 (2011) 9.
[221] E.M. Ryymin, M.L. Honkela, T.R. Viljava, A.O.I. Krause, Appl. Catal., A Insight to sulfur species in the hydrodeoxygenation of aliphatic esters over sulfided NiMo/gamma-Al2O3 catalyst, 358 (2009) 42.
[222] J.G. Immer, H.H. Lamb, Energ. Fuel. Fed-Batch Catalytic Deoxygenation of Free Fatty Acids, 24 (2010) 5291.
[223] H.G. Manyar, C. Paun, R. Pilus, D.W. Rooney, J.M. Thompson, C. Hardacre, Chem. Commun. Highly selective and efficient hydrogenation of carboxylic acids to alcohols using titania supported Pt catalysts, 46 (2010) 6279.
[224] L.D. Field, S. Sternhell, J.R. Kalman, Organic Structures from Spectra, Fourth ed., John Wiley& Sons Ltd, West Sussex, England, 2008.

Curriculum vitae

Candidate's full name: Haiping Zhang

Universities attended:

Master's of Science in Biochemical Engineering, Tianjin University, Tianjin, P. R. China, 2005-2007

Bachelor's of Science in Biological Engineering, Tianjin University, Tianjin, P. R. China, 2001-2005

Publications:

1. Zhang, Haiping; Lin, Hongfei; Wang, Weizhi; Zheng, Ying; Hu, Peijun. Hydroprocessing of waste cooking oil over a dispersed nano catalyst: Kinetics study and temperature effect. Applied catalysis B: Environmental, 150 (2014) 238– 248.
2. Zhang, Haiping; Lin, Hongfei; Zheng, Ying. The role of cobalt and nickel in deoxygenation of vegetable oils. Applied catalysis B: Environmental, 160–161 (2014) 415–422.
3. Zhang, Haiping; Khatibi, Mona; Zheng, Ying; Lee, Kenneth; Li, Zhengkai; Mullin, Joseph V.. Investigation of OMA formation and the effect of minerals. Marine Pollution Bulletin, 60 (2010) 1433-1441.
4. Zhang, Haiping; Bai, Shu; Xu, Liang; Sun, Yan. Fabrication of mono-sized magnetic anion exchange beads for plasmid DNA purification. Journal of Chromatography B, 877 (2009) 127-133.
5. Zhang, Haiping; Lin, Hongfei; Zheng, Ying. Understanding of the effect of synthesis temperature on the crystallization and activity of nano-MoS_2 catalyst. Submitted.

6. Zhang, Haiping; Lin, Hongfei; Zheng, Ying. Hydrotreatment of light cycle oil over a dispersed MoS_2 catalyst. Submitted.
7. Zhang, Haiping; Lin, Hongfei; Zheng, Ying. Deactivation mechanism of unsupported MoS_2: a comparative study with supported catalyst**.** Submitted.
8. Zhang, Haiping; Lin, Hongfei; Zheng, Ying. Application of uniform design method in the optimization of hydrothermal synthesis for nano MoS_2 catalyst with high HDS activity. Submitted.
9. Zhang, Haiping; Lin, Hongfei; Zheng, Ying. Hydrothermal synthesis of nanocrystalline molybdenum sulfide: effect of medium acidity. To be submitted.
10. Zhang, Haiping; Lin, Hongfei; Zheng, Ying. Increase of curvature in the MoS_2 basal plane using hydrothermal method with organic solvent. To be submitted.
11. Zhang, Haiping; Lin, Hongfei; Zheng, Ying. The effect of cobalt on hydrothermal synthesis of unsupported MoS_2 and hydrotreatment of light cycle oil. To be submitted.
12. Zhang, Haiping; Lin, Hongfei; Zheng, Ying. The role of surfactant in hydrothermal synthesis of unsupported MoS_2 catalyst. To be submitted.
13. Dong, Zhen; Zhang, Haiping; Whidden, Tom; Zheng, Ying; Zhao, Jianshe. Study of low pressure Fischer-Tropsch synthesis for diesel fuel using a cobalt-based catalyst. Summited.
14. Yao, Songdong; Zhang, Haiping; Rogers, Kyle; Zheng, Ying; Guan, Weiwei. Hydrotreating performances of NiMo, CoMo, and NiW catalysts over an alumina-zeolite support. To be submitted.

15. Zhang, Xuezhu; Ma, Lijuan; Zhang, Haiping; Gan, Yiru. Determination of Tanshinones in Salvia miltiorrhiza Bunge by high-performance liquid chromatography with a coulometric electrode array system. Analytical Letters, 41 (2008), 1047-1058.
16. Ma, Lijuan; Zhang, Xuezhu; Zhang, Haiping; Gan, Yiru. Development of a fingerprint of Salvia miltiorrhiza Bunge by high-performance liquid chromatography with a coulometric electrode array system. Journal of Chromatography B, 846 (2007) 139-146.

Conference Presentations:

Oral Presentations:

1. Zhang, Haiping; Lin, Hongfei; Zheng, Ying. Highly dispersed nanocrystalline molybdenum sulfide prepared by hydrothermal synthesis as an unsupported model catalyst for ultra clean diesel, 21st Canadian Symposium on Catalysis, Banff, Alberta, 2010.
2. Zhang, Haiping; Zheng, Ying; Lee, Kenneth; Li, Zhengkai; Mullin, Joseph V. Investigation of OMA Formation and the Effect of Minerals, 22nd 33rd AMOP Technical Seminar on Environmental Contamination and Response, Halifax, Nova Scotia, Canada, 2010.
3. Zhang, Haiping; Lin, Hongfei; Zheng, Ying. Hydrodeoxygenation of waste cooking oil over a dispersed nano catalyst: Kinetics study, 22nd Canadian Symposium on Catalysis, Quebec City, Quebec, Canada, 2012.
4. Zhang, Haiping; Lin, Hongfei; Zheng, Ying. The role of Co and Ni in Hydrodeoxygention of canola oil, 63rd Canadian Chemical Engineering Conference, Fredericton, New Brunswick, Canada, 2013.

5. Zhang, Haiping; Lin, Hongfei; Zheng, Ying. Mechanism Study of Hydrothermal Synthesis of Dispersed MoS_2, 63rd Canadian Chemical Engineering Conference, Fredericton, New Brunswick, Canada, 2013.

Poster Presentations:

1. Zhang, Haiping; Lin, Hongfei; Zheng, Ying. "Hydrothermal synthesis of highly dispersed nanocrystalline MoS_2 and CoMoS", 21st International Symposium on Chemical Reaction Engineering, Philadelphia, PA, USA, 2010